# DOCTOR OF SCIENCE (DSC)

## Ion-materials interactions and their application

Whitlow, Harry James

*Award date:*
1998

*Awarding institution:*
University of Bath

# Ion-Materials Interactions and their Application

Submitted by Harry James WHITLOW

for the degree of DSc
of the University of Bath 1998





ProQuest LLC
789 East Eisenhower Parkway
P.O. Box 1346
Ann Arbor, MI 48106-1346

Dokumentutgivare: Avdelning för Kärnfysik, Lunds tekniska högskola

Dokumentnamn: D.Sc. avhandling

Dokumentbeteckning:

Handläggare:

Utgivningsdatum: 980318

Ärendebeteckning:

Författare

Harry J. WHITLOW



Dokumenttitel och undertitel

Ion materials interactions and their application
D.Sc. thesis submitted by Harry James WHITLOW for the degree of Doctor of Science of the University of Bath 1998

Referat (sammandrag)

The interaction of energetic ions and other charged particles with solid matter leads to a wealth of physical processes. This thesis comprises a collection of papers and an introductory commentary, which explore some aspects of how these interactions may be used for:

(i) Characterisation of thin surface layers of material,
(ii) Characterisation of energetic charged particles, and
(iii) Modification of materials by ion bombardment.

In (i) Elastic Recoil Detection using a detector system for measurement of Time of Flight and kinetic energy of recoiling target atoms has been developed as a quantitative method for elemental depth profiling of thin (0.5-1 $\mu$m) surface layers. This method has been applied to the study of reactions of metal/III-V structures, which are of importance for the semiconductor industry. (ii) MeV-ion – materials interactions have been used as the basis for developing Si p-i-n detectors for the CHICSi programme which will undertake experimental studies of heavy ion collisions at intermediate energies. This involved development and testing of extremely thin (10-12 $\mu$m) Si $\Delta$E detectors for characterising light- and intermediate mass charged particles as well as calibration of Si p-i-n detectors and their susceptibility to radiation damage. (iii) Nuclear Reaction Analysis (NRA) with resonant nuclear reactions has been used to study modification of material with ion beams. In the first study, the accumulation of fluorine in $BF_2^+$ ion implanted $WSi_2$ solid diffusion sources was investigated. The second study investigated if there was a correlation between photoluminescence and segregation of hydrogen to buried heterojunctions in plasma-etched III-V quantum-well structures. The ion bombardment in this case was during etching in an $Ar+CH_4$ plasma using an Electron Cyclotron Resonance (ECR) source.

Referat skrivet av
Förf

Förslag till ytterligare nyckelord: Ion Beam Analysis, Elastic Recoil Detection, Nuclear reaction Analysis, charged Particle detectors, Deleta-E detectors radiation damage, ion implantation, plasma etching, GaAs, Si, InP, metallisation

Klassifikationssystem och -klass(er)

Indextermer (ange källa)

Omfång: 181 sidor

Övriga bibliografiska uppgifter

Språk: engelska

Sekretessuppgifter

ISSN

ISBN

Dokumentet kan erhållas från: Avdelningen för kärnfysik
Lunds tekniska högskola
Box 118, 221 00 Lund

Mottagarens uppgifter

Pris

# ABSTRACT

The interaction of energetic ions and other charged particles with solid matter leads to a wealth of physical processes. This thesis comprises a collection of papers and an introductory commentary, which explore some aspects of how these interactions may be used for:

(i) Characterisation of thin surface layers of material,

(ii) Characterisation of energetic charged particles, and

(iii) Modification of materials by ion bombardment.

In (i) Elastic Recoil Detection using a detector system for measurement of Time of Flight and kinetic energy of recoiling target atoms has been developed as a quantitative method for elemental depth profiling of thin (0.5-1 μm) surface layers. This method has been applied to the study of reactions of metal/III-V structures, which are of importance for the semiconductor industry. (ii) MeV-ion – materials interactions have been used as the basis for developing Si p-i-n detectors for the CHICSi programme which will undertake experimental studies of heavy ion collisions at intermediate energies. This involved development and testing of extremely thin (10-12 μm) Si ΔE detectors for characterising light- and intermediate mass charged particles as well as calibration of Si p-i-n detectors and their susceptibility to radiation damage. (iii) Nuclear Reaction Analysis (NRA) with resonant nuclear reactions has been used to study modification of material with ion beams. In the first study, the accumulation of fluorine in $BF_2^+$ ion implanted $WSi_2$ solid diffusion sources was investigated. The second study investigated if there was a correlation between photoluminescence and segregation of hydrogen to buried heterojunctions in plasma-etched III-V quantum-well structures. The ion bombardment in this case was during etching in an $Ar+CH_4$ plasma using an Electron Cyclotron Resonance (ECR) source.

# DECLARATION

The work presented in this thesis is my own work. The extent of my contribution to papers published with co-authors is specified in Appendix I.

Lund, Sweden, the 18 March 1998

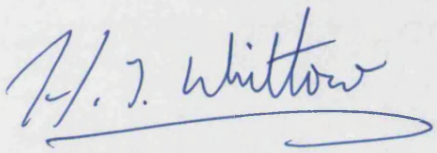

Harry J. WHITLOW

Witnessed,

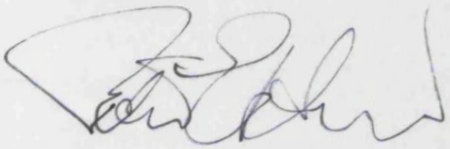

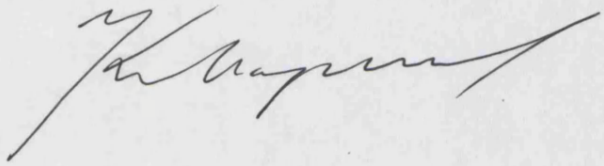

# DEDICATION

*To my family.*

# TABLE OF CONTENTS

**ION-MATERIALS INTERACTIONS AND THEIR APPLICATION** ..... 1

**ABSTRACT** ..... 1

**DECLARATION** ..... 3

**DEDICATION** ..... 4

**TABLE OF CONTENTS** ..... 5

**PREFACE** ..... 8

**ACKNOWLEDGEMENTS** ..... 9

**PART-I** ..... 11

**CHAPTER I INTRODUCTION** ..... 12

1. THE INTERACTION OF ENERGETIC IONS AND MATTER ..... 12

*1.1.1 Ion Beam Analysis* ..... *13*

*1.1.2 Charged-Particle Detection and Spectroscopy* ..... *14*

*1.1.3 Ion Beam Modification of Materials* ..... *14*

**CHAPTER 2 CHARACTERISATION OF THIN LAYERS USING ELASTICALLY SCATTERED RECOILS** ..... 15

The naming of the technique ..... 16

*2.1.1 Fundamentals* ..... *17*

*2.2.1 Initial Development and Application of ToF-E Elastic Recoil Detection in Si Microelectronic Technology* ..... *21*

Paper I: **Quantitative Mass and Energy Dispersive Recoil Spectrometry: Resolution and Efficiency Considerations.** H.J. Whitlow, G. Possnert and C.S. Petersson, Nucl. Instrum. and Methods B27(1987)448. ..... 21

Paper II: **Mass-dispersive recoil spectrometry studies of oxygen and nitrogen redistribution in ion beam –synthesised buried oxynitride layers in silicon.** H.J. Whitlow, C.S. Petersson, K.J. Reeson and P.L.F. Hemment, Appl. Phys. Lett. 52(1988)1871 ..... 21

*2.2.2 Energy and Mass calibration* ..... *22*

Paper III: **Multivariate Analysis Method for Energy Calibration and Improved Mass Assignment in Recoil Spectrometry**. M. El Bouanani, M. Hult, L. Persson, E. Swietlicki, M. Andersson, M. Östling, N.

Lundberg, C. Zaring, D.D. Cohen, N. Dytlewski, P.N. Johnston, S.R. Walker, I.F. Bubb and H.J. Whitlow, Nucl. Instrum. and Methods B94(1994)530. 22

*2.2.3 Detector efficiency* 23

Paper IV: **Thermally grown $SiO_2$ films for Elastic Recoil Detection Analysis.** H.J. Whitlow, A.B.C. Andersson and C.S. Petersson, Nucl Instrum. and Methods B36(1989)53. 23

*2.2.4 Mass separating power* 24

Paper V: **Mass Resolution of Recoil Fragment Detector Telescopes for 0.05-0.5A MeV Heavy Recoiling Fragments,** H.J. Whitlow, B. Jakobsson and L. Westerberg, Nucl. Instrum. and Methods A310(1991)636.24

Paper VI: **Empirical characterisation of Mass Distribution Broadening in ToF-E Recoil Spectrometry.** M. Hult, M. El Bouanani, L. Persson, H.J. Whitlow, M. Andersson, C. Zaring, M. Östling, D.D: Cohen, N. Dytlewski, I.F. Bubb, P.N. Johnston and S.R. Walker, Nucl. Instrum. and Methods B101(1995)263. 25

*2.2.5 Analysis of III-V semiconductor structures* 26

Paper VII: **High-resolution recoil spectrometry for separate characterisation of Ga and As in $Al_xGa_{(1-x)}As$ structures.** M. Hult, H.J. Whitlow and M. Östling, Appl. Phys. Lett. 60(1992) 219. 26

Paper VIII: **Rapid Thermal Annealing Induced Reactions of Co/GaAs Thin Film Structures using Mass and Energy Dispersive Recoil Spectrometry.** M. Hult, H.J. Whitlow, M. Östling, M. Andersson, I. Linderberg, K. Ståhl J. Appl. Phys. 75(1994)835. 26

Paper IX: **Formation of thin films of $CoSi_2$ on GaAs.** M. Hult, L.Persson, M. El Bouanani, H.J. Whitlow, M. Andersson, M. Östling, N. Lundberg, C. Zaring, K. Georgesson, D.D. Cohen, N. Dytlewski, P.N. Johnston and S.R. Walker. J. Appl. Phys. 77(1995)2435. 28

**CHAPTER 3 CHARACTERISATION OF MEV CHARGED PARTICLES WITH SILICON DETECTORS 29**

3.1 SILICON CHARGED PARTICLE DETECTOR BASICS 29

Paper X: **Measurements of the Response Function of Silicon Diode Detectors for Heavy Ions using a Time of Flight Technique,** R. Ghetti, B. Jakobsson and H.J. Whitlow, Nucl. Instrum. and Methods A317(1992)235. 32

**Paper XI: Thin Detectors for the CHICSi ΔE-E Telescope.** L. Evensen, T. Westgaard, V. Avdeichikov, L. Carlén, B. Jakobsson, Y. Murin, A. Oskarsson,, A.Siwek, H.J. Whitlow, E.J. Van Veldhuizen, L. Westerberg and M. Guttormsen. IEEE Trans. Nucl. Sci. 44(1997) 629. 33

**Paper XII: Effects of Energy Deposition in Silicon p-i-n Diode Detectors.** H.J. Whitlow, S.J. Roosendaal, M. El Bouanani, R. Ghetti, P.N. Johnston, B. Jakobsson, R. Hellborg, H. Petersson, P. Omling, Z. Wang and the CHIC collaboration. Nuclear Instrum. and Methods B (In press). 34

Paper XIII: **Extremely thin Silicon ΔE detectors for Ion Beam Analysis.** H.J. Whitlow, T. Winzell and G. Thungström, Nucl. Instrum. and Methods B (In press). 35

**CHAPTER 4 MODIFICATION OF MATERIALS WITH ION BEAMS 3**

4.1 ION BEAM MATERIALS MODIFICATIONS 36

Paper XIV: **Ion-Implantation Induced Fluorine Agglomeration in Tungsten Disilicide Prepared by Low Pressure Chemical Vapour Deposition.** C.S. Petersson, H.J. Whitlow, J. Keinonen, F.M. d'Heurle, F. Le Goues, R.V. Joshi, G. Scilla and O. Thomas, Nucl. Instrum. and Methods B40/41(1989)595. 37

Paper XV: **$^1H(^{15}N,\alpha\gamma)^{12}C$ Nuclear Resonance Broadening Measurements of Hydrogen Incorporation during Plasma Etching of GaAs and $Ga_xIn_{(1-x)}As$ Quantum Wells.** L. Person, H.J. Whitlow, J. Keinonen,

P. Torri, I. Maximov, L. Samuelsson, K. Knox and K.G. Malmqvist. Nucl. Instrum. and Methods B89(1994)346 ..... 38

PART II - **RESEARCH PAPERS** ..... **40**

**APPENDIX 1 EXTENT OF CONTRIBUTION TO THE PAPERS INCLUDED IN THIS THESIS** ..... **153**

**APPENDIX 2 CURRICULUM VITAE AND SUMMARY OF RESEARCH AND TEACHING WORK** ..... **155**

APPENDIX 3 **LIST OF SCIENTIFIC PUBLICATIONS** ..... **169**

**REFERENCES** ..... **178**

# PREFACE

This thesis comprises selected papers submitted for award of the degree of Doctor of Science at the University of Bath. The scientific works included were selected to provide an objective and balanced view of my research activities in the field of ion-solid matter interactions, over the past decade or so. The criteria for selection were;

(i) That the work has been published, or accepted for publication, in a peer-reviewed archiving journal of a high international standard.

(ii) That there is minimum overlap with work submitted for the Swedish "oavlönad docent" status (literally translated: unpaid reader/associate professor).

(iii) I have made a substantial contribution to the paper.

Unfortunately, this proved to be a difficult task because only a few publications have yet appeared in print from the CHICSi project which has constituted a significant part of my research effort since 1990. In common with similar projects in the high-energy nuclear physics community, the papers on these research activities will be published when the commissioning phase of the work is complete. Furthermore, the research has spanned a wide range of topics. Therefore, *to provide structured guidance to the reader and emphasise interrelations between papers spanning a number of research fields, an introductory section is included.* This introduction is intended to be a commentary and ***not*** a detailed review.

Research with accelerators, because of its nature, is characterised by collaborative teamwork. It follows that the resulting papers are multi-author works. Moreover, the house rules of different journals for multi-author lists and affiliations implies that the extent of the contributions from the various authors often cannot be judged from the order of the list of authors. My contribution to each of the papers is thus specified in Appendix I.

# ACKNOWLEDGEMENTS

Along the path of becoming a researcher, I have had the great privilege of working under the leadership of very eminent scientists. My first steps in research were taken at the University of Sussex under the guidance of my D. Phil. supervisor Professor Sir Michael Thompson and subsequently Professor Peter Townsend. My mentors as a postdoctoral researcher were Professor Hans Henrik Andersen in Århus, Professor Juhani Keinonen in Helsinki and Rektor Professor Bo Sundqvist in Uppsala. Subsequently I worked under the leadership of Professor Sture Petersson at the Royal Institute of Technology, Stockholm and Professor Klas Malmqvist in Lund. Each one of these people has influenced my development in complementary and positive ways.

I also have learnt a great deal from senior collaborators. Space does not permit me to do more than mention the names of, Prof. Peter Treacy, Prof. John O' Connor, Barry Farmery, Dr. David Hole, dr. Jørgen Bøttiger, dr. Flemming Besenbacher, Prof. Asko Antilla, doc. Mikko Hautala, doc. Eero Rauhala, doc. Jyrki Risannen, doc. Armas Fontell, Prof. Mikael Östling, Prof. Göran Possnert, Dr. Karen Reeson, Prof. François d'Heurle, Prof. Bengt Svensson, A. Prof. Peter Johnston, Prof. Ian Bubb, Dr. David Cohen, Dr. Nick Detlyski, Prof. Bo Jakobsson, doc. Ragnar Hellborg, Prof. Lars Samuelsson, doc. Lars Montelius, doc. Lars Westerberg, dr. Margaretha Andersson, Dr. Mohamed El Bouanani, Prof. John Knox, Prof. Yugang Wang, Dr. Lars Evensen and Dr. Trond Westgaard.

I am also grateful to the students whom I have co-supervised or worked closely with. In rough chronological order Dr. Maria Erola, Doc. Perrti Tikkanen, dr. Carina Zaring, dr. Thomas Ericsson, dr. Hao Jiang, dr. Anders Ingemarsson, dr. Erik Johannson, Scott Walker, dr. Ivan Maximov, tek. lic. Göran Thungström. Special thanks are due to my "own" Ph.D. students, dr. Roberta Ghetti, dr. Mikael Hult, dr. Leif Persson, tek. lic. Yanwen Zhang and fil. lic. Thomas Winzell as well as project students, Tom Sørensson, Bjarne Stenum, Sten Køgh Nielsen, Christina Andersson, Anneke Kleinpenning, Sander Roosendaal, Annette Gimsenius, Jacek Jaworowski, Mats Leandersson and Patrik Jönsson

This work and that of my co-authors which is reported here has been financially supported by The Science and Engineering Research Council, North Atlantic Treaty Organisation, The British Council, The Academy of Finland, The Nordic Committee for Accelerator based Research, Knut and Alice Wallenberg Foundation, The Royal Physiographical Society in Lund, The Australian, Department of Industry Trade and Commerce, Australian Institute for Nuclear

Science and Engineering, The Werner Gren Foundation, The Swedish Institute, The Swedish Natural Science Research Council and The Swedish Board of Technical Development (STU-F) and NFR/NUTEK under the auspices of the Nanometer Structure Consortium.

The most vital contribution has been the support of my family. Even from a young age, I had a interest in science that my parents encouraged and supported through School, Technical College and University. Accelerator-based research imposes the need to spend late-nights in the laboratory and frequent periods away from home. I am therefore very grateful to my wife Ingegerd, and our children, Sarah, Susan and Caroline who have always been a great support, even if it has been hard at times. It is no understatement to say that the work in this thesis would not have come into being without their love and support.

# PART-I

# INTRODUCTORY COMMENTARY

# CHAPTER 1

# INTRODUCTION

## 1. THE INTERACTION OF ENERGETIC IONS AND MATTER

It is today well established that matter is made up of atoms, which in turn are constituted of nuclei and electrons. It follows that an energetic projectile ion*, consisting of a nucleus and associated electrons can interact with the electrons and nuclei that make up the target. These interactions take the form of nucleus-nucleus and nucleus-electron scattering as well as electron transfer between the electronic systems of the ion and target. At MeV energies the ion nuclei have enough energy to excite nuclear reactions in some nuclei, knock out target nuclei from their equilibrium positions thereby creating energetic target atoms, as well as excite inner and outer shell electrons in the electronic structure of the target. [1] The fact that the energy is transferred to both the nuclei and electronic system leads to a wide plethora of coupled processes taking place as the result of impingement of a single MeV ion. Figure 1.1 illustrates the complexity, diversity and the *main* interrelation of the processes taking place in a solid material at equilibrium on which a single MeV energy ion impinges. Inspection of Figure 1 reveals that, the path leading to a particular process may be very indirect and the energy associated with that process may travel by several different routes. A general observation from Figure 1.1 is that ion impingement can result in:

- Heating (phonon generation and meV excitations of the electronic system).
- The emission of radiation and particles from the material.
- Structural changes in the material.

The latter not only includes stored (Wigner) energy in defects but also changes in the morphology and molecular structure such as chemical changes (e.g. cross-linking and scission of polymer chains).

In this thesis, we shall be exclusively concerned with the latter two effects. However, it is noted that thermal and non-linear phonon effects may explain the intact sputtering of labile biomolecules and surface crater formation resulting from MeV ion bombardment. Moreover,

---

* The term "ion" here is used to denote an accelerated atom. The charge state is usually indeterminate and may even be zero (neutral).

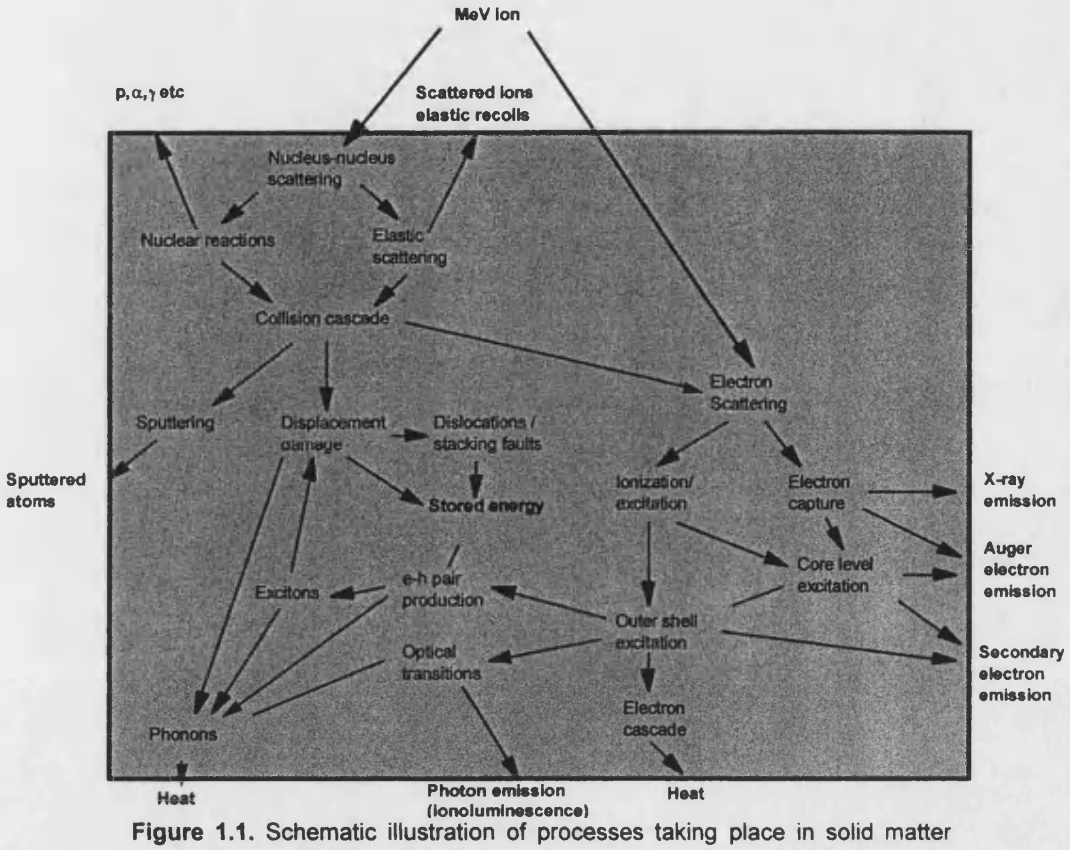


**Figure 1.1.** Schematic illustration of processes taking place in solid matter resulting from bombardment with a MeV ion.

phonon measurement is of technical importance for detecting dark matter [2], X-rays [3] and elusive double-beta decays[4].

### 1.1.1 Ion Beam Analysis

*Ion Beam Analysis* is a generic term which describes analytic methods where samples is irradiated with ions and signals from the interactions shown in Fig. 1.1 are used to characterise the target material (sample). For example, the well-established Particle Induced X-ray Emission (PIXE) method [5,6] is based on energy dispersive measurements of the X-rays emitted when a sample is irradiated with MeV ions. Other characteristic signals, which have been used for analysis, are sputtered neutrals and ions, charged particles, elastically-recoiling target atoms, X-ray and γ-ray photons, secondary and Auger electrons, optical photon emission, and induced charge. In this thesis, research on the use of elastically scattered recoiling target atoms as well as γ-rays emitted from characteristic nuclear reactions [12] have been used to investigate some effects associated with low energy ion bombardment.

### 1.1.2 Charged-Particle Detection and Spectroscopy

In charged particle detection, the deposited energy causes production of a measurable signal. The signal may originate from any of the processes in Fig. 1.1. E.g. *prompt* photon emission as in the case of the well known NaI (Tl) scintillation spectrometer [7] where a pulse of light indicates the impingement of a particle. Furthermore, the size of the signal produced is a measure of the amount of energy deposited in the material by the incident particle. Another example is thermoluminescence [8] dosimetry where modification of the electronic configuration of the material is used for *integral* measurements of radiation dose. Generally one is often interested not only in registering the occurrence of a charged particle but also determining other parameters such its energy, mass, nuclear charge and momentum vector. One approach is to combine dispersing magnetic and electrostatic elements to form a *spectrometer* or *hodoscope*, another is to make use of differences in the interaction with matter for different charged particles to make multidispersive measurements.

### 1.1.3 Ion Beam Modification of Materials

Bombardment with MeV ions presents a variety of possibilities for modification of materials. The simplest form is ion implantation where foreign atoms are introduced into a host. This is widely used for doping of semiconductors because the process is inherently more controllable that diffusion. If the dose is sufficiently high and the implanted ion species reacts chemically with silicon ion implantation may be used to form buried and surface layers of metalloid and oxide phases [20]. MeV ion bombardment can also introduce modification via the energy deposited in electronic excitation. A well-known example is ion tracks in insulating materials. As the ion penetrates solid material about half the energy loss is due to exchange electrons from, and excitation of electrons within, a radius [1] of ~0.5 nm of the ion trajectory. For a 65 MeV $Cu^+$ ion in a typical insulator dE/dx ~3.5 keV $nm^{-1}$, which corresponds to average excitation of 45 eV per atom within 0.5 nm radius. This is comparable with the ionisation energy for the II-IV ionisation state for many elements. An uncompleted area in the jigsaw puzzle is exactly how this intense ionisation around the ion track is coupled to low-energy excitations. (E.g. the instigation of structural changes at the molecular level and heat in the form of phonons and electron motion.) However, we note that it is now believed that electronic excitation can lead to displacement damage similar for nuclear energy deposition through self-trapped excitons.

# Chapter 2

# CHARACTERISATION OF THIN LAYERS USING ELASTICALLY SCATTERED RECOILS

## 2.1 ELASTIC RECOIL DETECTION

A major driving force in the development of Ion Beam Analysis (IBA) techniques since the 1960's has been their use for quantitative analysis of thin films in microelectronic research. IBA techniques based on MeV ions such as Rutherford Backscattering Spectrometry [9,10,11] (RBS) are especially useful for this application because they are inherently quantitative and yield elemental depth distribution information. Although RBS is applicable to a wide range of microelectronic analysis applications, it is limited for the following reasons:

(i) The low sensitivity for light elements such as nitrogen because of small scattering cross sections.

(ii) Superposition of the light element signal on a background from heavier matrix elements.

RBS thus is difficult to apply for some important classes of microelectronic structures such as light and medium heavy elements on III-V substrates, thin oxide and nitride layers and polymer/semiconductor systems. Nuclear Reaction Analysis (NRA) [12, Papers XIV, XV,19] can often be used (e.g. Chapter 4 below) to circumvent this problem, however these are limited to analysis of a particular isotope ($^{13}C$, $^{15}N$, $^{18}O$ etc.) which often have a low natural abundance. Furthermore, there is a lack of suitable nuclear reactions for the analysis of medium heavy elements ($Z > 20$).

In order to overcome the difficulties associated with conventional IBA techniques, interest has been focused on Elastic Recoil Detection Analysis (ERD (A)) techniques [19,22,23]. These techniques are based on measurement of target atoms that recoil out of the sample as the result of high-energy ion bombardment.

Sputter profiling methods are often named as well-established sensitive analytical depth profiling techniques for light and heavy elements. Some brief comment is therefore justified as

why ERD has been developed. Whilst it is quite true that Secondary Ion Mass Spectrometry (SIMS) has a high sensitivity and sputter XPS/Auger can even yield chemical information, ***SIMS and sputter XPS/Auger are simply not inherently quantitative methods.*** The principal causes for this are ion bombardment induced artefacts such as ion beam induced segregation [13,14,17,15], ion beam mixing [16] and composition transients in the sputtered flux etc. Consequently, the sputtered flux and surface composition will depend on the previous sputtering history [15]. It follows the analytical signal from the surface of sputtered ions will depend in some complex way on the depth distribution of the elements present in the sample. This difficulty is particularly acute for interface structures, which are an important class of structures encountered in microelectronic research and development. The situation is even more complex and difficult for SIMS because the ionisation yield depends on the electronic nature of the surface. This is not to say the techniques are totally without value as a quantitative analytical tool. However, the author has often observed the uncritical adoption and use of these instruments in analytical situations where they are poorly suited.

*The naming of the technique*

The naming of the technique has been diffuse over the years. Elastic Recoil Detection Analysis (ERDA), Elastic Recoil Detection (ERD), Recoil Detection (RD), High Energy Elastic Recoil Detection (HEERD), Heavy Ion Ion Elastic Recoil Detection Analysis (HIERDA), Forward Recoil Elastic Scattering (FRES), Recoil Spectrometry (RS) are some of the names (with associated acronym) used in the early literature. The name Elastic Recoil Detection Analysis was used by L'Ecuyer et al [24] who are often attributed with the first report of the technique. (Their report is preceded by that of Cohen et al [21]). These authors have made simple detection measurements where hydrogen concentrations were determined. More recently true spectroscopic measurements have been made. The present author, and co-workers proposed, and used the term *Recoil Spectrometry (RS)* on the grounds; (i) it was concise, (ii) it emphasised the fact that spectroscopic measurements are made the elemental depth distributions, (iii) it indicated the close similarity to the well-established Backscattering Spectrometry technique and (iv) there is no reason why the recoils need the result of elastic scattering. A recommendation was made at the 12$^{th}$ International Ion beam Conference [18] in the favour of the more common ***Elastic Recoil Detection (ERD), or Elastic Recoil Detection Analysis (ERDA). It was also recommended that optional prefixes be used to denote the primary beam or type of measurement*** (e.g. $^{12}$C ERD, coincidence ERD). In compliance with this recommendation, later publications here have used ERDA whilst early publications use RS to denote the technique.

### 2.1.1 Fundamentals

The underlying basis of ERD is binary elastic scattering of nuclei, which is illustrated schematically in Figure 2.1. For our purpose, we may neglect the internal structure of these nuclei and assume that they can be represented by massive point charges.

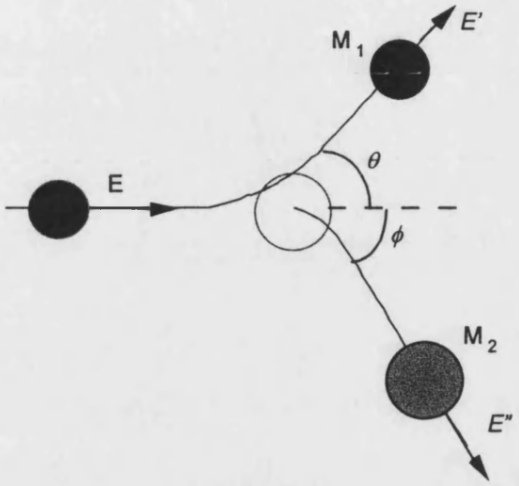


**Figure 2.1.** Schematic illustration of a binary elastic collision between two atomic nuclei.

The fraction of the incident particle energy $E$ which is transferred to the recoiling target atom in the elastic collision is governed only by the two masses $M_1$ and $M_2$ and the recoil angle $\phi$ in the laboratory frame according to [25]:

$$E'' = \Lambda E$$
$$\Lambda = \frac{4M_1M_2}{(M_1 + M_2)^2}\cos^2\phi \tag{2.1}$$

The probability of recoiling at angle $\phi$ is for a Coulomb interaction force, (which is appropriate for scattering from bare nuclei) can be expressed as the differential statistical cross section $d\sigma/d\Omega$, which is the probability per incident ion for scattering into a solid angle interval of $d\sigma$ steradian.

$$\frac{d\sigma}{d\Omega} = \left[\frac{Z_1Z_2e^2(1 + M_1/M_2)}{8\pi\varepsilon_0 E}\right]\frac{1}{\cos^3\phi} \quad \text{(SI)} \tag{2.2}$$

The technique is very similar to RBS and by analogy with RBS and for the geometry shown in Fig. 2.2 the energy difference $\Delta E$ between recoils of element $A$ from the surface and depth $x$ in the material is:

$$\Delta E = E_1 - E_2 = {}_{Ion}[\varepsilon]^A_{AB}(Nx) \tag{2.3}$$

The *stopping cross-section factor* [26] is:

$$ {}_{Ion}[\varepsilon]^{A}_{AB} = \frac{\Lambda_{Ion}\varepsilon_{in}}{\cos\theta_1} + \frac{{}_{A}\varepsilon_{out}}{\cos\theta_2} \tag{2.4} $$

($Nx$) is the number of atoms per unit area in the layer (Fig. 2.2) extending from the surface to depth x. Similarly, the signal height from element $A$ is,

$$ H_a = \frac{N_A}{N_{AB}}\left(\frac{d\sigma_A}{d\Omega}\right)_{Ion}\frac{E_{ch}}{[\varepsilon]^{A}_{AB}}\eta_A \tag{2.5} $$

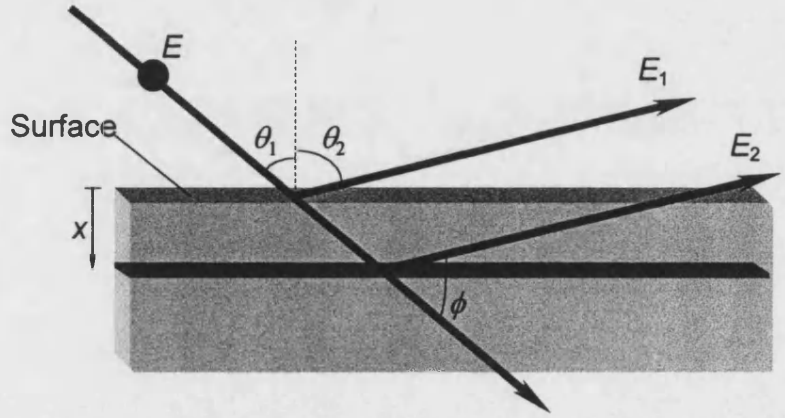


**Figure 2.2.** Geometrical configuration for Elastic Recoil Detection Analysis.

$N_A/N_{AB}$ is the atomic fraction of $A$ in the target $AB$, $E_{ch}$ is the energy channel width and $\eta_A$ the detection efficiency for recoils of element $A$. *These equations are important because they constitute the basis for quantitative analysis with ERD.* Equations 2.3-2.5 differ from their RBS counterparts only in that additional index is needed in the stopping cross section factor ${}_{Ion}[\varepsilon]^{A}_{AB}$ to account for the different atomic species of the ion and outgoing recoil atoms. The detector efficiency $\eta_A$ is usually omitted in RBS because it is infinitesimally less than unity for Si charged-particle detectors. In RBS, the analytical information is extracted from the energy distribution of the scattered ions. (Fig. 2.3(a)) These ions originated in the ion source of the accelerator and hence the energy distribution is a superposition of information from, (i) the mass of the elements in the sample and (ii) their depth distribution. This implies that it is not possible to uniquely determine the depth distributions of individual elements when the energy signals are overlapping. In ERD (Fig. 2.3(b)) the recoiling target atoms themselves are detected. The energy spectrum, in RBS carries superposed depth and elemental mass information. However, in contrast to RBS the contributions from different elements to the composite ERD spectrum can be separated by using detector systems that determine the elemental identity of each recoil. A number of schemes can be to achieve this separation. One of the most straightforward is to use a transmission geometry where the scattered ion and recoil are simultaneously detected [27].

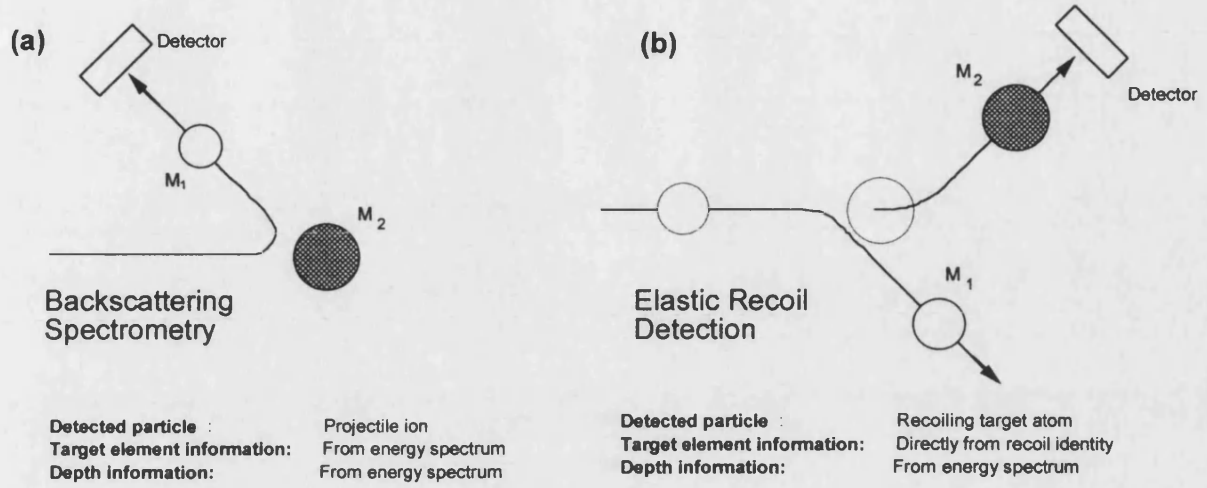


**Figure 2.3.** Detected particle modes in (a) RBS and (b) ERD.

Kinematics may then be used to assign the recoil identity. This was the first reported form of multidispersive ERD measurement [28]. The measurement of scattered ion and recoil are carried out in-coincidence. This makes coincidence ERD especially useful for measuring trace amounts of light elements in a Nuclear Microprobe in Scanning Transmission Ion Microscopy (STIM) mode, [29] because the background contributions to the signals are inherently low even when the detectors subtend large solid angles. This type of measurement is not well suited to research in semiconductor technology because a thin sample is required. Thinning semiconductor samples is a difficult and tedious process, which introduces a severe risk of inadvertent sample modification. For this reason detection of the recoils in a glancing-incidence glancing-exit reflection geometry, (Fig. 2.2) is preferred because no sample preparation is needed. Magnetic and electrostatic spectrometers have the best energy resolution for this type of measurement, however their use is restricted by small solid angle and the fact the recoil charge state distribution must be established for quantitative analysis.

Another approach, which is discussed in Chapter 3, is to use a ΔE-E detector telescope to measure the effective charge on the recoil nucleus (atomic number) and energy. Mainly gas ionisation detectors have been used. These are limited by the energy-loss in the entrance window of the gas cell, which sets the low-energy threshold. Thin silicon ΔE detectors are being developed [Paper XIII], which open new possibilities because the low-energy threshold is much smaller and they are compatible with Ultra High Vacuum techniques.

## 2.2 ELASTIC RECOIL DETECTION USING A TIME of FLIGHT AND ENERGY DISPERSIVE DETECTOR TELESCOPE

In ToF-E ERD, a detector telescope is used to measure the Time of Flight (ToF) $T$ and energy $E$ for each recoil. This, in the non-relativistic limit (which is appropriate at the energies used here), is related to the mass $M_2$ of the recoil according to:

$$E = \tfrac{1}{2} M_2 (L/T)^2, \text{ and, } M_2 = 2E(T/L)^2 \quad (2.6)$$

The geometrical configuration used is illustrated in Fig. 2.4. $T_1$ and $T_2$ are a pair of time detectors separated by a drift length $L$. These time detectors consist of a thin carbon foil (~5 μg $cm^{-2}$) through which the ions traverse with a small energy loss, leading to emission of prompt secondary electrons (Fig. 1.1). These electrons are collected, usually after amplification by channel-plate electron multipliers, and the resulting electrical pulses is used to start and stop a fast clock, which measures the time of flight (T). A tutorial review on time detectors is presented elsewhere [30].

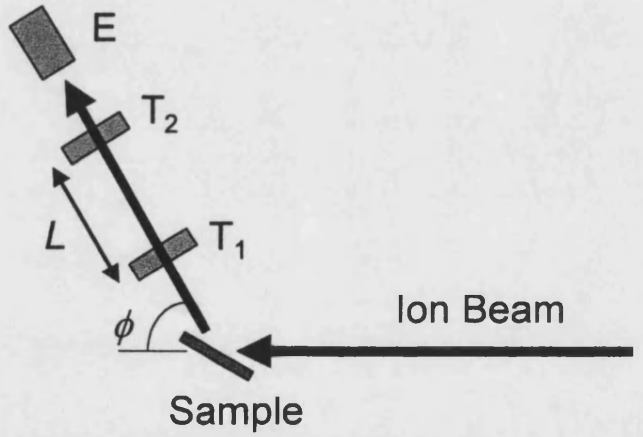


**Figure 2.4.** Geometrical configuration for ToF-E ERD. E is a Si diode charged particle energy detector used to measure the recoil energy. $T_1$ and $T_2$ are carbon-foil time detectors separated by a drift length $L$.

The main thrust of the work has been focused on developing ToF-E ERD for quantitative analysis in research on microelectronic technology and nanoscience. The overall philosophy has been to let the requirements of the research applications govern the development of the technique. In the following the contributions to development of the technique in different papers is outlined.

### 2.2.1 Initial Development and Application of ToF-E Elastic Recoil Detection in Si Microelectronic Technology

*Paper I:* **Quantitative Mass and Energy Dispersive Recoil Spectrometry: Resolution and Efficiency Considerations.** H.J. Whitlow, G. Possnert and C.S. Petersson, Nucl. Instrum. and Methods B27(1987)448.

This seminal paper outlines the basic theory for ERD and describes the ToF-E ERD set-up in Uppsala for multidispersive measurements of recoil mass and energy. This paper for the first time showed the analytical power of being able to separate the contributions to the energy spectrum according to the different mass elements present in the sample. This is beautifully demonstrated for study of the thermal reaction of a 360 nm Mg film with a Si substrate at 250 °C for 30 min in vacuum. Mg could be completely separated from Si, and surface C and O impurities were completely isolated signals. This was in stark contrast to RBS analysis of the same samples. In the RBS case the Mg and Si signals are not separated and the light impurity signals were completely buried in the counting statistical variations of the background signal from heavier elements. The paper also presents early estimates for the mass resolution and the relative detection efficiency for C and Si.

*Paper II*: **Mass-dispersive recoil spectrometry studies of oxygen and nitrogen redistribution in ion beam –synthesised buried oxynitride layers in silicon.** H.J. Whitlow, C.S. Petersson, K.J. Reeson and P.L.F. Hemment, Appl. Phys. Lett. 52(1988)1871.

This paper represented a very timely application of ToF-E ERD because it addresses a question that was important for the emerging SIMOX (Separation by Implanted Oxygen) wafer technologies. Namely, what happens to co-implanted nitrogen impurities, and could nitrogen co-implantation be exploited to reduce the SIMOX processing temperature. The results showed that the nitrogen segregated to the $SiO_2$/Si interfaces on either side of the buried oxide layer as this formed during thermal processing. This work was later extended to study the content and behaviour of co-implanted carbon impurities in SIMOX wafers [31,32] as well as the part played by oxygen in the formation of some transition metal silicides [33].

### 2.2.2 Energy and Mass calibration

In order to perform any kind of quantitative analysis it is essential to calibrate the instrument in order that the measurement results can be expressed in terms of absolute units. There are two basic approaches to establishing a calibration in terms of absolute units.

- The first approach by to perform a relative measurement against one or more, reference standards specifically chosen for the measurement in question. (An example of this is the spiking of samples in Particle Induced X-ray Emission with a known concentration of a reference element. [5,6])
- The second approach is to use an understanding of the factors that govern the response function of the instrument to establish the calibration of the instrument in terms of an absolute scale. This in turn may also rely on a few well-chosen reference standards.

In general, the preferred approach depends on the particular analytical measurement in question. In quality control applications, it may be most expedient to perform relative measurements against reference standards. In other situations, where it may not be convenient or impossible to prepare a suitable reference material, the second approach is preferable.

From the initial studies described in section 2.1, it became clear that effort had to be devoted to establishing techniques for energy and mass calibration. The early work was based on a calibration law for fission fragments proposed by Schmitt et al [34] in 1965 and early tests [Paper X] showed it could be used for light recoils. Strong evidence that this calibration law was inadequate was that plots of recoil mass assigned from equation 2.6 vs. recoil energy $E$, departed from straight lines corresponding to constant mass. When work on III-V materials was started the situation became especially critical because it became necessary to establish an energy calibration for recoils from $^{12}C$ through to $^{197}Au$.

*Paper III*: **Multivariate Analysis Method for Energy Calibration and Improved Mass Assignment in Recoil Spectrometry**. M. El Bouanani, M. Hult, L. Persson, E. Swietlicki, M. Andersson, M. Östling, N. Lundberg, C. Zaring, D.D. Cohen, N. Dytlewski, P.N. Johnston, S.R. Walker, I.F. Bubb and H.J. Whitlow, Nucl. Instrum. and Methods B94(1994)530.

This paper reports development of a calibration procedure for ToF-E ERD that is based on the use of the ToF section to tag recoils of known mass with their energy. For this a number of homogenous reference samples with known isotopic mass such as $^{7}Li$, Be, C, $^{27}Al$, $SiO_2$, Mn, $^{59}Co$, GaP, InP, $^{181}Ta$ and $^{197}Au$ are used. The calibration is done in the following steps.

- A straight-line calibration for the ToF was established using the high-energy edges corresponding to recoil atoms and scattered ions from the surface of the known reference samples. In this case, the ToF is calibrated against the magnetic field along the ion trajectory through the analysing magnet. This is stabilised by a nuclear magnetic resonance probe, which in turn had been calibrated against resonant nuclear reactions. A check using the $^{16}O(\alpha,\alpha)^{16}O$ resonant elastic scattering resonance at 3.045 MeV revealed the absolute uncertainty to be within a few keV for $^4He^+$ ions.
- The mean ToF $T$ and known recoil mass $A$ are used to calculate the recoil energy for a number of small energy channel number intervals. These could be fitted to a second order polynomial in channel number $X$:

$$E(X,A) = (c_0 + c_1 A) + (c_2 + c_3 A)X + (c_4 + c_5 A)X^2 \qquad (2.7)$$

  $c_0,\ldots,c_5$ are the calibration constants.

- When the absolute energy calibration (equation 2.7) has been established the absolute mass of each unknown recoil $M_2$ of each recoil can be assigned according to:

$$M_2 = k\frac{c_0 + c_2 + c_4 X^2}{\left[(L^2/2t^2) - c_1 - c_3 - c_5 X^2\right]}, \qquad (2.8)$$

where $t$ is the calibrated ToF and $k$ is a constant that relates $M_2$ to the correct units.

### 2.2.3 Detector efficiency

So far, we have considered how to establish a quantitative calibration that permits the energy channel number to be converted to an absolute energy. This allows a depth scale to be assigned for each recoil species. The second part of the work, which is still in progress, is concerned with determining the detection efficiency $\eta_A$. This is important because it follows from equation 2.5 that $\eta_A$ is needed to establish the concentration scale for the element in question. For most analytical purposes, it is sufficient to know the detection efficiency relative to some standard element.

*Paper IV:* **Thermally grown $SiO_2$ films for Elastic Recoil Detection Analysis.** H.J. Whitlow, A.B.C. Andersson and C.S. Petersson, Nucl Instrum. and Methods B36(1989)53.

This paper explored the suitability of thermally oxidised $SiO_2$ films as reference standards for determining the detection efficiency. This was motivated by the need to be able to quantify the oxygen concentration in Si-based semiconductor structures. [Paper II, 31-33,35-39] It was found

that the thermally oxidised films showed no evidence of stoichiometry changes during irradiation. Moreover, the detection efficiency exhibited an energy dependence that suggested it was correlated with the stopping in the carbon foils of the time detectors [66].

This finding has been confirmed in a more recent, (unpublished work). Figure 2.5, which is taken from this study, shows that the detection efficiency of a ToF system with two carbon-foil time detectors follows a single continuous curve when plotted vs. the energy deposited in the carbon foil. Furthermore, as one might expect the detection efficiency decreases as the discriminator threshold is increased, presumably because more secondary electrons are required to trigger the discriminators and thereby register a hit.

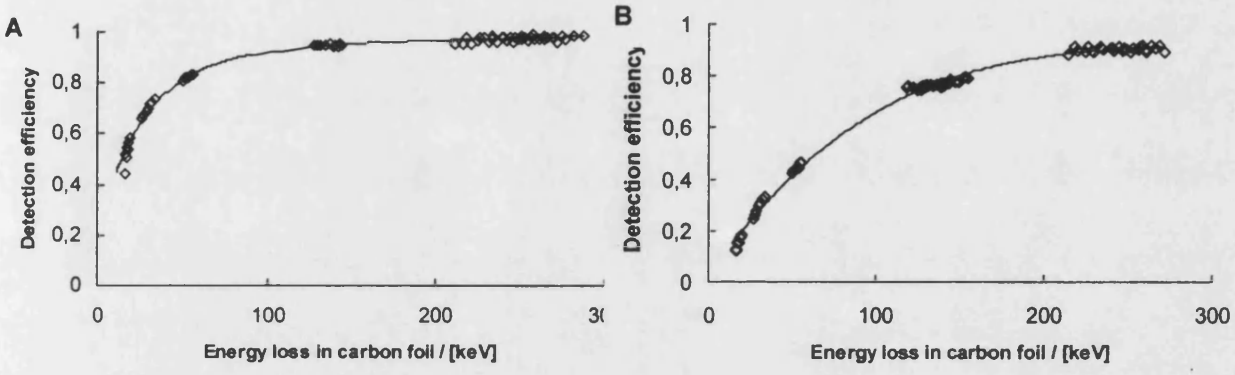


Figure 2.5. Stopping power dependence of the normalised detection efficiency of detector telescope consisting of a pair of carbon-foil detector time detectors. The data points represent the relative efficiency for $^{7}$Li, $^{9}$Be, $^{11}$B, $^{12}$C, $^{24}$Mg, $^{27}$Al, $^{27}$Si, $^{55}$Mn, $^{59}$Co and $^{63,65}$Cu recoils vs. energy deposited in a 4 $\mu$g cm$^{-2}$ carbon foil. (A) Discriminator thresholds -50 mV. (B) Discriminator thresholds -125 mV. (H. J. Whitlow and Yanwen Zhang et al, unpublished data.) The solid lines are empirical fits to the data.

### 2.2.4 Mass separating power

*Paper V:* **Mass Resolution of Recoil Fragment Detector Telescopes for 0.05-0.5A MeV Heavy Recoiling Fragments**, H.J. Whitlow, B. Jakobsson and L. Westerberg, Nucl. Instrum. and Methods A310(1991)636.

This paper presents a comprehensive systematic experimental and theoretical study of factors governing the mass separating power of ToF-E detector telescopes. The work reported in the paper was part of a design study for a detector system that will be used to study recoil fragments from heavy ion collisions at intermediate energies at a heavy-ion storage ring accelerator. Experimental data on these collisions is important to collect because phase changes may occur

in nuclear matter after states of high compression that are thought to exist in super-novae and neutron stars. The theoretical estimates and experimental data were in good agreement, revealing that the major contribution to the mass broadening was associated with the energy resolution of the Si E detector. The contribution from geometric effects and the resolution of the time detector was small compared to that for the energy detector for timed flight lengths $L$ of 0.2 m and greater. This work had an important economic implication because it showed that a small compact (low cost) detector telescope array that subtended a large solid angle could be fabricated without sacrificing attainable mass resolving power.

Paper VI: **Empirical characterisation of Mass Distribution Broadening in ToF-E Recoil Spectrometry.** M. Hult, M. El Bouanani, L. Persson, H.J. Whitlow, M. Andersson, C. Zaring, M. Östling, D.D: Cohen, N. Dytlewski, I.F. Bubb, P.N. Johnston and S.R. Walker, Nucl. Instrum. and Methods B101(1995)263.

For a number of analysis procedures it is important to be able to describe the dependence of mass broadening on recoil mass and energy. This is necessary for the decomposition of signals from elements with near-lying isotopes [Papers VII, VIII, IX, 40,41,43-47]. It is also important in analysis procedures under development where a model sample structure is refined by comparing the calculated 2-dimensional mass vs. energy distribution with the experimentally measured histogram [42]. From Paper IV, it was known that the mass broadening is dominated by the energy resolution of the Si energy detector. Unfortunately, there is no analytical description of how the energy resolution of these detectors varies as a function of recoil energy and mass. We investigated the shape of the mass instrument function and found (i) it was well described by a Gaussian and (ii) that over the energy range of interest $\sigma$ for the Gaussian was well fitted by the empirical expression:

$$\sigma(E,A) = C_1 + C_2 A^{3/2} E^{-1} + C_3 A^2 E^{-2/3} + C_4 A E^{1/2}, \qquad (2.8)$$

where $C_1,\ldots,C_4$ are constants. This parameterisation of the mass broadening was an essential step for analysis of InP semiconductor structures. [40,45,46] In these structures Pd, In and scattered $^{127}I$ signals are partially superposed., Parameterisation of the mass broadening has also been a critical step in development of a direct analysis procedure based on transformation of a non-linear into a linear-regression [41].

### 2.2.5 Analysis of III-V semiconductor structures

*Paper VII:* **High-resolution recoil spectrometry for separate characterisation of Ga and As in $Al_xGa_{(1-x)}As$ structures.** M. Hult, H.J. Whitlow and M. Östling, Appl. Phys. Lett. 60(1992) 219.

GaAs structures represent a particularly challenging class of structures for MeV ion beam analysis because the large and closely similar masses of the naturally occurring isotopes $^{69}Ga$, $^{71}Ga$ and $^{75}As$, with natural abundance of 60.1, 39.9 and 100 at. %, respectively. The implication is that it is difficult to apply RBS to GaAs systems because the light element signals will be superposed on a dominating substrate signal. Furthermore, the small difference in isotope masses for Ga and As implies that it is not possible use RBS to separately characterise the Ga and As distributions except for the few nm closest to the surface.

This paper demonstrated for the first time separate characterisation of Ga and As down to a depth of 550 nm using ToF-E ERD with a 64 MeV $^{127}I^{11+}$ beam. *This has been an essential development for our continuing research programme on the study of metal/III-V semiconductor reactions.* The paper also introduced some other technical developments, namely, improvement of the mass resolution deriving the energy signal from the ToF and a procedure for minimising cross-talk by selecting the interval, which contribute to the elemental signals.

Paper VIII: **Rapid Thermal Annealing Induced Reactions of Co/GaAs Thin Film Structures using Mass and Energy Dispersive Recoil Spectrometry.** M. Hult, H.J. Whitlow, M. Östling, M. Andersson, I. Linderberg, K. Ståhl. J. Appl. Phys. 75(1994)835.

This paper is the seminal paper in a series [PapersVIII, IX, 40,43,45,47] on the reaction of GaAs and InP with thin metal surface layers. From a technological viewpoint, the reaction of thin metal films on semiconductors is of critical importance for microelectronic technology. Ever increasing demands on improved component speed and reduced size require the development of metallisation and contacts that can be formed in a controlled manner on a nm scale and that are stable and reliable over a wide envelope of operating conditions. The thermal stability of metallisation layers is of particular importance because devices such as high power lasers may operate at very elevated temperatures. The fundamental information that is of particular importance is the *phases formed at equilibrium* and the phases formed in *the approach to equilibrium.* Equilibrium phase diagrams for closed systems at thermodynamic equilibrium

provide an importance reference point. However, metal/III-V semiconductor systems differ from the ideal ternary phase diagram case in that:

- The starting point is metal + III-V semiconductor and not a homogeneous single-phase mixture.
- The supply of metal is finite, whilst the supply of III-V semiconductor is essentially infinite.
- Unless the system is capped, volatile components may be lost from the system.

In Paper VII, thermal reactions of the thin film Co/GaAs system have been studied by combination of glancing incidence X-ray Diffraction (XRD) and ToF-E ERD. The XRD measurements where used to monitor the phases that were formed in the surface layer whilst ToF-E ERD was used to determine how the depth distributions of Co, Ga and As evolved during the thermal reaction. In addition, the sample surface topography was monitored using Scanning Electron Microscopy (SEM). The findings of the study showed the reaction of this system was complex with the formation after heat treatment at 400-550 °C of a pseudo-binary eutectic mixture of $CoGa_x$ ($0.32 \leq x \leq 0.59$) and CoAs. At higher temperatures (550 – 650 °C) As was lost from the surface layer.

The results of the series of papers [Papers VIII,IX,40,43,45,47] are summarised in Table 2.1 below.

**Table 2.1 Summary of metal/II-V reactions.**

| System | Nature | Low temperature. | Intermediate temperature. | High temperature |
|---|---|---|---|---|
| Ti/InP | Very reactive forms stable phosphides | ≤250 °C interface reaction Ti + In | 350 °C TiP + Ti + In. | ≥ 400 °C TiP Not all film reacted at 500° C |
| Cr/InP | Very reactive forms tenacious phosphides | ≤ 250 °C Cr + In | 350 - 450 °C Cr, In, CrP, $Cr_{12}P_7$ | 500 °C CrP + In |
| Ni/InP | Reactive forms indides and phosphides | ≤250 °C No reaction | 350 °C $Ni_2InP$ | 500 °C $Ni_2InP$ |
| Pt/InP | Near noble forms indides and phosphides | ≤250 °C No reaction | 350 °C $Pt_5InP$ | 500 °C $PtIn_2$ + $PtP_2$ + $Pt_3In_7$ slight P loss |
| Pd/InP | Near noble forms indides and phosphides | ≤100 °C Slight reaction | 150-400 °C $Pt_5In_2P_2$ | ≥450°C PdIn, P loss |
| Co/GaAs | Reactive forms galides and arsenides | ≤400 °C No reaction | 450 - 550 °C CoGa-CoAs eutectic | 550 - 650 °C CoGa, Loss of As. |

Table I reveals that transition metals such as Ti and Cr which readily form phosphides react preferentially with the P releasing In. In the Ti case, a thin barrier layer appears to form, which inhibits further reaction even at 500 °C. In the less reactive Ni case, which is known to have a region of many metastable states, the ternary phase $Ni_2InP$ formed both at low temperatures and

high temperature (500 °C). The near noble metals Pd and Pt both form ternary phases at low temperature, however these are not formed at 500 °C but instead a mixture of $PtIn_2$ and $PtP_2$ is formed. In the Pd case, the phosphide is evidently not stable and phosphorus release took place.

*Paper IX:* **Formation of thin films of $CoSi_2$ on GaAs.** M. Hult, L.Persson, M. El Bouanani, H.J. Whitlow, M. Andersson, M. Östling, N. Lundberg, C. Zaring, K. Georgesson, D.D. Cohen, N. Dytlewski, P.N. Johnston and S.R. Walker. J. Appl. Phys. 77(1995)2435.

Metalloid phases such as slicides, germanides and carbides offer interesting possibilities for contact and interconnect metallisation of III-V semiconductors because they are often good conductors and chemically stable and thereby less susceptible to reaction with the underlying III-V substrate. $CoSi_2$ is particularly interesting in this connection because it has low resitivity (16 $\mu\Omega$ cm [48]) and a high temperature stability [49]. Moreover, it can be readily formed by thermal reaction of thin-films of Co and Si.

In Paper IX, we studied using the formation of $CoSi_2$ by thermal reaction of Si/Co/GaAs using the same techniques as in Paper VIII. It was found that the reaction between Co and Si required temperatures of 300 °C or greater. However, at temperatures below 400 °C the Ga and As moved towards the surface, probably as a result of the formation of $CoGa_x$ and CoAs [Paper VIII]. This movement was not observed at temperatures of 500 – 700 °C and there is only evidence of the formation of $CoSi_2$. With excess, Si distributed in the silicide layer or at the $CoSi_2$/GaAs interface. Recently, this work has been extended to study the formation and reaction of $PdSi_2$ with GaAs and GaAs-AlAs alloys [47], which is another technologically important system.

# Chapter 3

# CHARACTERISATION OF MeV CHARGED PARTICLES WITH SILICON DETECTORS

## 3.1 SILICON CHARGED PARTICLE DETECTOR BASICS

Reverse biased Si diode structures have been used as the workhorse tool for measuring the energy of light and heavy ions as well as other charged particles* since the 1960's [50,51]. The basic idea is illustrated in Fig. 3.1. High-energy charged particles penetrating matter lose most of their energy because of various electronic excitations of the medium and projectile. This creates a *track* of ionised atoms and high- and low-energy electrons along the trajectory of the particle. In a semiconductor, this perturbation of the electronic system relaxes with the result that a *plasma column* of electron-hole pairs is created which extends along the ion trajectory in the semiconductor. The number of electron-hole pairs $N_{e+h}$ created in the plasma column is related to the energy deposited by the particle in electronic processes $E_{el}$ according to:

$$N_{e+h} = E_{el}/\xi \tag{3.1}$$

For Si $\xi$ is 3.65 eV and is largely independent of if the particle is a photon, electron, proton or heavy ion. It should be noted that even if the nuclear stopping is considerable, much of the energy transferred to the recoil in nucleus-nucleus scattering contributes to electron-hole pair formation because of electronic stopping of the energetic recoils. The basic idea of a silicon diode detector is to convert the energy deposited along the ion track into an electrical signal by collecting the charge carriers in the plasma column on electrodes in an electric field. Most real semiconductors are extrinsic and in order to sustain a sufficiently large collecting field it is necessary to deplete the region between the collecting electrodes of free charge carriers. This

---

* *Charged-particle* is here taken to mean not just energetic ions, electrons, $\pi^{\pm}$ etc. but also energetic neutral atoms which lose energy in the same way as energetic ions as they traverse matter.

can be effectively done by making a Schottky- or a p-n junction. The charge pulse from the $n^+$ region is usually converted to a voltage $V_o$ using a Miller integrator as a charge sensitive amplifier. Then:

$$V_o = \frac{1}{C}\int i.dt = \frac{eE_{dep}}{2C\xi} \tag{3.2}$$

The factor 2 in the denominator in equation 3.2 is a consequence of the charge collection being made only from the $n^+$ contact.

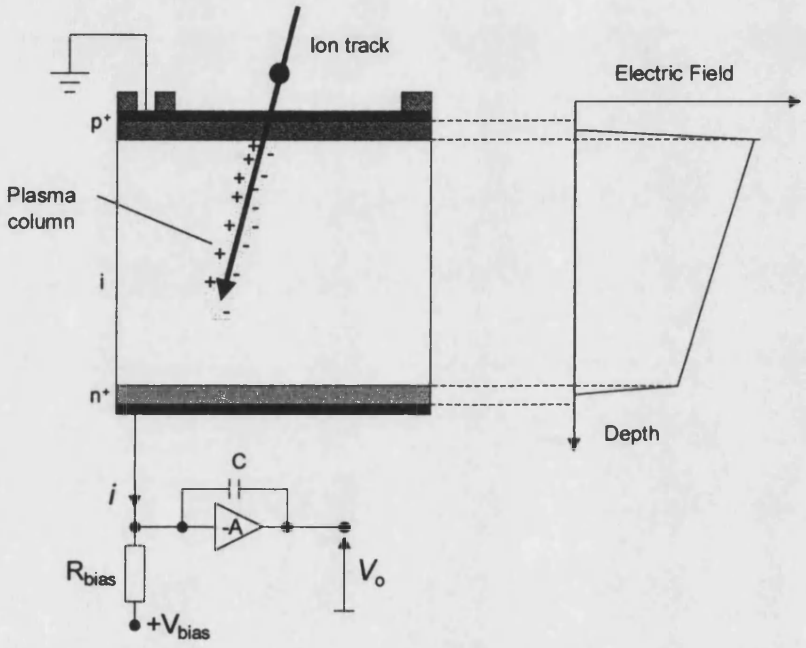


**Figure 3.1.** Schematic illustration of the principle of a p-i-n charged particle detector.

A p-i-n diode charged particle detector usually consists of a high resitivity wafer of n-Si. The front- and rear-faces are heavily $p^+$ and $n^+$ doped, respectively, to a depth of several hundred nm. The doping in the $p^+$ and $n^+$ layers is much greater than the background doping of the substrate. Then even for moderate reverse bias the depleted region extends right throughout the n region and into the $p^+$ and $n^+$ contact layers. (Fig 3.1) In this case, the diode can be considered to consist of a pseudo-intrinsic (*i*-) layer sandwiched between thin ( 0.1 μm) highly doped $p^+$ and $n^+$ contact layers. The *i*-layer extends almost entirely throughout the wafer thickness (up to ~1 mm) and consequently the junction capacitance can be small, which is very advantageous from a noise viewpoint. The thermal noise and leakage is also smaller for a p-i-n diode because the built-in barrier potential is considerably larger for Si p-i-n structures than for Au/n-Si Schottky barriers. In addition, p-i-n detector can also be heated to 200-300 °C without

detrimental effects. (The junction properties of a Au/n-Si junction would be destroyed because of in-diffusion of Au, which is a known minority carrier lifetime-killer, into the Si. [67]) This large thermal budget is an important advantage because it allows p-i-n detectors to be subjected to bake-out of U.H.V. vacuum chambers without special precautions and recovery of the radiation damage induced leakage current by moderate heat treatment. [Paper XII]

Si p-i-n diode detectors are fabricated by conventional microelectronic processing techniques. Si p-i-n diode structures are widely used in photodiodes. (Si p-i-n photodiodes can be used as charged-particle detectors with energy resolutions comparable with Au/n-Si detectors. [52-54]) Microelectronic technology permits the realisation of detectors with special configurations such as microstrip and charge division detectors for simultaneous position and energy measurement. Microelectronic processing technology also may be used to fabricate detectors on thin membranes. These detectors can be made so thin that the charged particle penetrates right through, depositing only part of its energy, $\Delta E$, in the thin detector. The residual energy $E_{res}$ is measured in a second detector that is sufficiently thick to completely stop the charged particle. (See Fig. 3.2)

In this case of a $\Delta E$ detector of thickness $t$:

$$\Delta E = \int_0^t \frac{dE}{dx} dx \approx \frac{dE}{dx} t, \tag{3.3}$$

provided that $t$ is a small fraction of the ion range. i.e. $\Delta E \propto dE/dx$. For heavy charged particle with sub-relativistic energies the Bethe-Bloch formula [55,56] for energy loss of particles with velocity greater than the electron velocities in the target, [57] reduces to:

$$\frac{dE}{dx} = \frac{Z_1^2 Z_2 e^4}{2\pi\varepsilon_0 M_1 v_1^2} \log_e \left( \frac{2M_1 v_1^2}{I} \right) \quad \text{(SI)} \tag{3.4}$$

Here $I$ is an effective excitation energy obtained by summation over all the oscillator strengths in the target. The small higher order shell-correction and Barkhaus terms have been omitted in equation 3.4. Approximating the logarithmic term equation 3.3 as a constant, for a given particle energy $1/2\, M_1 v_1^2$, $dE/dx \propto Z_1^2$. Then for small detector thickness the nuclear charge number $Z_1$ is nearly proportional to $\Delta E$. This provides a convenient method to determine the nuclear charge (atomic number) $Z_1$ of a charged particle as well as its total energy, $E = \Delta E + E_{res}$. In order to overcome the difficulty that the energy calibration depends on the isotopic identity $(Z_1, A_1)$ of a charged particle it is convenient to first determine the identity on a plot of $\Delta E$ vs. $E_{res}$ such as shown in Figure 3.2-b. This figure illustrates $\Delta E$ vs $E_{res}$ for recoils at $\phi = 45°$ for $^{1}H$, $^{12}C$, $^{14}N$ and $^{16}O$ recoils from a thin nitride layer deposited by Chemical Vapour Deposition on a silicon substrate. The incident ions were 40 MeV $^{35}Cl^{5+}$. It turns out that the signals are

separated on a ΔE vs. $E_{res}$ plot even when the thickness *t* is a large fraction of the ion range. This is because much of the energy deposition in electronic excitation takes place around the end of the range in the so-called Bragg peak.

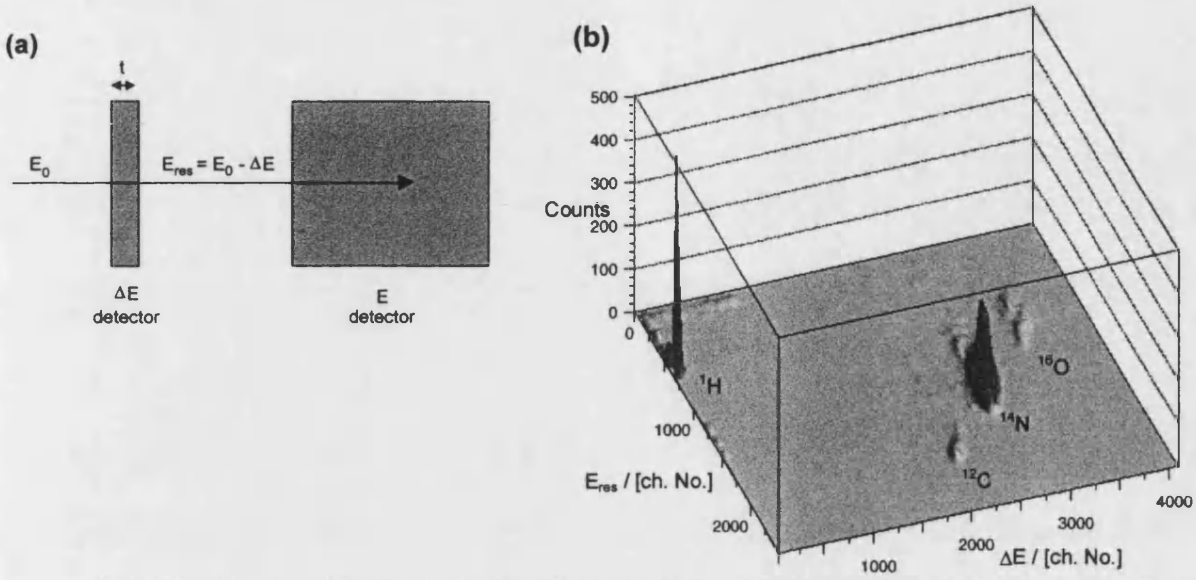


**Figure 3.2.** (a) Schematic illustration of a ΔE-E detector telescope. (b) Two-dimensional histogram of ΔE vs E for $^{1}H$, $^{12}C$, $^{14}N$ and $^{16}O$ recoils at $\phi$ = 45° from a 76 nm thick silicon nitride layer on a silicon substrate bombarded with 40 MeV $^{35}Cl^{5+}$ ions. (H.J. Whitlow and Yanwen Zhang et al, unpublished data.)

Much of the work undertaken on Si detectors has been undertaken as to answer specific requirements during development of the CHICSi detector system. CHICSi an array of ~550 ΔE-E detector telescope modules that will be used to study heavy ion collisions at intermediate energies [58]. Each module is read out by a single custom developed readout chip that combines analogue spectroscopy pre-amplifier-shaper -sample and hold chains with fast discriminator and digital trigger circuits for pile-up control and identification. In addition, a wide angle ToF-E recoil detector array will be used to measure the low energy (0.05-0.3A MeV) recoiling target residues.

*Paper X:* **Measurements of the Response Function of Silicon Diode Detectors for Heavy Ions using a Time of Flight Technique,** R. Ghetti, B. Jakobsson and H.J. Whitlow, Nucl. Instrum. and Methods A317(1992)235.

The objectives of this paper were to investigate the response of Si detectors for low energy heavy ions. In particular, we were interested in how to establish a calibration relating pulse

height to energy for heavy recoil nuclei and how the energy resolution varied depending on recoil mass number and energy. The paper is significant because it introduced the use of the ToF recoil telescope section as a means of probing the response of the Si detectors by tagging energetic recoils with their energy. This technique was subsequently used in Paper III and Paper VI. The results showed that the first moment of the response function (energy calibration) could be well described by a simple straight-line calibration for a given recoil species. The dependence of the slopes and intercepts for different recoil species showed a straight-line dependence on recoil mass for each detector investigated. Surprisingly, the recoil mass dependence varied widely from one detector to another. It was also found that the second moment fitted Amsel et al's [59] empirical law well.

***Paper XI:*** **Thin Detectors for the CHICSi ΔE-E Telescope.** L. Evensen, T. Westgaard, V. Avdeichikov, L. Carlén, B. Jakobsson, Y. Murin, A. Oskarsson,, A.Siwek, H.J. Whitlow, E.J. Van Veldhuizen, L. Westerberg and M. Guttormsen. IEEE Trans. Nucl. Sci. 44(1997) 629.

The CHICSi programme required the construction of thin detectors in the 10 to 15 μm thickness range in large quantities (1200). A major technological challenge was development of technology for production and testing of the thin detectors for the CHICSi programme. Previously, Si ΔE detectors with thickness below 10 μm were commercially available, however they were only available with small circular active areas of a few mm and in small numbers with a high unit cost. Circular detectors are unsuitable for detector arrays because they cannot be packed into arrays without significant interstitial dead areas between the active regions.

Together, with SINTEF Electronics and Cybernetics in Oslo we embarked on a joint programme to develop 10-15 μm thick ΔE detectors with 10 x 10 mm active area. This was a two stage programme. The first stage covered the development of thin detectors for the CHICSi programme. The second stage covered production of the detectors for CHICSi. After evaluation of a number of production techniques it was decide to fabricate the ΔE detectors using a two-step anisotropic etch technique that is based on tetramethylammonium hydroxide (TMAH). This had the advantage that conventional lithography could be used to define the membrane region. In order to minimise mask-making costs a common front-side mask-set was developed that was used for the 10-15 μm ΔE, 300 μm and 500 μm detectors needed for CHICSi. The etched membrane region on the rear side of the 10-15 μm ΔE detectors was defined by an additional rear-side mask.

This paper is particularly significant because it documents a very successful interaction between academic researchers and industry that lead to a new product. The second (production) phase is now complete and off-line alpha-particle tests indicate that the thickness and resolution requirements are well satisfied.

*Paper XII:* **Effects of Energy Deposition in Silicon p-i-n Diode Detectors.** H.J. Whitlow, S.J. Roosendaal, M. El Bouanani, R. Ghetti, P.N. Johnston, B. Jakobsson, R. Hellborg, H. Petersson, P. Omling, Z. Wang and the CHIC collaboration. Nuclear Instrum. and Methods B (In press).

As pointed out above, most of the energy deposited by a charged particle causes electronic excitation which leads to electron-hole pairs. As noted above, a significant fraction of the energy deposited in nuclear scattering, contributes to electron-hole pair production. The remaining fraction is associated with the formation of displacement damage. This can in turn lead to electrically active centres in the semiconductor that can degrade the measurement resolution. This is mainly because the associated leakage current increase can lead to a calibration drift. This comes about because the increased leakage current associated with the electrically active defect centres, causes an increased voltage drop across the bias resistor (Fig. 3.1). This in turn reduces the collecting field within the depleted layer in the detector leading to less efficient charge carrier collection that manifests itself as a calibration drift.

In this work, we show that the damage factor $\alpha$, (the rate of leakage current increase per unit ion dose), scales linearly over almost 6 decades with energy deposited in nuclear processes. This span corresponds to particles from fast pions to heavy nuclei. It turns out that this is independent if the (dense) end of range damage is within the detector or outside as for the case of our thin $\Delta E$ detectors. This is fortuitous because it allows us to scale according to the energy deposited in nuclear processes the extensive data set on degradation of detectors under irradiation collected for the CERN Large Hadron Collider (LHC) project. (Conversely, one may simulate the effects of high-dose pion irradiation with protons with a few MeV energy.) It was also found that the increase of leakage current could be restored by a low temperature heat-treatment at 150 °C. This finding was commensurate with Deep Level Transient Spectroscopy (DLTS) measurements which showed a reduction of defects after annealing. Moreover, the DLTS results suggest that the recovery is mediated by interactions between defects such as divacancies and E- and A-centres. Unfortunately, the strain broadening and shift of the energy levels coupled with

the limited energy resolution of DLTS prevented unique identification of the defects centres and elucidation of the exact mechanism of this interaction.

Paper XIII: ***Extremely thin Silicon ΔE detectors for Ion Beam Analysis.*** *H.J. Whitlow, T. Winzell and G. Thungström, Nucl. Instrum. and Methods B (In press).*

The objective of this paper was to highlight in the form of an overview for IBA applications, the work done in developing thin ΔE detectors for the CHICSi programme. The paper presents theoretical estimates of the maximum ΔE detector thickness in terms of energy per nucleon. Quasi-theoretical estimates have been made of the ΔE vs. residual energy E signals and associated broadening associated with energy straggling for energies above and below the maximum in the stopping power curve. These strongly suggest that it is meaningful to develop ΔE detectors with thickness of 1 μm or below for IBA applications. The challenges associated with the mechanical stability of large area extremely thin detectors were shown surmountable by presentation of the concept and results from a novel vertically integrated ΔE-E detector telescope [60]. Control of the large Electronic Noise Contribution (ENC) associated with the large capacitance of these thin detectors was also shown to be realistic by matching the large detector capacitance with high transconductance Metal Oxide Field Effect Transistors (MOSFET).

At the 13$^{th}$ International Conference on Ion Beam Analysis, this work was named amongst the most significant new innovations presented at the conference.

# Chapter 4

# MODIFICATION OF MATERIALS WITH ION BEAMS

## 4.1 ION BEAM MATERIALS MODIFICATIONS

Most of the ways solid matter interacts physically with its environment are via the surface. It follows that many of the properties of a solid body may be changed by altering the surface layer. The thickness of the surface layer depends on the interaction in question. For example, the optical reflection properties of a dielectric may be changed by altering a surface layer a few wavelengths thick. The efficiency of an oxidation catalyst may be drastically reduced by fraction of an atomic layer coverage of heavy metals. Similarly, the corrosion resistance of a steel bridge girder can be enhanced by a paint film a hundred or so microns thick.

Ion beam techniques open new vistas for modifying surface layers because the penetration depth varies from a few atomic layers at eV energies to 10's of μm for ~1A MeV energies. Most of the processes in Figure 1.1 can be used as the basis for materials modification. For example, *ion implantation* is a standard production method used in microelectronic industry to produce doped layers with a well-defined depth and lateral extension in semiconductors. In ion implantation energetic ions of dopant atoms from an accelerator bombard the semiconductor and penetrate a distance that is governed by their energy. Another, lesser-known, example is the production of filter elements for separating 0.1-5 μm sized particles such as viruses and small bacteria. These can be produced by utilising the fact that change in electronic structure along an MeV-ion track causes a significant enhancement of dissolution rate of the material by an enchant. Selective etching then forms channels through the material with nanometer dimensions. Ion beam materials modification is a field of research where thousands of papers are published per year. Therefore, no overview will be attempted here. Instead, two papers will be highlighted that demonstrate how IBA methods have been used to study issues in ion beam modification of materials of technological importance. The work on both issues was instigated in both cases as the result of questions posed by industrial collaborators.

Ion bombardment is widely used in micro- and nanoelectronic processing technology. For example:

- Plasma etching is widely used to remove unwanted material to fabricate grating- and mesa-structures for quantum wires and dots.
- Sputtering is widely used to deposit layers of metals and compounds for contacts and interconnects,
- Ion implantation is used to directly produce doped regions as well as indirectly to form solid diffusion sources for shallow junctions by incorporating the dopant into an overlying poly-Si or metalloid layer.
- Ion Beam Synthesis is utilised to produce buried oxide and silicide layers. [Paper II]

MeV IBA techniques are particularly powerful methods for the analysis of the effects of ion bombardment. This is because they can be used to analyse lattice damage and distributions of elements in the 50 nm – 1 μm depth range that corresponds to the modified layer thickness that results from ion beam processing. Of particular interest is the incorporation of foreign atoms because even low concentrations may drastically modify the electrical and optical behaviour of the semiconductor by formation of electrically active centres. Here the application of Nuclear Reaction Analysis (NRA) methods is illustrated using some ion bombardment induced modification issues in microelectronic and nanoelectronic technology. These methods can be based on detection of charged-particle reaction products [61] or γ-ray photons [62].

*Paper XIV:* **Ion-Implantation Induced Fluorine Agglomeration in Tungsten Disilicide Prepared by Low Pressure Chemical Vapour Deposition**. C.S. Petersson, H.J. Whitlow, J. Keinonen, F.M. d'Heurle, F. Le Goues, R.V. Joshi, G. Scilla and O. Thomas, Nucl. Instrum. and Methods B40/41(1989)595.

Solid diffusion sources formed by implantation of the dopant species into a refractory metal silicide are an essential key to the scaling down of component size in microcircuits. $WSi_2$ layers, which are in equilibrium with silicon at high temperature, can be deposited by Low Pressure Chemical Vapour Deposition (LPCVD) by reduction of a mixture of $WF_6$ and $SiF_4$ by hydrogen:

$$WF_6 + 2SiF_4 + 7H_2 \rightarrow WSi_2 + 14HF. \qquad (4.1)$$

This is an attractive route for formation of the silicide layer because it is a low-temperature process and furthermore, the reaction parameters can be adjusted to selectively deposit $WSi_2$ on Si but not $SiO_2$. In part of an investigation on solid diffusion sources, it was observed that voids formed in LPCVD-$WSi_2$ following bombardment with $Sb^+$ dopant ions and heat treatment for diffusion. SIMS analysis suggested that these might be associated with the agglomeration of fluorine incorporate in the film. However, the result was questionable because of the uncertain influence of implanted Sb on the $^{19}F^-$ ion yield. NRA using the Nuclear Resonance Broadening (NRB) technique [12,62] with the 340 keV proton energy resonance in the $^{19}F(p,\alpha\gamma)^{16}O$ reaction was used to depth profile the fluorine. The result showed enhanced fluorine concentrations of up to 0.3 at. % at depths around the maximum in the implanted Sb range distribution and at the $WSi_2$/Si interface. This constitutes strong, but not conclusive evidence that the voids contained fluorine.

*Paper XV:* **$^1H(^{15}N,\alpha\gamma)^{12}C$ Nuclear Resonance Broadening Measurements of Hydrogen Incorporation during Plasma Etching of GaAs and $Ga_xIn_{(1-x)}As$ Quantum Wells.** L. Person, H.J. Whitlow, J. Keinonen, P. Torri, I. Maximov, L. Samuelsson, K. Knox and K.G. Malmqvist. Nucl. Instrum. and Methods B89(1994)346.

Hydrogen in semiconductors can introduce significant modifications of the optical and electronic structure because it can both passivate defect sites as well as acting an active defect centre on its own, or in combination with a foreign atom site. Photoluminescence (PL) yield reduction factors of 100 have been claimed for hydrogen passivation of shallow and deep donor levels [65] as well as some deep levels associated with impurities in III-V semiconductors [65]. Plasma etching in a $CH_4/H_2$ plasma is widely used for etching quantum well, wire and dot structures. One might anticipate that hydrogen would diffuse to buried heterojunctions in quantum well/wire/dot structures because this would lower the free energy by reducing the interfacial stress. It was therefore interesting to our colleagues in the Nanometer Structure Consortium to determine if plasma etching introduced hydrogen into GaAs and if the hydrogen decorated buried heterojunctions. In order to confirm that hydrogen was involved we should combine an non-optoelectronic method that directly identifies hydrogen with changes in the PL yield.

As the amounts of hydrogen that were trapped were anticipated to be small, we used the low background nuclear resonance profiling facility at Helsinki University. The measurements used the inverse reaction $^{15}N(^1H,\alpha\gamma)^{12}C$ reaction which has a sharp ($\Gamma$ ~1.3 keV [63]) resonance at 6.385 MeV $^{15}N^{2+}$ energy. The sample is surrounded by a BGO scintillation detector that

subtends close to $4\pi$ steradian solid angle. This is surrounded by an annular plastic scintillator, which is used to veto Compton scattering events shield and provide active shielding of the background associated with cosmic particles. The whole target/detector system is enclosed in a 80 mm thick lead shield with a cadmium lining and situated in a room lined with silica bricks ~17 m underground in granite rock.. This permitted measurement of hydrogen concentrations with a Minimum Detection Limit (MDL) of ~30 ppm in bulk material and considerably less if the hydrogen was localised at a single depth such as a quantum well interface.

Quantum well structures with a series of quantum wells located 200 nm below the surface was blanket etched in $CH_4/H_2$ plasma with bias voltages of 50 – 300V applied to the sample. The results showed that although the amount of hydrogen in the outer 100 nm increased with increasing substrate bias during etching (higher ion energy), the hydrogen did not penetrate deeper than 100 nm. Furthermore, no hydrogen build up was seen at the depths corresponding to the depth of the first quantum well after etching. This is consistent with the PL measurement, which showed no H-related peaks. A reduction of PL intensity from the quantum well was seen with increasing bias, this might be associated with the increased radiation damage for higher energy ions.

# PART II - RESEARCH PAPERS

Nuclear Instruments and Methods in Physics Research B27 (1987) 448–457
North-Holland, Amsterdam

# QUANTITATIVE MASS AND ENERGY DISPERSIVE ELASTIC RECOIL SPECTROMETRY: RESOLUTION AND EFFICIENCY CONSIDERATIONS.

Harry J. WHITLOW [1], Göran POSSNERT [2] and C. Sture PETERSSON [1]

[1] *The Royal Institute of Technology, Department of Solid State Electronics, Box 70033, S-10044 Stockholm, Sweden*
[2] *Uppsala University, Department of Radiation Sciences, Box 535, S-75121 Uppsala, Sweden*

Received 23 January 1987 and in revised form 18 March 1987

A time of flight–energy recoil telescope system for mass and energy dispersive recoil spectrometry has been applied to study the formation of $Mg_2Si$ layers and depth profiling of $Ga_{(1-x)}Al_xAs$ quantum well structures. Measurements of the energy (depth) dependence of the mass resolution showed that the telescope could be used over the energy range from 5 to 18 MeV to distinguish between recoils of 1 amu mass difference up to mass 28 amu. The energy dependence of the detection efficiency was found to be independent of the recoil energy for $^{12}C$ and $^{28}Si$ recoils and no strong evidence for a recoil species dependence of the detection efficiency for recoils heavier than $^{16}O$ was found.

## 1. Introduction

In recent years elastic recoil detection analysis (ERDA) has found wide application for depth profiling light elements [1–30]. In contrast to the isotope-specific nuclear reaction analysis (NRA) methods conventionally used for light element analysis, a number of elements may be analysed simultaneously by ERDA [1–7] in a similar way to Rutherford backscattering spectrometry (RBS). Unlike RBS where the scattered projectile ions are detected, in ERDA it is the recoiling target atoms themselves that are detected. The recoiling target atoms carry not only energy (depth information) but also atomic number and mass information. In conventional ERDA which is often used to profile hydrogen and helium in samples with $\approx 2$ MeV $\alpha$-particle projectiles this extra information is usually discarded and the energy (depth) resolution drastically degraded by the use of a thick absorber foil to discriminate against scattered projectiles [9–29]. A number of methods have been reported for extracting the extra recoil atomic number and mass information including, coincidence detection of scattered projectile and recoil [10,19,30], magnetic [6] and electromagnetic [8] momentum-energy analysis, $\Delta E$–$E$ recoil telescopes [5] and time of flight (TOF)–E recoil telescopes [1–3]. For our primary area of application: the study of light elements in semiconductor structures, recoil coincidence measurements are of limited application since they require the use of a thin-film specimen. Recoil momentum-energy analysis using an electromagnetic spectrometer [6,8] is also of minor interest since the recoil charge state distribution must be known in order to establish a quantitative concentration scale. $\Delta E$–$E$ recoil telescopes give recoil atomic number–energy information, but are limited in application due to recoil energy straggling in the window of the $\Delta E$ gas detector. A further disadvantage is that a counter-gas handling system is required. TOF–E recoil telescopes, which give recoil mass–energy information, on the other hand have good energy (depth) resolution if the time detectors are based on the detection of secondary electrons from thin carbon foils. From the viewpoint of quantitative ion beam analysis both the $\Delta E$–$E$ and TOF–E telescopes have the advantage that they are insensitive to the recoil charge state. If recoil atomic number, mass and energy identification are required, as in many nuclear physics experiments [31–33], a TOF section may be combined with a $\Delta E$–$E$ telescope. For our work on semiconductor structures a TOF–E telescope is clearly most suitable because, (a) it has the best energy (depth) resolution, and (b) we are primarily interested in targets of natural isotopic composition and since no naturally occurring isobars exist at significant concentrations up to 40 amu, the atomic number for low and medium mass recoils can be uniquely assigned from the recoil mass.

Although particle identification telescopes have been used in nuclear physics for about 20 years, relatively little use of them has so far been made for ion beam analysis. As a step in the development of this technique we have investigated the mass discrimination as a function of energy and the energy dependence of the relative detection efficiency.

0168-583X/87/$03.50 

## 2. Basic considerations

In the laboratory frame the recoil kinematic factor $\Lambda$ is given by:

$$E' = \Lambda E, \tag{1}$$

$$\Lambda = \frac{4M_1M_2}{(M_1 + M_2)^2}\cos^2\phi,$$

where $E$ and $E'$ are the energies, $M_1$ and $M_2$ the masses of the projectile ion and recoil, respectively, and $\phi$ the angle between incident ions direction and the recoil direction. The differential cross section assuming Rutherford scattering in the laboratory frame for recoils in SI units at angle $\phi$ is:

$$\frac{d\sigma}{d\Omega} = \left[\frac{Z_1Z_2e^2(1 + M_1/M_2)^2}{\pi\epsilon_0 E}\right]\frac{1}{\cos^3\phi}, \tag{2}$$

where $Z_1$ and $Z_2$ are the atomic numbers of projectile and recoil. By analogy with RBS formalism [24] $\Delta E$ the energy difference between recoils from a depth $x$ in a target of atomic density $N$ with energy $E_1$ and from the surface with energy $E_0$ is

$$\Delta E = E_0 - E_1 = Nx_p[\epsilon]_r^m, \tag{3}$$

where the energy-loss factor is

$$_p[\epsilon]_r^m = \frac{\Lambda\epsilon_{in}^p}{\cos\theta_1} + \frac{\epsilon_{out}^r}{\cos\theta_2}. \tag{4}$$

Here m, p and r respectively denote matrix, projectile and recoil. $\epsilon$ is the stopping cross section and $\theta_1$ and $\theta_2$ are the angles the ingoing projectile and outgoing recoil make to the target surface normal. The $\epsilon$ values used here were calculated using the program STOP of Ziegler et al. [35].

## 3. Experimental

Fig. 1 shows the experimental configuration used. The projectile ions were 48 MeV $^{79}Br^{8+}$ which were obtained from the tandem accelerator of the University of Uppsala. This projectile was chosen since:

(a) The depth resolution is optimized through eq. (4) by arranging that the projectile energy and the energy of the light and medium mass ($10 < M_2 < 30$) recoils from near the surface lie between 0.6 and 1.0 MeV/amu; close to the maximum in the stopping cross sections $_p\epsilon_{in}$ and $_r\epsilon_{out}$.

(b) The ion can be easily generated from NaBr using our Cs sputter ion source [36].

(c) A beam of Br ions with a sharply defined energy of the $8^+$ and adjacent charge states can be produced with a gas stripper [37].

In order to prevent excessive dead time due to the detection of scattered projectiles [4] the recoil angle $\phi = 45°$ was chosen so as to lie outside the cone of half angle $\theta_{max}$ into which the incident projectiles can be scattered. $\theta_{max}$ is

$$\theta_{max} = \arcsin(M_1/M_2). \tag{5}$$

(Even in conventional ERDA the $\approx 10\ \mu$m thick mylar foil, which is used to prevent detection of dominant scattered particle flux and gives the dominant contribution to the energy resolution, can be disposed of if provided $\phi > \theta_{max}$ [7].) The ion beam was collimated to 1 mm diameter by a collimator 300 mm from the target and the beam current was a few nA. The specimens were mounted on a 20-position target wheel on a two-axis goniometer driven by stepper motors. The analysis chamber was turbo-pumped to a vacuum of $10^{-6}$ mbar.

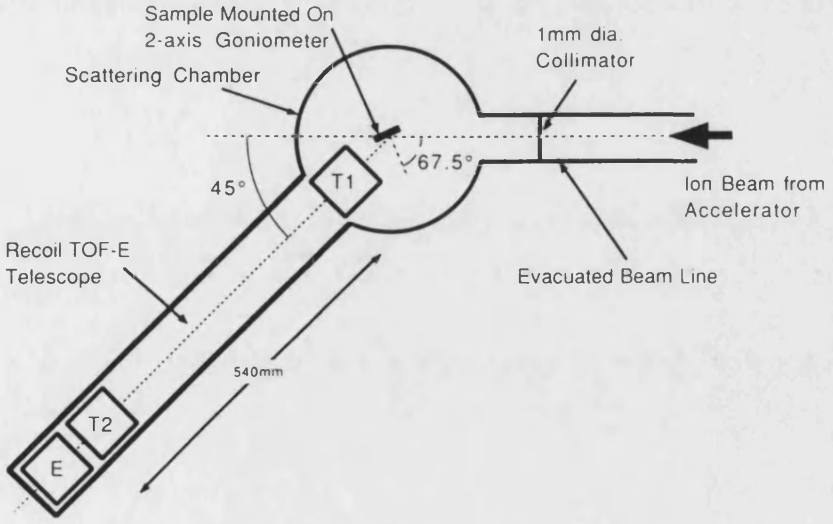


Fig. 1. Schematic diagram of the experimental configuration. E is the silicon surface barrier energy detector. T1 and T2 are the carbon foil time detectors.

## 2. Basic considerations

In the laboratory frame the recoil kinematic factor $\Lambda$ is given by:

$$E' = \Lambda E, \tag{1}$$

$$\Lambda = \frac{4M_1M_2}{(M_1 + M_2)^2}\cos^2\phi,$$

where $E$ and $E'$ are the energies, $M_1$ and $M_2$ the masses of the projectile ion and recoil, respectively, and $\phi$ the angle between incident ions direction and the recoil direction. The differential cross section assuming Rutherford scattering in the laboratory frame for recoils in SI units at angle $\phi$ is:

$$\frac{d\sigma}{d\Omega} = \left[\frac{Z_1Z_2e^2(1 + M_1/M_2)^2}{\pi\epsilon_0 E}\right]\frac{1}{\cos^3\phi}, \tag{2}$$

where $Z_1$ and $Z_2$ are the atomic numbers
and recoil. By analogy with RBS
energy difference bet
target of ato
surf

## 3. Experimental

Fig. 1 shows the experimental configuration used. The projectile ions were 48 MeV $^{79}Br^{8+}$ which were obtained from the tandem accelerator of the University of Uppsala. This projectile was chosen since:

(a) The depth resolution is optimized through eq. (4) by arranging that the projectile energy and the energy of the light and medium mass ($10 < M_2 < 30$) recoils from near the surface lie between 0.6 and 1.0 MeV/amu; close to the maximum in the sto
cross sections $_p\epsilon_{in}$ and $_p\epsilon_{out}$.

(b) The ion can be easily ge
our Cs sputter io

(c) A bea

**Erratum**

**Quantitative Mass and Energy Dispersive Elastic Recoil Spectrometry: Resolution and Efficency Considerations.**

H.J. Whitlow, G. Possnert and C.S. Petersson, Nuclear Instruments and Methods in Physics Research B27(1987)448.

There is a missprint in equation 2. Equation 2 should read:

$$\frac{d\sigma}{d\Omega} = \left[\frac{Z_1Z_2e^2(1 + M_1/M_2)}{8\pi\varepsilon_0 E}\right]^2\frac{1}{\cos^3\phi} \tag{2}$$

...e target
... The specimens
...tion target wheel on a two-
...riven by stepper motors. The analysis
... was turbo-pumped to a vacuum of $10^{-6}$ mbar.

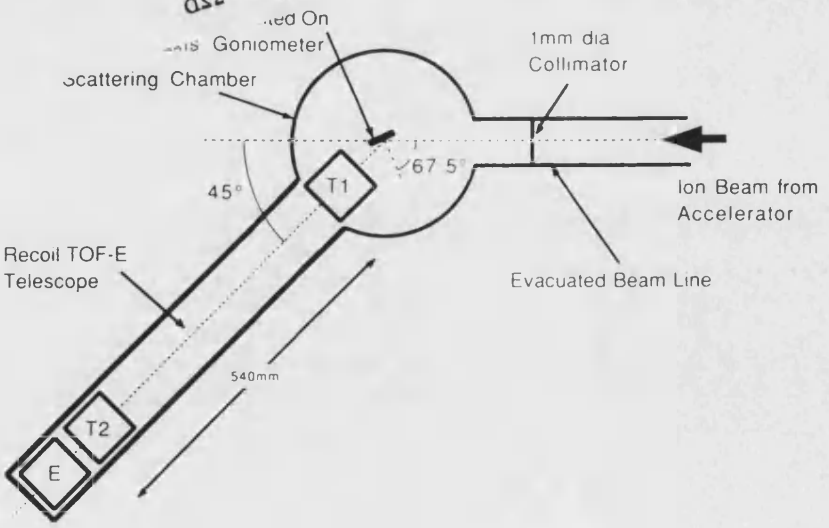


Fig. 1. Schematic diagram of the experimental configuration. E is the silicon surface barrier energy detector, T1 and T2 are the carbon foil time detectors.

The recoil telescope (fig. 1) consists of two time detectors T1 and T2 operated in a start–stop configuration and a 100 $mm^2$ silicon surface-barrier detector collimated to an active circular area of diameter 12 mm for energy measurement. Two time detectors are used since initial experiments with a single time detector used as a start detector and a stop signal extracted from the surface barrier detector, showed that the time scale was distorted. This distortion is presumably a consequence of the ion-species dependence of the plasma delay [38]. A small aperture in front of the first time detector T1 restricts the solid angle seen by the telescope to 0.13 msr which in addition to reducing the dead time that comes from extraneous events in the first time detector also has the effect of improving the energy resolution by reducing the angular dispersion [3] of the telescope. Over the years a number of time detectors have been reported [31,32,39–43] based on the detection of secondary electron emission from thin foils placed in the particle path. The time detectors are of the electrostatic mirror type [39,40] and are based on the design of Busch et al. [39] with the negative time signal taken from a flat anode plate roughly terminated with 50 Ω impedance to ground. This type of time detector was chosen in preference to the tilted foil type [31,32], since the carbon foil is normal to the recoil trajectory which simplifies their use in recoil telescopes with adjustable timed-flight lengths. The electron trajectory from the foil to the channel plate is isochronous (facilitating the fabrication of large area detectors with good time resolution) and also the construction is simpler than for the coaxial [33,42] and magnetic 1/2 turn cyclotron type [1–3,41]. The electrode voltages are supplied from an in-vacuum 126 MΩ resistor chain which also provides 920 V bias across each channel plate. The first time detector had a thinner carbon foil (3 $\mu g\ cm^{-2}$) than the second detector (10 $\mu g\ cm^{-2}$), in order to minimize the effect of scattering in the first foil on the time resolution. The measured time resolution 5.4 MeV α-particles was 200 ps fwhm for a 20 mm diameter sensitive area.

The electronics which is shown in fig. 2 is conventional. The negative pulses from the time detectors are amplified and fed to a pair of fast discriminators which generate negative NIM pulses for the time amplitude converter and positive pulses for the slow coincidence logic. The coincidence logic is arranged to generate convert pulses for the ADCs when all the detectors register an event. The data are stored on a disk file organized as event records of two 16-bit words corresponding to the energy and time signals. A typical data set of $10^6$ events occupies 2.5 Mbyte.

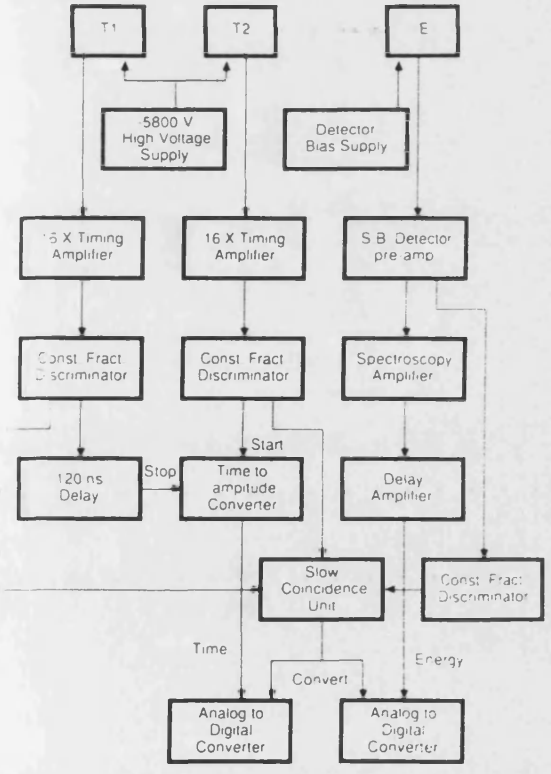


Fig. 2. The electronic setup for the TOF–E recoil telescope

## 4. Results and data analysis

The data were sorted off-line to yield mass-energy matrices, mass spectra and mass-gated energy spectra using the relation:

$$\mathcal{M} = \mathcal{E}\,(\tau - \tau_0)^2. \qquad (6)$$

Here $\mathcal{E}$ is the recoil energy (channels), $\tau$ the flight time (channels), $\tau_0$ a zero time channel to compensate for electronic delays etc. and $\mathcal{M}$ the recoil mass (channels). $\tau_0$ is an adjustable parameter that is adjusted so that the isotopes lie on lines parallel to the energy axis on a mass–energy plot. A potential problem is that the mass-defect and thick effective dead-layer of the combined surface-barrier detector and time detectors lead to an energy scale that is distorted both as a function of mass and energy [33]. Despite this it was found that except for recoil energies below 5 MeV, a single value of $\tau_0$ could be found that fitted all masses over the range 10 to 75 amu. The distorted energy scale can give rise to problems with the depth scale. Two approaches are possible: either the time signal and an assumed mass is used to calculate the true recoil energy [1–3], or the surface barrier detector is calibrated for each recoil species of interest. The first approach is difficult since deviations in the timed flight path due to wrinkles in the carbon foil etc. and timing walk due to the differing pulse amplitudes have to be controlled. We have adopted the latter approach since calibration can be simply carried out by holding the accelerator voltage constant,

The recoil telescope (fig. 1) consists of two time detectors T1 and T2 operated in a start–stop configuration and a 100 $mm^2$ silicon surface-barrier detector collimated to an active circular area of diameter 12 mm for energy measurement. Two time detectors are used since initial experiments with a single time detector used as a start detector and a stop signal extracted from the surface barrier detector, showed that the time scale was distorted. This distortion is presumably a consequence of the ion-species dependence of the plasma delay [38]. A small aperture in front of the first time detector T1 restricts the solid angle seen by the telescope to 0.13 msr which in addition to reducing the dead time that comes from extraneous events in the first time detector also has the effect of improving the energy resolution by reducing the angular dispersion [3] of the telescope. Over the years a number of time detectors have been reported [31,32,39–43] based on the detection of secondary electron emission from thin foils placed in the particle path. The time detectors are of the electrostatic mirror type [39,40] and are based on the design of Busch et al. [39] with the negative time signal taken from a flat anode plate roughly terminated with 50 Ω impedance to ground. This type of time detector was chosen in preference to the tilted foil type [31,32], since the carbon foil is normal to the recoil trajectory which simplifies their use in recoil telescopes with adjustable timed-flight lengths. The electron trajectory from the foil to the channel plate is isochronous (facilitating the fabrication of large area detectors with good time resolution) and also the construction is simpler than for the coaxial [33,42] and magnetic 1/2 turn cyclotron type [1–3,41]. The electrode voltages are supplied from an in-vacuum 126 MΩ resistor chain which also provides 920 V bias across each channel plate. The first time detector had a thinner carbon foil (3 $\mu g\ cm^{-2}$) than the second detector (10 $\mu g\ cm^{-2}$), in order to minimize the effect of scattering in the first foil on the time resolution. The measured time resolution 5.4 MeV α-particles was 200 ps fwhm for a 20 mm diameter sensitive area.

The electronics which is shown in fig. 2 is conventional. The negative pulses from the time detectors are amplified and fed to a pair of fast discriminators which generate negative NIM pulses for the time amplitude converter and positive pulses for the slow coincidence logic. The coincidence logic is arranged to generate convert pulses for the ADCs when all the detectors register an event. The data are stored on a disk file organized as event records of two 16-bit words corresponding to the energy and time signals. A typical data set of $10^6$ events occupies 2.5 Mbyte.

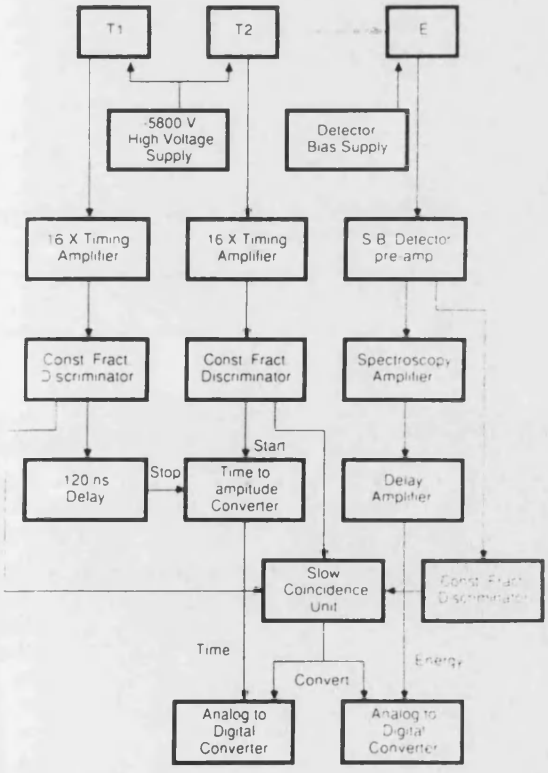


Fig. 2. The electronic setup for the TOF–E recoil telescope

## 4. Results and data analysis

The data were sorted off-line to yield mass-energy matrices, mass spectra and mass-gated energy spectra using the relation:

$$M = k(\tau - \tau_0)^2 \qquad (6)$$

Here $k$ is the recoil energy (channels), $\tau$ the flight time (channels), $\tau_0$ a zero time channel to compensate for electronic delays etc. and $M$ the recoil mass (channels). $\tau_0$ is an adjustable parameter that is adjusted so that the isotopes lie on lines parallel to the energy axis on a mass–energy plot. A potential problem is that the mass-defect and thick effective dead-layer of the combined surface-barrier detector and time detectors lead to an energy scale that is distorted both as a function of mass and energy [33]. Despite this it was found that except for recoil energies below 5 MeV, a single value of $\tau_0$ could be found that fitted all masses over the range 16 to 75 amu. The distorted energy scale can give rise to problems with the depth scale. Two approaches are possible: either the time signal and an assumed mass is used to calculate the true recoil energy [1–3], or the surface barrier detector is calibrated for each recoil species of interest. The first approach is difficult since deviations in the timed flight path due to wrinkles in the carbon foil etc. and timing walk due to the differing pulse amplitudes have to be controlled. We have adopted the latter approach since calibration can be simply carried out by holding the accelerator voltage constant,

(calibrated to ± 2 keV) and by measuring the recoil-edge positions from standard targets with homogeneous composition, for projectile ions of different charge state. Furthermore the adjustable parameter $\tau_0$ does not influence the energy scale (which can be determined solely by experimentally accessible quantities) but is only needed to establish the recoil mass. This data analysis method is a standard technique in nuclear physics. It has the clear advantages over the real-time gating technique that have up till now been used, by Thomas and Fallavier [1–3], (because the data for all recoil masses and energies can be taken in one pass) and over the event-by-event software gating of Groleau et al. [4], (because only one adjustable parameter is needed to determine the recoil mass). Probably the most important advantage is that the use of a 3-d presentation of the mass energy matrix provides a powerful survey of the sample and the ability to directly select the gating criterion for each recoil species.

The data analysis is illustrated in fig. 3. The sample is a silicon substrate with 300 nm Mg deposited on the surface by e-beam evaporation which is shown schematically in fig. 3a. Fig. 3b shows a time–energy contour plot of the raw data. Fig. 3c shows the corresponding mass–energy contour plot. The data in the lower part of Fig. 3c have been expanded to show the $^{12}C$ and $^{16}O$ signals that are a result of the native oxide and surface contamination. The mass spectrum of these data shown in fig. 3d demonstrates that recoils with 1 amu spacing can be separated at mass 28. The corresponding energy spectra gated on $^{28}Si$, $^{24}Mg$, $^{16}O$ and $^{12}C$ are presented in figs. 3e–g. The method is considerably more sensitive than RBS for light elements in a heavy matrix since there is no substrate background. This is illustrated in fig. 3d where a surface peak in the oxygen signal can be clearly discerned. The RBS spectrum for normally incident 2.4 MeV $\alpha$-particles backscattered at 168° (fig. 3h) from the same sample shows only a trace of surface oxide. This sample was one of a series in which we are investigating the thermal reaction between silicon and magnesium to form $Mg_2Si$ a semiconducting silicide. Fig. 4a–d shows the mass–energy plot, the $^{16}O$, $^{28}Si$ and $^{24}Mg$ gated energy spectra and RBS spectrum from a piece of the same sample that was annealed in vacuum at 250 °C for 30 min. Comparison with figs. 3b and 3d–e shows that silicon has moved towards the surface and a homogeneous layer of composition $Mg_{2.28\pm0.11}Si$ has been formed. This composition is in agreement with the rather less reliable composition $Mg_{2.05}Si$ obtained from the comparison of simulated RBS spectra [44] with an experimental RBS spectrum from the same sample and the published result of Chu et al. [45]. Close inspection of the rather unsharp $^{28}Si$ edge in Fig. 4 and the $^{16}O$ signal figs. 3d and 4a shows that oxidization of Si has taken place at the surface.

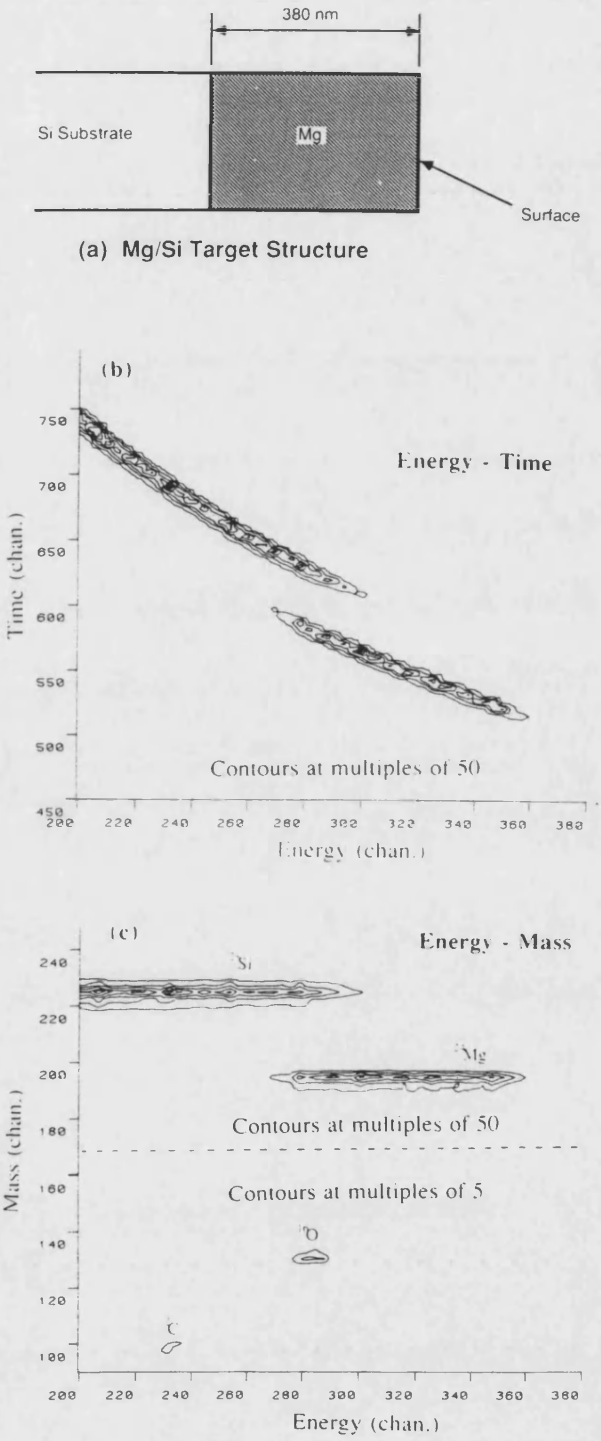


Fig. 3(a–c). Analysis of data from a 300 nm Mg overlayer on a silicon substrate. (a) Schematic target structure. (b) Contour plot of the raw data sorted as energy vs time. (c) Contour plot of the same data sorted as an energy vs mass plot. The contour scale in the lower part of the plot has been expanded to show the $^{16}O$ and $^{12}C$ signals from surface contamination.

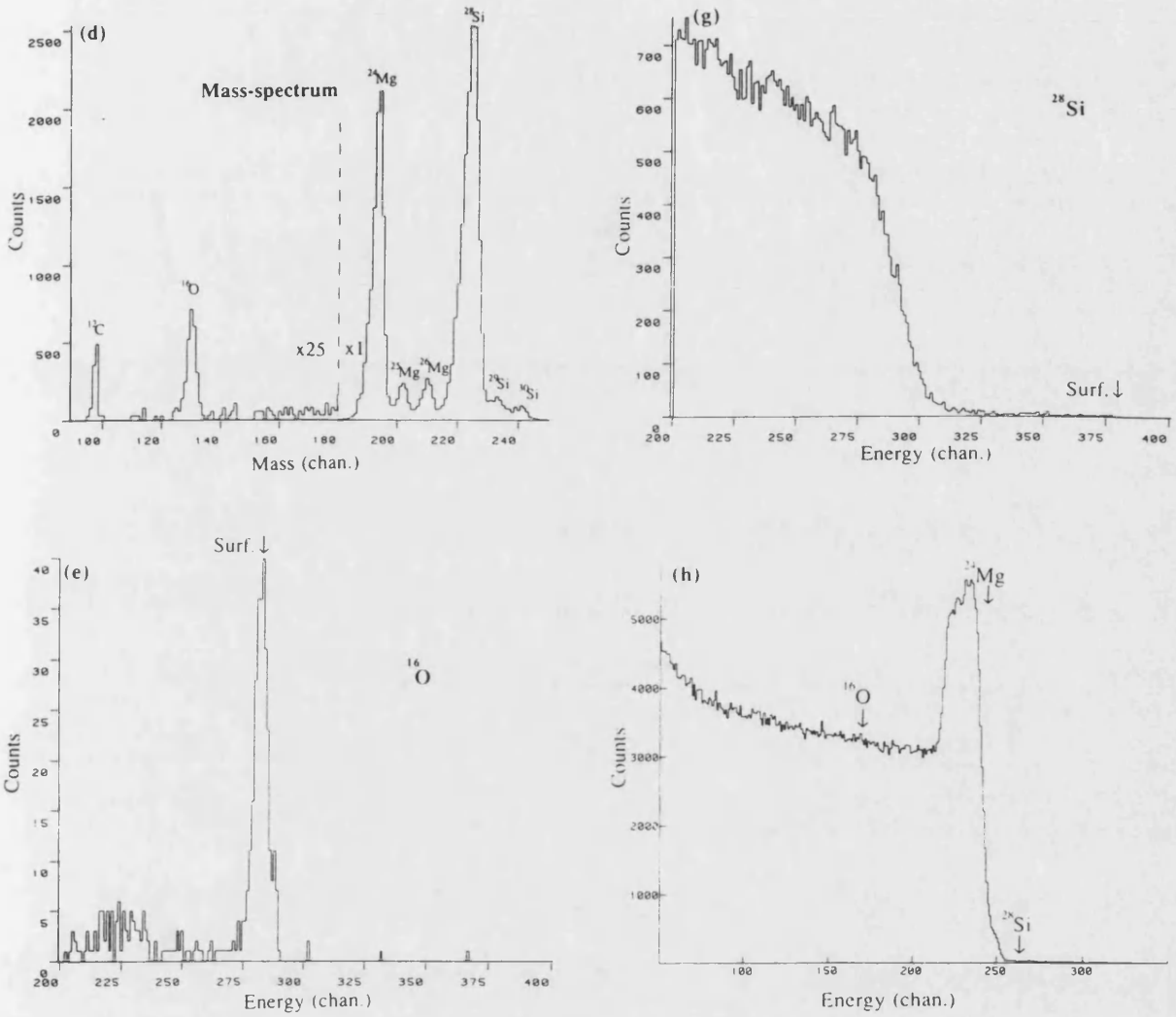


Fig. 3(d–h). Analysis of data from a 300 nm Mg overlayer on a silicon substrate. (d) Mass spectrum obtained from the data in fig. 3c. (e) $^{16}O$ recoil energy spectrum. (f) $^{24}Mg$ recoil energy spectrum. (g) $^{28}Si$ recoil energy spectrum. (h) RBS spectrum for normally incident 2.4 MeV $\alpha$-particles backscattered at 168°. The arrows denote the surface positions for $^{16}O$, $^{24}Mg$ and $^{28}Si$.

Fig. 5 shows an isometric-plot of the low-mass region of the mass–energy matrix obtained from a sputter-deposited TiB layer on a carbon substrate. In addition to the $^{10}B$ and $^{11}B$ signals from the sputter deposited film, signals from $^{14}N$ and $^{16}O$ included in the film by admission of air during sputtering can be clearly discerned. As a further example of the application of the method, fig. 6b shows the recoil energy spectrum gated on $^{27}Al$ from the $Ga_{(1-x)}Al_xAs$ quantum-well structure in which $x$ is varied from 0 to 0.3 in steps as a function of depth as shown in fig. 6a. Fig. 6b

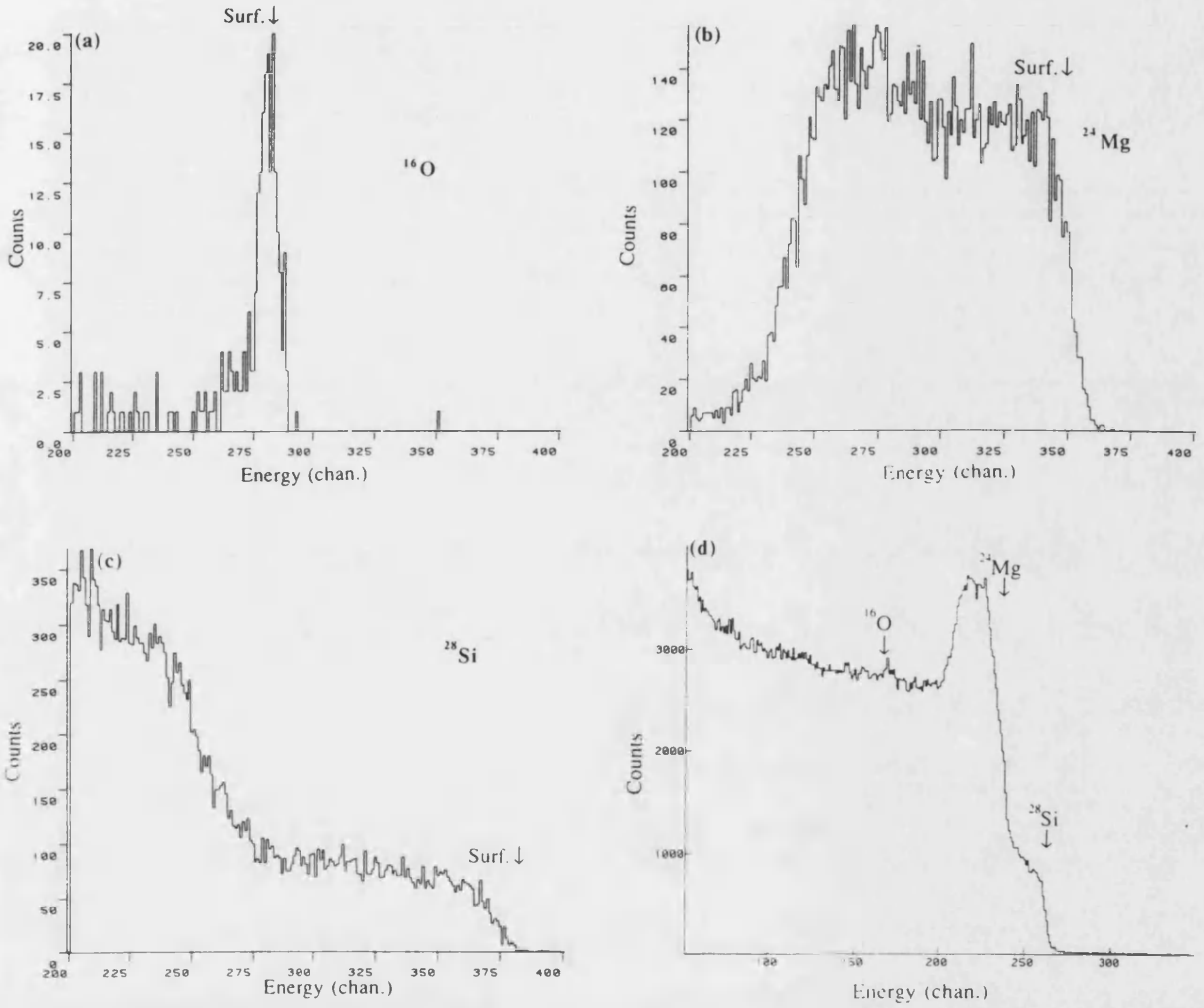


Fig. 4. The same sample as in fig. 3 annealed in vacuum for 30 min at 250 °C to form a $Mg_2Si$ layer (a) $^{16}O$ recoil energy spectrum. (b) $^{24}Mg$ recoil energy spectrum. (c) $^{28}Si$ Recoil energy spectrum. (d) RBS spectrum for normally incident 2.4 MeV $\alpha$-particles backscattered at 168°. The arrows denote the surface positions for $^{16}O$, $^{24}Mg$ and $^{28}Si$.

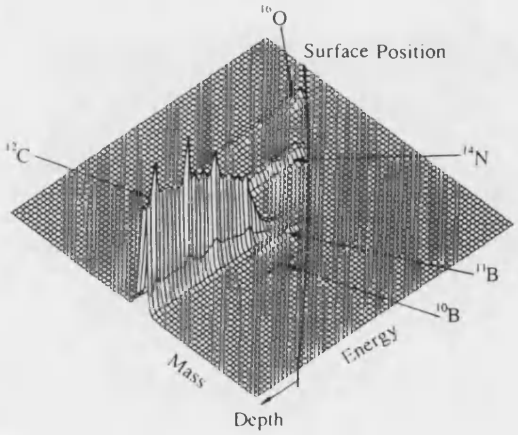


Fig. 5. Isometric plot of the low mass region of an overlayer containing Ti, O, N and B on a carbon substrate.

illustrates the good depth resolution obtained by this method ( ≈ 80 nm fwhm at 500 nm depth in the quantum well structure).

## 5. Performance of the recoil telescope

From the viewpoint of quantitative ion beam analysis the energy and mass resolutions and efficiency of the system are critical parameters. Fig. 7 shows the overall energy resolution of the system for a number of recoil

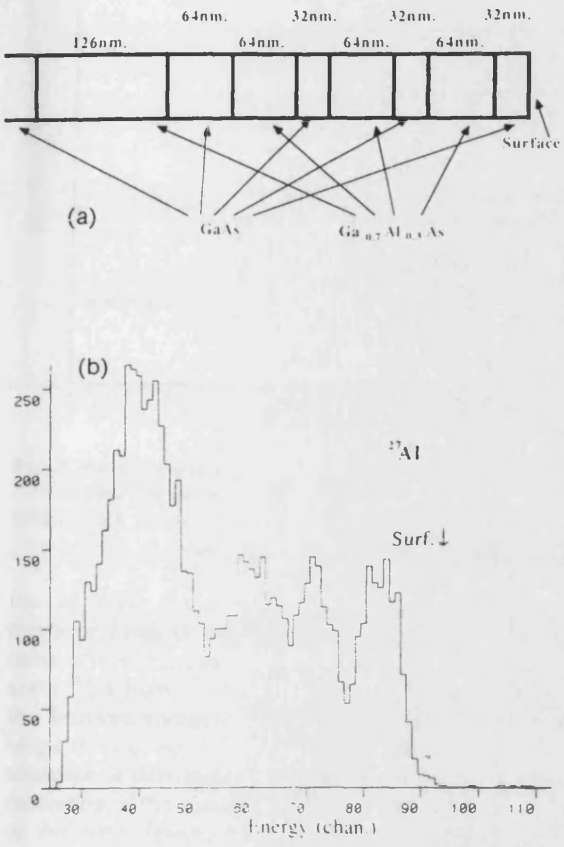


ig. 6. (a) Schematic diagram of the $Ga_{(1-x)}Al_xAs$ quantum ell structure specimen. (b) $^{27}Al$ recoil energy spectrum from the quantum well structure.

pecies. The data in fig. 7 were obtained from the width f the high energy edges corresponding to the surface of omogeneous specimens bombarded with 48 MeV Br ons. The overall energy resolution is contributed to by oth the *intrinsic* contribution from the recoil telescope nd the *extrinsic* system dependent contribution from he kinetic angular dispersion and the energy spread of he accelerator beam. Both the intrinsic and extrinsic ontributions are recoil species and energy dependent. The dominant contribution to the intrinsic energy reso- ution of the recoil telescope is the surface detector esolution. Despite the widespread use of silicon surface arrier detectors there is rather scanty information on their energy resolution for particles heavier than 6 amu in the 0.5–1 MeV/amu region [33,46,47]. Some of us [46] have studied the energy resolution in the 2–20 MeV region for $^{4}He$, $^{7}Li$, $^{11}B$, $^{12}C$ and $^{16}O$ particles. At energies corresponding to surface recoils for our system ($\phi = 45°$, 48 MeV Br) the energy resolution for $^{12}C$ and $^{16}O$ recoils is 75 and 90 keV (fwhm) respectively. The resolution is expected to degrade with increasing mass and energy to $\approx 1.1$ MeV fwhm for fission fragments with mass 80 [33]. (It is possible that the resolution of the detector used here has been degraded by radiation damage from an estimated dose of $3 \times 10^6$ heavy particles $mm^{-2}$.) The contribution from straggling in the carbon foils of the time detectors with a total thickness of 13 $\mu g\ cm^{-2}$ ($\approx 65$ nm) is estimated according to the Bohr formula [48,49] to be a negligible 9 keV for $^{75}As$ surface recoils from 48 MeV Br projectiles. The dominant extrinsic contribution is due to the kinetic angular dispersion [$= (\partial E/\partial\phi)\delta\phi$] [13] of the system. For the extreme case of 48 MeV $^{79}Br^{8+}$ on $^{75}As$ at $\phi = 45°$ it is 360 keV and thus also a significant contribution to the overall energy resolution of 660 keV fwhm (fig. 7). The spreading of the accelerator beam energy is estimated to be $\sim 15$ keV fwhm which is also a small contribution. For recoils from below the target surface the energy straggling and multiple scattering also contribute to the degradation of the energy resolution. Although these target dependent terms are analytically rather intractable [50] their effect can be at least qualitatively estimated from the broadening of the buried interfaces in figures 3f–9, 4c and 6b.

The mass resolution of the telescope $\Delta M$ (fwhm) is shown in fig. 8 as a function of the recoil energy for recoils from $^{12}C$, $^{16}O$, $^{27}Al$ and $^{75}As$. This data was obtained from the fwhm of energy-gated mass-spectra from samples with homogeneous composition (the carbon substrate of fig. 5, $Al_2O_3$, and a thick film of $Ga_{0.76}Al_{0.24}As$). In the $^{75}As$ case the fwhm was used to determine the fwhm in order to minimize interference from a nearby $^{71}Ga$ peak. The mass resolution $\Delta M$ is small for high energy light recoils and except for the very lowest energies is rather independent of recoil energy. As a rule of thumb, assuming Gaussian mass distributions, two isotopes of equal intensity spaced 1 amu are completely resolved if $\Delta M$ (fwhm) $< 0.78$ amu. Reference to figs 3d and 8 shows that this is achieved

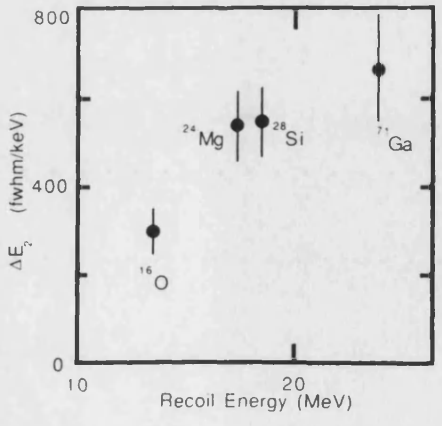


Fig. 7. Recoil telescope energy resolution for $^{12}C$, $^{16}O$, $^{28}Si$ and $^{71}Ga$ recoils determined from the width of surface edges.

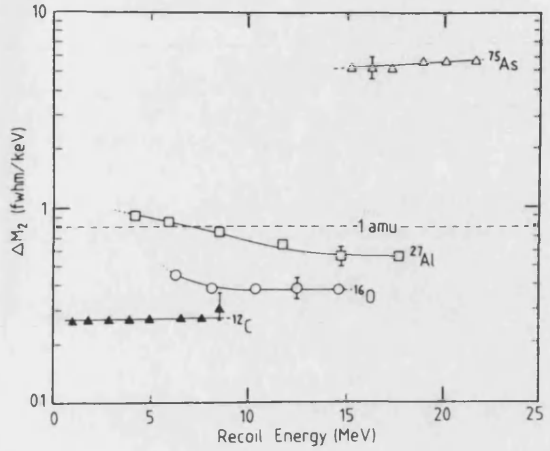


Fig. 8. Mass resolution vs. recoil energy for $^{12}C$, $^{16}O$, $^{27}Al$ and $^{75}As$ recoils. The dotted line marked t amu denotes the region below which two isotopes of equal intensity separated by one mass unit can be resolved.

for $M_2 \leq 28$. An interesting application is separate depth profiling of Ga and As in $Ga_{(1-x)}Al_xAs$ structures which requires $\Delta M < 3.12$ amu in order to separate $^{71}Ga$ from $^{75}As$. The mass resolution is related to the intrinsic energy- and time-resolutions of the telescope through eq. (6). The mass resolution of a TOF-E telescope is determined through eq. (6), by the energy resolution of the energy detector, the intrinsic resolution of the time detectors, and the scattering and energy straggling in the 3 $\mu g\ cm^{-2}$ thick carbon foil of the first time detector T1. The time dispersion of the telescope,

$$dT/dE\ [ns/MeV] = 19.5M\ [amu]^{1/2} E\ [MeV]^{-3/2}$$
$$\approx 1.5\ ns/MeV$$

for recoils in the mass range 12 to 75 amu, at energies corresponding to the ejection from the surface by 48 MeV $^{79}Br$ projectiles. Thus an upper limit of the energy straggling in the first foil of 80 keV gives a time spreading of $\approx 150$ ps. This contribution increases with decreasing recoil energy. The changes in the timed-flight length caused by the few particles that are scattered in the first foil give a negligible contribution to the time resolution. Except for the very lowest energy ($E < 10$ MeV) heavy recoils ($M > 75$ amu) the maximum contribution from scattering in the first foil is much less than 80 ps. It may be argued that since the energy resolution $\Delta E$ of surface barrier detectors is smallest for low energy recoils [46] then from eq. (6) the increase in $\Delta M$ is associated with the energy straggling in the carbon foil of the first detector. The increase in $\Delta M$ with increasing recoil mass $M_2$ is probably a consequence of the degradation of the surface barrier detector resolution.

The efficiency of the recoil telescope is an important parameter for quantitative ion beam analysis. Fig. 9

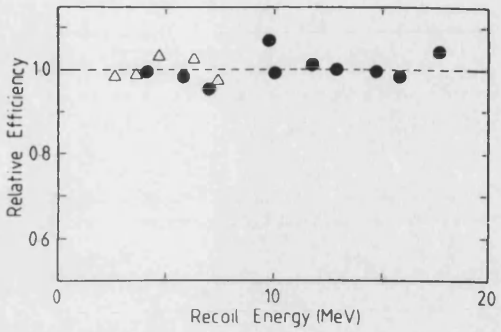


Fig. 9. Relative efficiency vs recoil energy for $^{12}C$ (open triangles) and $^{28}Si$ (closed circles) recoils.

shows the relative efficiency vs. recoil energy of the telescope for $^{12}C$, $^{28}Si$ recoils from targets with homogeneous composition. The relative efficiencies were by determining the height of the recoil signal in mass-gated energy spectra from a layer with a fixed number of atoms $cm^{-2}$ via eqs. (3) and (4) using the energy loss ratio method [34] in combination with the mean energy approximation [34] to determine the energy before scattering and target thickness. Inspection of fig. 9 shows that the efficiency for carbon is energy independent over the range 3 to 8 MeV and for silicon 5 to 18 MeV. We do not expect any significant relative efficiency fall-off at higher energies since the stopping power of the carbon foils and hence the number of secondary electrons does not fall below the low energy (5–8 MeV) values. Although we are unable to ascertain the absolute efficiency of the recoil telescope since the three detectors have slightly different solid angles, the relative heights of the $^{16}O$ and $^{28}Si$ signals from a 247nm thick $SiO_2$ layer grown on Si by wet oxidation gave a O to Si ratio of $1.86 \pm 0.15$. The deviation from stoichiometry is within the error limits and bearing in mind that ion-irradiated silica tends to lose oxygen [51] and probable uncertainties in the stopping power values used [35], one can infer that over the O–Si region there is no strong dependence of telescope efficiency on the recoil atomic number. The energy deposited in electronic processes (and hence the secondary electron emission coefficient [52]) is for $^{16}O$ recoils about 50% than that for $^{28}Si$ recoils. The increase in electronic stopping with increasing recoil mass suggests that the relative detection efficiency for recoils heavier than $^{16}O$ should be independent of the recoil atomic number. The relative detection efficiency for recoils lighter than oxygen however can be expected to decrease due to the decreasing electronic energy deposition [43].

## 5. Conclusions

(a) A time of flight–energy recoil telescope for mass and energy dispersive ERDA has been constructed

that is suitable for depth profiling light elements with a mass resolution of better than 1 amu for recoil masses $M_2 < 28$ amu.

(b) The system is suitable for depth profiling of light elements in a heavy matrix with a high sensitivity due to the absence of a substrate background which is observed with conventional ERDA and RBS.

(c) The energy (depth) resolution is much higher than for conventional ERDA where a thick foil is used to discriminate against scattered projectiles. Typically 80 nm fwhm for Al at 500 nm depth in GaAlAs is possible.

(d) The relative telescope efficiency is energy independent over the range 5 to 18 MeV for Si recoils and 3 to 8 MeV for carbon recoils. At least over the O-Si region no strong dependence of the efficiency on the recoil atomic number is observed.

We are grateful to Dr. B.U.R. Sundqvist and Dr. P. Håkansson for help and advice in the initial stages of the project and for the loan of electronic modules. We are also grateful to Dr. H.-O. Blom for preparation of the B : N : O : Ti/C sample used for calibration and Dr. J. Whiteaway of STL Laboratories Plc UK for the loan of the quantum-well structures.

## References

[1] J.P. Thomas, M. Fallavier, D. Ramedame, N. Chevarier and A. Chavarier, Nucl. Instr. and Meth. 218 (1983) 125.
[2] J.P. Thomas and M. Fallavier, Proc. Int. Symp. on Three day In-depth Review on Nuclear Accelerator Impact in the interdisciplinary Field, Padova, Italy (May 30th–1st. June 1984) eds., P. Mazzoldi and G. Moschini.
[3] J.P. Thomas, M. Fallavier and A. Ziani, Nucl. Instr. and Meth. B15 (1986) 443.
[4] R. Groleau, S.C. Gujrathi and J.P. Matin, Nucl. Instr. and Meth. 218 (1983) 11.
[5] M. Petrascea, I. Berceanu, I. Branucus, A. Buta, C. Grame, I. Lazar, I. Mihai, M. Petrovic, V. Simon, M. Mihaila and I. Gita, Nucl. Instr. and Meth. B4 (1984) 396.
[6] C.R. Gossett, Nucl. Instr. and Meth. B15 (1986) 481.
[7] G. Ross and B. Terreault J. Appl. Phys. 51 (1980) 1259.
[8] G.G. Ross, B. Terreault, G. Gobeil, C. Boucher and G. Veilleux, J. Nucl. Mater. 128/129 (1984) 730.
[9] D.C. Ingram, A.W. McCormic, P.P. Pronko, J.D. Carlson, and J.A. Wollam, Nucl. Instr. and Meth. B6 (1985) 430.
[10] S.S. Klein Nucl. Instr. and Meth. B15 (1986) 464.
[11] C. Nölscher, K. Brenner, R. Knauf and W. Schmidt, Nucl. Instr. and Meth. 218 (1983) 116.
[12] J. Bøttiger, J. Nucl. Mater. 78 (1978) 161.
[13] A. Turos and O. Meyer, Nucl. Instr. and Meth. B4 (1984) 92.
[14] C. Moreau, E.J. Knatautas, R.S. Timsit, R. Grodeau, Nucl. Instr. and meth. 218 (1983) 111.
[15] A. Turos, H. Frey, O. Meyer, W. Möllerand, J.M. Pirrung, Phys. Status Solidi A83 (1984) 437.
[16] L.S. Wielunski, R.E. Benenson and W.A. Lanford, Nucl. Instr. and Meth. 218 (1983) 120.
[17] C.C.P. Madiba, J.F.P. Sellschop, H.J. Annegarne and B.R. Appleton, Nucl. Instr. and Meth. 218 (1983) 409.
[18] L. Wielunski, R. Benenson, K. Horn and W.A. Lanford Nucl. Instr. and Meth. B15 (1986) 469.
[19] M.F.C. Willemsen, A.M.L. Theunissen and A.E.T. Kuiper, Nucl. Instr. and Meth. B15 (1986) 492.
[20] F. Pászti, E. Kótai, G. Mezey, A. Manuaba, L. Pócs, D. Hildebrant and H. Strusny, Nucl. Instr. and Meth. B15 (1986) 486.
[21] J.A. Sawicki, H.H. Plattner, I.V. Mitchell and J. Gallant, Nucl. Instr. and Meth. B15 (1986) 475.
[22] T.W. Conlon, Nucl. Instr. and Meth. B9 (1985) 311.
[23] L.G. Earwaker, J.P.G. Farr, P.E. Grzeszczyk, I. Sturland and J.M. Keen, Nucl. Instr. and Meth. B9 (1985) 317.
[24] B.L. Doyle and P.S. Peercy, Appl. Phys. Lett. 34 (1979) 811.
[25] P.J. Mills, P.F. Green, C.J. Palmström, J.W. Mayer, and E.J. Kramer, Appl. Phys. Lett. 45 (1984) 957.
[26] H.-S. Chang, Z.-Y. Zhou, F.-C. Yang, Z.-W. Xu and Y.-H. Ren Nucl. Instr. and Meth. 218 (1983) 601.
[27] S. Yamaguchi, Y. Fujino, S. Nagata, H. Kaneko, K. Hashimoto and Hirabayashi, Nucl. Instr. and Meth. 218 (1983) 598.
[28] T.T. Bardin, T.G. Pronko and A. Joshi, Thin Solid Films 119 (1984) 429.
[29] P.F. Green and B.L. Doyle, Nucl. Instr. and Meth. B18 (1986) 64.
[30] B.L. Cohen, C.L. Fink, and J.H. Dengan, J. Appl. Phys. 43 (1972) 19.
[31] B. Sundqvist, H. Berggren, K.H. Flodkvist, A. Johansson and I. Koersner, IEEE Trans. Nucl. Sci. NS-24 (1977) 652..
[32] K.-H. Flodqvist, A spectrometer for low energy light heavy ions, Tandem Accelerator Laboratory Uppsala Report TLU 112/85.
[33] E. Weissenberger, P. Geltenbort, A. Oed, F. Gönnenwein and H. Faust, Nucl. Instr. and Meth. A248 (1986) 506.
[34] W.-K. Chu, J.W. Mayer and M.-A. Nicolet (eds.) Backscattering Spectromery (Academic Press, New York, 1978).
[35] J.F. Ziegler, J.P. Biersack and U. Littmark, The Stopping and Range of Ions in Solids, vol. 1 of The Stopping and Ranges of Ions in Matter ed., J.F. Ziegler (ed.) (Pergamon, New York, 1985).
[36] J. Åström and G. Possnert, The Uppsala cesium sputter ion source, Tandem Accelerator Laboratory Uppsala Report TLU 102/83.
[37] G. Amsel and B. Maurel, Nucl. Instr. and Meth. 218 (1983) 183.
[38] W. Bohne, W. Galster, K. Grabisch and H. Morgenstern, Nucl. Instr. and Meth. A240 (1985) 145.
[39] F. Busch, W. Pfeffer, B. Kohlmeyer, D. Schüll and F. Pühhoffer, Nucl. Instr. and Meth. 171 (1980) 71.
[40] R.L. Kavalov, Yu. L. Margaryan, M.G. Panyan and G.A. Papyan, Nucl. Instr. and Meth. A237 (1985) 543.
[41] A.M. Zebelman, W.G. Meyer, K. Halbach, A.M. Poskanzer, R.G. Sextro, G. Gabor and D.A. Landis, Nucl. Instr. and Meth. 141 (1977) 439.
[42] A. Oed, G. Barreau, F. Gönnenwein, P. Perrin, C. Ristori and P. Geltenbort, Nucl. Instr. and Meth. 179 (1981) 265.
[43] W.N. Lennard, H.R. Andrews, M. Freeman, I.V. Mitchell, D. Phillips, D.A.S. Walker and D. Ward, Nucl. Instr. and Meth. 203 (1982) 565.

[44] S. Eskildsen, private communication (1985) Mac-RBSim version 11.2 RBS simulation program.
[45] W.K. Chu, S.S. Lau, J.W. Mayer, H. Müller and K.N. Tu, Thin Solid Films 25 (1975) 393.
[46] M. Östling, C.S. Petersson, P. Johansson, A. Wikström and G. Possnert Nucl. Instr. and Meth. B15 (1986) 729.
[47] S. Petersson, P.A. Tove, O. Meyer, B. Sundqvist and A. Johansson, Thin Solid Films 19 (1973) 157.
[48] N. Bohr, Philos. Mag. 30 (1915) 581.
[49] E. Bonderup, Lecture Notes, Penetration of charged particles through matter, 2nd ed. (Institute of Physics, Aarhus Universitet, Denmark, 1981) pp. 83–91.
[50] H.J. Whitlow, D. Phil. Thesis, Univ. of Sussex (1980).
[51] G. Betz and G.K. Wehner, in: Sputtering by particle bombardment II, ed., R. Behrisch Topics in Applied Physics, vol. 52 (Springer, Berlin, 1983) p. 11.
[52] J. Schou, Phys. Rev. B22 (1980) 2141.

# Mass-dispersive recoil spectrometry studies of oxygen and nitrogen redistribution in ion-beam-synthesized buried oxynitride layers in silicon

Harry J. Whitlow and C. Sture Petersson
*The Royal Institute of Technology, Department of Solid State Electronics, S-100 44 Stockholm, Sweden*

Karen J. Reeson and Peter L. F. Hemment
*Department of Electronic and Electrical Engineering, University of Surrey, Guildford, Surrey, GU2 5XH, Great Britain*

(Received 12 February 1988; accepted for publication 26 March 1988)

Mass-dispersive recoil spectrometry has been employed to study the influence of annealing conditions in ion-beam-synthesized silicon oxynitride structures prepared by implantation of $1.8\times10^{18}$ and $1\times10^{17}$ 200 keV $^{16}O^+$ and $^{14}N^+$ ions $cm^{-2}$, respectively, at approximately 600 °C. Subsequent annealing at 1200 and 1300 °C leads to redistribution of the implanted oxygen to form a buried oxide layer with nitrogen segregation to the buried $SiO_2$/Si interfaces. Implantation with $N^+$ subsequent to $O^+$ followed by annealing at 1200 °C for 2 h was found to lead to both a lower oxygen content and lower channeling detectable defect concentration in the overlying silicon film than if the order of implantation was reversed. No significant dependence on order of implantation was observed after annealing at 1300 °C for 5 h.

A promising new technique for the production of silicon-on-insulator (SOI) structures for the fabrication of radiation-resistant low-leakage complementary metal-oxide-semiconductor (CMOS) very large scale integration (VLSI) circuits is ion beam synthesis (IBS). In this technique oxygen and/or nitrogen ions of 100–400 keV are implanted into a silicon substrate maintained at a high temperature.[1,2] After subsequent thermal processing a buried insulating layer of silicon dioxide [commonly termed SIMOX (separation by implanted oxygen)] or nitride with sharp interfaces is formed. Implanted $SiO_2$ films fabricated by this technique are of high quality, and the overlying Si has a sufficiently low defect density ($\approx10^6\,cm^{-2}$) that high performance devices can be fabricated in it by using standard processing techniques.[3–5] However, the high annealing temperatures of $\geqslant$1300 °C required to produce abrupt Si/$SiO_2$ interfaces can lead to problems associated with impurity contamination and damage of the furnace if conventional quartz tube furnaces and windings are used. Lower annealing temperatures (around 1200 °C) are required for implanted $Si_3N_4$ films, but these films show high leakage currents that are associated with crystallization of the nitride layer.[6] Moreover, there is currently a controversy as to whether residual nitrogen in the silicon film may give rise to anomalous donor centers. In an effort to combine the superior characteristics of the oxide with the lower annealing temperatures of the nitride, implanted oxynitride layers are beginning to attract considerable attention.[7,8]

Discrepancies have recently been reported in the literature relating to the volume concentration of nitrogen in the silicon overlayer of SIMOX structures measured using secondary ion mass spectroscopy (SIMS).[9,10] This is also likely to be a problem with IBS oxynitrides since the low self-diffusion of nitrogen in nitrogen-rich layers may, at sufficiently high doses, lead to bubble formation. The presence of gas-containing voids will lead to systematic underestimation of oxygen and nitrogen content in all forms of sputter profiling because of explosive release of gas when the wall thickness is sputter eroded below the critical value for rupture.[11] Furthermore, in the case of SIMS, nitrogen profiling is complicated because of interference of the $^{14}N^+$ signal with $^{28}Si^{2+}$ ions. Recently mass-dispersive recoil spectrometry has been developed for *quantitative* depth profiling of light and medium mass elements[12–14] in a manner similar to Rutherford backscattering spectrometry. In this technique, which does not rely on sputter erosion, high-energy ($\approx$0.8 MeV/amu) heavy ions impinge on the specimen to be analyzed at a glancing angle. Recoiling target atoms ejected at a fixed recoiling angle are detected in a detector telescope that identifies the energy and mass[12,13] or energy and atomic number[14] for each recoil.

To quantitatively assess how the implanted nitrogen and oxygen redistribute during annealing and how the implantation sequence affects their distribution and the crystalline quality of the overlying silicon, we have employed mass-dispersive recoil spectroscopy in combination with $^4He$ channeling to obtain quantitative depth profiles of the oxygen and nitrogen concentrations and to elucidate the defect density in the overlying silicon.

Device quality (100) single-crystal silicon wafers were implanted sequentially with 200 keV $^{16}O^+$ and $^{14}N^+$ ions to doses of $1.8\times10^{18}$ and $1\times10^{17}$ ions $cm^{-2}$, respectively. For sample A the oxygen was implanted prior to the nitrogen, while for sample B the nitrogen was implanted first. During implantation, the substrate was maintained at a temperature of approximately 600 °C using ion beam heating. Conductive heat losses, during implantation, were minimized by isolating the substrate from the sample plate by means of small silicon tips. After implantation the specimens were capped with 5000 Å $SiO_2$, cut, and annealed at either 1200 °C for 2 h or 1300 °C for 5 h using a nitrogen ambient and, in the latter case, a SiC furnace tube.

The silicon, oxygen, and nitrogen depth profiles were measured using mass-dispersive recoil spectrometry using a setup closely identical to that described previously.[12,13] The principal difference is that the timed flight length has been

 0003-6951/88/221871-03$01.00  

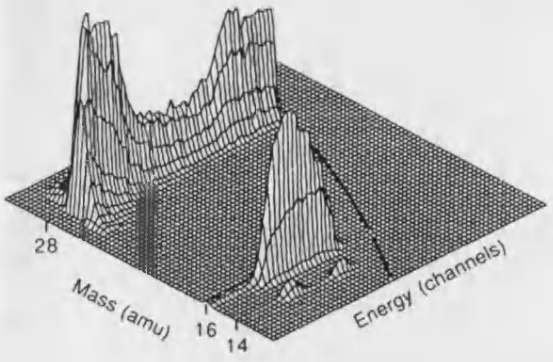


FIG. 1. Isometric plot of the sorted mass-recoil energy matrix for sample B ({100}Si implanted with $1\times10^{17}$ $N^+$ followed by $1.8\times10^{18}$ $O^+$ 200 keV ions $cm^{-2}$, respectively, at 600 °C and annealed at 1300 °C for 5 h). The thick line indicates the energy of recoils from the surface.

increased to 738 mm. The samples were irradiated with 48 MeV $^{81}Br^{8+}$ ions incident at 67.5° to the surface normal. Recoiling target atoms ejected at 45° to the incident beam direction were detected in a time-of-flight energy (TOF-E) detector telescope, and the data were stored using a computer. The resulting time-energy data set was sorted off-line to yield recoil energy spectra for $^{14}N$, $^{16}O$, and $^{28}Si$ recoils. The defect content of the overlying silicon film was measured using Rutherford backscattering spectrometry (RBS) and ion channeling with 1.5 MeV $^4He^+$ channeling at the University of Surrey.

Figure 1 shows the sorted mass-recoil energy matrix for sample B annealed at 1300 °C for 5 h. Inspection shows that the silicon, oxygen, and nitrogen signals are sufficiently well resolved in mass to permit unambiguous interpretation and identification of the masses. The dip in the silicon signal corresponds to the buried oxide layer. The two peaks for a mass of 14 amu correspond to nitrogen that has segregated to both of the buried $Si/SiO_2$ interfaces. In Figs. 2 and 3 the oxygen and nitrogen recoil energy spectra for sample A, normalized with respect to the silicon substrate signal, are presented as a function of annealing conditions. (These recoil energy spectra can be interpreted in a similar manner to RBS spectra by considering them to be the "RBS signal" for the isotope in question.[12])

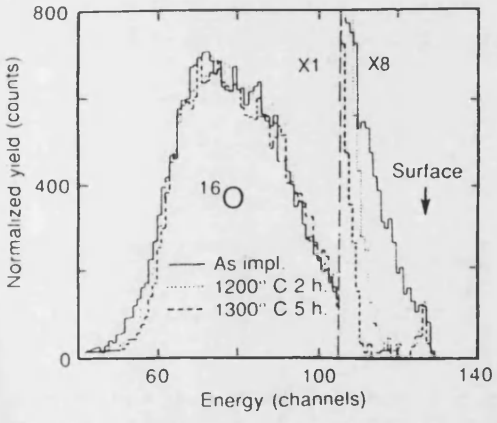


FIG. 2. Annealing dependence of the $^{16}O$ recoil spectra from sample A ({100}Si implanted with $1.8\times10^{18}$ $O^+$ followed by $1\times10^{17}$ $N^+$ 200 keV ions $cm^{-2}$, respectively, at 600 °C). In the near surface region the yield has been magnified to show $^{16}O$ redistribution in the silicon overlayer. The yield data has been normalized with respect to the $^{28}Si$ substrate signal.

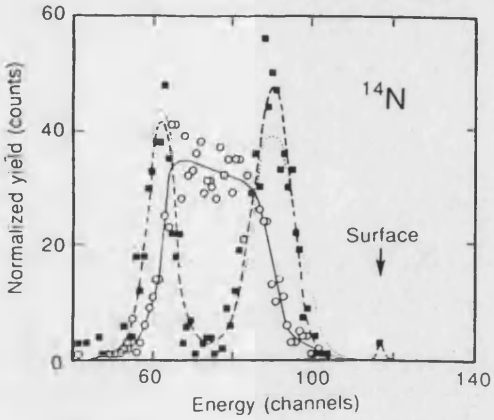


FIG. 3. Annealing dependence of the $^{14}N$ recoil spectra from sample A ({100}Si implanted with $1.8\times10^{18}$ $O^+$ followed by $1\times10^{17}$ $N^+$ 200 keV ions $cm^{-2}$, respectively, at 600 °C). The solid trend line (open circles), dotted trend line, and dashed trend line (closed squares) denote the as-implanted, 1200 °C 2 h and 1300 °C 5 h anneals, respectively. The yield data have been normalized with respect to the $^{28}Si$ substrate signal.

The as-implanted $^{16}O$ distributions (Fig. 2) were independent of the order of $O^+$ and $N^+$ implantation. Both samples A and B have a "plateau" region characteristic of implantation above the critical fluence $\phi_c$ for formation of a stoichiometric compound[1,15] and tails that extend into both the overlying silicon film and deeper into the silicon substrate. No special significance should be paid to the $^{16}O$ surface peaks since these will depend on whether the capping oxide is completely stripped and on the vacuum environment during analysis. The unannealed nitrogen distributions, in contrast to the oxygen distributions, are dependent on the order of implantation. In the case of sample A (Fig. 3), where the $N^+$ implantation at a fluence $\phi < \phi_c$ is subsequent to the $O^+$ implantation, the $^{14}N$ is concentrated in the near stoichiometric portion of the implanted oxygen distribution. Presumably, this is due to $O^+$-irradiation-induced migration of nitrogen into amorphous $SiO_2$ where its solubility is greater than in silicon. However, when the $N^+$ ions are implanted first (sample B), the nitrogen distribution is more spread out with both deeper and shallower tails and a superposed peak corresponding to radiation-induced segregation to the deeper, but not the shallower, buried $SiO_2/Si$ interface.

Annealing at 1200 °C for 2 h causes the $^{16}O$ distributions to redistribute towards the buried layer (Fig. 2). The deeper $SiO_2/Si$ interface became sharper for both samples. However, the behavior at the shallower buried $SiO_2/Si$ interface is dependent on the order of implantation. If the $O^+$ implantation is prior to the $N^+$ implantation (sample A), the oxygen migrates from the overlying silicon (Fig. 2). Additionally, stepped edges on the $^{16}O$ recoil spectrum and RBS random spectrum develop, which is indicative of the formation of oxynitride phase(s). Furthermore, in the overlying

silicon film at the surface and at intermediate depths, the concentration of defects detected by ion channeling decreased to a level commensurate with virgin silicon. However, when the order of implantation is reversed (sample B), the shallow tail of the $^{16}O$ distribution is invariant under annealing and the channeling-detectable damage extends almost to the surface of the overlying silicon. Annealing at 1200 °C for 2 h gave rise to bimodal $^{14}N$ distributions in both samples because of segregation of nitrogen to the flanks of the buried oxide layer. The area and spreading of the near surface $^{14}N$ peak into the overlying Si film was greater for sample A. This is in qualitative agreement with SIMS measurements[8] which show an enhanced $^{14}N$ content in the overlying Si film when $N^+$ is implanted subsequent to $O^+$. The invariance of the $^{16}O$ distribution and dechanneling yield when nitrogen is implanted first can be associated with trapping of the oxygen in nitrogen-stabilized precipitates in the overlying silicon. This might be due to the formation of an oxynitride coating around the oxygen precipitates which effectively acts as a diffusion barrier.[8]

The $^{16}O$ profiles and RBS spectra for both samples A and B, after annealing at 1300 °C for 5 h, were very similar with more abrupt $SiO_2$/Si buried interfaces than those obtained after the 1200 °C anneal. The $^{16}O$ content of the silicon overlayer was also reduced relative to the 1200 °C anneal (Fig. 2). As for the case of the 1200 °C anneal, there was evidence of oxynitride phase formation at the shallow $SiO_2$/Si interface. The interfacial peaks in the $^{14}N$ distributions are also sharper (Fig. 3); however, in the case of sample B ($N^+$ prior to $O^+$ implantation) there was a lower nitrogen content in the buried oxide layer. For both samples the dechanneled yield was close to that for virgin silicon, even at depths close to the shallow $SiO_2$/Si buried interface. Evidently, annealing at 1300 °C for 5 h is sufficient to break up the nitrogen-stabilized oxygen precipitates formed when the $N^+$ implantation is carried out first (sample B).

Travel support from the British Council is gratefully acknowledged.

[1]P. L. F. Hemmet, Mater. Res. Soc. Symp. Proc. **53**, 207 (1986).
[2]C. Jaussaud, J. Margail, M. Bruel, and J. Stoemenos, in Proceedings of the Materials Research Society, Fall Meeting, Boston, Dec. 1987 (to be published).
[3]J. R. Davis, in *Proceedings of the 17th European Solid State Device Research Conference, Bologna, Italy, Sept. 1987*, edited by P. E. Calzolari and G. Soncini (University of Bologna, Bologna, 1987), p. 525.
[4]J. R. Davis, G. F. Hopper, K. J. Reeson, and P. L. F. Hemment, IEEE Trans. Electron Devices **34**, 1713 (1987).
[5]S. S. Christoloveanu, S. Gardner, C. Jaussaud, J. Margail, A. J. Auberton-Hervé, and M. Bruel, J. Appl. Phys. **62**, 2793 (1987).
[6]R. Kwor and S. Polcheopek (unpublished results).
[7]K. J. Reeson, P. L. F. Hemment, J. A. Kilner, R. J.Chater, C. D. Meekison, C. Marsh, G. R. Brooker, and J. R. Davis, Vacuum **36**, 891 (1986).
[8]K. J. Reeson, P. L. F. Hemment, C. D. Meekison, C. D. Marsh, G. R. Booker, R. J. Chater, J. A. Kilner, and J. Davis, Nucl.Instrum. Methods B (in press).
[9]G. E. Davies and S. Prussin, in Proceedings of the Materials Research Society, Fall Meeting, Boston, Dec. 1987 (to be published).
[10]J. A. Kilner, R. J. Chater, S. Biswas, P. L. F. Hemment, and K. J. Reeson, in Proceedings of the Materials Research Society, Fall Meeting, Boston, Dec. 1987 (to be published).
[11]B. Scherzer, in *Sputtering by Particle Bombardment II*, edited by R. Behrisch, Vol. 52 of Topics in Applied Physics (Springer, Berlin, 1983), p. 272.
[12]H. J. Whitlow, G. Possnert,and C. S. Petersson, Nucl. Instrum. Methods B **27**, 448 (1987).
[13]H. J. Whitlow, A. B. Ch. Anderson, and C. S. Petersson, Nucl. Instrum. Methods (in press).
[14]A. M. Behrooz, R. L. Headrick, L. E. Sieberling, and R. W. Zurmühle, Nucl. Instrum. Methods B **28**, 108 (1987).
[15]K. J. Reeson, Nucl. Instrum. Methods B **19/20**, 267 (1987).

ELSEVIER

Nuclear Instruments and Methods in Physics Research B 94 (1994) 530–536

NIM B
Beam Interactions with Materials & Atoms

# Multivariate analysis method for energy calibration and improved mass assignment in recoil spectrometry

Mohamed El Bouanani [a,*], Mikael Hult [a], Leif Persson [a], Erik Swietlicki [a], Margaretha Andersson [b], Mikael Östling [c], Nils Lundberg [c], Carina Zaring [c], David D. Cohen [d], Nick Dytlewski [d], Peter N. Johnston [e], Scott R. Walker [e], Ian F. Bubb [e], Harry J. Whitlow [a]

[a] *Department of Nuclear Physics, Lund Institute of Technology, Sölvegatan 14, S-223 62 Lund, Sweden*
[b] *Department of Inorganic Chemistry, Uppsala University, Box 531, S-751 21 Uppsala, Sweden*
[c] *Department of Electronics, Solid State Electronics, Royal Institute of Technology, P.O. Box Electrum 229, S-164 40 Kista, Sweden*
[d] *Australian Nuclear Science and Technology Organisation, PMB 1, Menai 2234, Lucas Heights, Australia*
[e] *Department of Applied Physics, Royal Melbourne Institute of Technology, GPO Box 2476V, Melbourne 3001, Australia*

Received 26 June 1994; revised form received 28 July 1994

**Abstract**

Heavy ion recoil spectrometry is rapidly becoming a well established analysis method, but the associated data analysis processing is still not well developed. The pronounced nonlinear response of silicon detectors for heavy ions leads to serious limitation and complication in mass gating, which is the principal factor in obtaining energy spectra with minimal cross talk between elements. To overcome the above limitation, a simple empirical formula with an associated multiple regression method is proposed for the absolute energy calibration of the time of flight–energy dispersive detector telescope used in recoil spectrometry. A radical improvement in mass assignment was realized, which allows a more accurate and improved depth profiling with the important feature of making the data processing much easier.

## 1. Introduction

Recoil spectrometry (RS) using high energy heavy ions and multiparameter dispersive detector systems has recently attracted considerable interest. RS can be used to characterise the depth profiles of light and medium heavy elements in complex structures. In particular, the technique can be applied to study light and medium heavy elements in a heavy matrix, such as III–V semiconductor based structures [1–6]. RS is similar to RBS, but with the important difference that the recoiling target atoms are detected rather than the scattered incident ions. These recoils carry information on both the depth of origin and their atomic number or mass. Two basic types of measurements are possible, i.e., nuclear-charge energy dispersive measurements using $\Delta E$–$E$ detector telescopes [6] and mass and energy dispersive measurements using time of flight (ToF)–energy dispersive detectors [1–5,7–10]. The latter type of measurement will be considered here.

### 1.1. Mass assignment and energy calibration

In mass and energy dispersive RS the measured parameters are the recoil ToF and the energy of each recoil. The ToF is the time taken for a recoil atom to travel a fixed distance $L$ [8–10], which is commonly measured by detecting the burst of secondary electrons, ejected when the recoil passes through the carbon foils of a time pickoff detector. The energy is subsequently determined using a silicon surface barrier detector or p-i-n diode in which the recoils are stopped. Usually, the channel number $X$, corresponding to the pulse amplitude of the energy detector, is assumed to be proportional to the recoil energy and independent of mass. Then the mass $M$ for each recoil can be assigned according to:

$$M = KX(T - T_0)^2 \qquad (1)$$

$T$ is the time channel number, $K$ is an arbitrary constant chosen to give a suitable mass range and $T_0$ is an adjustable parameter for electronic delay corrections etc. [11]. The assigned mass and the true isotopic mass are denoted $M$ and $A$, respectively. Fig. 1 presents contour plots of two-dimensional mass–energy histograms for a soda-lime glass with and without a layer of gold evaporated onto the surface. Data from these samples were

* Corresponding author, Email: mohamed.el_bouanani@pixe.lth.se, fax +46 46 104 709, tel. +46, 46 107 682/107 631.


*SSDI* 0168-583X(94)00298-3

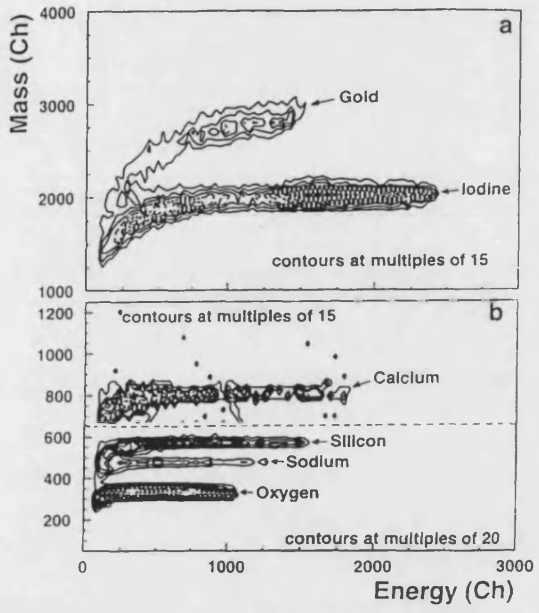


Fig. 1. A contour plot of the 2-dimensional mass–energy ($M-X$) histogram for 64 MeV $I^{10+}$ incident ion beam with mass assignment according to Eq. (1). (a) Scattered iodine and recoil gold data from a Au/glass sample, (b) oxygen, sodium, silicon and calcium data from a soda-lime glass sample without Au overlayer.

soda-lime glass with and without a layer of gold evaporated onto the surface. Data from these samples were selected because they span a wide range of recoil energies and masses. Inspection of Fig. 1 shows that the signals from the different isotopes do not lie along straight iso-mass lines. The deviation is more pronounced for heavy recoils at low energies. Often, it is necessary to adjust $T_0$ for each element in order to select a mass cut with minimum interference from other isotopes. This has the disadvantage that no absolute mass calibration can be established. Alternatively a polygon cut in the $M-X$ plane around the signal could be used. These methods for mass selection are quite satisfactory when the signals from the different isotopes are well separated, such as for light elements, C, O, Si etc. or high energy recoils that originate close to the surface. However, they are difficult to apply when the cross talk between signals is large as a result of poor mass resolution for large mass recoils or wide energy ranges. Moreover, the selection of $T_0$ and mass-cut or a polygonal cut requires a subjective judgement which precludes automatic analysis procedures and increases the overall uncertainty in the measurement.

From Eq. (1) it is evident that the deviations of the isotope signals from straight iso-mass lines must be associated with the relation of recoil energy to channel number $X$ or the ToF to the time channel number $T$. If one neglects the vanishingly small differences in energy losses in the carbon foil of the first time detector and nonlinearities in the ToF measurement it follows that the deviations from straight iso-mass lines in Fig. 1 can be attributed to the relation of recoil energy to channel number $X$.

Several approaches for improved energy calibration have been proposed. One simple approach is to determine the so-called energy defect $E_d$ [12–16], which is a mass, charge (atomic number) and energy dependent parameter. Then,

$$E = E_a + E_d. \tag{2}$$

$E_a$ is the apparent energy which is the energy of an alpha particle yielding the same pulse height. The energy defect $E_d$ is the difference between the true energy $E$ of the corresponding recoil and its apparent energy. This method requires calibration of the silicon detector with alpha particles and a high precision pulser. In addition, an iteration procedure is needed to determine the mass $M$ for each recoil, which may be computationally inefficient especially when one is dealing with more than $10^5$ recoils per spectrum, as is usual in recoil spectrometry studies of metal/III–V compounds.

Schmidt et al. and Weissenberger et al. [17,18] have proposed a calibration formula for fission fragments which is based on four parameters $\beta_1-\beta_4$ according to:

$$E = A(\beta_1 X + \beta_2) + \beta_3 X + \beta_4. \tag{3}$$

Although Eq. (3) was intended to have a validity restricted to the narrow energy and mass range of fission fragments, Ghetti et al. [19] found it could be applied with reasonable accuracy for a relatively wide range of recoil masses and energies, namely in the $0.05A-0.2A$ MeV (energy range spanned by recoiling target residues from intermediate energy heavy ion collisions). They noted that $\beta_1-\beta_4$ varied significantly from detector to detector. We studied the extension of the above method to the $0.05A-0.9A$ MeV energy range corresponding to our RS measurements. The improvement as judged from the straightness of the isotope signals in plots of 2-dimensional mass–energy histograms was inadequate. In particular, the deviations were, as one anticipates from Eq. (3), predominating for the larger recoil masses. The reason is that the pulse height response of the silicon detector is assumed to be linearly dependent on both mass and energy which turns out to be inaccurate for large energy and mass ranges.

A significant feature in ToF–$E$ recoil spectrometry experiments, is that if the mass of the recoils is known, their absolute energy between the two time detectors may be determined accurately from the measured ToF. This may be used to establish the energy calibration of the silicon detector over the same mass and energy ranges as are spanned in the experimental measurements. We emphasise that this calibration strictly establishes the relation between the recoil energy between the two time detectors and the silicon detector pulse height. This energy calibration is thus applicable for mass assignment. To assign the depth of origin for the recoils, one is interested in the energy of the recoils as they leave the sample surface i.e.

before they enter the carbon foil of the first time detector. This may be obtained by applying a small correction to take account of the energy loss in the carbon foil.

In this paper, we present a procedure for establishing the relation between the channel number corresponding to the silicon detector pulse height ($X$) and the recoil energy ($E$). The procedure is based on the use of a number of standard samples and on ToF measurements for the determination of the absolute energies of the recoils. We will also demonstrate how this calibration may be used to improve recoil-mass assignment by removing the deviation of the signals from straight iso-mass lines in the recoil mass–energy plane.

## 2. Experiment

77 MeV $^{127}I^{10+}$ and 64 MeV $^{127}I^{9+}$ from the ANTARES Tandem accelerator at ANSTO, Lucas Heights were used as projectile ions. These impinged at an angle of 60° to the sample surface normal. Recoiling target atoms, ejected at an angle of 45° to the incident beam direction, were detected in a recoil detector telescope with a timed flight length $L$ of 437.5 mm. The carbon foil thicknesses were $\sim 5\ \mu g\,cm^{-2}$ (see Refs. [3,4] for details). The standard samples used for the calibration were Au/glass, glass, $CuInSe_2$/glass and Mo/glass. The soda-lime glass substrates contained oxygen, sodium, silicon and calcium. The energy and time ADC conversion results for each recoil were stored sequentially in a computer file using a standard data-acquisition system. The data analysis was done interactively using the CERN Physics Analysis Workstation (PAW) code [20] using our specially written TASS macro command set [21].

## 3. Empirical formula for energy calibration of silicon particle detectors

In measurements using a ToF–$E$ detector telescope, the ToF can be determined with a high degree of accuracy. Using calibration samples with different masses it is straightforward to establish the time calibration from the position $T_s$ of the edge in the time spectra corresponding to recoils from the surface layer, as shown in Fig. 2.

$$t_s = L\sqrt{\frac{A_2}{2(E_s - \Delta E)}}\,, \tag{4}$$

$$E_s = \frac{4A_1A_2}{(A_1+A_2)^2}\cos^2\phi\, E_0. \tag{5}$$

Here $t_s$ is the ToF of the recoil from the surface with an energy $E_s$, $A_1$ and $A_2$ are the isotopic masses of the projectile and recoil, respectively, $E_0$ is the incident beam energy and $\phi$ is the recoiling angle. It should be born in mind that the energy loss when the recoils traverse the first, but not the second carbon foil, leads to a negligibly

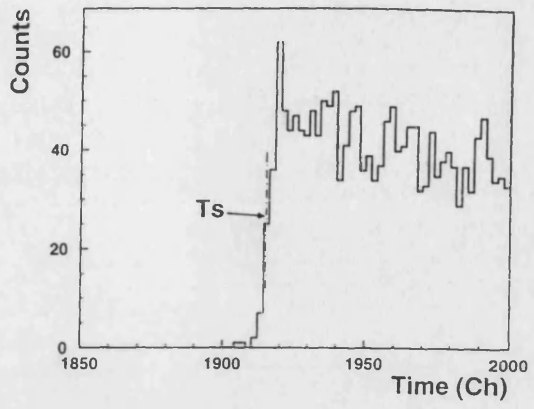


Fig. 2. A time spectrum for $^{16}O$ recoils from a soda-lime glass sample using 64 MeV $I^{9+}$ as incident ion beam.

small increase in the mean ToF. A correction $\Delta E$, calculated using the Ziegler, Littmark and Biersack [22] code for stopping cross sections was applied to correct for the energy loss in the carbon foil of the first time detector. Figs. 3a and 3b illustrate the ToF calibration obtained by this method and the deviation $\Delta T$ of the ToF data from a straight line fit. This deviation is less than 200 ps (see Fig. 3b) and is quite small compared to the time resolution of the ToF setup used in the measurements, which was less than 600 ps.

Once the time calibration has been established, the energy of recoils with known masses can be determined with very high accuracy. Using the above method, the behaviour of the energy response of the silicon detector for

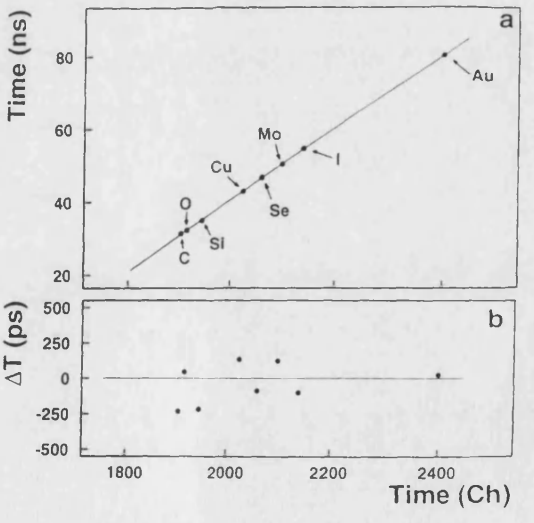


Fig. 3. (a) The time calibration of the ToF detector determined from the positions of surface edges in the time spectra of carbon, oxygen, silicon, copper, selenium, molybdenum, iodine and gold. (b) The deviation of the measured data points (time values of surface edges of the above recoils) in Fig. 3a from the straight line fit.

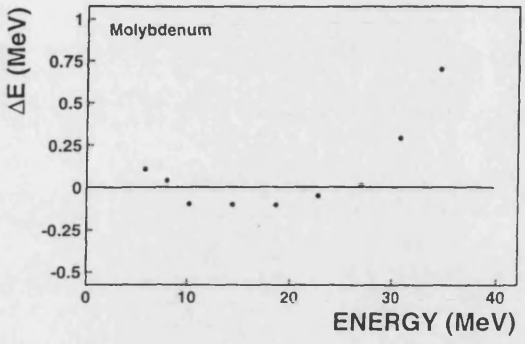


Fig. 4. The deviation, $\Delta E$, of the mean values of the Si detector pulse height from the least square fitted straight-line law to the energy derived from the ToF for molybdenum recoils.

nonlinear response of the Si detector starts to become pronounced for Cu and heavier recoils in the energy range of 2–40 MeV). Fig. 4 presents $\Delta E$, the deviation of the Si detector from a straight line law vs. the absolute energy extracted from the ToF for Mo recoils. (Here the atomic mass of Mo was used to calculate the energy.) Inspection of Fig. 4, as well as inspection of similar plots for the other isotopes, suggested that a second order polynomial law would yield a good energy calibration:

$$E_i = a_0 + a_1 X + a_2 X^2. \tag{6}$$

It was found that the polynomial coefficients $a_0$, $a_1$ and $a_2$ could be represented by a straight line law dependence on recoil mass $A$. In this case we may write:

$$E = (c_0 + c_1 A) + (c_2 + c_3 A) X + (c_4 + c_5 A) X^2, \tag{7}$$

where $c_0, \ldots, c_5$ are the silicon detector coefficients which are valid for a given detector. One approach would be to independently determine $a_0$, $a_1$, $a_2$ in Eq. (6) for some recoil reference elements, and hence $c_0, \ldots, c_5$ from Eq. (7). The situation is complicated because the recoil energy interval spanned in our measurements varies with recoil mass. This manifests itself mainly in the determination of the second order coefficient $a_2$, which is very sensitive. Here we propose the use of a multiple regression model to determine $c_0, \ldots, c_5$ accurately, that can use all the $X$ and $T$ values from recoils for a few selected calibration samples.

## 4. Multiple regression procedure

Rewriting Eq. (7) in terms of new variables $X_1, \ldots, X_5$.

$$E(X, A) = c_0 + c_1 X_1 + c_2 X_2 + c_3 X_3 + c_4 X_4 + c_5 X_5, \tag{8}$$

where $X_1 = A$, $X_2 = X$, $X_3 = AX$, $X_4 = X^2$ and $X_5 = AX^2$, reduces Eq. (7) to a regression formula where $c_0, \ldots, c_5$ are the parameters.

For the $i$-th recoil with mass $A_i$ the energy $E_i$ can be obtained from the ToF $t_i$ according to:

$$E_i(X_i, A_i) = \frac{A_i L^2}{2 t_i^2}. \tag{9}$$

This is applied for each of the $n$ recoils in our data set. The $n$ equations that are thus obtained can be expressed in matrix form as follows:

$$\begin{pmatrix} E_1 \\ \vdots \\ E_n \end{pmatrix} = \begin{pmatrix} 1 & X_{11} & X_{12} & X_{13} & X_{14} & X_{15} \\ \vdots & & & & & \vdots \\ 1 & X_{n1} & X_{n2} & X_{n3} & X_{n4} & X_{n5} \end{pmatrix} \begin{pmatrix} c_0 \\ c_1 \\ c_2 \\ c_3 \\ c_4 \\ c_5 \end{pmatrix} + \begin{pmatrix} e_0 \\ e_1 \\ \vdots \\ e_n \end{pmatrix},$$

i.e.

$$E = [\mathbf{X}]C + e, \tag{10}$$

where $E$ is the vector of the energy from the ToF, $[\mathbf{X}]$ the matrix containing the experimental data (mass number $A$ and energy channel number $X$), $C$ is the vector of the silicon detector parameters and $e$ is the vector of error components assumed to represent only random fluctuations and how well the above equations fit the experimental data. The $C$ parameters can be estimated using the principle of least squares [23] as:

$$C = ([\mathbf{X}^T][\mathbf{X}])^{-1}[\mathbf{X}]^T E. \tag{11}$$

To determine the parameters of the silicon detector, vector $C$, a Fortran program was developed to perform the above matrix calculation. Manipulation of a $n \times 6$ matrix where $n \approx 10^6$ is computationally tedious. This may be significantly reduced by choosing only a limited number of aggregate data values, as shown in Fig. 5 in the case of

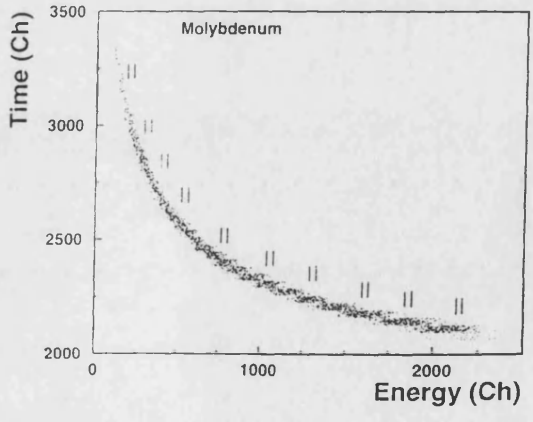


Fig. 5. A contour plot of a 2-dimensional time–energy histogram for molybdenum obtained with 77 MeV $I^{10+}$ as incident ion beam. The vertical parallel lines indicate the regions corresponding to the representative data values used in the calibration.

molybdenum. Thus, the matrix dimensions are considerably reduced which simplifies and speeds up the calculations. The representative data points were spaced equally over the energy ranges spanned by oxygen, silicon, copper, molybdenum, iodine and gold recoils. For a fixed energy channel number $X$, the corresponding mean ToF $t$ which is linearly related to the channel number $T$ was obtained from the time projection with a symmetrical gating around $X$. The gate interval was between 20 and 50 channels (depending on the counting statistics). Subsequently, the corresponding absolute energy $E_i$ is calculated for each representative data point. Here the number of selected representative data events was 53, implying a matrix dimension of $53 \times 6$. The calculated parameters of the energy silicon detector were then: $c_0 = 0.344$, $c_1 = 1.0573 \times 10^{-2}$, $c_2 = 1.3413 \times 10^{-2}$, $c_3 = 3.959 \times 10^{-5}$, $c_4 = 0.3976 \times 10^{-6}$ and $c_5 = -0.8306 \times 10^{-8}$. Note that one can choose any set of representative data events for the determination of the above silicon detector parameters. The calculated parameters $c_0, \ldots, c_5$ remain stable if the representative data chosen reasonably reflect the whole energy and mass range scanned by the corresponding RS measurements. It should also be born in mind that the above values are not universal and are specific for the silicon detector and experimental setup (amplifier gain, ADCs, etc).

This energy calibration was subsequently used to assign the mass $M$ of recoils from their known time of flight $t$ and energy channel number $X$ by:

$$M = k \frac{c_0 + c_2 X + c_4 X^2}{\left( (L^2/2t^2) - c_1 - c_3 X - c_5 X^2 \right)}. \qquad (12)$$

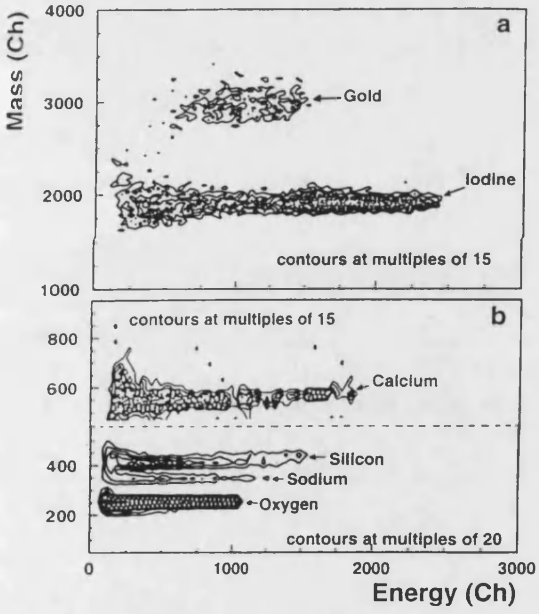


Fig. 6. A contour plot of the same data as Fig. 1 sorted with mass assignment according to Eq. (11).

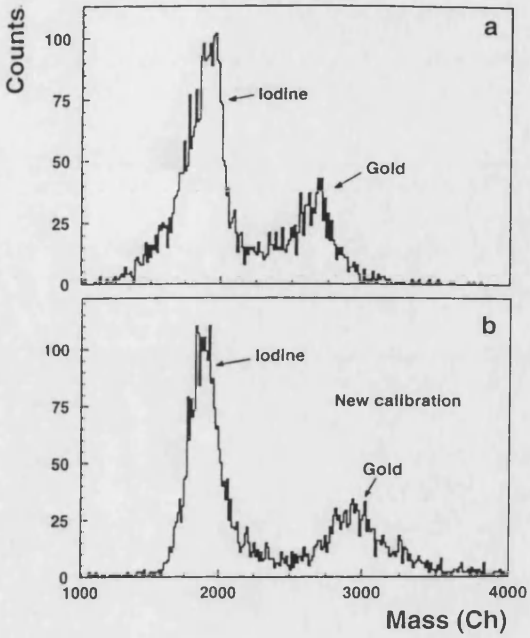


Fig. 7. 1-dimensional histograms of the assigned mass distributions for iodine and gold for silicon energy channel number interval ($X$) 100 to 1000 (3.250–18.645 MeV for molybdenum). (a) From data in Fig. 1a, Eq. (1). (b) From data in Fig. 5a, Eq. (11).

Here $k$ is a constant that relates the absolute mass, $M = kA$. In Fig. 6 the data is the same as in Fig. 1 but the mass $M$ has been determined using Eq. (12). Comparison of the two figures shows that the procedure described above leads to a distribution of the signals for the different isotopes along straight lines of constant $M$. Figs. 7a and 7b, present the mass histograms for $^{127}$I and $^{197}$Au using respectively Eq. (1) and Eq. (12) for mass assignment. In particular it may be seen that the low mass tail on the $^{127}$I signal is removed and the valley between $^{127}$I and $^{197}$Au is deeper, implying that the separation is improved. As a further example where the improvement in mass assignment can be clearly seen, Fig. 8 presents a contour plot of the 2-dimensional mass–energy histogram for a Ni/InP sample (that had been heat treated in vacuum at 350°C for 30 min). In Figs. 8a and 8b, the masses have been assigned using respectively Eq. (1) and Eq. (12).

## 5. Discussion

It is evident from the above, that the proposed procedure, based on the six calibration constants $c_0, \ldots, c_5$ (Eq. (7)) clearly leads to a considerable improvement in the alignment of the recoil data along iso-mass lines in mass–energy space. The closely linear ToF response shown in Fig. 3 implies that the deviation of the data from straight horizontal lines of constant mass in Figs. 1 and 7a, (where

Eq. (1) is used to assign $M$) can only be associated with nonlinearities in the silicon diode detector response. These nonlinearities might be associated with details as to how the energy is coupled into charge-carrier generation in the detector, dead layer and plasma-recombination effects as well as electronic nonlinearities [14,19,24,25]. A detailed discussion of how these effects influence the linearity [16,26,27] is outside the scope of this paper. In connection with this, it should be born in mind that the ToF, and hence the measured energy of the recoil, corresponds to the energy of the recoil between the two carbon foils. Thus the calibration between $X$ and recoil energy $E$ relates to the energy traversing between the foils and not the true ejection energy of the recoil (i.e. between the sample and the first carbon foil). The other experimental parameter in the energy determination is the recoil mass, which is determined by the reference sample material and taken to be the isotopic mass. It is thus interesting to consider the effect of the first carbon foil on both the energy calibration and the measurements. Table 1 presents an example of the energy loss, fractional change in ToF and shift of mass number assignment for some isotopes of interest. Inspection of this table shows that the effect is negligible especially for the lighter isotopes. If the objective of the energy calibration is restricted to mass-assignment then correction for energy loss in the first carbon foil is not necessary because the recoil mass is unaltered on traversing the foil.

The energy loss in the carbon foils, although typically

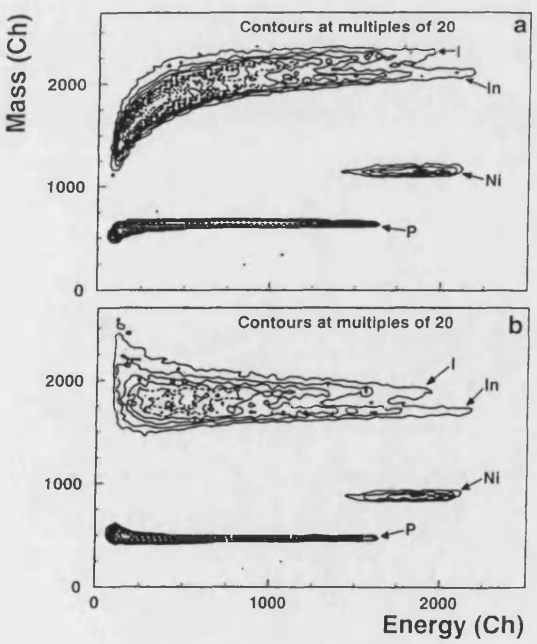


Fig. 8. Contour plot of a mass–energy histogram for 77 MeV $I^{10+}$ as incident ion beam on a Ni(50 nm)/InP sample with mass assignment according to: (a) Eq. (1), (b) Eq. (11).

Table 1
The effect of energy loss in the 5 $\mu g\,cm^{-2}$ thick carbon foil of the first time detector for carbon, oxygen, silicon, molybdenum, iodine and gold. The ToF correspond to a flight length of 437.5 mm. $\Delta E$ (keV), $\Delta M$ (u) and $\Delta$TOF (ns) are respectively the energy loss in the first carbon foil, the mass and the time overestimations

| Recoil | $E$ [MeV/A] | TOF [ns] | $\Delta E$ [keV] | $\Delta M$ [u] | $\Delta$TOF [ns] |
|---|---|---|---|---|---|
| $^{12}C$ | 0.1 | 99.88 | 31 | 0.027 | 1.32 |
| | 0.4 | 49.94 | 35 | 0.003 | 0.18 |
| | 0.9 | 33.29 | 30 | 0.001 | 0.05 |
| $^{16}O$ | 0.1 | 99.88 | 41 | 0.035 | 1.30 |
| | 0.4 | 49.94 | 50 | 0.004 | 0.19 |
| | 0.9 | 33.29 | 45 | 0.001 | 0.05 |
| $^{28-30}Si$ | 0.1 | 99.88 | 60 | 0.059 | 1.08 |
| | 0.4 | 49.94 | 91 | 0.010 | 0.20 |
| | 0.8 | 35.31 | 98 | 0.004 | 0.08 |
| $^{63-65}Cu$ | 0.1 | 99.88 | 91 | 0.135 | 0.72 |
| | 0.2 | 70.63 | 136 | 0.073 | 0.38 |
| | 0.5 | 44.67 | 182 | 0.023 | 0.13 |
| $^{95}Mo$ | 0.05 | 141.25 | 50 | 0.290 | 0.76 |
| | 0.2 | 70.63 | 154 | 0.110 | 0.29 |
| | 0.4 | 49.94 | 210 | 0.044 | 0.14 |
| $^{127}I$ | 0.05 | 141.25 | 75 | 0.502 | 0.84 |
| | 0.15 | 81.55 | 147 | 0.191 | 0.32 |
| | 0.3 | 57.67 | 220 | 0.088 | 0.17 |
| $^{197}Au$ | 0.05 | 141.25 | 147 | 1.397 | 1.06 |
| | 0.1 | 99.88 | 172 | 0.550 | 0.44 |
| | 0.15 | 81.55 | 202 | 0.352 | 0.28 |

less than 1% of the recoil energy (Table 1), may influence the depth scale which is determined by the energy difference between recoils from the surface and recoils originating from a certain depth. Taking Mo recoils as an example, the effect of the energy loss in the first foil (Table 1) corresponds, in the worst case, to an energy loss of about 150 keV. Furthermore, if the recoil energy distribution is derived from the ToF, to gain the advantage of the improved energy resolution [1] over that of a silicon detector, it will be necessary to apply a correction.

The question as to the extent of the validity of Eq. (7) is also important. As stressed, this is strictly a polynomial approximation to the response of the silicon diode detector to recoils that have not passed through the second carbon foil. It may be used for absolute energy calibration of any ToF–$E$ detector telescope. A further aspect concerns the energy range spanned by the calibration. The procedure adopted here determines the best fit constants $c_0, \ldots, c_5$ for recoils over energy regions that are actually used in the recoil measurements ($0.05A$–$0.9A$ MeV). The above calibration is expected to remain valid if applied to an extended energy range in which the silicon detector energy

response is well approximated by the second order polynomial of Eq. (6). It is evident that conventional calibration of the telescope for recoils over a fixed energy interval for different masses recoils would yield calibration constants that were not as accurate for our particular application.

## 6. Conclusions

(i) Nonlinearities in the assigned recoil mass using a ToF–$E$ detector telescope are chiefly associated with the silicon detector response function.

(ii) The use of a second order polynomial calibration law with six parameters, effectively suppresses the deviation of the assigned mass distribution from a constant iso-mass line over (at least) the isotopic mass $A = 12$–$198$ and energy $E = 2$–$40$ MeV range and allows an absolute mass calibration to be established.

(iii) The time of flight measurement provides a convenient method for calibration of the recoil detector telescope for a wide variety of isotopes and energies.

## Acknowledgements

The authors would like to thank the ANSTO staff who work on the ANTARES facility for their commitment to the project. Also the support of the Australian Institute of Nuclear Science and Engineering (AINSE) and its staff, the Australian Department of Industry, Technology and Commerce (DITAC) and Carl Trygger's Foundation are gratefully acknowledged. MEIB and MH acknowledge the support of the Swedish Institute and the Crafoord Foundation and the Royal Academy of Sciences (especially Letterstedts resestipendiefond). SRW acknowledges the support of an Australian Post-graduate Research Award.

## References

[1] M. Hult, H.J. Whitlow and M. Östling, Appl. Phys. Lett. 60 (1992) 219.

[2] M. Hult, H.J. Whitlow, M. Östling, M. Andersson, Y. Andersson, I. Linderberg and K. Stahl, J. Appl. Phys. 75 (1994) 835.

[3] M. Hult, H.J. Whitlow, M. Östling, N. Lundberg, C. Zaring, D.D. Cohen, N. Dytlewski, P.N. Johnston and S.R. Walker, Nucl. Instr. and Meth. B 85 (1994) 916.

[4] P.N. Johnston, S.R. Walker, I.F. Bubb, D.D. Cohen, N. Dytlewski, M. Hult, H.J. Whitlow, C. Zaring and M. Östling, Nucl. Instr. and Meth. B 85 (1994) 907.

[5] P. Goppelt, G. Gebauer, D. Fink, M. Wilpert, Th. Wilpert and W. Bohne, Nucl. Instr. and Meth. B 68 (1992) 235.

[6] J.P. Stoquert, G. Guillaume, M. Hage-Ali, J.J. Grob, C. Ganter and P. Siffert, Nucl. Instr. and Meth. B 44 (1989) 184.

[7] H.J. Whitlow, Proc. High energy and heavy ion beams in materials analysis workshop, Albuquerque, NM, 1989, eds. J.R. Tesmer, C.J. Maggiore, M. Nastasi, J.C. Barbour and J.W. Mayer (Material Research Society, Pittsburgh, 1990) p. 73.

[8] H.J. Whitlow, ibid., p. 243.

[9] H.J. Whitlow, B. Jakobsson and L. Westerberg, Nucl. Instr. and Meth. A 310 (1991) 636.

[10] H.J. Whitlow, G. Possnert and C.S. Petersson, Nucl. Instr. and Meth. B 27 (1987) 448.

[11] H. Breuer, N.R. Yoder, A.C. Mignerey, V.E. Viola, K. Kwiatkowski and K.L. Wolf, Nucl. Instr. and Meth. 204 (1983) 419.

[12] R. Groleau, S.C. Gujrathi and J.P. Martin, Nucl. Instr. and Meth. 218 (1983) 11.

[13] S.B. Kaufman, E.P. steinberg, B.D. Wilkins, J. Unik and A.J. Gorski, Nucl. Instr. and Meth. 115 (1974) 47.

[14] B.D. Wilkins, M.J. Fluss, S.B. Kaufman, C.E. Gross and E.P. Steinberg, Nucl. Instr. and Meth. 92 (1971) 381.

[15] E.P. Steinberg, S.B. Kaufman, B.D. Wilkins, C.E. Gross and M.J. Fluss, Nucl. Instr. and Meth. 99 (1972) 309.

[16] M. Ogihara, Y. Nagashima, W. Galster and T. Mikumo, Nucl. Instr. and Meth. A 251 (1986) 313.

[17] H.W. Schmidt, W.E. Kiker and C.W. Williams, Phys. Rev. 137 (1965) B837.

[18] E. Weissenberger, P. Geltenbort, A. Oed, F. Gonnenwein and H. Faust, Nucl. Instr. and Meth. A 248 (1986) 506.

[19] R. Ghetti, B. Jakobsson and H.J. Whitlow, Nucl. Instr. and Meth. A 317 (1992) 235.

[20] Application Software Group, Computing and Networks Division, CERN, Geneva, Switzerland.

[21] H.J. Whitlow et al., TASS, internal report, available upon request.

[22] J.F. Ziegler, J.P. Biersack and U. Littmark, The stopping and Ranges of Ions in Solids, vol. 1, The Stopping and Ranges of Ions in Matter, ed. J.F. Ziegler (Pergamon, Oxford, 1985).

[23] N.R. Draper and H. Smith, Applied Regression Analysis (Wiley, 1966).

[24] E.C. Finch, M. Asghar, M. Forte, G. Siegert, J. Grief, R. Decker and the Lohengrin Collaboration, Nucl. Instr. and Meth. 142 (1977) 539.

[25] H.J. Whitlow and M. Hautala, J. Appl. Phys. (to be submitted).

[26] L. Cliche, S.C. Gujrathi and L.A. Hamel, Nucl. Instr. and Meth. B 45 (1990) 270.

[27] H. Funaki, M. Mashimo, M. Shimizu, Y. Oguri and E. Arai, Nucl. Instr. and Meth. B 56/57 (1991) 975.

Nuclear Instruments and Methods in Physics Research B36 (1989) 53–59
North-Holland, Amsterdam



# THERMALLY GROWN $SiO_2$ FILM STANDARDS FOR ELASTIC RECOIL DETECTION ANALYSIS

Harry J. WHITLOW, A.B. Christina ANDERSSON and C. Sture PETERSSON

*The Royal Institute of Technology – Electrum, Department of Solid State Electronics Box 1298, S-164 28 Kista, Sweden*

Received 1 February 1988 and in revised form 2 August 1988

Thin-film $SiO_2$/Si structures, prepared by wet oxidation of (111)Si wafers have been investigated as reference standards for establishment of the energy and mass scales as well as the energy dependence of the detection efficiency in elastic recoil detection analysis (ERDA). 48 MeV $^{81}Br^{8+}$ ion incident 67.5° to the surface normal at fluences up to $2\times10^{14}$ ions $cm^{-2}$ did not lead to statistically significant oxygen loss ( < 5%) from the film nor to stoichiometry changes ( < 5%). Furthermore no evidence of energy broadening due to surface charging was observed. The detection efficiencies of the recoil telescope were constant within ±5% over the energy interval 9–12.7 MeV for $^{16}O$ recoils and ±3% over the interval 13–17.5 MeV for $^{28}$ Si recoils, respectively. The detection efficiency for 12.7 MeV $^{16}O$ was 72% that of 17.5 MeV $^{28}Si$ recoils. This efficiency variation may be associated with the dependence of the secondary electron yield on the electronic stopping in the carbon foil.

## 1. Introduction

In many ion beam analytical techniques the use of standard reference samples considerably simplifies the establishment of energy, depth and concentration scales. In the case where a single type of particle or radiation is detected, for example in proton induced X-ray emission (PIXE), proton induced gamma emission (PIGE), Rutherford backscattering spectrometry (RBS) and nuclear resonance broadening (NRB), a few well chosen standards may suffice to establish the energy and depth scales. Absolute concentration scales may then be determined ab initio from the geometry, detection efficiency, cross-sections and absorbtion coefficients. Alternatively and more directly, standards internal to the sample, such as a substrate signal height or a signal from an element with which the sample has been spiked can be used to determine the absolute concentration scale.

Recently mass-dispersive and atomic number-dispersive recoil spectrometry, which is a development of elastic recoil detection analysis (EDRA), has been developed for simultaneous depth profiling of light elements in both light and heavy matrices. These techniques are based on the measurement of recoil atomic number and energy or mass and energy in a $\Delta E$–$E$ [1–3] or time of flight-energy (TOF-E) [4–11] detector telescope, respectively. For quantitative applications three parameters, recoil-energy, -mass (or atomic number) and detection efficiency may need to be calibrated.

If a silicon surface barrier detection is used for energy determination, the mass defect makes it imperative that the energy scale is established for each and every recoil species of interest. Even in conventional ERDA where an absorber foil is employed to prevent excessive dead times due to detection of scattered projectiles [12–19], this is necessary because the energy scales for different elements will vary according to their energy deposition in the absorber foil. For TOF-E telescopes this requirement is somewhat alleviated if the energy is derived from the time of flight between two carbon foil detectors [5–7] since no plasma delay needs to be taken into account. The energy calibration can be determined as for NRB and RBS from the surface peak position from a thin overlayer or an edge position from a thick homogeneous target.

The mass (or atomic number) calibration of the telescopes can be carried out in a number of ways, most simply a multi-element reference sample can be used. This reference specimen need not be homogeneous, and the carbon and oxygen signals associated with surface contamination can often be employed as convenient mass (and energy) calibration markers.

The most demanding calibration of the detector telescope is that of the detection efficiency. The detection efficiency may vary as a function of recoil energy and atomic number in TOF-E recoil telescopes, and possibly, also for some $\Delta E$–$E$ telescopes. In TOF-E telescopes, (such as the one employed here), where timing information is obtained by detection of secondary electrons that are emitted when a recoil passes through a thin carbon foil, the detection efficiency is critically limited by the requirement that sufficient electrons are ejected for the resulting pulse to be registered. The detection efficiency of the silicon surface barrier will only differ slightly from unity, a consequence of the infinitesimal fraction of the particles that are scattered out of the detector without creating a sufficient number

0168-583X/89/$03.50 

of electron–hole pairs to register a recoil. Thus the overall detection efficiency of a TOF-E telescope will be chiefly determined by the detection efficiency of the carbon foil time detectors.

Two approaches are possible to determine the detector telescope efficiency. A thin film standard with a known fixed number of atoms may be used (such as the anodized tantalum standards developed by Amsel et al. [20,21]) and the beam energy scanned so as to obtain recoils of different known energies. This method has the disadvantage that unless the atoms are implanted the number of atoms may change due to ion-induced desorption or a contribution from surface contamination. Alternatively, a thick calibration standard with a well defined homogeneous stoichiometry can be used with the energy dependence obtained via the stopping powers.

The energy dependence of the detector efficiency $\beta_A(E_2)$ is of importance for depth profiling since, by analogy with RBS formalism [22], the height of signal $H^A(E_2)$ corresponding to recoils of isotope A with energy $E_2$ is given by:

$$H^A(E_2) = Q\frac{d\sigma_A(E_1)}{d\Omega}\delta\Omega\xi_A\left(\frac{E_{ch}^A m}{{}_p[\epsilon]_A^{A'B'}\cos\theta_1}\right)\beta_A(E_2), \quad (1)$$

where $E_1$ is the projectile ion energy immediately prior to scattering, $E_{ch}$ is the energy step (per channel) in the recoil energy spectrum, $\xi$ the relative abundance of the isotope, $m$ the atomic fraction of element A′ in the target, $\delta\Omega$ is the solid angle subtended by the detector telescope, $\theta_1$ the angle the impinging projectile beam makes to the target surface normal and $Q$ the number of incident projectile ions. Here primed letters denote elements and unprimed letters a specific isotope of the element. The sub- and superscripts A, B, p and s refer to, the isotopes A and B, the projectile ion and the matrix, respectively. The differential Rutherford cross section for isotope A recoiling at angle $\phi$ into solid angle $d\Omega$ is:

$$\frac{d\sigma_A(E_1)}{d\Omega} = \left[\frac{Z_p Z_A e^2(1 + M_p/M_A)}{8\pi\epsilon_0 E_1}\right]^2 \frac{1}{\cos^3\phi}. \quad (2)$$

The stopping cross section factor is given by:

$${}_p[\epsilon]_A^{A'B'} = \frac{\Lambda_A {}_p\epsilon_{in}^{A'B'}}{\cos\theta_1} + \frac{{}_A\epsilon_{out}^{A'B'}}{\cos\theta_2}, \quad (3)$$

where ${}_p\epsilon_{in}^{A'B'}$ and ${}_A\epsilon_{out}^{A'B'}$ are the stopping cross sections for the projectile and isotope A respectively in A′B′ and $\theta_2$ is the angle the outgoing beam makes to the target surface normal, $\Lambda_A$ the fraction of energy transferred to recoils of isotope A as a result of scattering is

$$\Lambda_A = \frac{4M_p M_A}{(M_p + M_A)^2}\cos^2\phi. \quad (4)$$

Then for a homogeneous compound of two elements with stoichiometry $A'_mB'_n$ the ratio of heights corresponding of two isotopes A and B from elements A′ and B′ respectively is:

$$\frac{H_{A'B'}^A(E_2^A)}{H_{A'B'}^B(E_2^B)} = \frac{d\sigma_A(E_1)}{d\sigma_B(E_1)}\frac{\xi_A}{\xi_B}\frac{E_{ch\,p}^A[\epsilon]_B^{A'B'}}{E_{ch\,p}^B[\epsilon]_A^{A'B'}}\frac{\beta_A(E_2^A)}{\beta_B(E_2^B)}\frac{m}{n}. \quad (5)$$

$SiO_2$/Si structures are especially interesting as calibration standards since they are easy to fabricate and analysis of metal–oxide–semiconductor MOS structures are of great importance for microelectronic technology, which is our primary field of research. Furthermore in our system [4] $^{28}Si$ may readily be distinguished from $^{29}Si$ and $^{30}Si$ (with natural abundances of 92.21, 4.70 and 3.09 at.% respectively) and oxygen is in practice monoisotopic since $^{17}O$ and $^{18}O$ isotopes have natural abundances of 0.037 at.% and 0.204 at.% respectively. In order to be of practical use as a standard for establishment of energy scales and detection efficiency the material must have a well defined stoichiometry and this should not be changed by ion bombardment. It is well known that radiation damage can induce density changes in silica due to irradiation-induced devitrification (see e.g., ref. [23]). Preferably the material should be stable under heat treatment up to at least 300 °C since bake-outs are usually needed if the measurements are to be carried out in ultrahigh vacuum. Thermally grown oxide films are known to be durable on thermal processing up to 1200 °C as evidenced by their use as diffusion masks and oxide caps during thermal processing. A further desirable characteristic is that the films should not be insulating because surface charging can augment the energy of charged particles entering and exiting through the surface, according to their charge state. *Thin* thermally-grown oxide films on silicon substrates do not usually exhibit noticeable surface charging under MeV ion bombardment since the charge can leak away via the substrate.

In order to directly ascertain the suitability of thermally grown $SiO_2$ films as reference standards in MeV ion beam analysis, mass-dispersive recoil spectroscopy with 48 MeV $^{81}Br$ projectiles has been employed to directly check for irradiation-induced stoichiometry changes. Subsequently these reference standards have been used to investigate the energy dependence of the detector telescope efficiency for $^{16}O$ and $^{28}Si$ recoils.

## 2. Experimental

The $SiO_2$/Si structures were prepared according to the process listed in table 1. The thickness of the oxide layers was determined by ellipsometry to be 428 nm

Table 1
Wet oxidation process

| Step | Gas | Notes [a] | Action | Time | Furnace temperature (°C) |
|---|---|---|---|---|---|
| 1 | $N_2$ | 1, 2 | load furnace | | 625 |
| 2 | $N_2$ | | ramp up temperature | 30 min. | to 950 |
| 3 | $H_2 + O_2$ | 3 | wet oxidation | 2h. 30 min | 950 |
| 4 | $N_2$ | | purge | 30 min | 950 |
| 5 | $N_2$ | | ramp down temperature | 1h. 20 min | to 625 |
| 6 | $N_2$ | | stabilize | 15 min | 625 |
| 7 | $N_2$ | | unload furnace | | 625 |

[a] Notes:
1 The samples were standard 3 in. diameter 16–24 Ωcm resistivity, boron doped, float zone refined silicon wafers with a (111) surface.
2 The wafers were mounted on a silica holder with the faces to be oxidized perpendicular to the gas flow along the furnace. The spacing between wafers was 5 mm. Two dummy wafers were placed both in front and behind the samples to equilibrate the gas flow.
3 6.6 sl $min^{-1}$ $H_2$ burnt in 6.1 sl $min^{-1}$ $O_2$.

using an experimentally derived refractive index of 1.472. This is in good agreement with a value of 420 nm obtained by Rutherford backscattering spectrometry (RBS) using 2.4 MeV α-particles backscattered at 168° and assuming the density to be that of bulk fused quartz The samples were subsequently divided and loaded onto a 20-position target wheel mounted on a two-axis goniometer. 48 MeV $^{81}Br^{8+}$ ions were obtained from the University of Uppsala EN tandem accelerator. The recoil spectrometry system which is essentially the same as we have described previously [4] and is shown schematically in fig. 1. The changes made to the system reported previously are that the first time detector T1 has been moved further away from the sample to reduce the solid angle subtended by this detector (and hence dead time) and the timed flight length has been increased to 738 mm. A Faraday cup can be moved into the beam after preset time intervals in order to permit the sample to be irradiated sequentially in a controlled manner. The time detectors are of the electrostatic electron mirror type [24]. The voltage applied to the time detectors (which feeds the resistor chains which bias the channel plates [4]) was set such the counting rate was independent of applied voltage.

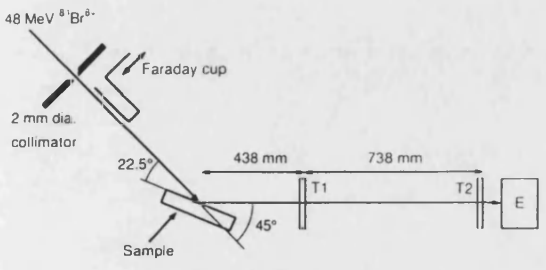


Fig. 1. The experimental setup.

## 3. Results and discussion

To ascertain the stability of the standards under irradiation with 48 MeV $^{81}Br^{8+}$ ions a series of recoil spectra were taken from the same area of one sample for successively longer irradiation times. Fig. 2 shows the data obtained during the longest irradiation of the $SiO_2/Si$ structure. The sorted mass energy matrix is presented in fig. 2(a). The oxygen signal is well separated from the silicon signals. The small peak seen in the foreground is due to $^{12}C$ which originates from hydrocarbon surface contamination. It is of no consequence for the analysis. In fig. 2(b) and (c) the recoil energy spectra for $^{28}Si$ and $^{16}O$ recoils are presented. The very weak low energy tail on the $^{16}O$ recoil energy distribution (fig. 2a and b) is of uncertain origin and was disregarded in the subsequent analysis. This tail will be contributed to by recoils that have undergone multiple scattering in the target and also by the small fraction of recoils that lose energy because of scattering from the time detector grids. Significant tails have also been observed when the ion beam had poor energy definition. For each irradiation step the following yields were evaluated.

$A^{16O}$ – total area of the $^{16}O$ signal,

$H^{28Si}_{SiO_2}$ – surface height of the $^{28}Si$ signal,

$H^{16O}_{SiO_2}$ – surface height of the $^{16}O$ signal,

$H^{28Si}_{Si}$ – substrate height of the $^{28}Si$ signal.

The heights $H$ were normalized to give the yield per channel. The energy intervals used to determine the signal heights are indicated in fig. 2(b) and (c). The relative dose was obtained from $H^{28Si}_{Si}$ the signal height

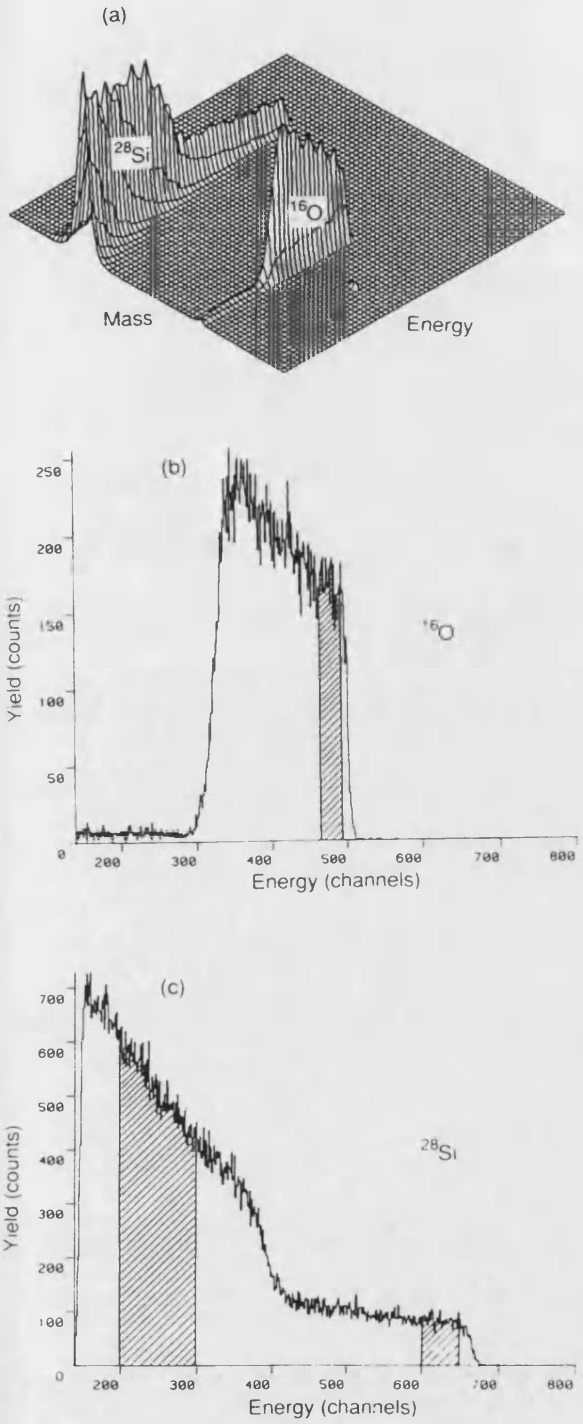


Fig. 2. Recoil data from the data set corresponding to the largest ion fluence (total ion fluence $2\times10^{14}$ ions cm$^{-2}$). (a) Isometric plot of the sorted mass-energy matrix from the $SiO_2$/Si standards. (b) Recoil energy spectrum for $^{16}O$ recoils. (c) Recoil energy spectrum for $^{28}Si$ recoils. The regions used to determine the surface heights and silicon substrate height are indicated by shading.

in substrate region of the spectra [fig. 2(c)]. Since this is directly related to the number of incident particles, and more important, it is insensitive to their charge-state, this was used to define the *relative* ion fluence. The relative uncertainty is thus limited by counting statistics and the standard deviation decreases from 5% at the lowest dose to 0.4% at the highest. The absolute ion fluence was determined from the irradiation time and the beam current measured using the Faraday cup just in front of the sample. The uncertainty here is estimated to be $\pm10\%$ and is contributed to by the uncertain charge exchange experienced by the $Br^{8+}$ ions along the beam path from the analysing magnetic to the sample.

In fig. 3 the ratios of the $^{16}O$ to $^{28}Si$ yields vs ion fluence are presented. Considering first the loss of oxygen from the oxide layer (fig. 3a), the ratio of the total area of the oxygen signal $A^{16O}$ to the $^{28}Si$ substrate height $H_{Si}^{28Si}$ does not show any strong dependence on ion fluence. The influence of channeling of the Br ions in the substrate was checked by comparing the ratio between $H_{Si}^{28Si}/H_{SiO_2}^{28Si}$ for 3 samples that were rotated randomly with respect to each other in the target holder. No indication of channeling effects was observed. Over the ion fluence range investigated, 5 of the 7 data points in fig. 3a lie within the standard counting errors (indicated by the error bars) of the constant trend line. Consequently there is no evidence for a statistically significant loss of $^{16}O$ from the $SiO_2$ film for ion fluences from $10^{12}$ to $2\times10^{14}$ ions cm$^{-2}$. Fitting the data of fig. 3a showed that if an irradiation induced $^{16}O$ loss takes place it is less than 5 at.%. From this upper limit the minimum detectable sputtering loss rate of $^{16}O$

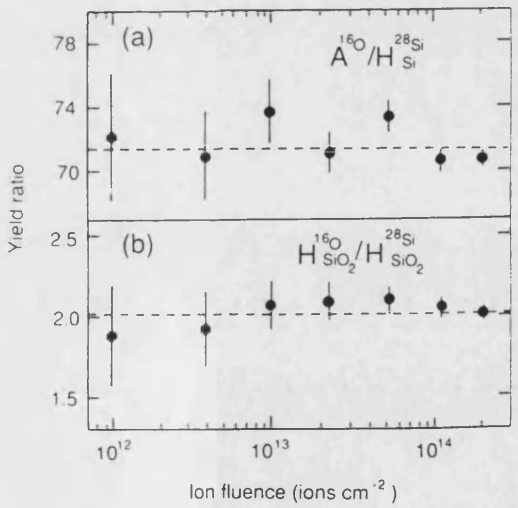


Fig. 3. Yield ratios vs 48 MeV $^{81}Br^{8+}$ ion fluence (a) $A^{16O}/H_{Si}^{28Si}$, (b) surface signal height ratio $H_{SiO_2}^{16O}/H_{SiO_2}^{28Si}$. The heights H are expressed as counts per channel, whilst the area $A^{16O}$ corresponds to the total area of the $^{16}O$ signal.

from the oxide layer is estimated to be 520 atoms ion$^{-1}$ for 48 MeV $^{81}Br^{8+}$ ions incident at an angle of 67.5° from the surface normal. (This upper limit for the $^{16}O$ partial sputtering yield is larger than the Si partial sputtering yield data of Qiu et al. [25] for 20 MeV Cl bombardment of $SiO_2$, scaled according to $(dE/dx)^n$ with $n$ less than about 3.5.)

The surface height ratio for $^{16}O$ to $^{28}Si$ recoils vs ion fluence is presented in fig. 3b. This parameter reflects any change in stoichiometry within 75 nm of the $SiO_2$ film surface. The data in fig. 3b is grouped within the counting statistical error of a constant trend line. Thus there is no statistically significant evidence of a change in composition. Statistical analysis of the data showed that any change in stoichiometry lay within the range of oxygen loss of $-3$ to $+5$ at.%. Thus one can infer that thin $SiO_2$ films on Si are largely insensitive to the effects of 48 MeV $^{81}Br$ irradiation at ion fluences between $10^{12}$ to $2 \times 10^{14}$ ions cm$^{-2}$. (We cannot rule out the possibility that a change takes place at fluences below $10^{12}$ ions cm$^{-2}$.) This is in marked contrast to what is observed for polymers such as PVC [10,26] which show very dramatic composition changes during 48 MeV Br ion irradiation.

Weak visible colour changes were observed at the edges of the irradiated area after the sample was removed from the vacuum chamber. These may be associated with optical interference effects arising from irradiation induced refractive index [27] or density changes and/or thickness changes due to loss of material of the film from sputtering or deposition of hydrocarbon layers on the surface.

Since $SiO_2$ is an insulator, surface charging may lead to a change of energy of the incoming and outgoing charged particles. This will manifest itself as an energy spreading and a shift in the position of the edge. Comparison of the $^{28}Si$ edges in energy spectra obtained from a $SiO_2$/Si standard and a Si slice that was etched in HF 1 : 10 solution showed a statistically insignificant change in edge channel number of less than 24 keV ( < one channel) and no change in the broadening of the edge. Presumably, the intense plasma generated by the fast ions in the oxide provided an efficient conduction mechanism across the thin oxide film that inhibits surface charging.

Fig. 4 shows the relative energy dependence of the telescope detection efficiencies $\beta_A(E_2)$ for $^{16}O$ and $^{28}Si$ recoils vs. recoil energy. This data was derived using the mean energy approximation [22] with the assumptions that: scattering is described by the Rutherford formula [eq. (2)], the oxide film is stoichiometric and the energy channel width is constant. In spite of the scatter of the data points in fig. 4 that is associated with the counting statistics, the relative efficiency for $^{16}O$ recoils decreases significantly ($\approx 5\%$) with increasing recoil energy. For $^{28}Si$ recoils the efficiency may be constant or decrease

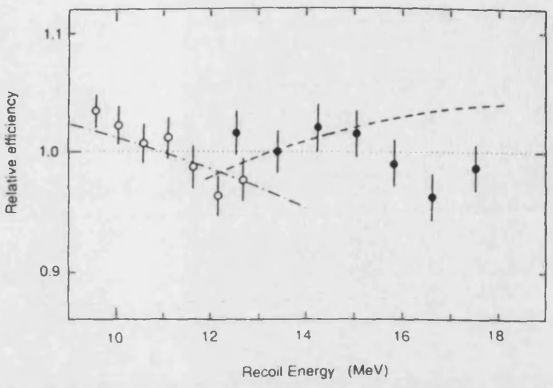


Fig. 4. Relative efficiency of the TOF-E telescope vs recoil energy for $^{16}O$ (open circles) and $^{28}Si$ recoils (closed circles), obtained from the data of fig. 2. The error bars denote the uncertainty due to counting statistics. The electronic energy loss in carbon vs recoil energy, arbitrarily normalized to the ordinate scale, for $^{16}O$ and $^{28}Si$ recoils, is indicated by the dot-dashed and the dashed lines, respectively.

($\leq \approx 3\%$) with increasing recoil energy. The effect of non-Rutherford cross-sections can be ruled out since at the projectile energies involved, 40–48 MeV, the LSS [28] universal $t$ parameter for collisions between $^{81}Br$ projectiles with $^{16}O$ and $^{28}Si$ lies in the range 110–170. Screening effects first become significant at the 10% level (required to explain the data of fig. 4) for $t$ values below about 10 [29]. Moreover the projectile energy of 48 MeV is much less than that required to overcome the Coulomb barrier, which for head-on collisions is 183 and 193 MeV for $^{81}Br \rightarrow {}^{16}O$ and for $^{81}Br \rightarrow {}^{28}Si$ respectively. Consequently deviations from Rutherford cross sections associated with nuclear reactions can also be neglected. The validity of the assumption of constant energy channel width was checked experimentally in a separate experiment by referring the mean value of the energy signal derived from the surface barrier detector to an energy derived from the flight time between the two carbon foil detectors. The latter was calibrated using the calculated flight times for $^{16}O$ and $^{28}Si$ recoils from the surface. The relative variation in energy channel with $\delta E^{A^+}/E^{A^+}$ was $2.5 \pm 1\%$ and $3 \pm 2\%$ for $^{16}O$ and $^{28}Si$ recoils over the energy range spanned by fig. 4. This is insufficient to explain the energy dependence of the detection efficiency for $^{16}O$ recoils.

The influence of errors in the stopping cross sections on the results of fig. 4 is more difficult to ascertain since little experimental data has been published. The vast majority of the experimental data agree within $\pm 20\%$ of the values given by the STOP code [30] used here with a mean error of 7.4%. However we expect errors in the stopping cross section to have only a minor influence since we are working close to the maximum in the stopping power curve where the energy dependence is

small and moreover it is only errors in the relative energy dependence that can influence the results of fig. 4. This is supported by the observation that the difference in the thickness of the oxide film determined from the recoil energy spectra using the surface and mean energy approximations is small. Assuming the density to be that of bulk fused quartz (2.20 $gcm^{-3}$) the surface approximation yielded thicknesses of 440 nm for $^{16}O$ and 443 nm for $^{28}Si$ recoils. Using the more exact mean energy approximation [22] these values changed to 432 and 466 nm, respectively. These values are in good agreement with the results of the RBS and ellipsometry measurements.

The ratio of the detection efficiencies $\beta_{^{16}O}$(12.7 MeV)/$\beta_{^{28}Si}$(17.5 MeV) corresponding to recoils from just below ($\approx$ 40 nm) the surface was 0.72 with a counting statistical error of $\pm$0.02. $\beta_{^{16}O}$(12.7 MeV)/$\beta_{^{28}Si}$(17.5 MeV) varied in the range $\approx$0.5 to 1 from measurement session to measurement session. An actual value for $\beta_{^{16}O}/\beta_{^{28}Si}$ close to the assumed value of 1 presumably accounts for our previous observation [4] that the measured stoichiometry 1 : 1.86 for $SiO_2$ was within counting statistical error ($\pm$0.15) of the expected value of 1 : 2. Comparison of the theoretical estimates of the expected number of the recoils from the oxide films with the experimental yield gave absolute values for $\beta_{^{16}O}$(12.7 MeV) of 0.6 and $\beta_{^{28}Si}$(17.5 MeV) = 0.85. The uncertainty is principally associated with estimating the area of the beam impingement spot viewed by the detector and measurement of the ion beam fluence. The theoretical maximum detection efficiency of the detection telescope estimated from the optical transmission of the time detector grids is 0.8, suggesting that all the $^{28}Si$ (but not the $^{16}O$) recoils that do not impinge on a grid wire are detected.

The energy dependence of $\beta_A(E_2)$, (fig. 4), may be associated with the time detector efficiencies. Detection of a recoil by a time detector requires that sufficient electrons are produced by the electron multiplier to produce a pulse with amplitude that exceeds the threshold of the discriminator. The pulse height distribution from the channel plate electron multipliers is very broad and has a complex form [31]. Thus although the probability of detection of a recoil will depend on the number of secondary electrons emitted from the carbon foils, the pulse heights for a given number of secondary electrons are expected to vary widely. The reported mean number of electrons ejected in the *forwards direction* from carbon foils is quite high, e.g., from 5–10 $\mu g\ cm^{-2}$ thick carbon foils it is $\approx$ 5–10 electrons/ion for 5.5 MeV $\alpha$-particles and $\approx$ 30–50 for 10–20 MeV $^{16}O$ and $\approx$ 100 for 20 MeV $^{32}S$ ions [32–34]. However there is relatively little information [35] on the number of electrons ejected in the *backwards direction* (which are detected in the time detectors used here). According to the data of Pferdekämper and Clerck [35] the fraction of electrons emitted in the backwards direction is about 40% for $\alpha$-particles for energies of 0.48 and 1.5 MeV/amu and about 27% for fission fragments of 0.45, 0.52 and 0.95 MeV/amu. The electron energy distributions for forwards and backwards ejection also differed, with a larger fraction of low energy {< 230 eV and probably less than 20 eV [36]} electrons in the latter. This is probably a consequence of the small fraction of $\delta$-electrons that are backwards directed [33,37,38]. The number of secondary electrons produced by the carbon foils, and consequently the detection efficiency, is expected to depend on the energy deposited in electronic processes in the foils by the recoils [33,36,39]. Comparison of the relative energy dependence of the electronic stopping cross section for $^{16}O$ and $^{28}Si$ recoils with the relative detection efficiency (fig. 4) shows a correlation between strong energy dependence of $\beta_{^{16}O}(E_2)$ and the energy deposited by $^{16}O$ recoils in the carbon foil. The relative detection efficiency for silicon on the other hand, is constant or even has the opposite energy dependence to the electronic stopping cross section for $^{28}Si$ recoil in carbon. This may be understood if, as indicated by the estimates of the absolute detection efficiency, the electronic stopping cross section for $^{28}Si$ (398 eV/$10^{15}$ at. $cm^{-2}$ at 17.5 MeV), but not $^{16}O$ (184 eV/$10^{15}$ at. $cm^{-2}$ at 12.7 MeV [30]), recoils is sufficiently large to ensure that a sufficient number of secondary electrons is produced to ensure detection. $\beta_{^{28}Si}(E_2)$ for $^{28}Si$ recoils would then be energy independent whilst $\beta_{^{16}O}(E_2)$ will reflect the energy dependence of the electronic stopping.

The variations in the ratio $\beta_{^{16}O}$(12.7 MeV)/$\beta_{^{28}Si}$(17.5 MeV) in the range $\approx$ 0.5 to 1 from run to run seem to be associated with changes of the carbon foil and electronic setup. The inevitable surface contamination on the carbon foils may influence the secondary electron yield, especially for electrons with energies less than 10 eV [36], leading to variations in detection efficiency from foil to foil. Differences in thickness between foils might also lead to different secondary electron yields [34,36]. The detection efficiencies will also be dependent on the time-detector discriminator thresholds and the potential difference applied to the channel plate electron multipliers [24]. This implies that for each run, the detection efficiency should be established for each recoil isotope of interest. However for recoils with a high stopping power in carbon so that the detection efficiency approaches the theoretical maximum, extrapolation may alleviate the requirement to establish the efficiency calibration for each recoil species.

## 4. Conclusions

(a) Thin $SiO_2$ films on silicon substrates prepared by wet thermal oxidation of silicon wafers exhibited no

statistically significant loss of oxygen or change of composition under ion bombardment with 48 MeV $^{81}Br$ ions incident at 67.5° from the surface normal for doses up to $2 \times 10^{14}$ ions $cm^{-2}$. Thus the structures are suitable for use as composition standards in ERDA.

(b) The samples show no shift or broadening in the silicon edge energy associated with surface charging, implying that the structures may also be used as reference standards for mass and energy calibration in ERDA.

(c) The detection efficiency of the TOF-E recoil telescope determined from the $SiO_2$/Si standards depends on recoil atomic number and energy. The efficiency variations are associated with the carbon foil time detectors and are most probably related to the energy deposition in electronic processes in the carbon foils.

We are grateful to Thomas Eriksson for careful preparation of the samples used in this study.

## References

[1] L.E. Seiberling, Nucl. Instr. and Meth. B24/25 (1987) 526.
[2] A.M. Behrooz, R.L. Headrick, L.E. Seiberling and R.W. Zurmühle, Nucl. Instr. and Meth. B28 (1987) 108.
[3] M. Petrascea, I. Berceanu, I. Branucus, A. Buta, C. Grame, I. Lazar, I. Mihai, M. Petrovic, V. Simon, M. Mihaila and I. Gita, Nucl. Instr. and Meth. B4 (1984) 396.
[4] H.J. Whitlow, G. Possnert and C.S. Petersson, Nucl. Instr. and Meth. B27 (1987) 448. (There is an error in eq. (2) of this paper. It should be replaced by eq. (2) of the present work.)
[5] J.P. Thomas, M. Fallavier, D. Ramedame, N. Chevarier and A. Chavarier, Nucl. Instr. and Meth. 218 (1983) 125.
[6] J.P. Thomas and M.Fallavier, in: Proc. Int. Symp. on Three day in-depth review on the nuclear accelerator impact in the interdisciplinary field. Padova, Italy (May 30th–1st June 1984) eds. P. Mazzoldi and G. Moschini.
[7] J.P. Thomas, M. Fallavier and A. Ziani, Nucl. Instr. and Meth. B15 (1986) 443.
[8] R. Groleau, S.C. Gujrathi and J.P. Matin, Nucl. Instr. and Meth. 218 (1983) 11.
[9] S.C. Gujrathi, P. Aubry, L. Lemay and J.-P. Martin, Can. J. Phys. 65 (1987) 950.
[10] C. Chauvin, E. Sacher, A. Yelon, R. Groleau and S. Gujrathi, in: Surface and Colloidal Science in Computer Technology, ed. K.M. Mittal (Plenum, New York, 1986).
[11] A. Houdayer, P.F. Hinrichsen, S.C. Gujrathi, J.P. Martin, S. Monaro, L. Lessard, K. Oxorn, C. Janicki, J. Brebner, A. Belhadfa and A. Yelon, Nucl. Instr. and Meth. B24/25 (1987) 643.
[12] G. Ross and B. Terreault, J. Appl. Phys. 51 (1980) 1259.
[13] G.G. Ross, B. Terreault, G. Gobeil, C. Boucher and G. Veilleux, J. Nucl. Mater. 128/129 (1984) 730.
[14] D.C. Ingram, A.W. McCormic, P.P. Pronko, J.D. Carlson, and J.A. Wollam, Nucl. Instr. and Meth. B6 (1985) 430.
[15] S.S. Klein, Nucl. Instr. and Meth. B15 (1986) 464.
[16] C. Nölscher, K. Brenner, R. Knauf and W. Schmidt, Nucl. Instr. and Meth. 218 (1983) 116.
[17] J. Bøttiger, J. Nucl. Mater. 78 (1987) 161.
[18] A. Barcz, A. Turos, L. Wielun'sski and I. Skryznecka, Phys. Status Solidi A28 (1975) 293.
[19] H. Nagai, S. Hayashi, M. Aratani, T. Nozaki, M. Yanokura, I. Kohno, O. Kuboi and Y. Yatsurugi, Nucl. Instr. and Meth. B28 (1987) 59.
[20] G. Amsel, J.P. Nadi, C. Ortega, S. Rigo and J. Siejka, Nucl. Instr. and Meth. 149 (1978) 705.
[21] G. Amsel, J.P. Nadi, C. Ortega and J. Siejka, Nucl. Instr. and Meth. 149 (1978) 713.
[22] W.-K. Chu, J.W. Mayer and M.-A. Nicolet, Backscattering Spectrometry (Academic Press, New York, 1978).
[23] R.G. Saint-Jacques and C.P. Pells, Nucl. Instr. and Meth. B32 (1988) 288.
[24] F. Busch, W. Pfeffer, B. Kohlmeyer, D. Schüll and F. Pühlhoffer, Nucl. Instr. and Meth. 171 (1980) 71.
[25] Y. Qiu, J.E. Griffith, W.J. Meng and T.A. Tombrello, Radiat. Eff. 70 (1983) 231.
[26] H.J. Whitlow, A. Ingemarsson and G. Possnert, to be published.
[27] J. Heibei and E. Voges, Phys. Status Solidi (a)57 (1980) 609.
[28] J. Lindhard, M. Scharff and H.E. Schiøtt, K. Dan Vidensk. Selsk. Mat. Fys. Medd. 33 (1963) no 14.
[29] H.H. Andersen, J. Bøttiger and H. Knudsen, Phys. Rev. A7 (1973) 154.
[30] J.F. Ziegler, J.P. Biersack and U. Littmark, The Stopping and Range of Ions in Solids, vol. 1 of The Stopping and Ranges of Ions in Matter, ed. J.F. Ziegler (Pergamon, 1985).
[31] Hamamatsu, Characteristics and applications of microchannel plates, Technical Manual RES-0795 (Hamamatsu TV Co. Ltd., Japan).
[32] B. Sundqvist, H. Berggren, K.H. Flodkvist, A. Johansson and I. Koesner, IEEE Trans. Nucl. Sci. NS-24 (1977) 652.
[33] H.G. Clerc, H.J. Gehrhardt, L. Richter and K.H. Schmidt, Nucl. Instr. and Meth. 113 (1973) 325.
[34] E. Dietz, R. Bass, A. Reiter, U. Friedland and B. Huberg, Nucl. Instr. and Meth. 97 (1971) 581.
[35] K.E. Pferdekämper and H.G. Clerc, Z. Fys. A275 (1975) 223.
[36] H.J. Frischkorn and K.O. Groeneveld, Phys. Scripta T6 (1983) 89.
[37] F. Bell, G. Trollmann, H. Böckl and H.D. Betz, Nucl. Instr. and Meth. 194 (1982) 423.
[38] K. Kroneberger, A. Clouvas, G. Schlüssler, P. Koschar, J. Kemmler, H. Rothard, C. Biedermann, O. Heil, M. Buckhard and K.O. Groeneveld, Nucl. Instr. and Meth. B29 (1988) 621.
[39] J. Schou, Phys. Rev. B22 (1980) 2141, Nucl. Instr. and Meth. 170 (1980) 317.

Nuclear Instruments and Methods in Physics Research A310 (1991) 636–648
North-Holland

NUCLEAR INSTRUMENTS & METHODS IN PHYSICS RESEARCH
Section A

# Mass resolution of recoil fragment detector telescopes for 0.05–0.5 *A* MeV heavy recoiling fragments

Harry J. Whitlow [a], Bo Jakobsson [b] and Division Lars Westerberg [c]

[a] *Department of Nuclear Physics, Lund Institute of Technology, Sölvegatan 14, S-223 62 Lund, Sweden*
[b] *Division of Cosmic and Subatomic Physics, University of Lund, Sölvegatan 14, S- 223 62 Lund, Sweden*
[c] *The Svedberg Laboratory, Box 533, S-751 21 Uppsala, Sweden*

Received 5 July 1991

The factors governing the mass resolution for 0.05–0.5 *A* MeV recoil nuclei have been investigated for detector telescopes in which carbon-foil time zero detectors and ion-implanted silicon detectors are used to determine the time of flight and energy respectively. Experimentally determined second moments of the mass distribution have been compared with theoretical estimates based on literature data. The experimental mass resolution is in reasonably good absolute agreement with theoretical estimates. For low energy ( $< 0.3$ *A* MeV) particles the mass resolution is dominated by the contribution from the silicon detector and thus largely independent of timed flight length. In fact for detection of very low energy (0.1 *A* MeV) recoil nuclei timed flight lengths of less than 0.22 m are sufficient.

## 1. Introduction

The registration and identification of heavy recoiling particles is a topic that, because of experimental difficulties, has received little attention in experimental studies of heavy ion and hadron induced reactions. Much of the nuclear mass from the non-interacting part of the system is contained in these recoils and their distribution in angular and momentum space carries much important information about the reaction dynamics. The mass and energy can only be reasonably well determined with indirect methods like radiochemical technique [1,2], while track detectors like nuclear emulsions [3] or plastics [4] are able to register these recoils. The recoils are stopped in normal foil targets or thin windows proceeding detectors because of their very short range (a few μm).

In recent years various forms of recoil spectrometry (RS) based on elastic recoil detection analysis [5] have been developed and used in thin film materials research where they have proved to be very trenchant. The underlying principle of these measurements is that a detector telescope comprising a time-of-flight (TOF) stage and a silicon charged-particle detector [6–12] or a gas $\Delta E$–$E$ telescope [13–16] is used to determine both the identity and energy (and thereby depth of origin in the target) of (0.1–0.5 *A* MeV) recoiling nuclei from elastic scattering due to irradiation of the sample with a collimated beam of 0.5–1 *A* MeV heavy ions. This technique has been successfully used in a number of studies, including ion beam synthesis of buried layers for 3-D integration in microelectronics [17,18], studies of solid state chemical reactions [6,19,20] and even the breakdown of boundary lubrication films associated with lubrication oil additives [21].

The combination of extremely thin gas jet targets (a few $10^{13}$ atoms/cm$^2$ thick) and the intense circulating beams in storage rings, recently constructed or still in the construction phase, renders the recoiling target nuclei accessible for suitable detectors. (The gas target thickness corresponds to an average energy loss of about 0.01 *A* keV for a 0.1 *A* MeV $^{40}$Ar recoil – i.e. so thin that statistical stopping theory is not valid.) In an effort to study these heavy recoiling fragments we are developing a detector telescope system to measure the emission angle, mass and energy, based on the detector telescopes used for recoil spectrometry. The detector telescope will consist of a TOF section with carbon foil time detectors for determination of the velocity vector and ion implanted silicon p–i–n-diode detectors for determination of the energy of the recoil nuclei. These detectors were chosen because they are compatible with the requirements imposed by the gas jet target and storage ring environment. They are also insensitive to the atomic charge states of the recoiling nuclei and have low threshold detection energies [22–24]. The

recoil mass $M$ can be obtained directly from the TOF $T$ and energy $E$ according to:

$$M = 2E(T/L)^2, \quad (1)$$

where $L$ is the timed flight length. One of the most important parameters of such a detector telescope system is the mass resolving power. The objective of this work was to elucidate the interplay between the physical phenomenon and other factors that determine the mass resolution of TOF–$E$ telescopes in the 0.05–0.5 $A$ MeV energy region.

The mass resolving power can be conveniently parameterized by the distribution in mass $M$ for a single isotope because this will enable estimates of how well one can separate the signal associated with a weak isotope in the presence of a tail associated with a nearby strong isotope. Here we have chosen a simple approach and parameterised the uncertainty in mass in terms of the second moment $\delta M^2$ of the measured mass distribution and ignored higher moments. (It turns out that this is a reasonable approach because the mass resolutions could be closely approximated by Gaussian distributions.) The uncertainty in the measured particle mass $\delta M$ is then determined by the uncertainties in determining the flight time $\delta T$, energy $\delta E$ and timed flight length $\delta L$ according to:

$$\delta M^2 = \delta M_E^2 + \delta M_T^2 + \delta M_L^2. \quad (2)$$

Where $\delta M_E$, $\delta M_T$ and $\delta M_L$ are related to the uncertainties $\delta E$, $\delta T$ and $\delta L$ in determining the energy, time of flight and timed flight length respectively:

$$\delta M_E^2 = (\partial M/\partial E)^2 \delta E^2 = (M/E)^2 \delta E^2, \quad (3)$$

$$\delta M_T^2 = (\partial M/\partial T)^2 \delta T^2 = (8ME/L^2)\delta T^2, \quad (4)$$

$$\delta M_L^2 = (\partial M/\partial L)^2 \delta L^2 = (4M^2/L)^2 \delta L^2. \quad (5)$$

The uncertainties $\delta E$, $\delta T$ and $\delta L$ have in turn a number of contributions from phenomena such as the energy detector resolution, statistical fluctuations in stopping and geometrical variations of the timed flight length.

The mass resolution of TOF–$E$ telescopes at energies greater than about 0.5 $A$ MeV has been given some consideration [25–28], but with one exception [27], a naive assumption is made about the energy resolution namely: $\Delta E_{\mathrm{FWHM}}/E \approx 0.02$. Furthermore the effect of the time detector foils and geometric effects are not considered. This will probably not be serious at energies higher than 0.7 $A$ MeV but at low energies ($< 0.3$ $A$ MeV) the stopping in the foil is appreciable and its potential influence should be considered.

The approach adopted here was to determine experimentally $\delta M$ vs particle energy, mass number $A$ and timed flight length $L$ and compare these with theoretical estimates of the different contributions.

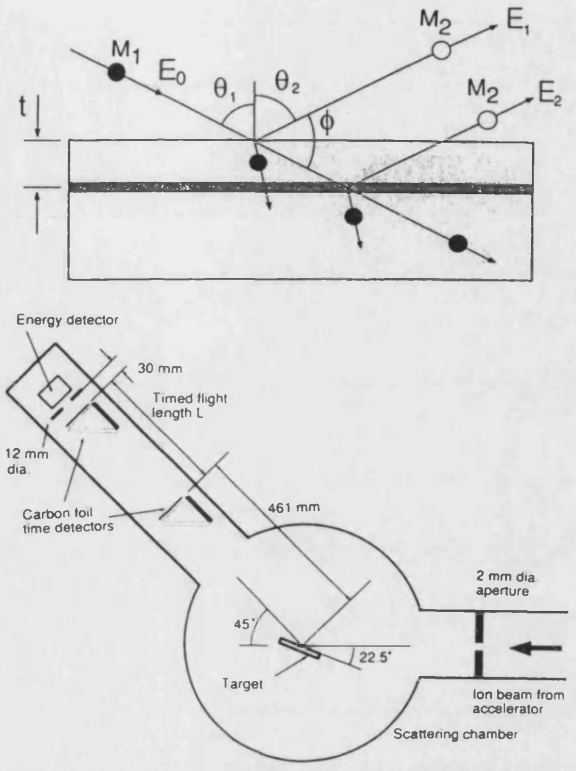


Fig. 1. Experimental configuration. (a) Principle for formation of recoil/scattered particles with a continuous energy distribution using glancing incidence/exit geometry. The filled circles denote the projectiles and the open circles the recoils. (b) Experimental setup.

## 2. Experimental

Heavy recoils with a continuous energy distribution were obtained using a standard glancing incidence/exit configuration for recoil spectrometry [6,12] with bulk targets containing the nuclei of interest. The principle is illustrated in fig. 1a. The maximum energy $E_1$ of the recoiling/scattered nuclei detected at a fixed scattering angle $\phi$ relative to the incident beam direction corresponds to elastic scattering from the surface layer of atoms:

$$E_1 = KE_0 \quad \text{(for scattered nuclei)}, \quad (5)$$

$$E_1 = \Lambda E_0 \quad \text{(for recoiling nuclei)}. \quad (6)$$

Where $K$ is the well known kinematic factor in Rutherford backscattering spectrometry [29]:

$$K = \frac{M_1^2}{(M_1 + M_2)^2}\left\{\cos\phi \pm \left[(M_2/M_1)^2 - \sin^2\phi\right]^{1/2}\right\}^2. \quad (7)$$

And $\Lambda$ the corresponding factor for recoils [6]:

$$\Lambda = \frac{4M_1M_2}{(M_1+M_2)^2}\cos^2\phi. \quad (8)$$

As the projectile ions penetrate deeper into the sample they lose energy and the outgoing scattered/recoiling particles also lose energy along the outward path. Thus the ejection energy $E_2$ depends on the depth at which scattering takes place. The energy distribution of primary recoils and scattered particles extends down to a cut off at a few eV, is similar to the case for sputtering [30], where the outgoing particles arrive at the surface with energy equal to the surface binding energy. At low energies there will be an additional flux of low energy recoils associated with sputtering of secondary recoils.

In all the experiments the bombarding ions were 48 MeV $^{81}Br^{8+}$ ions from the tandem accelerator at The Svedberg Laboratory. The targets and energy range of the recoils and scattered Br ions are listed in table 1. The targets were C (graphite) and GaP which both had natural isotopic abundances and are readily available, stable under vacuum and have one or two major isotopes separated by one mass unit at low ($\leqslant 35$) $A$ and two mass units at large ($> 35$) $A$. A reference target of $Al_2O_3$ was also used for mass calibration.

The experimental setup, which is similar to that in ref. [12] is shown schematically in fig. 1b. Two (closely) identical carbon foil detectors are used for the time of flight measurement rather than a single carbon foil start detector and deriving the stop signal from the silicon detector. This was chosen because earlier experiments [31] showed it extremely difficult to derive an accurate timing signal from the silicon detector, because of pulse shape variations associated with plasma delay [32], pulse transmission in the detector [33,34] and radiation damage [35]. The targets were loaded onto a 20-position target wheel which is mounted on a two axis goniometer in a 320 mm diameter scattering chamber. The detector telescope was contained in a side arm to the main scattering chamber and could be isolated by means of a gate valve, so as to allow the target wheel to be changed whilst maintaining the detector telescope under vacuum. The detector telescope is constructed from modules that are coupled together using standard vacuum fittings, a feature which allowed the timed flight length $L$ to be easily changed by simply inserting tube sections of different lengths between the time detector modules.

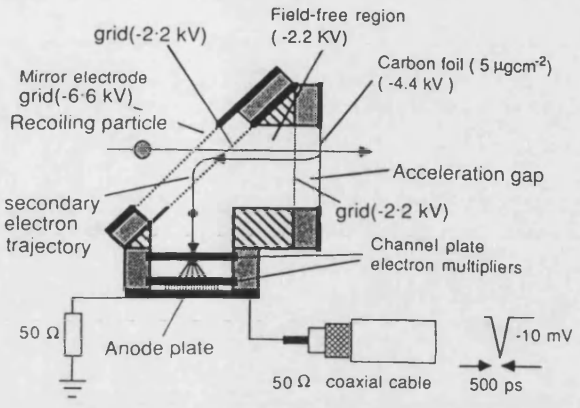


Fig. 2. Electrostatic mirror time detector principle. (After Busch et al. [36]).

The time detector modules house a carbon foil time zero detector, associated potential dividers and breakdown-current limiting resistors. The carbon foils were 5 $\mu g/cm^2$ thick ($2.7 \times 10^{17}$ atoms/$cm^2$) which corresponds to 14 nm assuming bulk graphite density. The time zero detectors, shown schematically in fig. 2, are of the electrostatic electron mirror type and are based on the design by Busch et al. [36]. These were originally chosen for this system because they do not require magnetic fields [37], have isochronous electron transport properties and the foil is perpendicular to the recoil trajectory (which results in minimum foil associated energy spreading and geometrical drift length variations). The nickel meshes used to define the accelerating and reflecting electric fields have a transparency $\approx 96\%$ yielding a total transparency for the whole telescope of about 75%. Such detectors have

Table 1
Energy ranges for recoiling and scattered nuclei

| Target | Process | Nuclei | Kinematic factor | Minimum energy [.4 keV] [a] | Maximum energy [$A$ keV] |
|---|---|---|---|---|---|
| Polished graphite block | Recoil | $^{12}C$ | 0.2248 | 75 | 898 |
| GaP | Recoil | $^{31}P$ | 0.3154 | 50 | 488 |
| | Recoil | $^{69}Ga$ | 0.4562 | 23 | 317 |
| | Recoil | $^{71}Ga$ | 0.4600 | 23 | 311 |
| GaP | Scattered | $^{81}Br$ | 0.4075 [b] | 20 | 408 |

[a] The low energy minima was determined by the range of the ADC conversion.
[b] Corresponds to scattering from $^{69}Ga$.

been used successfully by a number of other groups [38–41,63].

The energy detector was an Intertechnique [22,42] partially depleted 150 $mm^2$ ion implanted detector with a 100 $\mu$m depletion depth (IPB 150-100-16). This detector is bakable for UHV compatibility and for annealing out radiation damage. This detector had been exposed to an estimated recoil dose of a few times $10^7$ recoils/$cm^2$. To minimize the effect of degradation of the detector due to this irradiation the detector was baked at 225 °C for 1 hour to anneal out the irradiation induced defect centres. These centres are quite likely to be the divacancy, oxygen-vacancy and doubly charged divacancy [43]. The recoil fluence in this experiment was estimated to be a few $10^5$ recoils/$cm^2$. Immediately in front of this detector was a 12 mm diameter aluminium aperture (fig. 1b) which, because it subtends the smallest solid angle, defines the acceptance of the entire telescope for coincidence events. Prior to each measurement the telescope was aligned by sighting through the carbon foils and adjusting the position of the time detectors so that the centre of the circular carbon foils were coaxial with a line extending from the centre of the beam impingement spot to the centre of the aluminium aperture. The misalignment introduced by this procedure and fabrication tolerance are expected to contribute an uncertainty in timed flight length $\delta L$ of about 0.1 mm.

The electronics system consisted of standard NIM electronics and is essentially the same as described previously [6] with the exception that Phillips 6954 1.8 Ghz 50X pulse preamplifiers were used to amplify the signals from the time detectors and Phillips 6915 constant fraction timing discriminators were used. Open circuit transmission line stubs were fitted to the output of the time detectors to control ringing. The length of these stubs was selected by a cut and try method. The signals from the discriminators were fed to a time-to-amplitude converter (TAC) which was operated in an inverse start–stop mode in order to avoid the dead time associated with the greater solid angle subtended by the first time detector, which is especially problematic for large $L$. The energy channel consisted of a conventional preamplifier–spectroscopy-amplifier chain. Events that were registered in all three detectors were identified by a slow coincidence circuit. The slow coincidence signal triggers digitization of the energy and time signals in two ADCs and the pair of conversion results written in an event record to a sequential file for off-line analysis.

## 3. Data analysis

The event records were sorted off-line using a special sorting code [6] which generates two dimensional

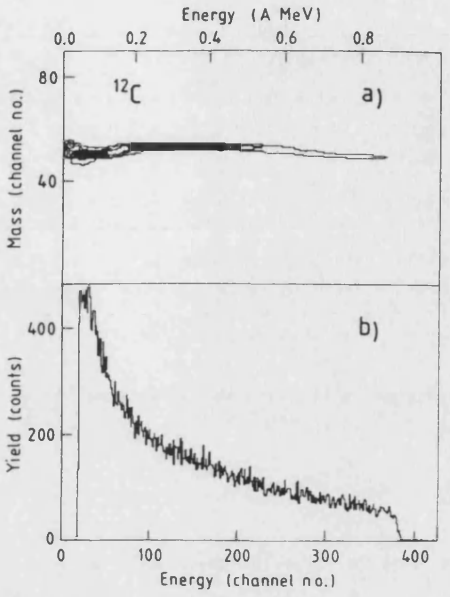


Fig. 3. (a) Contour plot of the 2-dimensional mass–energy histogram for the graphite target. (b) Corresponding singles plot of the energy spectrum for $^{12}$C recoils. $L$ = 213.5 mm.

histograms of the energy–time and mass–energy matrices as well as singles histograms of the mass, energy and time distributions. The mass $\mathcal{M}$ (in channel numbers) is assigned for each recoil according to:

$$\mathcal{M} = C\mathcal{E}(\mathcal{T} - \mathcal{T}_0)^2. \tag{9}$$

Where $\mathcal{E}$ and $\mathcal{T}$ are the energy and time ADC conversion results respectively, $C$ is a suitable constant which was chosen so that the mass scale spanned about 1000 channels and $\mathcal{T}_0$ is an adjustable parameter to correct for electronic delays etc., that was optimized for each isotope so that the corresponding signal lay along an isomass line in a contour plot of the mass–energy histogram. Fig. 3 shows such a contour plot for $^{12}$C recoiled from the graphite target for $L$ = 213.5 mm together with the corresponding energy singles spectra. Fig. 4 shows a similar plot corresponding to the GaP target and the corresponding mass singles spectra. An energy calibration for each isotope was carried out using the position of the high energy edges in the energy singles spectra. The deviations from a horizontal iso-mass line in the mass–energy contour plots is most probably associated with small non-linearities in the energy detector [24,65]. In previous experiments using the same electronics, comparison of the energies derived from the TOF and the silicon detector showed discrepancies of about 3% for $^{16}$O and $^{28}$Si recoils [12]. This is adequate for the present purpose because we do not use the absolute energy directly in the analysis. The mass scale in terms of mass units was established for each $\mathcal{T}_0$ value from the peak positions of reference

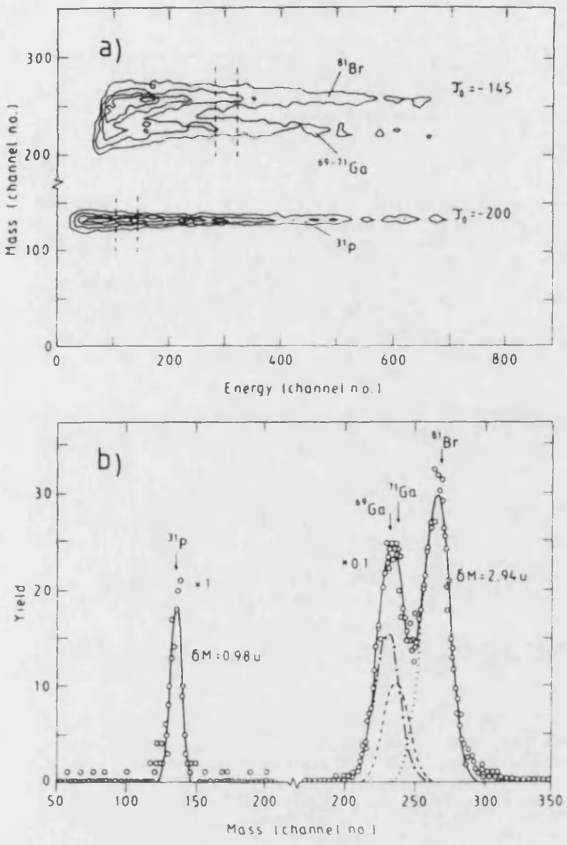


Fig. 4. (a) Contour plot of the 2-dimensional mass–energy histogram from the GaP target illustrating the good mass resolution obtained even for short timed flight lengths. ($E$ = 142 mm.) (b) Fitted mass spectra and data for 0.1 $A$ MeV $^{31}$P and $^{81}$Br. The fitting function (solid line) used to determine $\delta M$ for $^{81}$Br is the sum of three Gaussians (see text) indicated here by dotted and dashed lines. Different $\mathcal{T}_0$ values were used for the two regions in the spectra.

isotopes ($^{27}$Al, $^{16}$O, $^{12}$C, $^{31}$P). A check of this procedure based on the position of the fitted mass peaks showed it to be accurate to better than ±5% for $^{12}$C and $^{31}$P and ±15% for $^{81}$Br. (The mass scale exhibited a non-linearity that became larger for shorter timed flight lengths.)

The next step in the analysis was to sort the data to yield the mass spectra for each isotope in small energy slices. These mass spectra will be largely insensitive to any non-linearities in energy calibration because the energy slices are small. (≈ 6% for $^{12}$C, $^{31}$P and 12% for $^{81}$Br). The broadening was then parameterised in terms of the second moment about the mean $\delta M = \langle \Delta M^2 \rangle^{1/2}$ of the peak corresponding to the isotope in question. In the case of $^{31}$P where the peak is completely isolated from near lying signals this was calculated directly. In the $^{12}$C case a single Gaussian was fitted over the region where interference from $^{13}$C was minimal. (The peak shapes closely followed a Gaussian distribution.) The situation was more complex for the $^{69}$Ga, $^{71}$Ga and $^{81}$Br signals which were fitted to a function consisting of the sum of three Gaussians. The $^{69}$Ga and $^{71}$Ga Gaussians had identical $\sigma$ but with centres shifted by two mass units and amplitudes in the proportion to the natural isotopic abundance, (the difference in recoil cross section is negligible) whilst the third Gaussian corresponded to $^{81}$Br. Fitting was carried out using a conventional $\chi^2$ minimization procedure with the Ga and Br total areas, separation between $^{69}$Ga and $^{81}$Br and $\sigma$ for Ga and $^{81}$Br as free parameters. Fig. 4b illustrates the quality of the fit at 0.1 $A$ MeV for $^{81}$Br as well as a single Gaussian fitted to the $^{31}$P peak. The fitting was better for higher energies because $\delta M$ decreases with increasing energy. This approach neglects the (small) difference in mass resolution for the Ga isotopes and assumes the lineshape contribution for each isotope is Gaussian. This is a reasonable assumption at high energies but at low energies some deviations might be associated due to the appearance of shoulders on the energy detector pulse height distributions [44].

## 4. Theoretical estimates of mass resolution

Here we consider the contributions from various phenomena to the uncertainty in measured recoil energy $\delta E$, time of flight $\delta T$ and timed flight length $\delta L$. Considering first the uncertainty in energy

$$\delta E^2 = (\delta E_{E\mathrm{det}})^2 + (\delta E_{\mathrm{str}})^2 + (\delta E_{E\mathrm{th}})^2. \qquad (10)$$

This has contributions from the detector energy resolution $\delta E_{E\mathrm{det}}$, from straggling $\delta E_{\mathrm{str}}$ and thickness variation in the carbon foils $\delta E_{E\mathrm{th}}$. Similarly the contributions to the uncertainty in time of flight $\delta T$ are:

$$\delta T^2 = (\delta T_{T\mathrm{det}})^2 + (\delta T_{\mathrm{str}})^2 + (\delta T_{\mathrm{th}})^2. \qquad (11)$$

Here $\delta T_{T\mathrm{det}}$ is associated with the time resolution of the pair of time detectors, $\delta T_{\mathrm{str}}$ and $\delta T_{\mathrm{th}}$ are associated with velocity spreading brought about by straggling and thickness variations in the first carbon foil. The variations in timed flight length $\delta L$ are;

$$\delta L^2 = (\delta L_{\mathrm{config}})^2 + (\delta L_{\mathrm{align}})^2 + (\delta L_{\mathrm{ms}})^2 \qquad (12)$$

$\delta L_{\mathrm{config}}$ is the path length variation for those trajectories that are accepted by the telescope. $\delta L_{\mathrm{align}}$ is contributed to by misalignment and departure of the foil surface from planarity. Multiple scattering in the first carbon foil gives rise to $\delta L_{\mathrm{ms}}$ because of the associated path length variations.

Here we make some central assumptions for calculational purposes:

(a) That the energy straggling and foil homogeneity contributions to $\delta E$ and $\delta T$ are completely decoupled.

(b) That multiple scattering and energy straggling are completely decoupled.

(c) That the foils are thick enough that a statistical quasi-equilibrium is achieved [45] and yet sufficiently thin that only a small fraction of the particle energy is deposited in the foils.

(d) The effects of scattering by residual gas atoms in the telescope can be neglected.

(e) Particles that impinge on a time detector mesh wire are stopped and do not contribute to the broadening.

In reality assumption (a) is partly untrue in that particles with the greatest energy deviation from the mean will also have the largest velocity deviation. However the energy straggling and thickness variation contribution to $\delta E$ are the result of passing through two foils whilst the contribution to $\delta T$ is a result of passing through one foil. Within the framework of the transport equation approach and thin foils with near-normal penetration assumption (b) is not anticipated to be invalid provided assumption (c) is satisfied. Following Bohr [46], we anticipate that this condition is fulfilled if the single collision energy transfer is small compared with the width of the distribution. From Besenbacher [45] this corresponds to satisfaction of the relation:

$$Nx(\text{atoms/cm}^2) \geqslant 2\times 10^{20}\frac{E[\text{MeV}]}{Z_2(Z_1A_1)^2}. \qquad (13)$$

$N$ is the atomic density of the foil material and $x$ the thickness. For 5 $\mu$g/cm$^2$ thick carbon foils ($Nx = 2.7 \times 10^{17}$ (atoms/cm$^2$)) the right hand side of eq. (13) is $5.9\times 10^{17}$, $3.7\times 10^{16}$ and $2.4\times 10^{15}$ for 0.8 $A$ MeV $^{12}$C, 0.5 $A$ MeV $^{31}$P and 0.225 $A$ MeV $^{81}$Br respectively. Thus we anticipate that the quasi-equilibrium condition is fulfilled for all the particles of interest here with the exception of the highest energy $^{12}$C recoils.

The assumption (d) of negligible influence from the residual gas is justified because the equivalent thickness at the pressure where the telescope is operated ($10^{-5}$ mbar) corresponds to a thickness for the longest $L$ value of about $2.3\times 10^{13}$ mol/cm$^2$ (i.e. about 0.01% of the thickness of a carbon foil).

Neglection of scattering from the mesh wires in the time detectors (e) is not anticipated to contribute significantly to the broadening because: the overall transparency of the telescope is high ($\approx$ 75%) through all the grids traversed by the recoils, the mesh wire diameter ($\approx$ 200 $\mu$m) is very much larger than the recoil range and this coupled with the strong preferentiality for small angle scattering, implies that scattering of detected particles can only take place over a small fraction of the mesh wire circumference. (i.e. Only the vanishingly small fraction of particles that impinge on this part of the mesh wire circumference can be detected and contribute to broadening.)

### 4.1. Energy detector resolution $\delta E_{E\text{det}}$

In spite of the fact that silicon detectors have been widely available for about 30 years there is little information and understanding of the energy resolution for particles other than $^1$H and $^4$He. Recently Hinrichsen et al. [47] have studied the response of silicon surface barrier detectors for a wide range of heavy ions in the region $^4$He–$^{81}$Br with energies in the region 0.01–1.35 $A$ MeV. They find that Amsel et al.'s [48] simple empirical law,

$$\Delta E_{E\text{det}}[\text{keV}] = a + bE[\text{keV}]^{1/3}, \qquad (14)$$

for the FWHM of the detector pulse height distribution fits the sparse experimental data well over a restricted energy range. Here $a$ and $b$ are empirical constants. We used eq. (14) with Hinrichsens tabulated values of $a$ and $b$ for $^{12}$C and $^{81}$Br. For $^{31}$P where no experimental data is available $a = 12.75$ and $b = 10.23$ were obtained by interpolation according to atomic number from the $^{20}$Ne and $^{35}$Cl data collected in ref. [47]. The corresponding line lies in a reasonable position when plotted on fig. 4 of ref. [47]. We emphasize that the $\Delta E_{E\text{det}}$ values have a high degree of uncertainty not only because of this interpolation but also because at the highest energies (> 100 $A$ keV $^{81}$Br) it has been necessary to extrapolate outside the energy interval where eq. (14) is stated to be valid. There is no indication in the data of ref. [47] which suggests this is inappropriate. Furthermore we have employed ion implanted detectors whilst Hinrichsen et al.'s data is for surface barrier detectors. (The presence of a passivating surface layer (10 nm or so) on the ion implanted detectors may lead to some degradation in energy resolution over that of surface barrier detectors.) We converted the FWHM to the standard deviation $\delta E_{E\text{det}}$ by assuming the lineshape to the Gaussian ($\Delta E_{E\text{det}} = 2.35\delta E_{E\text{det}}$). This is anticipated to be a reliable assumption at high energies, however departures from Gaussian lineshape have been reported at low energies (< 60 $A$ keV) [44].

### 4.2. Energy straggling in the carbon foils $\delta E_{\text{str}}$

The statistical nature of the energy loss processes as the particles traverse the thin carbon foils in the time detector leads to an uncertainty in their exit energy. This is conveniently parameterised in terms of the mean square deviation $\Omega^2$ of the energy loss for light, high velocity ions in an electron gas corresponding to $Nx$ target atoms/cm$^2$ the well known Bohr formula [46] is appropriate [49]:

$$\Omega_B^2 = 4\pi Z_1^2 e^4 Z_2 Nx. \qquad (15a)$$

For low velocity heavy ions the situation is complicated by a number of factors which are discussed in detail by

Besenbacher et al. [50]. In particular, some electrons will have velocities lower than the Bohr velocity, strong fluctuations will arise because of spatial localization of a significant fraction of the electrons and variations in the projectile charge state. In the absence of any reliable theory we have simply corrected the Bohr value by a factor corresponding to the trend line through the $\Omega^2/\Omega_B^2$ plot of data from the literature by Besenbacher et al. [50]. (Efken et al.'s [51] carbon foil data where variations associated with inhomogeneity and thickening were thought to make a significant contribution was neglected). Then:

$$\delta E_{str}^2 = \Omega^2 = \left(\Omega^2/\Omega_B^2\right)\Omega_B^2. \tag{15b}$$

*4.3. Energy spreading from foil thickness variations* $\delta E_{th}$

For the present purposes we can conveniently classify homogeneity variations in the foils as holes and thickness variations. Holes do not influence the mass resolution because particles that impinge on a hole will not produce secondary electrons and thus escape detection. Thickness variations across the foil are more troublesome because they lead to a spreading of particle energies. Thickness variations can be classified as macroscopic and microscopic variations. Generally macroscopic variations are associated with the deposition geometry and source anisotropy and are usually quite small over the foil dimensions employed here. Deposition from an isotropic point source onto a flat substrate 250 mm away with constant sticking coefficient gives a ratio of macroscopic variation to film thickness of only $1.6 \times 10^{-7}$ over the surface of a 20 mm diameter foil. Microscopic thickness variations are more of a problem because they depend on deposition technique (ac or dc arc, sputtering etc.), geometry and deposition pressure. The surface topography of the substrate can also contribute to thickness variations. Here we have assumed that the rms thickness variation $\sigma_x$ is 10% of the foil thickness $x$. Then.

$$\delta E_{th} = \epsilon N \sigma_x. \tag{16}$$

Where $\epsilon$ is the energy loss cross section which was evaluated using Ziegler et al.'s STOP code [52].

*4.4. Temporal resolution of the time detectors* $\delta T_{Tdet}$

The resolution of the time detector is contributed to by (i) variations in the electron transit time from the carbon foil to the entrance plane of the channel plate electron multiplier, (ii) the time jitter of the electron multiplier and (iii) the time jitter of the electronic system.

(i) The electron transit time can be considered as being made up of the transit time over the 5 mm accelerating gap (5.1 ns) (see fig. 2) and the 40 mm field free region (2.9 ns). If we assume that mechanical tolerances and foil distortion introduce variations in trajectory lengths corresponding to standard deviations of 3% and 1% respectively, the associated temporal spreading is 70 and 29 ps, which combined give an overall transit time spreading $\delta T_{tt}$ of 76 ps. This value is about 50% greater than that measured by Stazecki et al. [39]. We believe our estimate to be more representative because the electrostatic field which causes the foil distortion is compensated out in the back to back configuration used by Stazecki et al.

(ii) The time jitter of the multi-channel plate (MCP) electron multipliers is more difficult to quantify [53]. According to Hamamatsu [54] an overall $\Delta t_{FWHM}$ of 180 ps was obtained for two scintillators followed by an MCP pair with 12.5 μm channel width and channel length/width ration of 50:1. Frazer has recently reported a detailed Monte Carlo based study [55] which includes saturation effects and finds that for a single MCP (15 μm channel width $L/D = 50:1$, $V = 900$ V) similar to that used here (Philips G12-25 with 12.5 μm channel width) that $\Delta t_{FWHM}$ varied between 47 to 80 ps according to accelerating voltage. The resulting time spread $\Delta T_{FWHM}$ for a cascaded pair of identical MCP is [55]:

$$\Delta T_{FWHM} = \sqrt{2}\,\Delta t_{FWHM}, \tag{17}$$

which for our MCP potential difference is 113 ps ($\delta T_{MCP} = 48$ ps for Gaussian spreading).

(iii) The function of the electronic system is to precisely determine the time when the electron shower associated with the passage of the particle impinges on the anode structure. The uncertainties can be associated with the timing walk in the discriminator and distortion of the pulse form. The pulse height distribution varied over a 100:1 dynamic range with significant weighting of smaller pulse heights, which according to the manufacturers specification [56] will give a time walk that corresponds to $\delta T_{el} = 80$ ps. The contribution to $\delta T_{el}$ from the time to amplitude converter is small in comparison (< 10 ps [57]) and thereby neglected. Pulse-form distortion where the pulse-form differs from pulse to pulse, is more difficult to quantify. It is contributed to by baseline shifts due to 50 Hz pickup as well as statistical noise in the MCP and amplifier chain. Observations of the trigger point monitor suggest this is small in comparison to the timing walk and thereby neglected.

The overall time spreading $\delta T_{Tdet}$ for a pair of identical detectors is then:

$$\delta T_{Tdet}^2 = 2\left(\delta T_{tt}^2 + \delta T_{MCP}^2 + \delta T_{el}^2\right). \tag{18}$$

Here $\delta T_{tt}$, $\delta T_{MCP}$ and $\delta T_{el}$ represent the contributions from the transit time, MCP and electronics respectively. $\delta T_{Tdet} = 170$ ps.

*4.5. Temporal spreading due to straggling in the first carbon foil* $\delta T_{str}$

The energy straggling in the first carbon foil will contribute to the time spreading because of the corresponding spreading in recoil velocity after passage through the foil. Then:

$$\delta T_{str}^2 = \Omega_1^2 (\partial T/\partial E)^2 = \Omega_1^2 \frac{ML^2}{8E^3}. \quad (19)$$

Here $\Omega_1^2$, the straggling in the first foil, was calculated according to eq. (15).

*4.6. Time spreading from thickness variations in the first foil* $\delta T_{th}$

A velocity spreading is associated with the thickness variations in the first carbon foil. Here as in section 4.3, the rms thickness variations were taken to be 10% of the foil thickness. Then substituting $\delta E_{th} = \epsilon N \sigma_x$ for $\Omega_1$ in eq. (16) gives:

$$\delta T_{th}^2 = \delta E_{th}^2 (\partial T/\partial E)^2 = M \frac{(L \epsilon N \sigma_x)^2}{8E^3}. \quad (20)$$

*4.7. Configurational spreading of the timed flight length* $\delta L_{conf}$

There is a spreading in the timed flight length $\delta L_{conf}$ that arises because of the finite range of acceptance angles subtended by the telescope. If $\beta_{max}$ is the half angle subtended by the telescope which has circular symmetry:

$$\delta L_{conf}^2 = L \beta_{max}^4. \quad (21)$$

In the present system $\beta_{max}$ is determined by a combination of the extent of the ellipsoidal (10.3 and 2 mm major and minor axes) interaction volume and the aluminium aperture in front of the energy detector at a distance of L + 461 mm from the centre of the interaction volume.

*4.8. Spreading of the timed flight length from multiple scattering* $\delta L_{ms}$

The statistical nature of scattering of a particle passing through a thin foil leads to not only spreading in energy but also ejection angle. This causes an associated spreading of timed flight length. Sigmund and Winterbon [58] have evaluated, using a transport equation approach, the distribution of ejection angle with foil thickness and interaction potential. For large foil thicknesses the distribution is Gaussian but with tails that become progressively more significant as the foil thickness decreases. (cf. fig. 5 of ref. [58]). Here we have used Sigmund and Winterbon's value for the half angle $\alpha_{1/2}$ for a Thomas–Fermi screened Coulomb potential and neglected the difference between $\alpha_{1/2}$ and the second central moment of the distribution. This was done because for the higher energy light particles the requirement of eq. (13) is not very well satisfied and thus we anticipate the ejection angle distribution to deviate somewhat from a Gaussian form. Then the spreading of timed flight length $\delta L_{ms}$ is;

$$\delta L_{ms}^2 = \frac{L}{2} \alpha_{1/2}^4. \quad (22)$$

*4.9. Timed flight length spreading from misalignment and distortion* $\delta L_{align}$

Deviation of the foils from exact parallelism arises because of finite mechanical tolerances in the telescope fabrication. These are estimated to contribute to a variation of less than 0.3 mm rms over the extent of the largest (second) foil. In practice the foils are not absolutely planar but are wrinkled because of the inevitable slackness that results from mounting on the foil holder by picking up a foil floating on the surface of water. Visual inspection of the foil surface showed that under the action of the electrostatic field from the acceleration grid these wrinkles are stretched out and the foil surface becomes bowed. This distortion was estimated to be 0.5 mm at the foil centre. In view of the large foil to foil variations anticipated we have taken the representative value of $\delta L_{align}$ of 0.5 mm rms.

## 5. Results and discussion

In figs. 5–7 the experimental second moment of the mass distribution $\delta M^2$ is presented as a function of particle energy, timed flight length and mass number $A$. The error bars designate the combined uncertainties from fitting and calibration. Figs. 5–7 also indicates the theoretical estimates of the different contributions to $\delta M$ expressed in mass units through eqs. (3)–(5). The theoretical estimates of $\delta L_{ms}$ and $\delta L_{config}$, which lie in the range $1.5 \times 10^{-5}$ to $6 \times 10^{-3}$ $u$, are vanishingly small and not plotted. From the results presented in figs. 5–7 the following observations were made:

(a) The experimentally determined mass spreading is greatest for low-energy particles and decreases with increasing particle energy. This behaviour is the same for $^{12}C$, $^{31}P$ and $^{81}Br$ recoils for all values of $L$ investigated, (see also ref. [6]).

(b) The experimentally determined mass spreading becomes greater as the particle mass increases. This behaviour is also observed for all values of $L$.

(c) The experimental mass spreading for $^{12}C$, $^{31}P$ and $^{81}Br$ particles with 0.1 $A$ MeV energy shows no

significant dependence on $L$ over the range 0.213 to 0.961 m.

(d) The sum of the theoretical contributions and experimental $\delta M$ have the same relative dependence on energy, timed flight length and mass but the latter is systematically some 25–30% greater than the theoretical estimate.

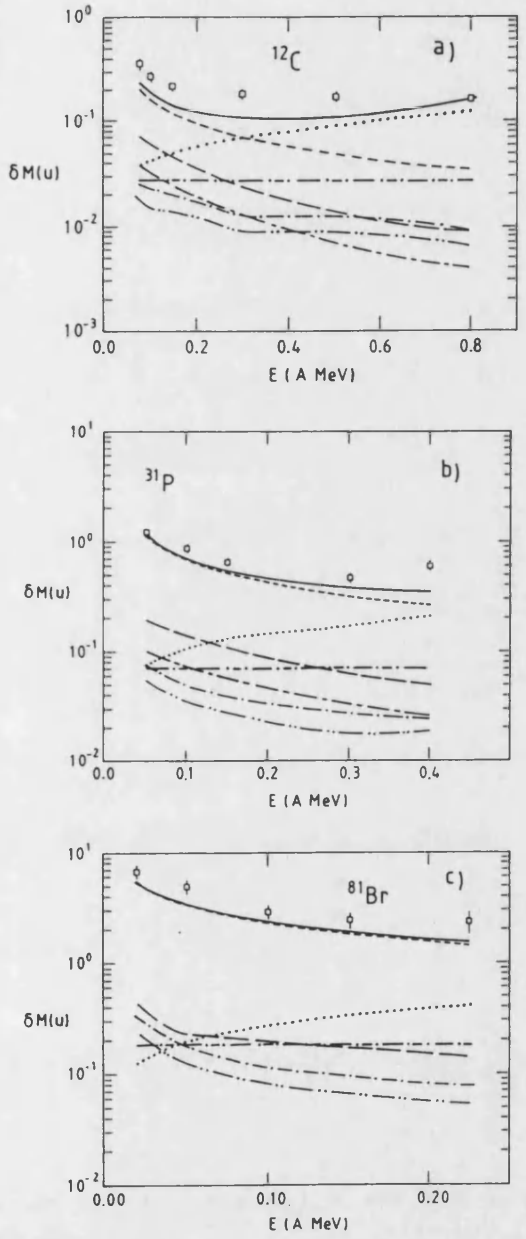


Fig. 5. Mass spreading $\delta M$ vs/energy for (a) $^{12}$C, (b) $^{31}$P and (c) $^{81}$Br recoils. Telescope timed flight length $L = 437.5$ mm. The filled squares denote the experimental data points whilst the lines denote cubic spline fits to the theoretical estimates of the contributions to $\delta A$, ——— sum (eq. (2)), - - - - - - $\delta E_{Edet}$, ····· $\delta T_{Tdet}$, ·-·-· $\delta E_{str}$, -··-··- $\delta T_{str}$, — — — $\delta E_{thr}$, -·—·—· $\delta T_{thr}$, ··-·—·-·· $\delta L_{align}$. (In (c) $\delta T_{th}$ is not shown because it is coincident with $\delta E_{str}$.

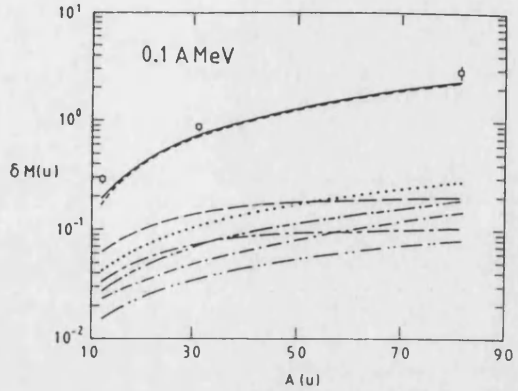


Fig. 6. Mass spreading $\delta M$ vs recoil mass for 0.1 $A$ MeV recoils. Telescope timed flight length $L = 437.5$ mm. See fig. 5 caption for legend.

(e) The contribution to $\delta M$ from the energy detector resolution $\delta E_{Edet}$ dominates at low energies ($< 0.3$ $A$ MeV) and especially so for $^{81}$Br recoils. The $\delta E_{Edet}$ contribution is independent of timed flight length $L$.

(f) The contribution to $\delta M$ from the time detector resolutions $\delta T_{Tdet}$ is the only contribution that becomes greater with increasing particle energy. This contribution becomes smaller for larger timed flight lengths.

(g) The contributions to $\delta M$ that are associated with the foils, $\delta E_{str}$, $\delta E_{th}$, $\delta T_{str}$, $\delta T_{th}$, have similar magnitude and all become smaller for increasing particle energies but are independent of $L$. They also become greater as the particle mass increases. The size of these contributions is small compared to the dominating contributions $\delta E_{Edet}$ and $\delta T_{Tdet}$.

(h) The contributions from timed flight length spreading $\delta L_{align}$ is energy independent but becomes smaller as $L$ increases. The size of this contribution is of similar size as the foil associated contributions and small in comparison to $\delta E_{Edet}$ and $\delta T_{Tdet}$.

(j) The low energy limit in fig. 5 was set by the limited time interval spanned by the TAC and this was optimized to satisfy the need for sufficient digitization accuracy to permit quantitative measurement of the mass broadening. Although the performance at the low energy limit has not been investigated here, 20 $A$ keV $^{81}$Br particles have been measured and on the basis of Lennard et al.'s results [23,24] there is no reason why lighter recoils cannot be measured at this energy.

The rather good agreement between the experimentally measured and the theoretical estimate is strongly indicative that the latter gives a good description of the interplay between the different contributions to the

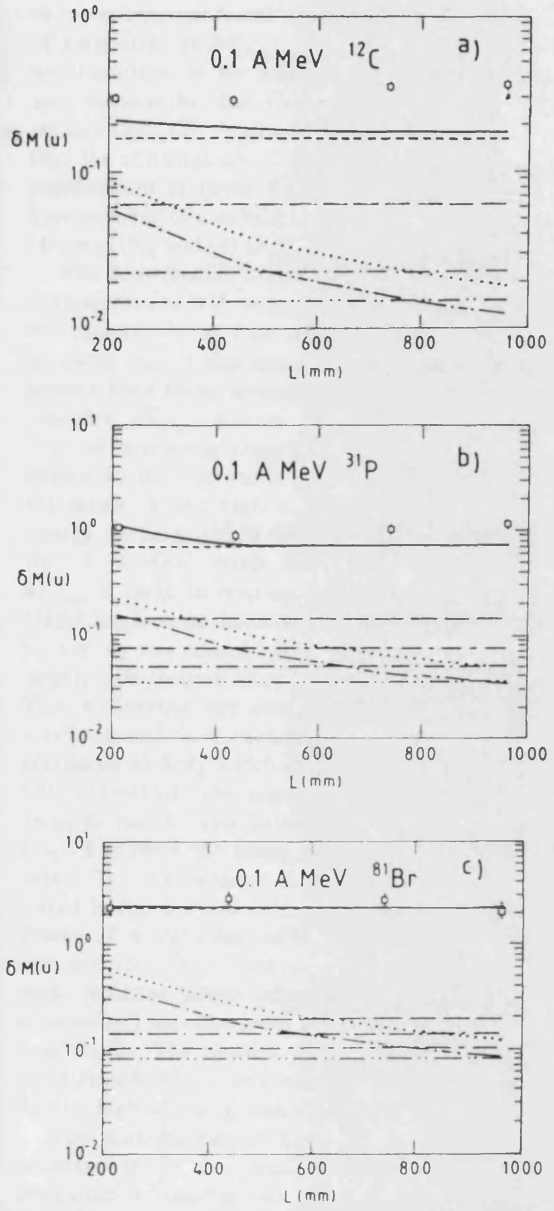


Fig. 7. Mass spreading $\delta M$ vs. timed flight length $L$ for (a) $^{12}$C, (b) $^{31}$P and (c) $^{81}$Br recoils with 0.1 $A$ MeV energy. See fig. 5 caption for legend.

mass spreading. Experiments with the data analysis procedure indicate the error in determining the width $\delta M$ of the experimental data is around 5% for $^{12}$C and $^{31}$P. The error is anticipated to be larger ($\approx \pm 15\%$) for $^{81}$Br where a sophisticated decomposition involving a number of assumptions is needed to determine the experimental $\delta M$ value and the uncertainty in the mass calibration is larger. *In view of the fact that the discrepancy is systematic and is greater than the anticipated uncertainty in the experimental data, it is most probable that the discrepancy is associated with the theoretical estimate.*

For low energies, $\leqslant 0.3$ $A$ MeV, (which corresponds to the range of energies with which most recoils will be produced in heavy ion collisions), the mass spreading is completely dominated by the contribution from $\delta E_{E\text{det}}$. This contribution becomes slightly more significant with increasing recoil mass. Thus the difference between the experimentally determined absolute $\delta M$ and the theoretical estimates will be strongly dependent on the uncertainty in the estimated $\delta E_{E\text{det}}$ values. It should be born in mind that Hinrichsen et al.'s [47] energy resolution data is for surface barrier detectors. A comparison by Gjurathi et al. [44] of surface barrier detectors with implanted p–i–n diodes, such as those employed here, showed a resolution degradation for the latter of the same magnitude as that required to explain the discrepancy between our experimental and theoretical values. A further possibility is that the heat treatment of the silicon energy detector prior to the measurements did not anneal out the radiation damage responsible for degradation of the energy resolution. *The domination of $\delta M$ by the $\delta E_{E\text{det}}$ contribution also implies that if a significant mass resolution improvement is to be made then the energy detector resolution must be improved.* It is anticipated that cooling the detector and front-end of the preamplifier will not significantly improve the energy resolution because the contribution from detector leakage currents and pre-amplifier noise is small compared to the statistical spreading in the number of electron hole pairs that are collected when a heavy particle is stopped in the detector [64]. For some applications gas ionization detectors may offer a superior energy resolution [14,59]. However gas diffusion through the thin window and the ever present risk of window rupture renders them somewhat incompatible with the UHV environment of a storage ring. Detectors based on bolometric calorimetry [62] may offer superior resolution for heavy ions over that of silicon detectors, although here the technology is in its infancy and the need for maintaining tens to thousands of square millimeters of detector surface at extreme cryogenic temperatures is not appealing from a technical viewpoint.

Considering next the contributions from the foils: here evidently both straggling and thickness variations contribute. The contributions to the energy spreading $\delta E_{\text{str}}$ and $\delta E_{\text{th}}$ are larger than the corresponding contributions to the time spread $\delta T_{\text{str}}$ and $\delta T_{\text{th}}$. $\delta E_{\text{str}}$ and $\delta T_{\text{str}}$ both scale as $x^{1/2}$ where $x$ is the foil thickness. Thus thicker foils could be used without significantly compromising the mass spreading $\delta M$. The contributions associated with thickness variations $\delta E_{\text{th}}$ and $\delta T_{\text{th}}$ on the other hand scale in proportion to $\sigma_x$, which was taken as 10% of the nominal foil thickness. Inspection

of figs. 5–7 reveals that a few-fold increase in $\sigma_x$ leads to a contribution from $\delta E_{th}$ that is of the same order of magnitude as $\delta E_{Edet}$. *The implication is that thickness variations in the foils must be held in check.* It is also noteworthy that the $\delta T_{str}$ and $\delta T_{th}$ are always smaller than $\delta E_{str}$ and $\delta E_{th}$ respectively. Furthermore that the contribution to $\delta M$ from $\delta T_{str}$ and $\delta T_{th}$ are independent of timed flight length $L$. The latter follows because of cancellation of the terms in $L^2$ in eqs. (4) and (19), and (4) and (20).

The contribution from the time detectors: here the contribution to $\delta M$ from $\delta T_{Tdet}$ becomes dominant in the case of $^{12}C$ at high energy ($\geqslant 0.3$ $A$ MeV). It is probable that it also becomes dominating at energies greater than those investigated here for $^{31}P$ and $^{81}Br$ provided $\delta E_{Edet}$ follows eq. (14) or shows a trend towards becoming energy independent. This is supported by the reports in the literature of good mass resolution in the high mass region $A \approx 80$ for high energy particles [35,38,60]. It is also noteworthy that for 0.1 $A$ MeV recoils the contribution to $\delta M$ from $\delta T_{Tdet}$ is small in relation to $\delta E_{Edet}$ even for short $L$ (213.5 mm). A further consequence of the domination of $\delta M$ by the contribution from $\delta E_{det}$ is that $\delta M$ is largely independent after timed flight length $L$ (fig. 7). This is because the contributions to $\delta M_T$ (eq. (4)) which depend on $L$ though eqs. (11) and (18) are small compared to $\delta M_E$ which is independent of $L$ (eqs. (3), (10), (14)–(16)). The implication is that for measurement of recoils from heavy ion collisions with energy $E \leqslant 0.1$ $A$ MeV the timed flight length can be reduced below 213 mm without degrading $\delta M$. This is illustrated in fig. 4 which demonstrates the mass resolving power of a telescope with $L = 142$ mm. *Thus small compact telescopes can be constructed without sacrificing mass resolving power where only small (and thereby economical) detector areas are needed to subtend large solid angles.* The shortest timed flight length that can be tolerated is then determined by the mass resolution for the highest energy recoils.

The contributions to $\delta M$ that are associated with uncertainties in the timed flight length are generally insignificant. Indeed the contributions $\delta L_{config}$ and $\delta L_{ms}$ can be completely neglected in the present system. It should be born in mind that these terms can become large, especially if a large first foil is close to an extended interaction volume. The contribution from $\delta L_{align}$, which is the largest of the geometrical contributions, is independent of particle energy and decreases for greater timed flight length $L$. Its size is comparable with the contributions from the foils.

From the experimental physicists viewpoint the most interesting questions are what is the mass separating power of the telescope and what are the limits to which this parameter can be optimized. As noted in the introduction this is governed by the distribution of mass spreading which here has been parameterised in terms of its second moment $\delta M$. For the case of Gaussian lineshapes (which are a good approximation) estimation of the cross-talk is trivial. If the isotope signals have a spacing of one mass unit $\delta M$ must be less than 0.22, 0.304, 0.390 and 0.620 for a cross-talks of 1, 5, 10 and 20% respectively. Inspection of figs. 5–7 show that for $A \leqslant 30$ individual isotopes may be easily separated. In the argon region ($A \approx 40$) features separated by two mass units may be readily discerned whilst in the krypton region ($A \approx 80$) the feature separation should be 3–4 mass units for discernment.

The fact that the mass spreading is dominated by the energy detector resolution sets a natural limit to the resolution for this type of telescope. It implies that individual isotopes cannot be resolved for $A > 30$. This situation will not be improved with certitude unless electromagnetic momentum analysis is employed, (which has significant disadvantages because of the need to know the atomic charge state distributions for each recoil species). We emphasize that even though the mass resolution is not sufficient for individual isotopes to be separated in the $A \approx 80$ region much useful information such as momentum distributions can be gleaned from the recoil telescope. A careful selection of the mass window criteria based on analysis of the mass distribution allowed reliable separation of $^{69-71}Ga$ from $^{75}As$ in a recoil spectrometry study of solid state reactions in $Al_xGa_{(1-x)}As$ thin-film structures [61].

## 6. Conclusions

(i) Recoil telescopes based on thin carbon foil time detectors and ion implanted silicon charged particle detectors can be used to measure the energy and mass of low energy (0.05–0.2 $A$ MeV) recoils from nuclear collisions.

(ii) The mass resolution improves with increasing recoil energy but is largely independent of timed flight length in the 0.2135–0.961 m. The mass resolution degrades with increasing recoil mass number $A$.

(iii) The experimentally observed mass resolution is reasonably well described by the theoretical estimate presented. The systematic discrepancy is most probably associated with the uncertainties in the estimate of energy detector resolution.

(iv) The mass resolution for low energy ($\leqslant 0.3$ $A$ MeV) recoils is dominated by the contribution associated with the energy detector resolution. At higher energies the time detector resolution increases and may even become dominant.

(v) For detection of heavy recoil nuclei with an energy of 0.1 $A$ MeV timed flight lengths of less than

0.2 m are sufficient for a time detector pair resolution of $\delta T_{Tdet} = 170$ ps (400 ps FWHM).

(vi) The thickness of the carbon foils may be increased without significantly degrading the mass resolution provided that thickness variations to not increase significantly.

(vii) The contribution from geometric uncertainties in the timed flight length are small in the present (small solid angle) system.

## Acknowledgements

The Swedish Board of Technical Development (STU-F) and Knut och Alice Wallenbergs Stiftelse are thanked for financial support. We are also grateful to the The Royal Institute of Technology, Department of Solid State Electronics, for loan of the scattering chamber, recoil telescope system and electronics.

## References

[1] A. Lleres, J. Crancon, J. Blachot, A. Gizon and H. Nifenecker, J. Phys. (Paris) C4 (1986) 365.
[2] K. Aleklett, W. Loveland, J.O. Liljenzin, L. Sihver and G.T. Seaborg, Lawrence Berkley Lab. Preprint LBL 29793 (1990).
[3] B. Jakobsson, G. Jönsson, B. Lindkvist, A. Oskarsson and K. Söderström, Z. Phys. A307 (1977) 293.
[4] J.D. Sullivan, P.B. Price, H.J. Crawford and M. Whitehead, Phys. Rev. Lett. 30 (1973) 136.
[5] B.L. Cohen, C.L. Fink and J.H. Degnan, J. Appl. Phys. 43 (1972) 19.
[6] H.J. Whitlow, G. Possnert and C.S. Petersson, Nucl. Instr. and Meth. B27 (1987) 448. (There is an error in eq. (2) of this article it should be replaced by eq. (2) of ref. 12.)
[7] R. Groleau, S.C. Gujathi and J.-P. Martin, Nucl. Instr. and Meth. 218 (1983) 11.
[8] S.C. Gujrathi, P. Aubry, L. Lemay and J.-P. Martin, Can. J. Phys. 65 (1987) 950.
[9] A. Hounayer, P.F. Hinrichsen, S.C. Gujrathi, J.P. Matrin, S. Monaro, L. Lessard, K. Oxorn, C. Janicki, J. Brebner, A. Belhadfa and A. Yellon, Nucl. Instr. and Meth. B24/25 (1987) 643.
[10] J.-P. Thomas, M. Fallavier, D. Ramedame, N. Chervarier and A. Chervarier, Nucl. Instr. and Meth. 218 (1983) 125.
[11] J.-P. Thomas, M. Fallavier and Z. Ziani, Nucl. Instr. and Meth. B15 (1986) 443.
[12] H.J. Whitlow, A.B. Ch. Andersson and C.S. Petersson, Nucl. Instr. and Meth. B36 (1989) 53.
[13] L.E. Seiberling, Nucl. Instr. and Meth. B24/25 (1987) 526.
[14] A.M. Behrooz, R.L. Hedrick, L.E. Seiberling and R.W. Zurmühle, Nucl. Instr. and Meth. B28 (1987) 108.
[15] M. Petrascea, I. Berceanu, I. Branucus, A. Buta, C. Grame, I. Lazar, I. Mihai, M. Petrovic, V. Simon, M. Mihaila and I. Gita, Nucl. Instr. and Meth. B4 (1984) 396.
[16] J.P. Stoquert, G. Guillaume, M. Hage-Ali, J.J. Grob, C. Ganter and P. Siffert, Nucl. Instr. and Meth. B44 (1989) 184.
[17] H.J. Whitlow, C.S. Petersson, K.J. Reeson and P.L.F. Hemment, Appl. Phys. Lett. 52 (1988) 1871.
[18] H.J. Whitlow, K.J. Reeson, P.L.F. Hemment and C.S. Petersson, in: Selected topics in Electronic Materials, eds. B.R. Appleton, D.K. Biegelsen, W.L. Brown and J.A. Knapp (Mat. Res. Soc. Extended Abstract EA18, Pittsburgh, PA, 1988) p. 149.
[19] P.A. Ingemarsson, T. Ericsson, G. Possnert and R. Wäppling, Hyperfine Interactions 46 (1989) 549.
[20] H. Jiang, H.J. Whitlow, M. Östling, E. Neimi, F.M. d'Heurle and C.S. Petersson, J. Appl. Phys. 65 (1989) 567.
[21] H.J. Whitlow, E. Johansson, P.A. Ingemarsson and S. Hogmark, submitted to Nucl. Instr. and Meth. B.
[22] L. Lavergne-Gosselin, L. Stab, M.O. Lampert, H.-Å Gustafsson, B. Jakobsson, A. Kristiansson, A. Oskarsson, M. Westenius, A.J. Kordyasz, K. Aleklett, L. Westerberg, M. Rydehell and O. Tengblad, Nucl. Instr. and Meth. A276 (1989) 210.
[23] W.N. Lennard, H.R. Andrews, M. Freeman, I.V. Mitchell, D. Phillips, D.A.S. Walker and D. Ward, Nucl. Instr. and Meth. 203 (1987) 565.
[24] W.N. Lennard, H. Geissel, K.B. Winterbon, D. Phillips, T.K. Alexander and J.S. Forster, Nucl. Instr. and Meth. A248 (1986) 454.
[25] E. Dietz, R. Bass, A. Reiter, U. Friedland and B. Hubert, Nucl. Instr. and Meth. 97 (1971) 581.
[26] G.W. Butler, A.M. Postkanzer and D.A. Lands, Nucl. Instr. and Meth. 89 (1970) 189.
[27] R.R. Betts, Nucl. Instr. and Meth. 162 (1979) 531.
[28] T.M. Gormier, R.S. Galik, E.R. Cosman and A.J. Lazzarini, Nucl. Instr. and Meth. 119 (1974) 145.
[29] W.K. Chu, M.A. Nicolet and J.W. Mayer, Backscattering Spectrometry (Academic Press, New-York, 1978).
[30] P. Sigmund, in: Sputtering by Particle Bombardment I, ed. R. Behrisch, vol. 47 of Topics in Applied Physics (Springer, Berlin, 1981) p. 9.
[31] H.J. Whitlow, unpublished results, 1986.
[32] W. Bohn, W. Galster, K. Grabisch and H. Morgenstern, Nucl. Instr. and Meth. A240 (1985) 145.
[33] N.R. Sanderson, B.R. Fulton and J.B.A. England, Nucl. Instr. and Meth. 137 (1976) 399.
[34] N.E. Sanderson, J.B.A. England, E.C. Pollacco and R.H. Bhommick, Nucl. Instr. and Meth. 153 (1978) 93.
[35] W.F.W. Schneider, B. Kohlmeyer, W. Pfeffer, F. Pühlhoffer and R. Bock, Nucl. Instr. and Meth. 123 (1975) 93.
[36] F. Busch, W. Pfeffer, B. Kohlmeyer, D. Schüll and F. Pühlhoffer, Nucl. Instr. and Meth. 171 (1980) 71.
[37] A.M. Zebelman, W.G. Meyer, K. Halbach, A.M. Poskanzer, R.G. Sextro, G. Gabour and D.A. Landis, Nucl. Instr. and Meth. 141 (1977) 439.
[38] W. Starechi, A.M. Stefanini, S. Lunardi and C. Signorini, Nucl. Instr. and Meth. 193 (1982) 499.
[39] G.D'Erosmo, V. Paticchio and A. Pantaleo, Nucl. Instr. and Meth. A234 (1985) 91.

[40] R.D. Heil, J. Drexler, K. Huber, U. Kneissl, G. Mank, H. Ries, H. Ströler, T. Weber and W. Wilke, Nucl. Instr. and Meth. A239 (1985) 545.
[41] L. Conradi, G. Montagnoli, D.R. Napoli, R. Spolane, A.M. Stefanini, Yu. Jincheng, S. Beghini, S. Scarlassara, G.F. Segato, F. Soramel and G. Signorini, Nucl. Instr. and Meth. A297 (1980) 461.
[42] R. Henck, Nucl. Instr. and Meth. A288 (1990) 278.
[43] A. Hallén, P. Håkansson, B.U.R. Sundquist and B.G. Svensson, Proc. 14th Nordic Semiconductor Meeting, June 1990, ed. O. Hansen (Univ. of Aarhuis, 1990) p. 153, and B.G. Svensson, B. Mohadjeri, A. Hallén, J.H. Svensson and J.W. Corbett, Phys. Rev. B43 (1991) 2292.
[44] S.C. Gujrathi, D.W. Hetherington, P.F. Hinrichsen and M. Bentourkia, Nucl. Instr. and Meth. B45 (1990) 260.
[45] F. Besenbacher, J.U. Anderson and E. Bonderup, Nucl. Instr. and Meth. 168 (1980) 1.
[46] N. Bohr, K. Dan. Vidensk. Selsk. Mat.-Fys. Medd. 18 (1948) no. 8.
[47] P.F. Hinrichsen, D.W. Hetherington, S.C. Gujrathi and L. Cliche, Nucl. Instr. and Meth. B45 (1990) 275.
[48] G. Amsel, C. Cohen and A. L'Hoir, in: Ion Beam Surface Layer Analysis vol. 2, eds. O. Meyer, G. Linker and F. Kappeler (Plenum, New-York, 1976).
[49] J.M. Anthony, Nucl. Instr. and Meth. 218 (1983) 803.
[50] F. Besenbacher, H.H. Andersen, P. Hvelplund and H. Knudsen, K. Dan. Vidensk. Selsk. Mat.-Fys. Medd. 40 (1981) no. 9.
[51] B. Efken, D. Hahn, D. Hischer and G. Wüsterfeld, Nucl. Instr. and Meth. 129 (1975) 219.
[52] J.F. Ziegler, J.P. Biersack and U. Littmark, The Stopping and Ranges of Ions in Solids 1, The Stopping and Ranges of Ions in Matter, ed. J.F. Ziegler (Pergamon, 1985).
[53] J.L. Wiza, Nucl. Instr. and Meth. 162 (1979) 587.
[54] Characterization and application of microchannel plates, Hamamatsu Technical manual RES-0795, (Hamamatsu, Japan).
[55] G.W. Frazer, Nucl. Instr. and Meth. A291 (1990) 595.
[56] Phillips Scientific 6915 data sheet (Phillips Scientific, New Jersey).
[57] EG&G Oretec, Biased TAC 457 manual (Oak Ridge, USA).
[58] P. Sigmund and K.B. Winterbon, Nucl. Instr. and Meth. 119 (1974) 541.
[59] M.H. Mendenhall, R.P. Livi and T.A. Tombrello, Proc. Int. Symp. on Three day in-depth review on the nuclear accelerator impact in the interdisciplinary field, eds. P. Mazzoldi and G. Moshini (Laboratori Nazionali di Lenaro, Padova, Italy) p. 156;
M.H. Mendenhall, Nucl. Instr. and Meth. B10/11 (1985) 596.
[60] W.F.W. Schneider, B. Kohlmeyer and R. Bock, Nucl. Instr. and Meth. 87 (1970) 253.
[61] M. Hult, M. Östling and H.J. Whitlow, submitted to Appl. Phys. Lett.
[62] H.H. Andersen, Nucl. Instr. and Meth. B15 (1986) 722.
[63] R.L. Kavalov, Yu.L. Margaryan, M.G. Panyan and G.A. Papyan, Nucl. Instr. and Meth. A237 (1985) 543.
[64] J.B.A. England, Techniques in Nuclear Structure Physics, part I (Macmillan, London, 1974) p. 94.
[65] L. Cliche, S.C. Gujrathi and L.A. Hamel, Nucl. Instr. and Meth. B45 (1990) 270.

ELSEVIER

Nuclear Instruments and Methods in Physics Research B 101 (1995) 263–266

NIM B
Beam Interactions with Materials & Atoms

# Empirical characterisation of mass distribution broadening in ToF–$E$ recoil spectrometry

Mikael Hult [a,1], Mohamed El Bouanani [a,*], Leif Persson [a], Harry J. Whitlow [a], Margaretha Andersson [b], Carina Zaring [c], Mikael Östling [c], David D. Cohen [d], Nick Dytlewski [d], Ian F. Bubb [e], Peter N. Johnston [e], Scott R. Walker [e]

[a] *Lund Institute of Technology, Department of Nuclear Physics, Sölvegatan 14, S-223 62 Lund, Sweden*
[b] *Department of Inorganic Chemistry, Uppsala University, Box 531, S-751 22 Uppsala, Sweden*
[c] *Department of Electronics, Solid State Electronics, Royal Institute of Technology, P.O. Box Electrum 229, S-164 40 Kista, Sweden*
[d] *Australian Nuclear Science and Technology Organisation, PMB 1, Menai 2234, Lucas Heights, Australia*
[e] *Department of Applied Physics, Royal Melbourne Institute of Technology, GPO Box 2476V, Melbourne 3001, Australia*

Received 22 September 1994; revised form received 27 January 1995

**Abstract**

The mass broadening function in mass and energy dispersive recoil spectrometry using a detector telescope for time-of-flight and energy determination, has been characterised for a number of isotopes in the range $A = 12$ to 197. The broadening was well described by a Gaussian function where the standard deviation is given by the empirical equation:

$$\sigma_A(E,A) = C_1 + C_2 A^{3/2} E^{-1} + C_3 A^2 E^{-2/3} + C_4 A E^{1/2}.$$

## 1. Introduction

Recoil Spectrometry (RS) based on Time-of-Flight (ToF) and Energy ($E$) dispersive detector telescopes has recently been attracting increasing interest for elemental profiling of light and medium heavy elements with atomic mass up to about 120 [1–7]. Unlike the case for RBS (Rutherford Backscattering Spectrometry) where the signals from the different elements are superimposed in the energy spectra, the distribution in the ToF–$E$ plane in principle allows the depth distributions for the different constituent isotopes to be uniquely determined. Rather than analysing directly the data distribution in the ToF–$E$ histograms, the data can be transformed to mass–energy ($M$–$E$) histograms [2] (see Fig. 1) using different transformation procedures [7–9]. In cases for $A \lesssim 30$, the isotope signals are well separated and separation is simple. In other cases, such as for the important material GaAs with naturally occurring isotopes $^{69}$Ga, $^{71}$Ga and $^{75}$As, the signals from different isotopes lie so close together that they are not completely separated (Fig. 1). Special procedures

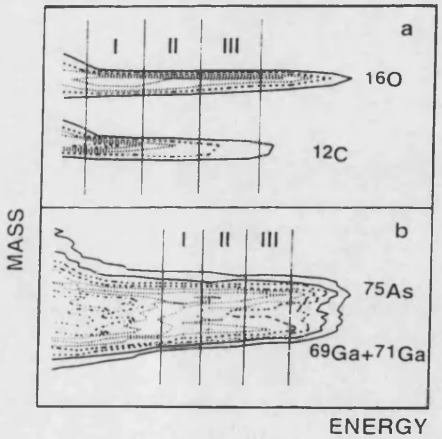


Fig. 1. Mass–energy contour plot of (a) $^{12}$C and $^{16}$O (b) $^{69}$Ga and $^{71}$Ga and $^{75}$As. The mass transformation has been carried out using the procedure of El Bouanani et al. [9].

* Corresponding author. Tel. +46 46 2227682, fax +46 46 2224709, E-mail: mohamed.el_bouanani@nuclear.lu.se.

[1] Present address: CEC–JRC, IRMM, Retieseweg, B-2440 Geel, Belgium.

[2] Here the isotopic mass that enters as a parameter in the equations is denoted by $A$, whilst the mass determined by the recoil telescope is denoted by $M$.


*SSDI* 0168-583X(95)00270-7

have been developed to handle such cases in which a mass slice for each element of interest is carefully selected so as to minimise the cross talk from the other elements [8]. These slice selection procedures are somewhat tedious and could be simplified through the use of a simple function that describes the mass broadening as a function of recoil energy $E$, and mass, $A$. One step in this direction was taken by El Bouanani et al. [9] who developed a method to remove the distortions of the distributions associated with nonlinearities in the silicon energy detector response. This results in straight mass lines in $M$–$E$ histograms and accurate mass and energy calibrations.

An attractive approach in the process of extracting quantitative depth information from a measurement would be to refine the depth distribution functions for the individual isotopes by comparing the calculated two dimensional recoil energy and mass distributions directly with the histograms of the experimental data. This requires the convolution of the calculated isotope energy distributions with the mass instrument function that describes the mass broadening of the detector telescope.

Knowledge of the mass broadening of ToF–$E$ detector telescopes will also be important for experiments at the CHICSI (Celsius Heavy Ion Collaboration SIlicon detector array) facility, that is presently under construction. In these experiments recoiling target fragments, from intermediate energy heavy ion collisions, will be detected using a ToF–$E$ detector telescope array. This will take advantage of the combination of extremely thin ($\sim 10^{13}$ at.cm$^{-2}$) gas jet targets with an intense circulating ion beam. Coincident detection of these fragments, which have been inaccesible for electronic detectors, will add considerably to the information about the reaction dynamics that can be gleaned from measurements of light particle distributions.

The objective of this study is to suggest a simple empirical formula, based on data using 77 and 91 MeV $^{127}$I projectiles, that describes the mass broadening of ToF–$E$ recoil telescopes for the purposes above.

## 2. Experimental

The recoil spectrometry measurements were performed using the "ANTARES" FN tandem accelerator at Lucas Heights Research Laboratories. 77 MeV $^{127}I^{10+}$ and 91 MeV $^{127}$I ions were employed as projectiles. The angle of incidence and exit were 60° and 75°, respectively, relative to the sample surface normal. The recoils (and scattered projectiles) were detected using a ToF–$E$ detector telescope at an angle of 45° to the incident beam direction. The detector system consists of two time detectors in which the secondary electrons, which are ejected when recoils pass through thin ($\sim 5$ μg/cm$^2$) carbon foils, are detected using multichannel plates. The flight length was 437.5 mm for these measurements. The silicon energy detector was a 100 mm$^2$ ion-implanted type [10] and located 25 mm behind the carbon foil of the second time detector. Details concerning the detection system are presented in Refs. [1,4,6]. The measurements at 77 and 91 MeV were made without changes to the settings of the detector telescope electronics.

The results presented here were obtained from the analysis of a variety of reference samples. The mass resolution was determined as a function of energy for the following isotopes: $^{12}$C, $^{16}$O, $^{27}$Al, $^{31}$P, $^{40}$Ca, $^{59}$Co, $^{69}$Ga, $^{92}$Mo, $^{127}$I and $^{197}$Au. The ToF–$E$ data for $^{12}$C, $^{16}$O and $^{69}$Ga were determined from analyses using 91 MeV $^{127}$I as projectiles whilst the others were determined from analysis using 77 MeV $^{127}$I. Isotopes with signals that were free of interference were mainly employed. The only exceptions were $^{92}$Mo and $^{69}$Ga.

## 3. Data evaluation

The ToF data was transformed to mass–energy histograms using the multivariate analysis procedure developed by El Bouanani et al. [9]. Fig. 1 shows the resulting $M$–$E$ contour plots of $^{12}$C, $^{16}$O and $^{69}$Ga, $^{71}$Ga, $^{75}$As. It is evident that the data lie along straight mass lines. The mass broadening was characterised by fitting Gaussian functions using a maximum likelihood method to the mass distribution for narrow energy slices (Fig. 2). In the case of elements with a single naturally occurring isotope a single Gaussian was used. The experimental data and typical fits for $^{12}$C and $^{16}$O are presented in Fig. 2. In the case of multi-isotope targets (GaAs and Mo), the fitted function was the sum of a number of Gaussians with an area that corresponded to the natural abundance and a position that corresponded to the known isotopic mass. Fig. 3 illustrates typical fits for $^{69}$Ga, $^{71}$Ga and $^{75}$As in GaAs. Inspection of Fig. 2 shows that the mass spreading is well described by a Gaussian broadening $\sigma$, which depends both on recoil mass and energy.

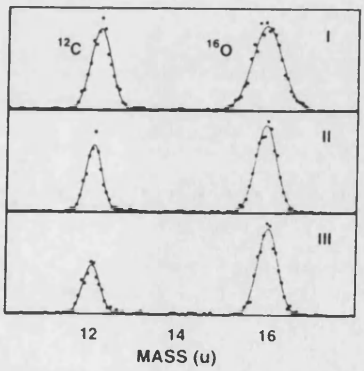


Fig. 2. Projection onto the mass axis of $^{12}$C and $^{16}$O from the energy intervals I, II and III in Fig. 1a). The data have been fitted with Gaussians.

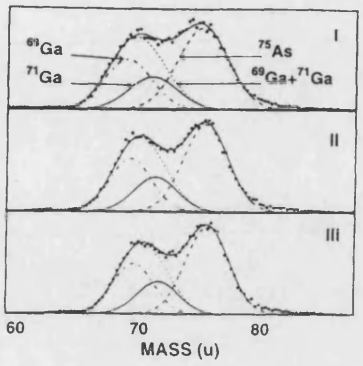


Fig. 3. Projection onto the mass axis of $^{69}$Ga and $^{71}$Ga and $^{75}$As from the energy intervals I, II and III in Fig. 1b. The fitting function is the sum of the three Gaussian distributions that are shown.

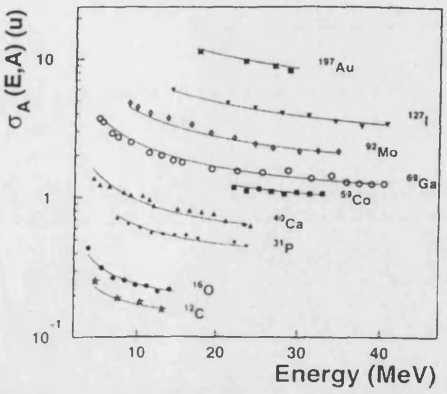


Fig. 4. $\sigma_A(E,A)$ versus energy $E$ for various recoil isotopes. The lines indicate the best fit for Eq. (5).

## 4. Results

The mass assignment in ToF–$E$ recoil spectrometry is realized using the non-relativistic relation according to:

$$M = 2E(T/L)^2. \tag{1}$$

The uncertainty in the mass assignment from Eq. (1) can be written as:

$$\delta M = M\left(\frac{\delta E}{E} + 2\frac{\delta T}{T} + 2\frac{\delta L}{L}\right). \tag{2}$$

From Whitlow et al. [11] the contributions associated with the flight length determination becomes significant for fast recoils (i.e. low mass and high energy recoils). They are very small in other cases and can be neglected. The dominant contributions in Eq. (2) are associated with the contribution to $\delta E$ from the energy detector resolution and to $\delta T$ from the time detector resolution.

Modelling of the energy detector resolution contribution in Eq. (2) was based on Amsel et al.'s [12] simple empirical expression:

$$\delta E_{\mathrm{det}} = a + bE^{1/3}. \tag{3}$$

This expression for intrinsic energy resolution $\delta E_{\mathrm{det}}$ fits the SSBD detectors data of Hinrichsen et al. [13] well. It has been shown also [14] that PIN photodiodes and conventional SSBD detectors have comparable energy resolutions.

By neglecting the contribution associated with the timed flight length and considering $\delta T$ constant, Eq. (2) can be expressed as:

$$\delta M = M(aE^{-1} + bE^{-2/3}) + cM^{1/2}E^{1/2}. \tag{4}$$

In fact the parameters $a$, $b$ and $c$ are mass dependent. These considerations simplified identification of the final form of the empirical fitting function for the standard deviation of the Gaussian:

$$\sigma_A(E,A) = C_1 + C_2A^{3/2}E^{-1} + C_3A^2E^{-2/3} + C_4AE^{1/2}, \tag{5}$$

where the fitted constants $C_1$, $C_2$, $C_3$ and $C_4$ are $5.01 \times 10^{-2}$, $7.63 \times 10^{-3}$, $1{,}69 \times 10^{-3}$ and $9.65 \times 10^{-4}$, respectively, when the units of $A$ and $\sigma$ are u and $E$ is in MeV. The $E^{-1}$ and $E^{-2/3}$ terms in Eq. (5) are associated with the energy detector resolution whilst the $E^{1/2}$ term is associated with the contribution from the time detector resolution. Fig. 4 shows the measured values of $\sigma_A(E,A)$ together with the fitted function (Eq. (5)). Inspection of Fig. 5 which shows the $\sigma_A(A,E)$ surface, reveals that the function is smooth without local minima or maxima. Strictly, Eq. (5) is valid only over the limited range of energies encountered in our experiments (indicated by the data points in Fig. 4).

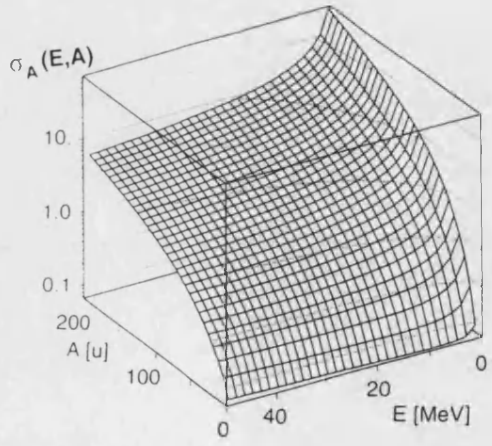


Fig. 5. Surface plot of the $\sigma_A(E,A)$ function (Eq. (5)).

## 5. Conclusions

(i) The broadening of the mass distributions in mass and energy dispersive recoil spectrometry using a ToF–$E$ detector telescope is well described using a Gaussian distribution.

(ii) The standard deviation of the Gaussian distribution is well described by Eq. (5) over the isotopic mass region $A = 12$–$197$. Eq. (5) should be generally applicable to all ToF–$E$ recoil telescopes over mass and energy ranges similar to those employed here, i.e. where the principal contributions to $\sigma$ are associated with the energy and time detector resolutions for heavy recoils and time detector resolution for fast light recoils.

## Acknowledgements

The authors would like to express their gratitude to the ANSTO staff who work on the ANTARES facility for their help. Also the support of the Australian Institute of Nuclear Science and Engineering (AINSE) and its staff, the Australian Department of Industry, Technology and Commerce (DITAC) are gratefully acknowledged. The Swedish authors would also like to acknowledge the Swedish Institute (SI), the Crafoord Foundation, the Royal Swedish Academy of Sciences (especially Letterstedt's resestipendiefond) and Carl Trygger's Foundation for financial support.

## References

[1] H.J. Whitlow, in: Proc. High Energy and Heavy Ion Beams in Materials Analysis, Albuquerque, 1989, eds. J.R. Tesmer, C.J. Maggiore, M. Nastasi, J.C. Barbour and J.W. Mayer (Materials Research Soc., Pittsburgh, PA, 1990) p. 73.

[2] E. Arai, H. Funaki, M. Katayama and K. Shimizu, Nucl. Instr. and Meth. B 68 (1992) 202.

[3] P. Goppelt, B. Gebauer, D. Fink, M. Wilpert, Th. Wilpert and W. Bohne, Nucl. Instr. and Meth. B 68 (1992) 235.

[4] H.J. Whitlow, G. Possnert and C.S. Petersson, Nucl. Instr. and Meth. B 27 (1987) 448.

[5] J.P. Thomas, M. Fallavier and A. Ziani, Nucl. Instr. and Meth. B 15 (1986) 443.

[6] M. Hult, H.J. Whitlow, M. Östling, C. Zaring, D.D. Cohen, N. Dytlewski, P.N. Johnston and S.R. Walker, Nucl. Instr. and Meth. B 85 (1994) 916.

[7] M. Hult, H.J. Whitlow, M. Östling, M. Andersson, Y. Andersson, I. Lindeberg and Kenny Ståhl, J. Appl. Phys. 75 (1994) 835.

[8] M. Hult, H.J. Whitlow and M. Östling, Appl. Phys. Lett 60 (1992) 219.

[9] M. El Bouanani, M. Hult, L. Persson, E. Swietlicki, M. Andersson, M. Östling, N. Lundberg, C. Zaring, D.D. Cohen, N. Dytlewski, P.N. Johnston, S.R. Walker and H.J. Whitlow. Nucl. Instr. and Meth. B 94 (1994) 530.

[10] M. Lindroos and Ö. Skeppstedt, Nucl. Instr. and Meth. A 306 (1991) 225.

[11] H.J. Whitlow, B. Jakobsson, L. Westerberg, Nucl. Instr. and Meth. A 310 (1991) 636.

[12] G. Amsel, C. Cohen and A. L'Hoir, in: Ion Beam Surface Layer Analysis vol. 2, O. Meyer, G. Linker and F. Kappeler, eds. (Plenum, New York, 1976).

[13] P.F. Hinrichsen, D.W. Hetherington, S.C. Gujrathi and L. Cliche, Nucl. Instr. and Meth. B 45 (1990) 275.

[14] S.C. Gujrathi, D.W. Hetherington, P.F. Hinrichsen and M. Bentourkia, Nucl. Instr. and Meth. B 45 (1990) 260.

# High-resolution recoil spectrometry for separate characterization of Ga and As in $Al_xGa_{(1-x)}As$ structures

Mikael Hult and Harry J. Whitlow
*Lund Institute of Technology, Department of Nuclear Physics, Sölvegatan 14, S-223 62 Lund, Sweden*

Mikael Östling
*Royal Institute of Technology, Department of Solid State Electronics, Box 1298, S-164 28 Kista, Sweden*

(Received 7 October 1991; accepted for publication 25 October 1991)

Mass and energy-dispersive recoil spectrometry, where the recoil energy is derived from the recoil time of flight, has been used to characterize the depth distribution of Al, Ga, and As in an $Al_xGa_{(1-x)}As$ quantum-well structure. Signals characterizing the Al, Ga, and As distribution with good separation between Ga and As (average crosstalk $<2\%$) could be obtained from depths less than 560 nm from the surface. The depth resolution of the As signal at the surface was 16 nm FWHM, which is considerably better than achieved using a silicon particle detector (34 nm).

Rutherford backscattering spectrometry (RBS) has over the past few decades proved to be an invaluable tool in microelectronic processing technology for quantitative elemental analysis and depth profiling. RBS has, however, found rather limited application in GaAs technology because of the poor mass resolution for the naturally occurring medium heavy isotopes $^{69}Ga$, $^{71}Ga$, and $^{75}As$. Moreover, the backscattering signals from light and medium heavy elements are often superimposed on a large background signal from the GaAs substrate. Recent developments in high-energy backscattering[1–5] have led to separation of As down to 40–150 nm from the surface, but the problem of superposition of signals from light and medium heavy elements remains.

The objective here is to demonstrate that recoil spectrometry, using a telescope instrumented for measurement of recoil energy and time of flight (TOF),[6–9] may be used to separately characterize depth distributions of Ga and As, as well as other elements, in GaAs structures down to depths of about 0.5 $\mu$m.

The experimental setup[6,7,10] was a glancing incidence/exit configuration where the ion beam impinged and the recoils exited at 67.5° to the sample surface normal. The detector telescope subtended a solid angle of 0.08 msr at 45° to the incident beam direction. The TOF was measured over a 738-mm flight path and the energy determined with a 100-mm$^2$ ion-implanted Si detector (SiTek[11]). The tandem accelerator at the Svedberg Laboratory in Uppsala was used to produce a 64-MeV $^{127}I^{11+}$ ion beam. These ions were chosen in preference to $^{81}Br^{8+}$, used previously, in order to avoid interference from scattered projectiles in the 75-u mass region (see Fig. 4 in Ref. 10).

The experimental TOF-energy data for each detected recoil was sorted off-line to derive a two-dimensional mass-versus-energy distribution. The mass, $M$, was derived from the energy, $E$, and TOF, $T$, according to $M=(T-T_0)^2(2E/L^2)$, where $T_0$ is an adjustable constant which is selected[6,10] to take care of electronic delays, etc. Figure 1 shows the two-dimensional recoil mass-energy distribution for an $Al_xGa_{(1-x)}As$ quantum-well structure. The $^{27}Al$, $^{69-71}Ga$, and $^{75}As$ signals can be clearly seen, as well as $^{16}O$ and $^{12}C$, which are primarily associated with the surface layer. The energy distribution of recoils for a particular isotope can be interpreted in a similar manner to RBS spectra by considering it to be the "RBS signal" from the isotope in question.[6,7,9]

The mass spectrum in the Ga-As region is presented in Fig. 2 for a Co-Ga-As reference sample measured under identical conditions to the data of Fig. 1. The data in Fig. 2 were obtained by integrating the two-dimensional mass-energy distribution over an energy range of 11.7–30 MeV, which corresponds to a depth interval extending down 500 nm below the surface in GaAs. A function consisting of a sum of three Gaussians was fitted to the data. The area and relative position of two of the Gaussians corresponded to the relative natural abundance and mass difference of $^{69}Ga$ and $^{71}Ga$, while the third corresponded to $^{75}As$. The Ga and As areas, positions, and widths were free parameters in the fitting. On the basis of the fit indicated in Fig. 2, the mass windows for Ga and As were chosen. These windows are marked by hatching in Fig. 2 and cover 83% and 74% of the Ga and As areas, respectively, with less than 2%

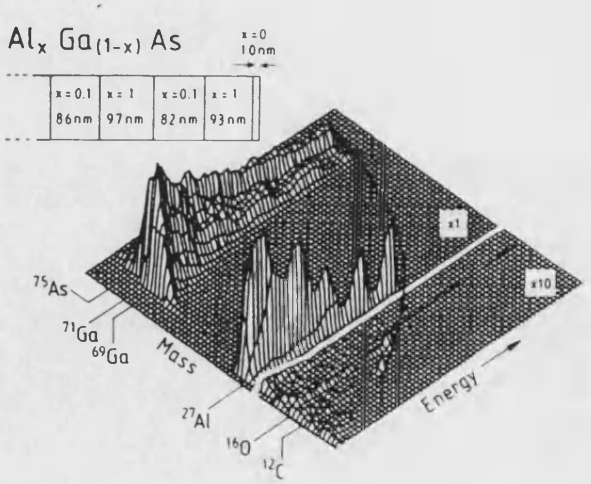


FIG. 1. Two-dimensional mass-energy distribution for an $Al_xGa_{(1-x)}As$ quantum-well structure. The solid line indicates the surface of the sample.

 0003-6951/92/020219-03$03.00  

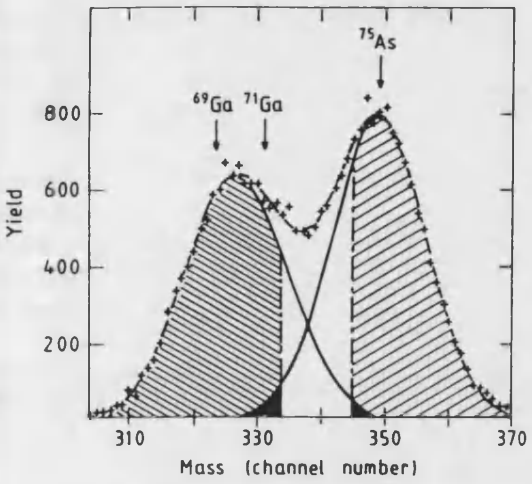


FIG. 2. Recoil mass distribution from a Co-Ga-As reference sample for 11.7–30-MeV recoils (0–500-nm depth in GaAs). The contributions from Ga and As have been determined by decomposition into three Gaussians. The hatches indicate the two mass windows and the crosstalk contributions are marked in black.

crosstalk (indicated in black). The fitted function describes well the low- and high-mass flanks of the Ga and As peaks, respectively (where influence from the other element is minimal) (Fig. 2). Thus the assumption of a Gaussian shape is not anticipated to significantly affect this estimate of crosstalk. The effect of small variations in the position and width[10] of the isotope peaks with recoil energy was checked by sorting the data to yield mass spectra for small recoil energy slices. The crosstalk, determined using the procedure above, increased with decreasing recoil energy (greater depth) from $<0.5\%$ at the surface to $<2\%$ and $<4.5\%$ for Ga and As, respectively, at a depth corresponding to 500 nm in GaAs.

The data from Fig. 1 was then sorted using the mass windows for Ga and As indicated in Fig. 2 to yield TOF distributions for $^{27}$Al, $^{69-71}$Ga, and $^{75}$As recoils. These TOF distributions were subsequently transformed to energy distributions using the procedure of Mendenhall and Weller,[12,13] with assumed masses of 27.0, 69.8, and 75.0 u for Al, Ga, and As, respectively. The resulting energy spectra were converted to equal channel-width energy spectra using linear interpolation. The recoil TOF was used to define the energy, rather than the silicon particle detector signal, because of the superior energy resolution attainable.[14,15] Figure 3 shows the recoil energy distributions derived from the TOF distribution for Al, Ga, and As. The oscillations in the Al and Ga signals corresponding to the depth distribution of these elements in the quantum-well structure can be clearly seen, whilst the As signal is characteristic of a homogeneous depth distribution. The energy resolution of the As surface edge in Fig. 3(c) is 0.6 MeV FWHM, which corresponds to a depth resolution of 16 nm FWHM in GaAs. The corresponding energy resolution for the silicon detector is 1.3 MeV FWHM. The energy resolution of the TOF-E detector telescope can be improved by increasing the timed flight length[10] up to a limit set by the effects of straggling and thickness variations in the foil of the first time detector.[10] This constitutes a significant advantage over $\Delta E$-$E$ detector telescopes,[16,17] where the resolution cannot easily be improved.

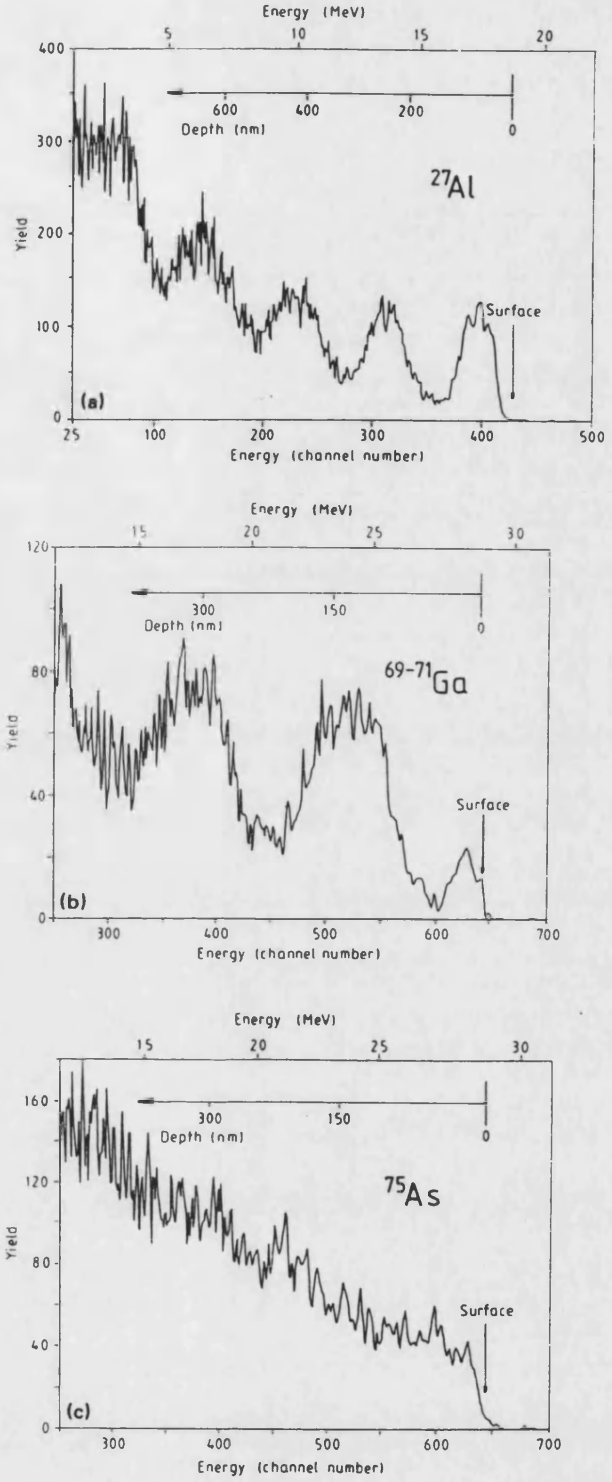


FIG. 3. Energy distributions from the data in Fig. 1, where the energy has been calculated using the recoil time of flight, for (a) Al, (b) Ga, and (c) As. The depth scale is derived from the known structure of the sample.

The depth of separation is governed by the fraction of Ga, As, and respective crosstalk spanned by the mass windows. This may be extended deeper at the expense of efficiency than the present 0.5 $\mu$m, which is 2–5 times greater than has been achieved with heavy-ion RBS.[3,5] Further-

more, even for thick samples, the Ga signal, and those of lighter elements, is almost completely free of background from As and heavier elements. The technique is not influenced by the chemical- and sputter-induced artifacts associated with sputter-Auger or secondary-ion mass spectrometry (SIMS). This opens new possibilities for direct measurement of the thickness and stoichiometry of III-V/GaAs quantum-well structures, which are inaccessible with RBS, as well as directly following solid-state reactions in GaAs structures.

Gunnar Landgren is kindly thanked for supplying the quantum-well structure. We are grateful to the Swedish National Board for Technical Development (STU-F) for financial support.

[1] A. Chevarier and N. Chevarier, Nucl. Instrum. Methods **218**, 1 (1983).
[2] M. R. Weller, M. H. Mendenhall, P. C. Haubert, M. Döbeli, and T. A. Tombrello, in *Proceedings of High Energy and Heavy Ion Beams in Materials Analysis*, Albuquerque, 1989, edited by J. R. Tesmer, C. J. Maggiore, M. Nastasi, J. C. Barbour, and J. W. Mayer (Materials Research Society, Pittsburgh, PA, 1990), p. 139.
[3] M. Östling and C. S. Petersson, Nucl. Instrum. Methods B **4**, 88 (1984).
[4] M. Döbeli, P. C. Haubert, R. P. Livi, S. J. Spicklemire, D. L. Weathers, and T. A. Tombrello, Nucl. Instrum. Methods B **56/57**, 764 (1991).
[5] M. Döbeli, P. C. Haubert, T. A. Tombrello, J. -I. Chyi, D. Huang, and H. Morkoç, Nucl. Instrum. Methods B **52**, 72 (1990).
[6] H. J. Whitlow, G. Possnert, and C. S. Petersson, Nucl. Instrum. Methods B **27**, 448 (1987). [There is an error in Eq. (2) of this paper, it should be replaced by Eq. (2) in Ref. 17.]
[7] H. J. Whitlow, A. B. Ch. Andersson, and C. S. Petersson, Nucl. Instrum. Methods B **36**, 53 (1989).
[8] J. P. Thomas, M. Fallavier, and A. Ziani, Nucl. Instrum. Methods B **15**, 443 (1986).
[9] H. J. Whitlow, in *Proceedings of High Energy and Heavy Ion Beams in Materials Analysis*, Albuquerque, 1989, edited by J. R. Tesmer, C. J. Maggiore, M. Nastasi, J. C. Barbour, and J. W. Mayer (Materials Research Society, Pittsburgh, PA, 1990), p. 73.
[10] H. J. Whitlow, B. Jacobsson, and L. Westerberg, Nucl. Instrum. Methods A (In press).
[11] M. Lindroos and Ö. Skeppstedt, Nucl. Instrum. Methods A **306**, 225 (1991).
[12] M. H. Mendenhall and R. A. Weller, Nucl. Instrum. Methods B **40/41**, 1239 (1989).
[13] M. H. Mendenhall and R. A. Weller, Nucl. Instrum. Methods B **47**, 193 (1990).
[14] M. Östling, C. S. Petersson, P. Johansson, A. Wikström, and G. Possnert, Nucl. Instrum. Methods B **15**, 729 (1986).
[15] H. J. Whitlow, in *Proceedings of High Energy and Heavy Ion Beams in Materials Analysis*, Albuquerque, 1989, edited by J. R. Tesmer, C. J. Maggiore, M. Nastasi, J. C. Barbour, and J. W. Mayer (Materials Research Society, Pittsburgh, PA, 1990), p. 243.
[16] J. P. Stoquert, G. Guillaume, M. Hage-Ali, J. J. Grob, C. Ganter, and P. Siffert, Nucl. Instrum. Methods B **44**, 184 (1989).
[17] A. M. Behrooz, R. L. Headrick, L. E. Seiberling, and R. W. Zurmühle, Nucl. Instrum. Methods B **28**, 108 (1987).

# Rapid thermal annealing induced reactions of Co/GaAs thin film structures: Studies using mass and energy dispersive recoil spectrometry

Mikael Hult and Harry J. Whitlow
*Lund Institute of Technology, Department of Nuclear Physics, Sölvegatan 14, S-223 62 Lund, Sweden*

Mikael Östling
*Royal Institute of Technology, Department of Solid State Electronics, Box 1298, S-164 28 Kista, Sweden*

Margareta Andersson, Yvonne Andersson, and Ingrid Lindeberg
*Uppsala University, Department of Inorganic Chemistry, Box 531, S-751 21 Uppsala, Sweden*

Kenny Ståhl
*Lund Institute of Technology, Department of Inorganic Chemistry, S-223 62 Lund, Sweden*

(Received 14 May 1993; accepted for publication 4 October 1993)

GaAs samples with a 100-nm-Co overlayer that had been subjected to rapid thermal annealing for 60 s at temperatures of 400–650 °C were analyzed using mass and energy dispersive recoil spectrometry. Separate characterizations of C, O, Co, Ga, and As depth distributions were performed. Both Ga and As had migrated to the surface at anneal temperatures higher than 450 °C. In a sample annealed at 650 °C, a clear enrichment of Ga in the outer 35 nm was observed. The composition for various depth intervals was determined for different temperatures. From Arrhenius plots, apparent activation energies were estimated to be about 0.6 eV for phase formation and 1.3 eV for diffusion. X-ray diffraction indicated that CoGa and CoAs phases were present in all the annealed samples. Scanning electron microscopy showed the surface to be reticulated after heat treatment, with grain growth at higher temperatures.

## I. INTRODUCTION

The development of GaAs technology is a field of research that has been the subject of much study. Considerable effort has been directed at clarifying the processes of interdiffusion and compound formation in metal-GaAs interfaces. In order to manufacture fast and reliable GaAs devices and complex optoelectronic components, stable electrical contacts are of utmost importance. The Co-Ga-As system is not fully understood but constitutes a highly interesting system, one which might be employed in various applications. In the literature[1,2] it has been suggested that the Co-Ga-As system exhibits a ternary phase ($Co_2GaAs$) which decomposes at temperatures higher than 400 °C. In addition, Lindeberg and Andersson[3] showed the presence of another ternary phase ($Co_3Ga_{0.5}As_{1.5}$) at 800 °C, one that has not been observed at 600 °C.[4] It is unclear at which temperature the reaction between Co and GaAs begins, although Shiau *et al.*[5] have reported observing a reacted layer at 260 °C after 2 h annealing, and Genut and Eizenberg[1] reported detecting an interfacial reaction after 30 min annealing at 325 °C. The objective of this investigation was to study the Co/GaAs reactions under the more extreme conditions of rapid thermal annealing (RTA).

Different techniques like Rutherford backscattering spectrometry (RBS) and Auger electron spectroscopy (AES) have been reported to give fruitful results in investigations of elemental depth distributions in Co-GaAs samples[1,2,4–9]. In this study mass and energy dispersive recoil spectrometry (RS) has been employed in order to separately characterize Co, Ga, and As in samples that have been exposed to RTA at temperatures of 400–650 °C. This way of measuring the depth profiles yields results similar to but considerably less ambiguous than RBS. It is particularly useful for the case of thin Co films on GaAs where overlapping signals in the RBS analysis can introduce artifacts in the evaluation despite the use of sophisticated computer fitting programs.

The phases formed in the thin film were also characterized by x-ray diffraction (XRD) to identify the chemical compound formed and by scanning electron microscopy (SEM) to characterize the development of the surface morphology.

## II. MATERIALS AND METHODS

### A. Sample preparation

The samples were fabricated using single-crystalline GaAs substrates oriented in the ⟨111⟩ direction. Layers of 100 nm of cobalt were deposited onto the samples using electron beam evaporation. The pressure during deposition was kept below $5\times10^{-6}$ mbar, and the deposition rate was about 0.5 nm/s. The heat treatments were performed in a rapid thermal annealing unit. The temperature rise to $T$ ($T$ =400, 450, 500, 550, 600, and 650 °C) occurred in approximately 2 s and was kept at $T$ for 1 min. The atmosphere was composed of 90% Ar and 10% $H_2$.

### B. The x-ray diffraction measurement

Data were collected using an INEL powder diffractometer equipped with a position sensitive gas detector

 0021-8979/94/75(2)/835/9/$6.00  

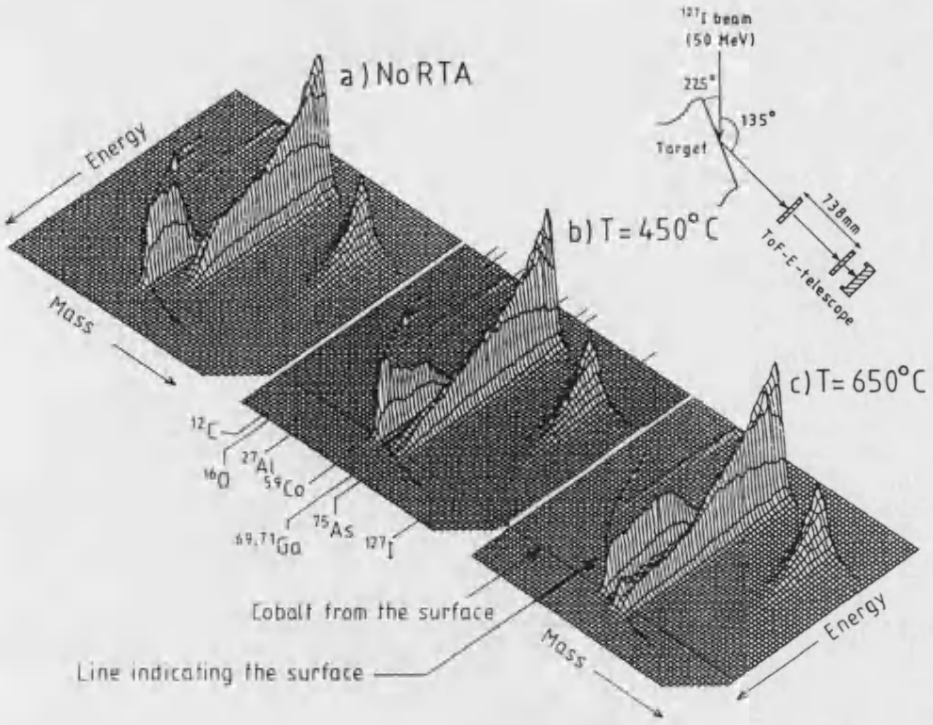


FIG. 1. Three-dimensional mass energy plots from three samples: (a) reference sample, (b) RTA at 450 °C, and (c) RTA at 650 °C.

(CPS120) covering 120°. The samples were mounted on a rotating sample holder in reflection mode with an incident angle of 2°. Each data set was accumulated for 20 h using Cu $K_\alpha$ radiation from a sealed x-ray tube source.

### C. The recoil spectrometry analysis

The measurements were carried out in a scattering chamber with a vacuum better than $10^{-6}$ mbar. The projectile ions were $^{127}I^{9+}$ ions at 50 MeV. Each sample was analyzed for approximately 1 h so that the unsuppressed accumulated charge was some 10 $\mu$C. The angles of incidence and exit were 67.5° relative to the sample surface normal, and the recoils were detected at 45° relative to the incident beam. The detector system, which is described in detail elsewhere,[10–12] consisted of a detector telescope comprised of two carbon foil time detectors and a silicon diode energy detector to detect the recoiling target nuclei's velocity and energy. The time of flight (ToF) length $L$ was 738 mm and the Si-diode energy detector was a 100 mm$^2$ ion-implanted type (SiTek).[13] From the velocity and energy of each nucleus it was possible to calculate the mass and thus to perform separate depth profiling of the elements present in the target. The mass (in channel numbers) was calculated using the formula

$$M = CE(t - t_0)^2, \tag{1}$$

where $E$ and $t$ are the energy and the time analog-to-digital converter (ADC) conversion results, respectively. $C$ is a suitable constant chosen so that the mass scale spans approximately 1000 channels, and $t_0$ is an adjustable parameter to correct for electronic delays, etc. Figure 1 shows some three-dimensional plots of the mass-energy data, where the signals from different isotopes can be distinguished. The iodine signal comes from multiple scattered iodine. Because of the kinematics, single scattered $^{127}$I cannot scatter 45° from $^{75}$As ($\theta_{max}$ for single scattering of $^{127}$I from $^{75}$As = 36.2°). The samples seem to be free from contaminants, although some $^{12}$C and $^{16}$O can be seen at the very surface. The weak $^{27}$Al signal comes from the target holder which has been hit by a small part of the ion-beam.

### D. Spectrum evaluation

Data were collected event-by-event and stored on a file disk for off-line evaluation. The first step in an evaluation is to determine $t_0$ for the different isotopes. This is done by first examining the data on a contour plot with mass and energy axes and adjusting $t_0$ so that the specific isotope lies along a line of constant mass. $t_0$ varies according to isotopes and energies involved, mainly because of the difference in stopping cross section when the isotopes pass through the carbon foils in the "time" detectors. Data for different energy intervals are totaled onto the mass axis, and the peak channel of the Gaussian peak is determined. This channel varies only slightly with energy interval when an acceptable $t_0$ is chosen.

The second step of the data evaluation is to set the proper mass gates for the isotopes. For isotopes that are well separated in mass, this is trivial when a proper $t_0$ value

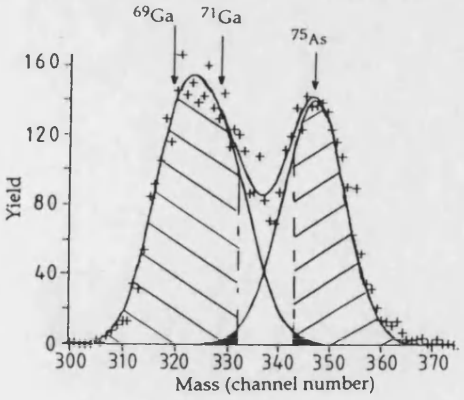


FIG. 2. Recoil mass distribution from the 650 °C sample for energy intervals of 20 to 25 MeV. The contributions from Ga and As have been determined by decomposition into three Gaussians. The hatches indicate the two mass windows. The crosstalk contributions are marked in black.

has been established. In the case of GaAs samples, where the mass separation between Ga and As is small, there is need for a more sophisticated gating procedure.[14] A function of a sum of three Gaussians was fitted to the data. The area and relative position of two of the Gaussians corresponded to the relative natural abundance and mass difference of $^{69}$Ga and $^{71}$Ga, while the third corresponded to $^{75}$As. The Ga and As areas, positions, and widths were free parameters in the fitting. On the basis of the fit indicated in Fig. 2, the mass windows for Ga and As were chosen. These windows are marked by hatching in Fig. 2 and cover 80% and 68% of the Ga and As areas, respectively, with less than 2% crosstalk (indicated in black).

The third step in the data evaluation is usually sorting the data into energy spectra for the different isotopes. Data are sorted using $t_0$ and the mass gates from steps 1 and 2. Subsequently, the energy spectra for Ga and As are corrected for the amount of data that is "gated away." An energy spectrum for an isotope can be interpreted in a similar manner as an RBS spectrum, where the highest energy corresponds to scattering (or recoiling) at the sample surface and hence lower energy corresponds to scattering (or recoiling) some distance below the surface. If different samples are to be directly compared, they have to be normalized. The simplest way of doing this is to normalize to the number of counts in some energy interval deep in the GaAs bulk.

One problem with interpreting an energy spectrum from a silicon surface barrier detector or a photodiode employed as a particle detector is that the pulse height varies between different particles with the same energy. Schmitt *et al.*[15–17] have proposed a semi-empirical formula for fission fragments, whereby the particle energy is linearly related to the channel number and particle mass. This is in good agreement with the detector employed here.[18] Thus, different energy scales have to be established for different isotopes in the analysis. Here we alleviate this problem and at the same time increase the energy resolution by converting the ToF signal into energy, as suggested by Mendenhall and Weller.[19,20] This can be done by first sorting the data for one isotope according to the above described routine and second by performing the time-to-energy conversion according to

$$E = mL^2/(2t^2), \tag{2}$$

where $E$ and $t$ are the energy and ToF of the recoil, respectively, $m$ is the mass of the isotope in question (table value), and $L$ is the flight length. A disadvantage of this procedure is that data are no longer in bins of equal energy width. The data were subsequently rebinned to equal bin width by taking the equidistant bin contents to be the average of the corresponding nonequidistant bin contents. The equidistant bin width was chosen to be greater or equal to the widest nonequidistant bin width. This is a safe procedure that avoids artifacts due to digitization errors associated with the assignment of differing numbers of nonequidistant bins per equidistant bin. The energy scale derived from the ToF is not recoil species dependent because there is a linear relationship between ToF and channel number, independent of the isotope mass.

The stoichiometry within a certain depth can be easily calculated in a manner similar to that of RBS. Thus, the scattering (recoil) cross sections ($\sigma_i$), stopping cross section factors $[(\varepsilon)_i]$, and detector efficiencies ($\beta_i$) for each isotope $i$ need to be determined. The STOP code of Ziegler *et al.*[21] has been employed to calculate the stopping cross sections. The scattering (recoil) cross sections have been considered to be Rutherford cross sections. A ratio between two atomic concentrations, $N_A$ and $N_B$, will thus be as follows

$$\frac{N_A}{N_B} = \frac{A_A \sigma_B (\epsilon)_A^{\text{matrix}} \Delta E_B \beta_B \gamma_A}{A_B \sigma_A (\epsilon)_B^{\text{matrix}} \Delta E_A \beta_A \gamma_B}. \tag{3}$$

$\Delta E_A$ is the energy interval in which the number of counts $A_A$ has been determined for element $A$. $\gamma_A$ is the fraction of the $A$ signal spanned by the mass gates. $(\epsilon)_A^{\text{matrix}}$ is the stopping cross section factor for element $A$ in the matrix in the mean energy approximation.[22] The mean energy for the iodine ions in the depth of interest has been determined using a computer algorithm which calculates the energy loss in small (e.g., 1 nm) slabs and step by step moves into the sample.[22] The detector efficiency $\beta$ is considered to be the same for the three elements Co, Ga, and As, because the stopping power in carbon is large and similar and because many secondary electrons are ejected from the carbon foils when penetrated by all three atomic species.

## III. RESULTS AND DISCUSSION

Figure 3 shows energy spectra for Co, Ga and As in a reference sample and in samples exposed to RTA at three anneal temperatures (450, 500, and 650 °C). The measured energy resolution can be seen in Table I. Figure 3 shows that Ga and As move toward the surface with increasing anneal temperature $T$ and reach the surface at $T = 500$ °C. Above this temperature an increase of the Ga signal in the

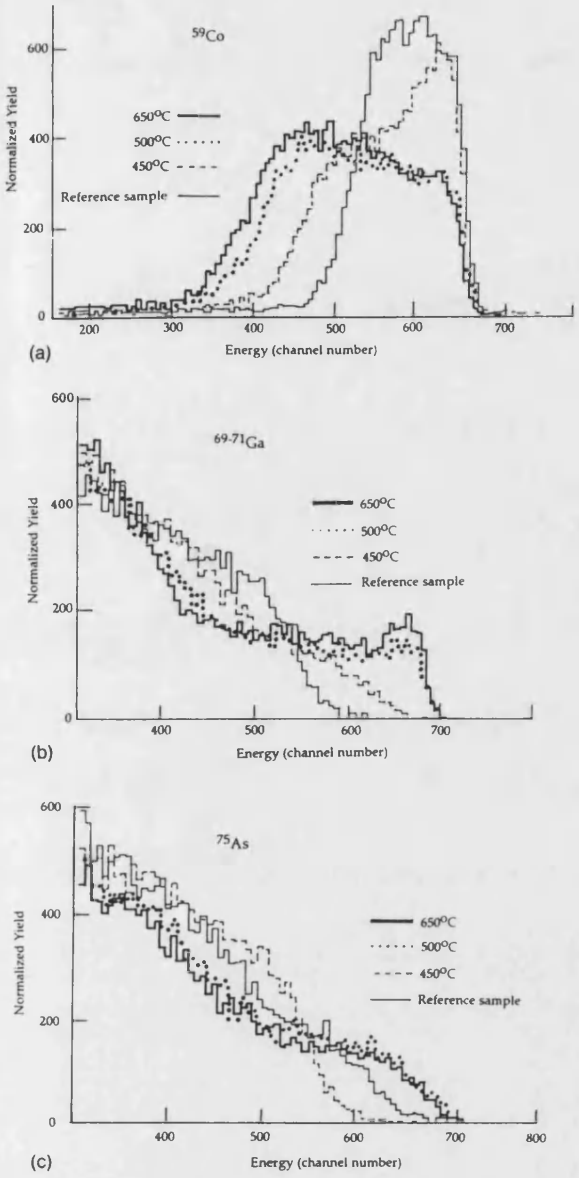


FIG. 3. Energy spectra as determined by the $E$ detector from four samples for (a) Co, (b) Ga, and (c) As.

top 35 nm can be seen. Opposite behavior can be seen for As. (One reason for this may be the higher vapor pressure for As.)

The $^{12}C$ and $^{16}O$ signals can be helpful for understanding the Co-Ga-As system. Both signals showed the same behavior. The oxygen energy spectra are shown in Fig. 4.

TABLE I. Energy detector resolution.

| Element | Energy (MeV) | Resolution (keV) | nm in Co $\rho=8.9$ g cm$^{-3}$ | nm in GaAs $\rho=5.7$ g cm$^{-3}$ |
|---|---|---|---|---|
| Co | 21.7 | 730 | 12 | 23 |
| Ga | 22.9 | 820 | 13 | 24 |

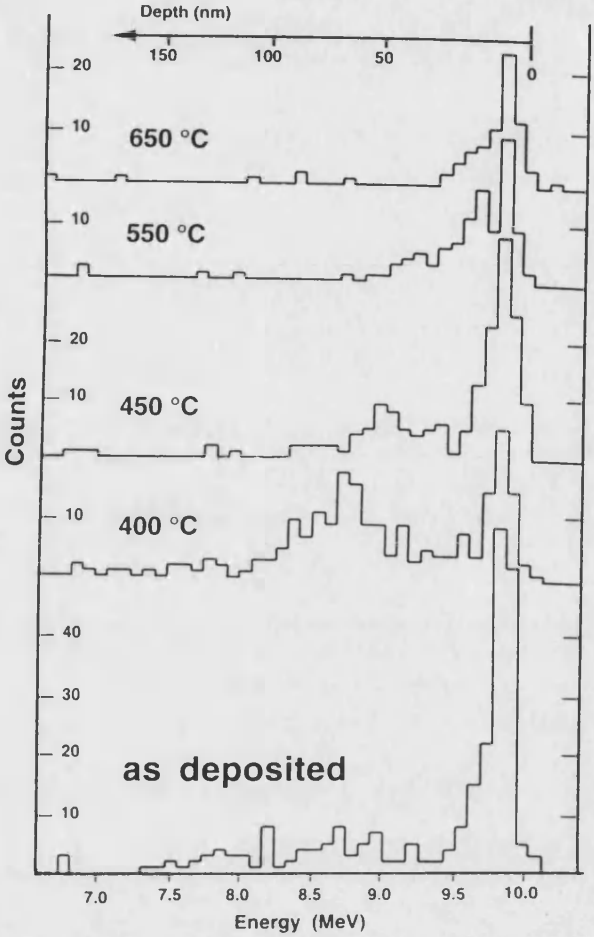


FIG. 4. Energy spectra for $^{16}O$ as determined by the $E$ detector from five samples.

In addition to the surface peak there is a fairly uniform distribution of oxygen within the Co layer in the reference sample, a distribution that moves toward the surface with increasing anneal temperature. This has been suggested[23] to be indicative of a rapid indiffusion of Co. It is not possible here to identify the moving species. Presumably, the outward migration of C and O indicates that phases formed in the reaction have low C and O solid solubilities, leading to C and O exclusion as the reaction progresses.

Figures 5(a)–5(u) show the energy spectra for Co, Ga, and As, where the energy is derived from the ToF signal. The measured resolution at the surface for Co and Ga recoils in GaAs ($\rho=5.7$ g cm$^{-3}$) and Co ($\rho=8.9$ g cm$^{-3}$) is shown in Table II. If the as-deposited Co film is amorphous, the depth resolution will be slightly worse because of the smaller, but less defined, density for amorphous Co ($\sim 7$ g cm$^{-3}$). Since the energy resolution, and hence the depth resolution, is better in Fig. 5 compared to Fig. 3, a more detailed analysis is provided in Fig. 5, where approximate depth scales are also indicated. The Co layer was nominally $100 \pm 5$ nm in the reference sample. The

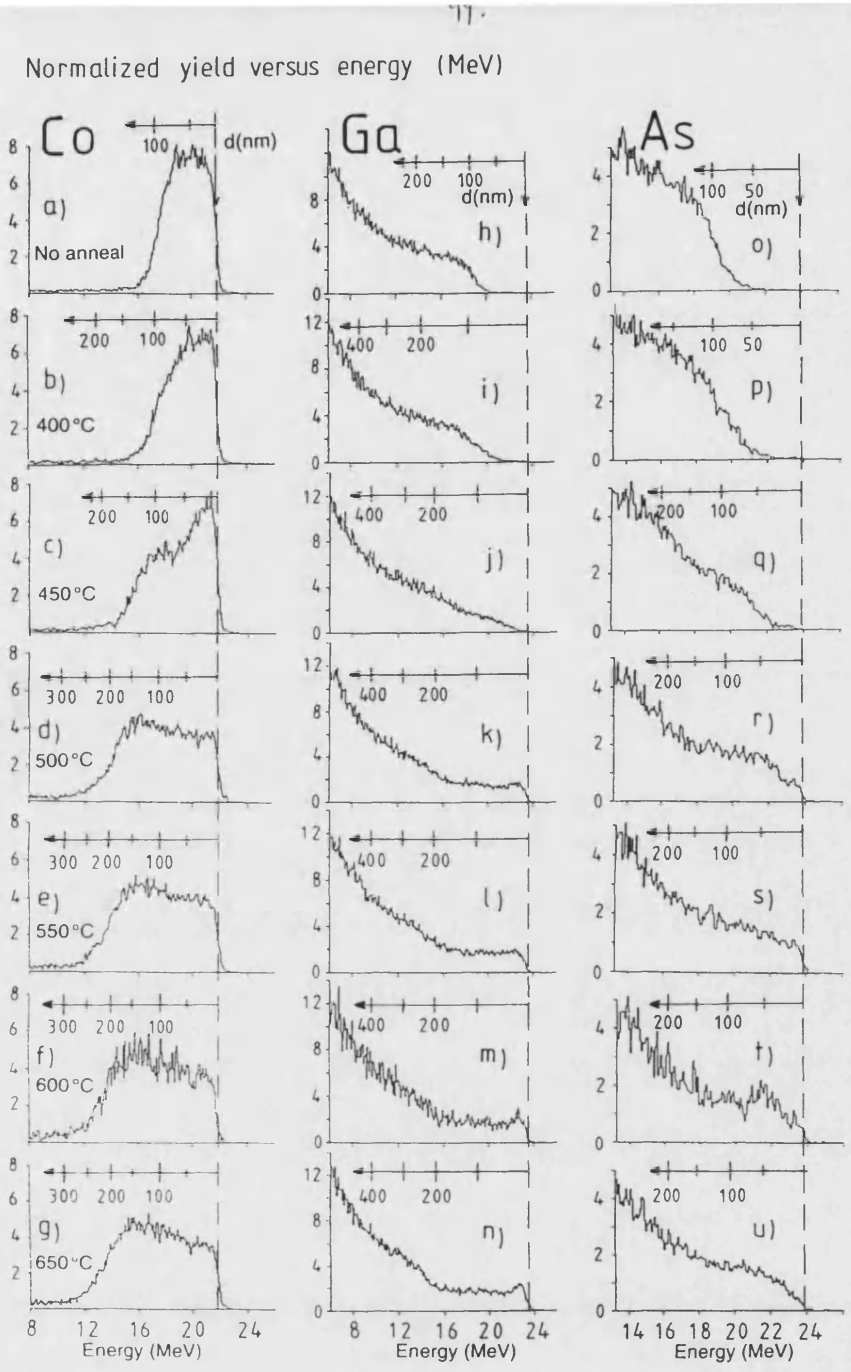


FIG. 5. Energy spectra calculated from ToF data for Co (a–g), Ga (h–n), and As (o–u) from all the samples in the investigation. The energies at the surfaces, which are indicated by the dashed lines, were 21.7, 22.9, and 23.3 MeV for Co, Ga, and As, respectively. In each spectrum there is a scale that gives an indication of the depth $d$ in the sample from which the recoil was scattered.

corresponding thickness of the Co layer determined from the recoil spectrum indicated a density of 7.3 g cm$^{-3}$, which is less than the bulk density of Co (8.9 g cm$^{-3}$) and indicates that the deposited layer may be (at least partly) amorphous.

The width of the interface in the spectrum from the reference sample is degraded from the surface value by

TABLE II. Energy resolution derived from ToF data.

| Element | Energy (MeV) | Resolution (keV) | nm in Co $\rho=8.9$ g cm$^{-3}$ | nm in GaAs $\rho=5.7$ g cm$^{-3}$ |
|---|---|---|---|---|
| Co | 21.7 | 550 | 9 | 16 |
| Ga | 22.9 | 590 | 9 | 17 |

straggling, interdiffusion, and multiple scattering. It can be estimated by calculating the width of the low energy flank of the Co signal. This width was 810 keV, which corresponds to an interval of 18 nm (calculated for a matrix of Co with a density of 7 g/cm$^3$). This strongly indicates that the interface is sharp and that only limited interdiffusion has occurred, if at all.

For the sample annealed at 400 °C [see Figs. 5(b), 5(i) and 5(p)] a short plateau (width: 2160 keV for Co) can be distinguished at 18 MeV for Co. This plateau is more pronounced in the $T_{anneal}=450$ °C spectrum (width: 4740 keV for Co), while in the $T_{anneal}=500$ °C spectrum, it has extended to the surface (width: > 8640 KeV for Co), and the curve indicates a uniform distribution of Co throughout the reacted layer (note that the Rutherford cross section increases with decreasing energy in this energy region). The plateau is clearly seen in the Ga (~17–22 MeV) and As (~18–21 MeV) spectra for temperatures of 500, 550, 600, and 650 °C. The shape of the energy spectra is drastically changed for the low anneal temperatures (400–500 °C). Higher annealing temperatures ( > 500 °C) do not drastically affect the shape of the spectrum for any of the three elements. However, the low energy edge for Co is somewhat broadened and has moved slightly toward lower energies; also an enrichment of Ga in the outer 35 nm is seen.

The previously mentioned plateau suggests the formation of certain phases. Arrhenius plots of the plateau width versus the reciprocal annealing temperature for each element yielded closely similar activation energies for phase formation by interfacial growth, assuming a temperature independent pre-exponential factor: Co: 0.7±0.15 eV (68 kJ/mol), Ga: 0.5±0.15 eV (48 kJ/mol), and As: 0.65 ±0.15 eV (63 kJ/mol). This is defined by two data points in each curve because the plateau extends to the surface at 500 °C and higher. These activation energies are comparable to the values of 0.6–0.7 eV for Co transport and the growth of $Co_2GaAs$ in the temperature range 325–400 °C reported by Genut and Eizenberg.[1] Characterization of our data in terms of the interfacial broadening [i.e., the diffusion length $\sqrt{Dt}$ where $D=D_0\exp(-E_a/kT]$ yielded $E_a$ values of Co: 1.4±0.3 eV, Ga: 1.0±0.4 eV, and As: 1.4 ±0.4 eV. Note that all these activation energies are *apparent* values because there are several reactions taking place rather than a single well defined process.

The stoichiometry has been calculated for three depth intervals, ~15, ~75, ~150 nm, corresponding to the near surface region, the plateau region, and the GaAs near interface region (Fig. 6). The plateau width is very small for the sample annealed at 400 °C but increases with annealing temperature, as does the depth interval for which the composition is calculated. Figure 6(a) shows that Ga and As have reached the surface after heat treatment at temperatures above 500 °C. Moreover, at temperatures of 600 °C or higher, where the "plateau" extends right to the surface, the Ga concentration is enhanced, while the As concentration is depleted. The composition after the 650 °C anneal is $Co_{0.54}Ga_{0.31}As_{0.15}$ in the near surface layer as compared to $Co_{0.57}Ga_{0.23}As_{0.20}$ and $Co_{0.58}Ga_{0.20}As_{0.22}$ for the plateau

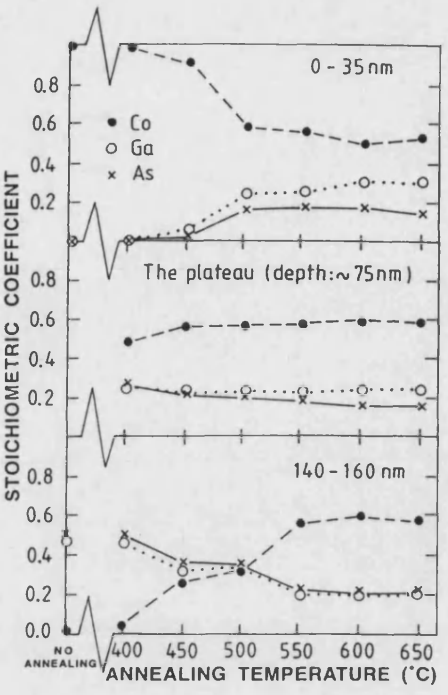


FIG. 6. The stoichiometry of the sample as a function of the anneal temperature for (a) 0–35, (b) the reacted layer (~75), and (c) 140–160 nm.

and bulk region, respectively. This might indicate that Ga out-diffusion is more pronounced than As out-diffusion, as others have reported indications of previously,[5,23] or that As is not strongly bonded in the phases formed and, because of its high vapor pressure, has been lost from the surface.

It is interesting to compare the phases formed as a result of rapid thermal processing of the Co—GaAs thin film couples to the anticipated phases from the ternary phase diagram established for (near) thermodynamic equilibrium conditions. Equilibria ternary phase diagrams for the Co-Ga-As system have been determined, e.g., by Shiau *et al.* at 600 °C (Ref. 4) and Lindeberg and Andersson at 800 °C.[3] In Fig. 7, a ternary phase diagram is shown; it is an estimate (based on Refs. 3 and 4) of the phase diagrams in the temperature interval 400–650 °C. It might be noted that $CoGa_x$ has a composition range in which $x$ lies between 0.32 and 0.59. Furthermore, there exist pseudobinary eutectic regions of $CoGa_x$—CoAs, and Co—$Co_2As$. This results in a complex ternary phase diagram with five two-phase regions (Fig. 7). For Co—GaAs reactions the overall composition will lie along the dotted line (in Fig. 7) extending from Co to GaAs. Moreover, in the thin film couples the Co supply is limited, but the Ga and As supply is almost infinite. The overall composition of the sample will then deviate only slightly from pure GaAs, lying in the three-phase region where pure GaAs, $CoGa_x$ (footpoint $\alpha$, Fig. 7), and a solid solution of $CoGa_x$ in CoAs (footpoint $\beta$, Fig. 7) are in equilibrium. [The footpoint compositions,

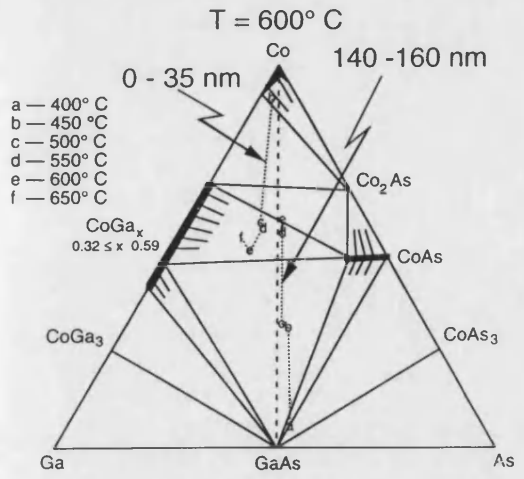


FIG. 7. The 400–650 °C equilibrium ternary phase diagram for the Co-Ga-As system. The composition for various anneal temperatures has been indicated for depth of (a) 140–160 and (b) 0–35 nm.

based on Electron Probe MicroAnalysis (EPMA),[5] correspond approximately to $\alpha$: CoGa (possibly a solid solution with up to 1.5% CoAs)[5] and $\beta$: up to 16.2% CoGa in CoAs.[4,5]]

In Fig. 7 the composition of the surface and a layer originally in the GaAs just below the Co/GaAs interface are plotted. Clearly, as the temperature increases, the composition in both layers approaches a similar final composition. The composition for different temperatures lies close to the dotted line corresponding to equal amounts of Ga and As in the reacted layer, although for the highest temperatures it deviates because of Ga enrichment/As depletion in the surface layer. It is also noteworthy to mention that the composition of the reacted layer, where it extends to the surface ($T_{anneal} \geq 500$ °C) lies within the two-phase region between $CoGa_x$ and CoAs and is always more Co rich than the tie line joining footpoints $\alpha$ and $\beta$ (Fig. 7). Presumably, this indicates that equilibrium has not been reached in the layer during rapid thermal annealing. The path to equilibrium must then go via the pseudobinary system where the $CoGa_x$ phase is more Co rich than the thermodynamic equilibrium case in which Ga As and the less Co rich phases $\alpha$ and $\beta$ are in equilibrium. This is consistent with XRD data (Table III) that indicate the

TABLE III. Possible phases as determined by x-ray diffraction measurement.

| RTA-temperature (°C) | Observed phases in XRD spectrum |
|---|---|
| As-deposited | GaAs, $\alpha$-Co only [2 0 0] |
| 400 | CoAs, CoGa |
| 450 | CoAs, CoGa only [1 1 0] |
| 500 | CoAs, CoGa only [1 1 0], GaAs only [111] |
| 550 | CoAs, CoGa |
| 600 | CoAs |
| 650 | CoAs |

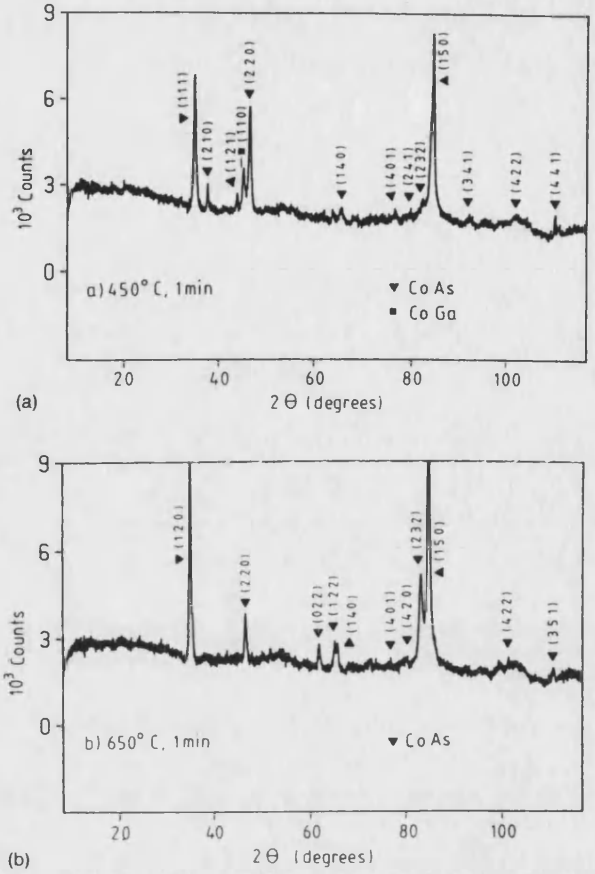


FIG. 8. XRD patterns from the sample annealed (a) at 450 and (b) at 650 °C.

presence of a CoAs phase and a less well defined CoGa phase.

In order to determine the phases present in the different samples, a study using x-ray diffraction was undertaken. Figure 8 presents two of the x-ray diffraction spectra from the 450 and 650 °C heat treatments. The data were difficult to interpret because the reacted layers were probably strained and some of the phases had varying compositions. This resulted in shifting and in broadening of the diffraction lines. The interpretation was further complicated by preferred orientation strongly modifying the relative intensities of the diffraction lines. Assignment of the diffraction line indexes from the different phases (Table III) was thus based solely on interplanar spacing; intensity data were disregarded. In the as-deposited sample only one $\alpha$-Co line could be identified (200) except for the GaAs peaks. This suggests that the as-deposited Co film may be partly amorphous. Except for GaAs, the dominant peaks in the heat treated samples were CoGa and CoAs (Table III). Some differences in these results as compared to others can be associated with differences in the orientation of the substrate.

Genut and Eizenberg described the reaction progress for a 30 min anneal.[1] The present results were highly sim-

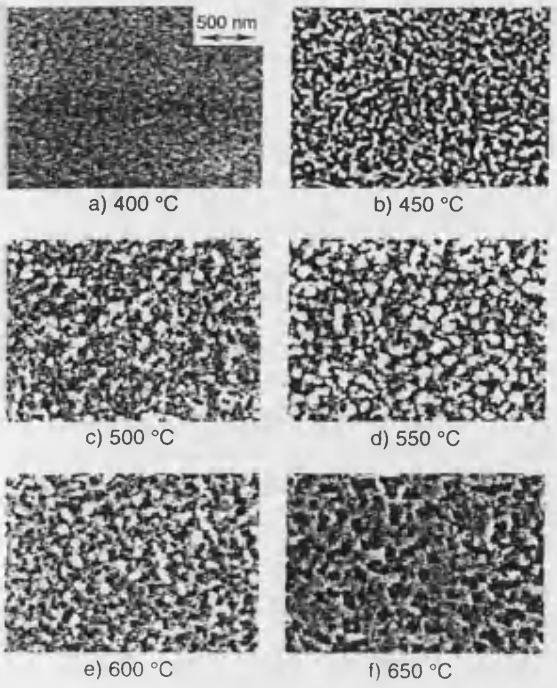


FIG. 9. SEM micrographs of the surface of the samples at (a) 400, (b) 450 (c) 500, (d) 550, (e) 600, and (f) 650 °C.

ilar except for a shift to higher temperatures of about +50 to 100 °C. For example, the spectra of Figs. 5(f), 5(m), and 5(t) (600 °C), together with the XRD results suggest that there is a CoGa layer near the surface and a CoAs layer underneath it. This was seen at 500 °C by Genut and Eizenberg. The difference is most probably due to the difference in annealing time.

The SEM in Fig. 9 shows a weak development of surface topography at 400 °C. At 450 °C and above the surface becomes completely reticulated. This is consistent with the recoil spectra [Figs. 5(j)–5(u)] showing that Ga and As only reach the surface for temperatures of 450 °C and above. Furthermore, the development of significant surface topography strongly suggests that the reaction proceeds via a nucleated growth rather than an interfacial growth mechanism. Inspection of Fig. 9 also shows that grain growth takes place for the higher temperatures. This constitutes further evidence that the film is not in equilibrium after the brief heat treatment and it may be that grain growth is associated with the approach to the equilibrium phase composition.

## IV. CONCLUSIONS

(i) Mass and energy dispersive recoil spectrometry can provide much pertinent information on separate Ga, As, and metal stoichiometric data and activation energies for metal film/GaAs interfacial reactions.

(ii) The reaction of Co overlayer on GaAs under RTA is characterized by complex growth mechanisms that exhibit some characteristics of interfacial growth and some characteristics of nucleated growth, with apparent activation energies of ~0.6 eV for phase formation and 1.3 eV for diffusion.

(iii) At high temperatures (550–650 °C) the Ga concentration relative to the As is enhanced at or near the surface, which may be associated with vertical phase separation and/or As loss due to evaporation.

(iv) The final composition in the reacted layer obtained after annealing for 1 min at least at 500 °C lies in the two-phase pseudobinary solution $CoGa_x$-CoAs region of the ternary equilibrium phase diagram.

(v) The measurements are in broad agreement with previously reported results for slow thermal annealing of the Co/GaAs system.[1,2,23]

## ACKNOWLEDGMENTS

The authors wish to thank the Swedish Board for Technical Development (STU-F) and the Swedish Research Council for Engineering Sciences for financial support. Wim van Berlo from the Swedish Institute of Microelectronics and Kristina Georgsson from the Department of Solid State Physics, Lund Institute of Technology, are kindly thanked for sample preparation and for the electron micrographs. We are also grateful to Professor François d'Heurle for helpful comments on the manuscript.

[1] M. Genut and M. Eizenberg, J. Appl. Phys. **66**, 5456 (1989).
[2] C. J. Palmström, C. C. Chang, A. Yu, G. J. Galvin, and J. W. Mayer, J. Appl. Phys. **62**, 3755 (1987).
[3] I. Lindeberg and Y. Andersson, J. Less-Common Metals **175**, 155 (1991).
[4] F.-Y. Shiau, Y. Zuo, J.-C. Chwen, X.-Y. Zheng, and Y. A. Chang, Z. Metallkd. **80**, 544 (1989).
[5] F.-Y. Shiau, S.-L. Chen, M. Loomans, and Y. A. Chang, J. Mater. Res. **6**, 1532 (1991).
[6] A. J. Yu, G. J. Galvin, C. J. Palmström, and J. W. Mayer, Appl. Phys. Lett. **47**, 934 (1985).
[7] C. J. Palmström, B.-O. Fimland, T. Sands, K. C. Garrison, and R. A. Bartynski, J. Appl. Phys. **62**, 4753 (1989).
[8] K. M. Yu, T. Sands, J. Jaklevic, and E. E. Haller, J. Appl. Phys. **62**, 1815 (1987).
[9] T. Sands, V. G. Keramidas, K. M. Yu, J. Washburn, and K. Krishna, J. Appl. Phys. **62**, 2070 (1987).
[10] H. J. Whitlow, G. Possnert, and C. S. Petersson, Nucl. Instrum. Methods B **27**, 448 (1987).
[11] H. J. Whitlow, A. B. Ch. Andersson, and C. S. Petersson, Nucl. Instrum. Methods B **36**, 53 (1989).
[12] H. J. Whitlow, B. Jakobsson, and L. Westerberg, Nucl. Instrum. Methods A **310**, 636 (1991).
[13] M. Lindroos and Ö. Skeppstedt, Nucl. Instrum. Methods A **306**, 225 (1991).
[14] M. Hult, H. J. Whitlow, and M. Östling, Appl. Phys. Lett. **60**, 219 (1992).
[15] H. W. Schmitt, W. E. Kiker, and C. W. Williams, Phys. Rev. **137**, B 837 (1965).
[16] E. Weissenberger, P. Geltenbort, A. Oed, F. Gönnehwein, and H. Faust, Nucl. Instrum. Methods A **248**, 506 (1986).
[17] S. B. Kaufman, E. P. Steinberg, B. D. Wilkins, J. Unik, A. J. Gorski, and M. J. Fluss, Nucl. Instrum. Methods **115**, 47 (1974).

[18] R. Ghetti, B. Jakobsson, and H. J. Whitlow, Nucl. Instrum. Methods A 317, 235 (1992).
[19] M. H. Mendenhall and R. A. Weller, Nucl. Instrum. Methods B 47, 193 (1990).
[20] M. H. Mendenhall and R. A. Weller, Nucl. Instrum. Methods B 40/41, 239 (1989).
[21] J. F. Ziegler, J. P. Biersack, and U. Littmark, *The Stopping and Ranges of Ions in Solids I, The Stopping and Ranges of Ions in Matter*, edited by J. F. Ziegler (Pergamon, New York, 1985).
[22] W. K. Chu, J. W. Mayer, and M. A. Nicolet, *Backscattering Spectrometry* (Academic, New York, 1978), p. 67.
[23] F.-Y. Shiau, Y. A. Chang, and L. J. Chen, J. Electron. Mater. 17, 433 (1988).

# Formation of thin films of $CoSi_2$ on GaAs

Mikael Hult, Leif Persson, Mohamed El Bouanani, and Harry J. Whitlow
*Lund Institute of Technology, Department of Nuclear Physics, Sölvegatan 14, S-223 62 Lund, Sweden*

Margaretha Andersson
*Uppsala University, Department of Inorganic Chemistry, Box 531, S-751 21 Uppsala, Sweden*

Mikael Östling, Nils Lundberg, and Carina Zaring
*Royal Institute of Technology, Department of Electronics, Solid State Electronics, P.O. Box Electrum 229, S-164 40 Kista, Sweden*

Kristina Georgsson
*Lund Institute of Technology, Department of Solid State Physics, Sölvegatan 14, S-223 62 Lund, Sweden*

David D. Cohen and Nick Dytlewski
*Australian Nuclear Science & Technology Organisation, PMB1, Lucas Heights, Menai 2234, Australia*

Peter N. Johnston and Scott R. Walker
*Royal Melbourne Institute of Technology, Department of Applied Physics, GPO Box 2476V, Melbourne 3001, Australia*

(Received 29 July 1994; accepted for publication 20 November 1994)

$CoSi_2$ exhibits the features of low resistivity and stability at elevated temperatures which make it interesting to employ for metallization on GaAs. The interfacial reactions in GaAs samples with thin film overlayers of Si and Co [Si(220 nm)/Co(50 nm)/(⟨100⟩-GaAs)] were studied using x-ray diffraction, scanning electron microscopy, x-ray photoelectron spectroscopy, and mass and energy dispersive recoil spectrometry. Samples were vacuum furnace annealed for time periods between 1 and 8 h at temperatures ranging from 300 to 700 °C. It was found that a $CoSi_2$ layer formed without observable reaction with the substrate at 500 °C and above. The excess Si (Si/Co atomic ratio of 2.41) remained near the surface as elemental Si and as $SiO_2$ for the 500 and 600 °C annealings. For the 700 °C annealing the excess near-surface Si was not observed. © *1995 American Institute of Physics.*

## I. INTRODUCTION

A crucial part of manufacturing GaAs devices and integrated circuits is the metallization process. There is a need for ohmic contacts that possess qualities like low resistivity, high degree of uniformity, and stability at elevated temperatures. These qualities become more crucial as device dimensions decrease. In recent heterojunction applications, for example, it is important to control the metallization process on a nanometer scale. Considerable efforts have been directed towards finding reliable contacts for GaAs and many different systems have been studied. In a comprehensive overview of GaAs metallizations by Palmstrøm and Morgan[1] it is stressed that the problems with alloyed ohmic contacts are of major concern for the development of GaAs technology. Metallization is also important for metal mastering in nanometer fabrication technology, Schottky barrier devices, etc.

Metal silicides have been employed in numerous applications in silicon integrated circuit (IC) technology. Contacts with higher stability and more uniform morphology can be produced using these materials.[2–4] Their use in GaAs technology have so far not been extensive. However, studies show that metal silicides may be advantageous to employ on GaAs structures (e.g., in self-aligned metal-semiconductor field-effect transistor (MESFET) technologies).[5,6] $CoSi_2$ is perhaps the most interesting metal silicide in this context. The resistivity is low (16 $\mu\Omega$ cm[7]), and the temperature stability is high. Studies show that $CoSi_2$ is stable up to 900 °C during conventional furnace annealing on a Si substrate and high stability has also been reported on SiC substrates.[8] This high stability is not expected on GaAs although stability has been shown up to at least 600 °C.[6] The $CoSi_2$ phase is formed very rapidly through nucleation, which may cause problems with consequential large grain sizes.

In this investigation Si(220 nm)/Co(50 nm)/⟨100⟩-GaAs samples were furnace annealed in the range 300–700 °C, and the reaction sequence was studied using different techniques. The basic idea was that the Si and Co would react to form $CoSi_2$ before any reaction took place with the substrate. The sample structure was deliberately formed with excess Si (2.41 Si atoms for every Co atom) with the intention of obtaining substitutional Si on Ga sites in a thin layer beneath the formed $CoSi_2$. The Si would then act as an $n^+$ contact doping similar to what was found for the Ge/Pd contact system.[9,10] Co was deposited prior to Si because it has better adhesion to GaAs although Si is stable on GaAs up to 800 °C which is not the case for Co on GaAs[11–13] where a reaction starts at around 300 °C.

No single technique can uniquely characterize the interfacial reactions. Here we have employed techniques to measure elemental depth distributions, chemical phases, as well as sheet resistance. The most common methods for elemental depth profiling are Rutherford backscattering spectrometry (RBS), secondary ion mass spectrometry (SIMS), and sputter-Auger electron spectroscopy (AES). All of these techniques suffer from restrictions in their applicability to the

 0021-8979/95/77(6)/2435/9/$6.00  

present problem. RBS may yield ambiguous results because of interfering signals from different elements and low mass impurities may be hidden under the large signal from the bulk. Furthermore, Ga and As are troublesome to analyze separately because of the small mass difference. SIMS and sputter-AES suffer from problems with matrix effects. These may be associated with different ionization probabilities from the multiple phases in the reacted film (and may also lead to loss of homogeneity in the sputter crater due to different sputter erosion rates).

In this work elemental depth distributions were determined using mass and energy dispersive recoil spectrometry (RS) which is a fairly new ion beam analysis technique.[6,14,15] The principal advantages with mass and energy dispersive RS are that both light and heavy elements can be separately studied simultaneously and that problems caused by chemical matrix effects are avoided since the technique is based on high-energy nucleus-nucleus scattering. In this study five samples were analyzed using 77 MeV $^{127}I^{10+}$ ions as projectiles. This permitted separation of C, O, Si, Co, Ga, and As.[6] The mass resolution is poorer for the larger recoil masses but generally it can be improved by increasing the recoil energy through use of a higher projectile energy[16,17] and/or a higher projectile mass. Two other samples were analyzed using 70 MeV $^{197}Au^{13+}$.

The samples were also analyzed using standard x-ray diffraction (XRD), scanning electron microscopy (SEM) and x-ray photoelectron spectroscopy (XPS) techniques.

## II. MATERIALS AND METHODS

### A. Sample preparation

Undoped 2 in. ⟨100⟩ GaAs wafers were exposed to a standard predeposition cleaning procedure consisting of a 1 min dip in trichloroethylene, acetone, and propanol, respectively. This was followed by a 5 min wash in a mixture of $HCl:H_2O$ (1:2) and a 15 s rinse in de-ionized water. The wafers were blown dry in nitrogen and subsequently loaded into the deposition system. The metallization was performed in a Balzer electron-gun evaporation system of type UMS-500. The base pressure prior to deposition was in the low $10^{-5}$ Pa region. 50 nm cobalt was deposited on the GaAs wafers sequentially followed by 220 nm Si which corresponded to a Si/Co atomic ration of 2.41. The deposition rates were about 0.2–0.6 nm/s.

Heat treatments were performed in a vacuum furnace equipped with a load-lock station ensuring a base pressure of $10^{-5}$ Pa. The duration was 1 h at temperatures of 300, 400, 500, 600, and 700 °C, except for two samples annealed at 350 °C for 2 and 8 h, respectively.

### B. Recoil spectrometry

In order to achieve the mass separating power needed to separately profile Ga and As, the use of high-energy heavy ions was a necessity. The measurements of the as-deposited sample and the samples annealed at 300, 400, 500, and 600 °C for 1 h were carried out using the "ANTARES" FN tandem accelerator at Lucas Heights, which provided 77 MeV $^{127}I^{10+}$ ions. In this setup the samples were mounted in a scattering chamber with beam incidence and recoil exit angles of 60° and 75°, respectively, relative to the sample surface normal [Fig. 1(a)].

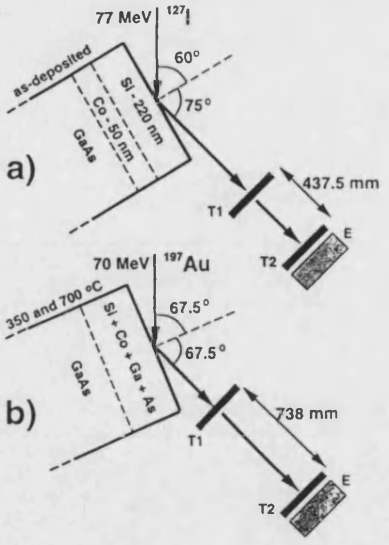


FIG. 1. The recoil spectrometry geometry for the two experimental setups; (a) Lucas Heights, (b) Uppsala.

Two samples (one annealed for 8 h at 350 °C and one annealed for 1 h at 700 °C) were analyzed using the EN tandem accelerator at The Svedberg Laboratory in Uppsala. For these measurements $^{197}Au^{13+}$ ions at 70 MeV were employed. The geometry was slightly different since both the angle of incidence and exit were 67.5° relative to the sample surface normal [Fig. 1(b)].

The ToF-E detector telescope[17–19] (employed to detect the recoiling target nuclei) was the same for both measurements. It consists of two carbon foil time-zero detectors with a variable flight path between them followed by a silicon diode detector. The flight length for the measurements in Lucas Heights was 437.5 mm while it was 738 mm in Uppsala. The silicon energy detector was placed 25 mm behind the second time detector. In this investigation the energy detectors (two similar ones were used) were 100 $mm^2$ ion-implanted silicon detectors (SiTek[20]). The recoiling target atoms were detected at an angle of 45° relative to the incoming $^{127}I$ ions (Fig. 1). More experimental details of this setup are found in Ref. 6. The depth resolution at the surface was found to vary between 20 and 40 nm full width at half-maximum (FWHM) depending on recoil atom and matrix for the samples analyzed with $^{127}I^{10+}$ as well as those analyzed using $^{197}Au^{13+}$. At the GaAs interface the depth resolution had decreased to approximately 40–60 nm FWHM.

The mass of each individual recoiling target atom can be assigned from the measurement of its time-of-flight and energy. This makes it possible to separate the recoil energy spectra (depth distributions) for the different elements in the sample. The recoil spectra presented in this work can be interpreted in a manner similar to RBS spectra except that

each spectrum only contains the signal from a single element.

Generally, the response of the silicon energy detector is somewhat nonlinear thereby it is difficult to establish an energy calibration. To overcome this problem we have recently developed a new calibration method[21] that takes advantage of the almost perfect linearity in the time-of-flight measurement. This calibration procedure was employed for evaluating the data in this investigation.

Converting the time-of-flight to energy can often improve the energy resolution considerably. This was not the case in this investigation because the ion and recoil energies were greater than employed in previous investigations[13,15] and (in the Lucas Heights measurements) a shorter flight length was used. In the Uppsala measurements a malfunction in the time analog to digital converter (ADC) degraded the mass resolution to the extent that the Ga and As signals could not be separately characterized and introduced considerable uncertainty in the trailing edge of the Co signal (in Fig. 9 at depths greater than 150 nm).

### C. X-ray diffraction

Phase analysis was performed by XRD using a Siemens D5000 diffractometer with Cu $K\alpha$ radiation ($\lambda$=0.15418 nm). The measurements were made using a standard $\theta$-$2\theta$ arrangement as well as a grazing incidence (incident angle 2°) setup. Theoretical diffraction patterns for the possible phases were calculated in order to simplify the identification. These were made using the program LAZY PULVERIX[22] and input values for unit cell dimensions and atom positions were taken from *Pearson's Handbook of Crystallographic Data for Intermetallic Phases*.[23] In general, these films exhibited strong texturing and therefore the identification was based only on the interplanar spacing corresponding to significant diffraction peaks.

### D. Scanning electron microscopy

For the morphological characterization of the interfaces and surfaces, cross-sectional micrographs of cleaved samples as well as micrographs of the surfaces were measured using a (JEOL JSM-6400F) scanning electron microscope.

### E. X-ray photoelectron spectroscopy

Examination of the chemical state of the remaining silicon at the surface in the 500, 600, and 700 °C annealed samples was carried out using XPS. A Perkin–Elmer PHD 5500 system was used for this purpose. In order to remove the native oxide and adsorbed oxygen, the surface was sputtered using $Ar^+$ ions for 5 s before measurement.

## III. RESULTS AND DISCUSSION

The sheet resistance measurement (Fig. 2) indicated that a low resistivity surface layer was formed after annealing at temperatures of 500 °C and above.

SEM micrographs of the surface showed that the surface morphology was the same for all samples [similar to the 600 °C annealing presented in Fig. 3(a)] except for the one

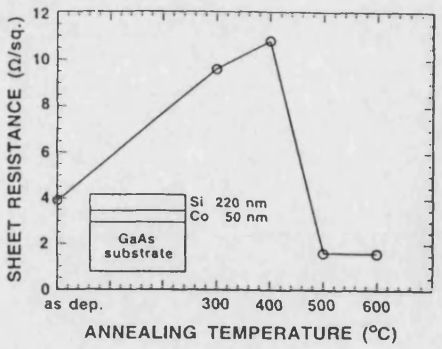


FIG. 2. Electrical sheet resistance vs annealing temperature for 1 h duration anneals.

annealed at 700 °C [Fig. 3(b)] where large grains appeared all over the surface.

The RS, XPS, cross-sectional SEM, and XRD results are presented in Figs. 4–12 and will be discussed below in order of anneal temperature. The yield in a RS spectrum is proportional to the concentration of an element but note that the yield of the normalized RS spectra from *different* elements cannot be compared. The recoil cross section closely follows the Rutherford cross section for recoils. This implies that the

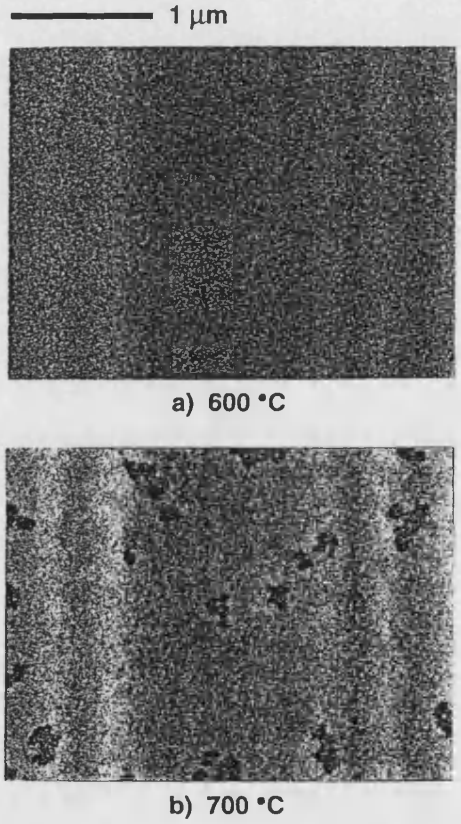


FIG. 3. SEM micrographs showing the surface morphology: (a) 600 and (b) 700 °C.

TABLE I. Widths associated with the leading and trailing edges of Si, Co, Ga, and As in the recoil spectra from samples annealed for 1 h and analyzed with the iodine-beam [Fig. 1(a)]. The edge widths are defined as the 12%–88% step height value.

| | Element edge | | Width (keV) | | |
|---|---|---|---|---|---|
| Annealing | as-deposited | 300 °C | 400 °C | 500 °C | 600 °C |
| Si-leading | 750 | 750 | 750 | 750 | 750 |
| -trailing | 1400 | 2300[a] | 2650[a] | 1300 | 1300 |
| Co-leading | 1600 | 1550 | 1750[a] | 1450 | 1450 |
| -trailing | 1900 | 2300[a] | 2500[a] | 2100 | 2100 |
| Ga-leading | 2500 | 5400[a] | 5600[a] | 2400 | 2400 |
| As-leading | 2600 | 5300[a] | 5300[a] | 2550 | 2550 |

[a]Some widths were difficult to define because they were not shaped like error functions (and could include steps). This could be associated with nucleation together with interfacial growth, non-uniform phase formation or simply poor pulse statistics. The uncertainty of those values is large. The uncertainty of the other values is less than 10%.

yield of recoils from a layer with homogeneous distribution of a certain element, increases as the recoil energy decreases (increasing depth). The yield is also dependent on the matrix because of differences in stopping cross section.

The edge widths in the RS spectra are of interest because they can indicate diffusion rates (although the change of depth resolution with energy and matrix must be considered).[13] The edge widths are defined as the 12%–88% step height value, which corresponds to the FWHM of a Gaussian broadening, listed in Table I.

### A. Reference sample

The Si signal in the RS spectrum (Fig. 4) is indicative of a uniform Si layer. The trailing edge is sharp (1400 keV) which supports assumptions that very little interdiffusion has taken place. The Co signal exhibits no well-defined plateau because the depth resolution is of the same magnitude as the width of the Co layer (50 nm). The Ga and As spectra (Fig. 5) are similarly shaped and have comparable widths. The approximate depth scale in Fig. 4 was derived using the STOP code[24] and from the known layer thicknesses assuming a density of Si and Co that is 90% of their bulk density. This density was assumed due to the partly amorphous deposited layers and resulted in that the number of deposited atoms were $9.9\times10^{17}$ and $4.1\times10^{17}$ atoms/cm$^2$ for Si and Co, respectively.

Figure 6 shows that there are C and O at the surface and that there is some C at the Co/GaAs interface. There is a fairly uniform, and low, distribution of O within the sample. The O concentration is higher in the overlayers than in the bulk. Counting statistical limitations prevent a more detailed discussion regarding C and O distributions.

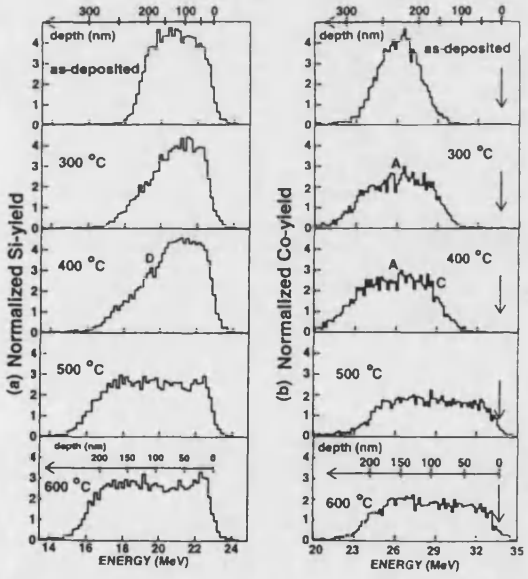


FIG. 4. Recoil energy spectra for (a) Si and (b) Co recoils from Si/Co/GaAs thin film structures heat treated in vacuum at different temperatures for 1 h. 77 MeV $^{127}I^{10+}$ ions were used as projectile ions. Note that the signals for different elements cannot be directly compared.

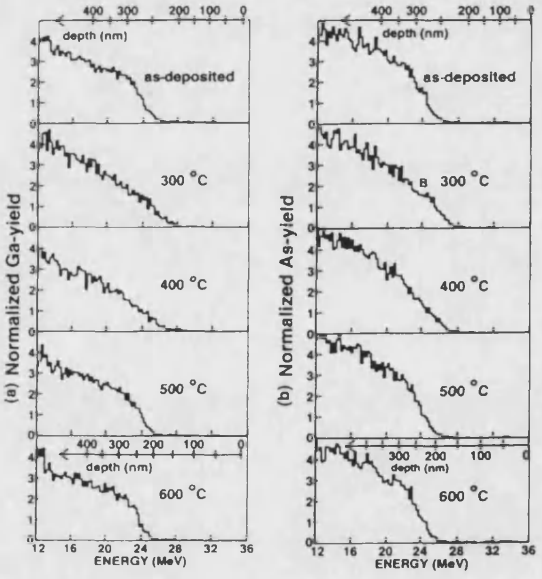


FIG. 5. As Fig. 4, (a) Ga and (b) As recoils.

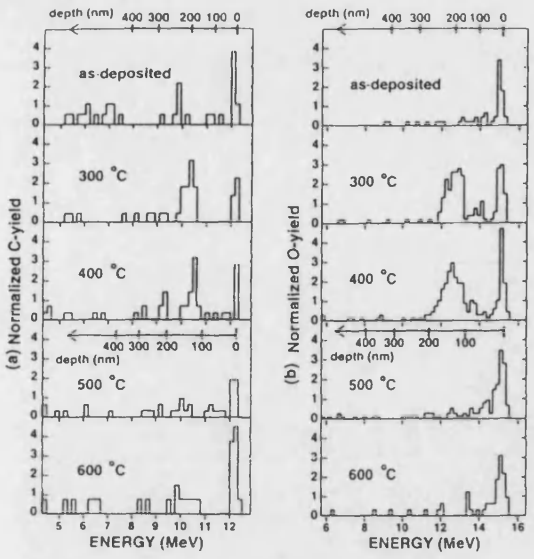


FIG. 6. As Fig. 4, (a) C and (b) O recoils.

No evidence of any reaction could be seen in the XRD spectrum and only peaks associated with Co, Si, and GaAs were observed. [The deposited Si and Co layers are clearly distinguishable in the cross-sectional SEM micrograph in Fig. 10(a).]

### B. 300 °C

From recoil data (Fig. 4) it is evident that Si has started to react with Co. There is no wide plateau in the Si trailing edge which makes stoichiometric calculations based on the yield in an interval with constant yield difficult.[13] It can thus be concluded that any uniform layer in this interface is not wider than ~50 nm. From the point "A" [Fig. 4(b)] towards higher energies in the Co spectrum there is some suggestion of a plateau which could be indicative of, e.g., a layer of $Co_2Si$. Indications of this can also be seen in the XRD spectrum (Fig. 7) where peaks from $Co_2Si$ appear accompanied by peaks associated with CoSi and Co(Ga,As). Reaction between Co and Si is expected at temperatures of 350 °C and above. The early start at 300 °C may be a consequence of the partly amorphous Si layer.

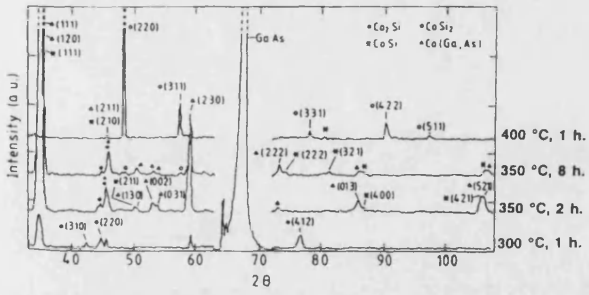


FIG. 7. X-ray Diffraction data for samples annealed at 300, 350, and 400 °C for different durations.

Inspection of the recoil data (Figs. 4 and 5) also reveal that Co has started to react with GaAs. This is apparent from the increased widths and the spread to higher energies of Ga and As leading edges and by the Co trailing edge. The step-like features of the Co trailing edge may indicate thin layers of constant stoichiometry. Point "A" is also indicated in the Co spectrum for 400 °C since the spectrum around that point is very similar to the Co spectrum for 300 °C. It could indicate a demarcation line between the Ga and As front edge and the Si trailing edge. In the XRD spectrum (Fig. 7) the Co(Ga,As) phase is observed. This phase can be indexed using the orthorhombic CoAs unit cell reported by Selte and Kjekshus[25] and can be described as a substitutional solid solution of Ga in CoAs. Some authors refer to this phase as $Co_2GaAs$. It is also possible that some amount of CoAs and CoGa can be present in the Co/GaAs interface.

No depth scales have been calculated in the RS spectra for this temperature. To calculate a depth scale in nm the knowledge of phases that are present and densities are essential. A rough estimate of the depths can be obtained by interpolating between the scales for 600 °C and as-deposited.

There are still two peaks in the C spectrum (Fig. 6). The interface peak has moved to a slightly higher energy. This is not necessarily indicative of an outward diffusion since higher stopping cross section gives the same result. The O spectrum exhibits a drastic change from the as-deposited case. There are definitely two peaks associated with the GaAs interface and the surface (the third one in the middle *may* arise from poor statistics).

[The cross-sectional micrograph in Fig. 10(b) is significantly different from the as-deposited micrograph. The Si layer seems homogeneous but the Co layer has reacted and formed an inhomogeneous area which is in accordance with the RS and XRD results.]

### C. 350 °C

Two different annealing times, 2 and 8 h, were used. The intention was that the low-temperature phases should develop during extended annealing and thus give a better chance of identification.

The XRD data (Fig. 7) indicate that after 2 h of heat treatment, the $Co_2Si$ which formed at 300 °C has almost disappeared. Except for the (220) peak of $Co_2Si$ (which is barely distinguishable), CoSi and Co(Ga,As) are now the only phases present as seen by XRD. The presence of a diffraction peak at about $d=0.2027$ nm ($2\theta=44.71°$) can be attributed to both $Co_2Si$ and CoGa. The extended homogeneity range of CoGa as well as the limited number of possible diffraction peaks make reliable identification very difficult. Least-squares refinement of the Co(Ga,As) unit cell dimensions reveals a slightly smaller unit cell than the CoAs one. The dimensional decrease is in consistency with the expectations from comparing the Ga and As atomic radii (0.122 and 0.125 nm). After an 8 h heat treatment the first signs of $CoSi_2$ formation can be seen, while CoSi and Co(Ga,As) are still the dominating phases.

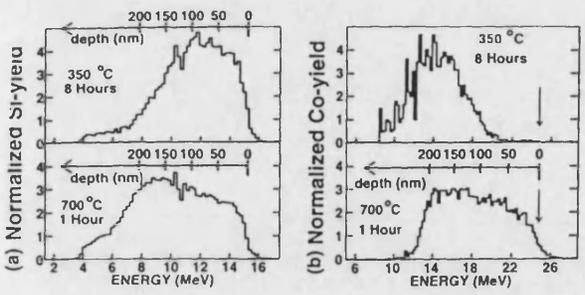


FIG. 8. As for Fig. 4, (a) Si and (b) Co single spectra from samples analyzed with the 70 MeV $^{197}Au^{13+}$ ions [Fig. 1(b)].

The recoil data of the Si and Co signals for the sample annealed for 8 h are presented in Fig. 8. The resemblance with the 300 and 400 °C spectra in Fig. 4 is obvious although the tail of the Si signal seems to extend further into the sample. As mentioned in Sec. II the uncertainty in the Co trailing edge for this sample is large because of interference with Ga. Although it was not possible to separate Ga from As (for this sample) it was possible to study the sum of the Ga and As signals which behaved in a manner similar to the corresponding spectra for the 300 and 400 °C.

### D. 400 °C

The recoil data (Figs. 4 and 5) are quite similar to the 300 °C case and only small differences can be seen. Point "A" in Fig. 4 may also indicate here the demarcation line between the bulk elements and Si. The XRD data (Fig. 7), however, has drastically changed and suggest that the formation of $CoSi_2$ is almost completed and only small amounts of CoSi and Co(Ga,As) remains. The recoil data reveal, however, that this is not the case. This apparent contradiction may be understood if, during the transformation of $Co_2Si$ to $CoSi_2$, both are simultaneously present but only the latter is in an ordered state and can contribute to the X-ray diffraction signal. In addition, texture effects might suppress the diffraction signals from $Co_2Si$. There is still a Si layer of about 100 nm near to the surface. Below this layer there is probably a thin layer of $CoSi_2$ denoted by the letters "C" and "D" in Fig. 4. CoSi is expected to exist below this layer.

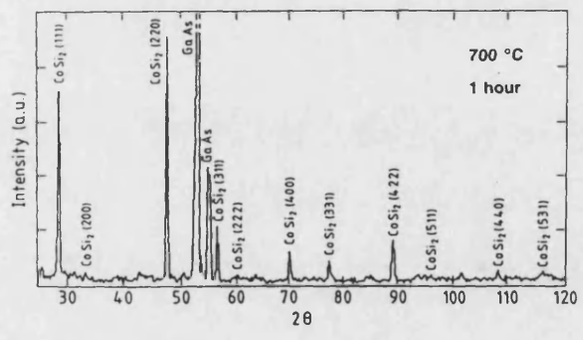


FIG. 9. X-ray diffraction data for the samples annealed at 700 °C for 1 h.

The cross-sectional micrograph is largely similar to the 300 °C annealing. The area in which a reaction is perceptible is, however, wider and the grains are slightly larger.

### E. 500 °C

$CoSi_2$ was the only phase that could be detected by XRD (except for GaAs). Figure 9 shows the XRD data for the 700 °C sample which are similar to the data for the 500 °C sample. Stoichiometric calculations on RS data also show that a fairly uniform layer of $CoSi_2$ has formed. The energy width of the Ga and As edges are reduced and even smaller than for the as-deposited sample. This is due to the lower stopping cross section of Ga and As in $CoSi_2$ compared to Co but it is also indicative of lack of reaction with the overlayer. The cross-sectional micrograph [Fig. 10(d)] also indicates that the interface is sharp and that grains (probably of $CoSi_2$) appear across the thin film overlayer.

There is a small, but significantly increased, Si signal from the near-surface indicated in Fig. 4. Since the atomic ratio of Si and Co is 2.41 there is an excess of $1.7\times10^{17}$ Si-atoms/cm$^2$ after $CoSi_2$ formation ($4.1\times10^{17}$ $CoSi_2$ molecules/cm$^2$). This corresponds to a uniform Si layer of 34 nm thickness. Co was not seen in the XPS analysis of the surface and the high-energy edge of the Co signal in the RS spectrum is slightly shifted to a lower energy (~550 keV, which corresponds to 17 nm in Si). Table I shows that the Co step at the surface is 1450 keV which corresponds to a depth resolution of 44 nm in Si and 23 nm in $CoSi_2$. The FWHM of the Si "surface peak" in the recoil spectrum is approximately 700 keV (corresponding to 36 nm in Si and 19 nm in $CoSi_2$) which is less than the 750 keV resolution at the surface. This is consistent with the XPS measurement that revealed that the silicon on the surface was both partly oxidized and partly pure. Figure 11 shows a region of the XPS spectrum for the 600 °C sample. The spectrum for the 500 °C sample was similar. In the cross-sectional micrograph [Fig. 10(d)] it is also possible to distinguish a narrow layer at the very top arising from elemental Si and $SiO_2$ [this narrow layer is more easily seen in the micrograph for the 600 °C annealing in Fig. 10(e)]. It is also clear from the recoil spectrum in Fig. 6 that oxygen is present in the surface layer and probably the layers below this. The "bulk peaks" which were seen in the C and O recoil spectra for the 300 and 400 °C annealings are not seen in Fig. 6. This is probably caused by the rapid formation of the thermodynamically stable $CoSi_2$ phase which prevented further reactions to take place. A gradient in the O concentration towards the surface can be distinguished which may indicate O out-diffusion.

### F. 600 °C

The XRD spectrum is similar to the spectrum for the 500 °C sample (Fig. 9). The Si recoil data (Fig. 4) are quite similar to the 500 °C data although the enrichment of Si at the surface is more pronounced. The Ga and As edges (Fig 5) are sharp, indicating a stable overlayer and the C and C spectra (Fig. 6) are similar to the 500 °C spectra.

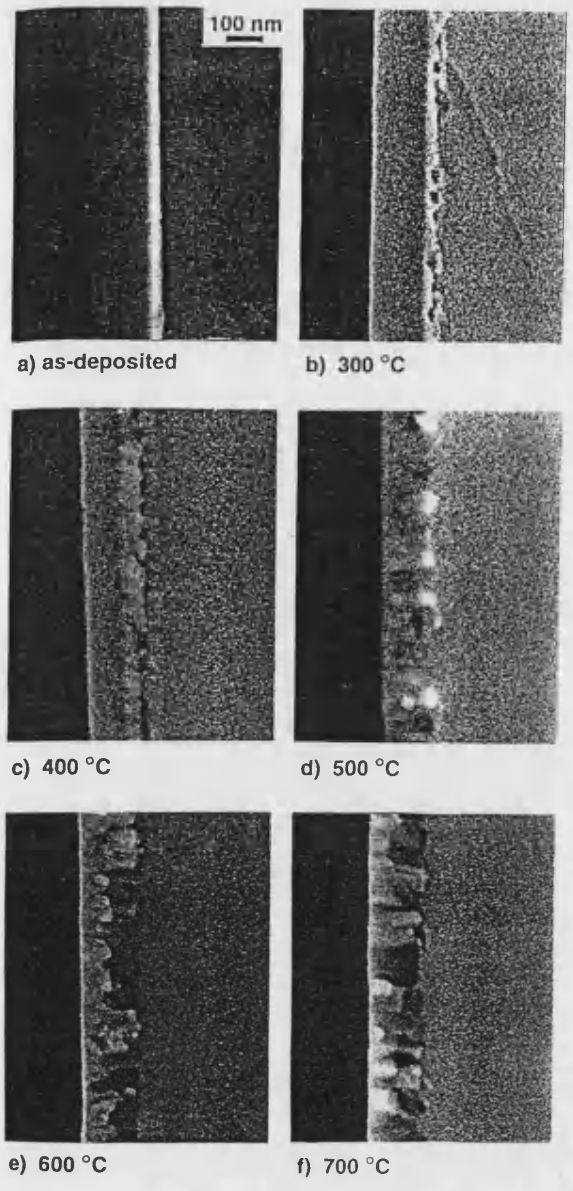


FIG. 10. Cross-sectional SEM micrographs: (a) as-deposited, (b) 300, (c) 400 (d) 500 (e) 600, and (f) 700 °C. The left (black) hand side of the micrographs is from above the surface, the center part is the thin film and the right hand side is the bulk GaAs.

In the XPS spectrum (Fig. 11) is seen a peak associated with Si and another associated with $SiO_2$ as in the 500 °C case.

The cross-sectional micrograph [Fig. 10(e)] indicates a sharp interface. The grains which appeared in the 500 °C annealing are somewhat larger here and they appear all across the thin film overlayer.

### G. 700 °C

The "surface peak" in the Si-recoil energy spectrum (Fig. 8) has disappeared and the leading edge is sharp, 900

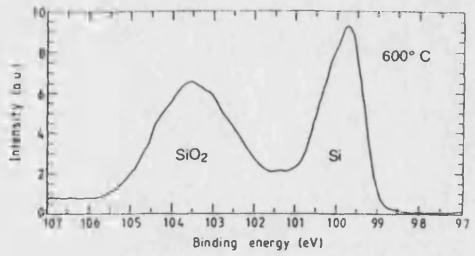


FIG. 11. Si and $SiO_2$ region of the XPS spectrum for the sample annealed at 600 °C for 1 h. No cobalt signal was detected.

keV FWHM (which corresponds to 31 nm in $CoSi_2$). The trailing edge is broad. The Co signal is indicative of a uniform layer extending from the GaAs interface to the surface. The leading edge of Co is 2100 keV FWHM (corresponding to 44 nm in $CoSi_2$). This value is relatively high which may indicate a nonhomogeneous surface layer. In contrast to the 500 and 600 °C data, the Co signal extends all the way to the energy corresponding to Co recoils from the surface (24 829 keV). This is confirmed by the XPS data (Fig. 12) where two Co peaks can be seen. These two peaks were not seen in XPS spectra from the 500 and 600 °C annealing. The leading edge of the sum of the Ga and As recoil energy distributions seems, however, to be reasonably sharp and closely similar to the data from the 500 and 600 °C samples.

The XRD spectrum presented in Fig. 8 is similar to the spectra from the 500 and 600 °C samples.

The interface as seen in the cross-sectional micrograph [Fig. 10(f)] is still sharp. There has, however, been considerable grain growth and some grains extend all the way from the interface to the surface (~200 nm). The observation that the Si "surface peak" has disappeared and the extension of the Co distribution all the way to the surface suggest that the

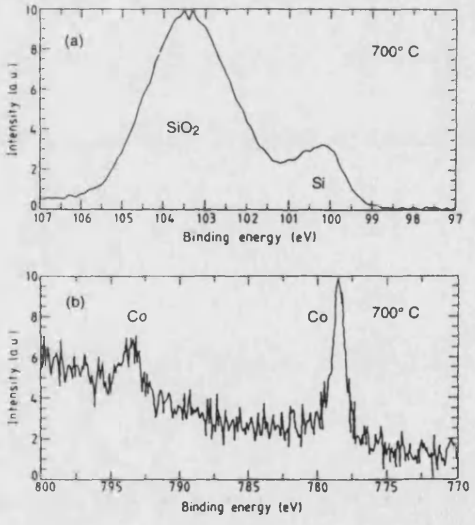


FIG. 12. XPS spectrum for the sample annealed at 700 °C for 1 h. (a) The Si and $SiO_2$ signal region. (b) The Co signal region.

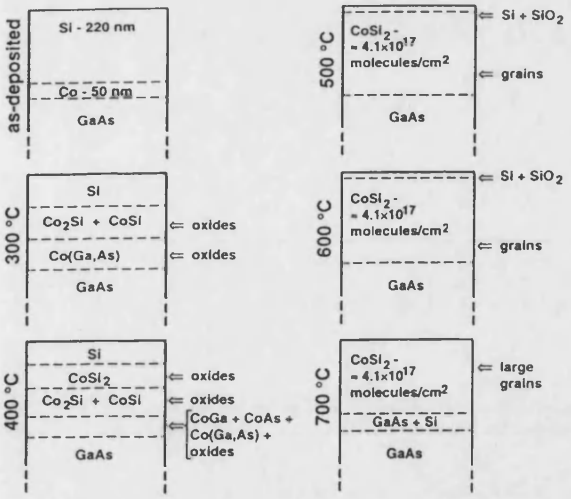


FIG. 13. Tentative schematic description of the reaction processes for the 1 h annealings.

excess Si is either distributed within the $CoSi_2$ layer or migrated to the $CoSi_2$/GaAs interface. This might be a consequence of the marked grain growth in the $CoSi_2$ layer at 700 °C because the resulting grain boundaries will provide an easy diffusion path from the surface. The broadening of the Si trailing edge might be indicative of Si buildup at the $CoSi_2$/GaAs interface, however, this is not conclusive as it may also be associated with the rougher surface morphology [Fig. 3(b)] for the 700 °C samples, as compared to the samples annealed at lower temperatures (≤600 °C).

A tentative description of the phase formation sequence based on these new data and on previous investigations[5] is shown in Fig. 13. The conditions where equilibrium phase diagrams are established are abrogated in this thin film study. There is essentially an infinite supply of bulk GaAs but a finite supply of Co and Si. The reaction is limited by atomic transport processes in the films and semiconductor and equilibrium may not be achieved. The presence of impurity-like oxygen also makes the situation more complicated. Under these conditions metastable phases may form and more phases than predicted by Gibb's phase rule may coexist. This means that ternary and even quaternary metalloid phases may form. The sequence of compound formation in thin films depends strongly on reaction kinetics. The kinetics of the Co/GaAs and Co/Si systems have been studied previously and the samples in this investigation can originally be considered as composed of both systems.[5] There are several equilibrium silicide phases; $Co_2Si$, CoSi, and $CoSi_2$. It is difficult to predict which phases may appear during annealing in these thin film samples since thermodynamic rules may not be applied here. Previous studies[4,5,26] have shown that $Co_2Si$ forms first (with Co as the main diffusing species). At higher anneal temperatures CoSi forms (with Si as the main diffusing species) and finally $CoSi_2$ forms by a nucleation process where Co is the main moving species. The present data support such a sequence of phase formation.

The kinetics of the Co/GaAs interface is not very different from the Co/Si system and has recently been subject to some study.[5,11–13,26,27] The reaction sequence for that system is Co/GaAs→Co(Ga,As)→CoGa+CoAs. Clearly, the $CoSi_2$/GaAs system is an interesting system in the context of metallization because a thermally stable interface may be formed. The main limitation arises from grain growth. Some grains in Fig. 10, for example, extend all the way through the thin film which is approximately 200 nm thick.

## IV. CONCLUSIONS

The findings from this study can be summarized as follows.

(i) No detectable reaction between the GaAs bulk and the $CoSi_2$ overlayer could be established for the samples annealed at 500, 600, and 700 °C. This indicates that $CoSi_2$/GaAs formed by thermal reaction constitutes a low electrical resistance metallization with high-temperature stability.

(ii) Cross-sectional micrographs indicated that the GaAs/$CoSi_2$ interface was sharp and that considerable grain growth took place as the annealing temperature was raised from 600 to 700 °C.

(iii) The excess surface Si stayed near to the surface and did not migrate to the GaAs during heat treatments at 500 and 600 °C for 1 h.

(iv) Annealing the sample for 1 h at 700 °C may lead to the loss of excess surface Si probably into the $CoSi_2$ layer and/or GaAs substrate.

(v) A reaction between Si and Co was observed already at 300 °C when annealed for 1 h.

(vi) The data support the suggestion that the phase formation sequence between Co and Si is $Co_2Si$→CoSi→$CoSi_2$.

(vii) The data support the suggestion that the phase formation sequence between GaAs and Co is Co(Ga,As)→CoGa+CoAs.

## ACKNOWLEDGMENTS

The authors would like to express their gratitude to the Australian Nuclear Science and Technology Organization (ANSTO) staff who work on the ANTARES facility for their help. Also the support of the Australian Institute of Nuclear Science and Engineering (AINSE) and its staff, the Australian Department of Industry, Technology, and Commerce (DITAC) are gratefully acknowledged. The Swedish authors would also like to acknowledge the Swedish Institute (SI), the Crafoord Foundation, the Royal Swedish Academy of Sciences (especially Letterstedt's resestipendiefond) and Carl Trygger's Foundation for financial support.

[1] C. J. Palmström and D. V. Morgan, in *Gallium Arsenide, Materials, Devices and Circuits*, edited by M. J. Howes and D. V. Morgan (Wiley, New York, 1986), p. 195.
[2] J. W. Mayer and S. S. Lau, in *Electronic Materials Science: For Integrated Circuits in Si and GaAs* (Macmillan, New York, 1990), p. 284.
[3] K. Maex, Mater. Sci. Eng. R: Reports **R11**, 53 (1993).
[4] A. H. Reader, A. H. van Homme, P. J. W. Weijs, R. A. M. Wolters, and D. J. Oostra, Rep. Prog. Phys. **56**, 1397 (1993).

[5]C. C. Hsu, G. L. Jin, J. Ho, and W. D. Chen, J. Vac. Sci. Technol. A **10**, 1020 (1992).
[6]M. Hult, H. J. Whitlow, M. Östling, N. Lundberg, C. Zaring, D. D. Cohen, N. Dytlewski, P. N. Johnston, and S. R. Walker, Nucl. Instrum. Methods B **85**, 916 (1994).
[7]L. Van den Hove, R. Wolters, K. Maex, R. De Keersmaecker, and G. Declerck, J. Vac. Sci. Technol. B **4**, 1358 (1986).
[8]N. Lundberg and M. Östling, Appl. Phys. Lett. **63**, 3071 (1993).
[9]E. D. Marshall, L. S. Yu, S. S. Lau, T. F. Kuech, and K. L. Kavanagh, Appl. Phys. Lett. **54**, 721 (1989).
[10]J. J. Thompson, S. P. Beaumont, A. H. Kean, and C. R. Stanley, Semicond. Sci. Technol. **5**, 596 (1990).
[11]M. Genut and M. Eizenberg, J. Appl. Phys. **66**, 5456 (1989).
[12]C. J. Palmström, C. C. Chang, A. Yu, G. J. Galvin, and J. W. Mayer, J. Appl. Phys. **62**, 3755 (1987).
[13]M. Hult, H. J. Whitlow, M. Östling, M. Andersson, Y. Andersson, I. Lindeberg, and K. Ståhl, J. Appl. Phys. **75**, 835 (1994).
[14]H. J. Whitlow, *Proceedings of the High Energy and Heavy Ion Beams in Materials Analysis*, Albuquerque, 1989, edited by J. R. Tesmer, C. J. Maggiore, M. Nastasi, J. C. Barbour, and J. W. Mayer (Materials Research Society, Pittsburgh, PA, 1990), p. 73.
[15]M. Hult, H. J. Whitlow, and M. Östling, Appl. Phys. Lett. **60**, 219 (1992).
[16]P. Goppelt, B. Gebauer, D. Fink, M. Wilpert, Th. Wilpert, and W. Bohne, Nucl. Instrum. Methods B **68**, 235 (1992).
[17]H. J. Whitlow, B. Jakobsson, and L. Westerberg, Nucl. Instrum. Methods A **310**, 636 (1991).
[18]H. J. Whitlow, G. Possnert, and C. S. Petersson, Nucl. Instrum. Methods B **27**, 448 (1987).
[19]H. J. Whitlow, *Proceedings of the High Energy and Heavy Ion Beams in Materials Analysis*, Albuquerque, 1989, edited by J. R. Tesmer, C. J. Maggiore, M. Nastasi, J. C. Barbour, and J. W. Mayer (Materials Research Society, Pittsburgh, PA, 1990), p. 243.
[20]M. Lindroos and Ö. Skeppstedt, Nucl. Instrum. Methods A **306**, 225 (1991).
[21]M. El Bouanani, M. Hult, L. Persson, E. Swietlicki, M. Andersson, M. Östling, N. Lundberg, C. Zaring, D. D. Cohen, N. Dytlewski, P. N. Johnston, S. R. Walker, I. F. Bubb, and H. J. Whitlow, Nucl. Instrum. Methods B **94**, 530 (1994).
[22]K. Yvon, W. Jeitschko, and E. Parthe, J. Appl. Crystallogr. **10**, 73 (1977).
[23]*Pearson's Handbook of Crystallographic Data for Intermetallic Phases*, edited by P. Villars, W. B. Pearson, and L. D. Calvert (American Society for Metals, Metals Park, Ohio, 1985).
[24]J. F. Ziegler, J. P. Biersack, and U. Littmark, *The Stopping and Ranges of Ions in Solids 1, The Stopping and Ranges of Ions in Matter*, edited by J. F. Ziegler (Pergamon, New York, 1985).
[25]K. Selte and A. Kjekshus, Acta Chem. Scand. **25**, 3277 (1971).
[26]F.-Y. Shiau, Y. A. Chang, and L. J. Chen, J. Electron. Mater. **17**, 433 (1988).
[27]F.-Y. Shiau, Y. A. Chang, and J. C. Lin, Materials Chem. Phys. **32**, 300 (1992).

Nuclear Instruments and Methods in Physics Research A317 (1992) 235–241
North-Holland

NUCLEAR INSTRUMENTS & METHODS IN PHYSICS RESEARCH
Section A

# Measurements of the response function of silicon diode detectors for heavy ions using a time of flight technique

Roberta Ghetti [a], Bo Jakobsson [a] and Harry J. Whitlow [b]

[a] *Division of Cosmic and Subatomic Physics, University of Lund, Sölvegatan 14, S-223 62 Lund, Sweden*
[b] *Department of Nuclear Physics, Lund Institute of Technology, Sölvegatan 14, S-223 62 Lund, Sweden*

Received 8 January 1992

A time of flight (TOF) method has been employed to study the response of silicon diode detectors to low energy (0.05–0.2 *A* MeV) recoiling nuclei from heavy ion collisions. The response function of five different silicon diode detectors to low energy $^{12}C$, $^{31}P$ and $^{81}Br$ recoils has been investigated and closely follows a straight line law for each recoil isotope. A simple relation between energy, pulse height and mass number, can be applied to establish an energy scale for the low energy recoils, provided that detector specific constants are used. The energy resolution of silicon diode detectors was comparable to that of surface barrier detectors but varied considerably from one detector to another.

## 1. Introduction

The detection and identification of recoiling nuclei from heavy ion collisions is of great interest because of the information obtainable about the reaction dynamics. Recoiling target residues (of masses ranging from about half of the target mass up to the target mass and energies less than 0.5 *A* MeV) carry information about the reaction plane, the impact parameter and the momentum transfer.

In fixed target experiments the vast majority of such low energy (0.05–0.2 *A* MeV) recoils is completely stopped in the target foil, but the combination of intense circulating beams and of extremely thin gas-jet targets ($< 10^{14}$ atoms $cm^{-2}$ thick) at storage rings opens the possibility of detection of these recoils using electronic detectors. For this purpose we are developing a time of flight (TOF) energy detector telescope system for the identification of the recoil mass, energy and emission angle. The recoil velocity (and hence energy per nucleon) will be determined from the TOF between a pair of thin carbon foil time detectors, whilst the total energy and position (angle) will be measured using a silicon diode detector, in which the recoils will be completely stopped. In this way the mass is determined and this, coupled with the angle, allows the recoil momentum vector to be completely determined.

Silicon diode detectors with both p–n [1,2] and p–i–n [3] doping configurations have been proposed as alternatives to conventional Au/Si surface-barrier detectors [4,5]. In particular silicon p–i–n and p–n detectors have lower leakage currents than surface-barrier detectors (low noise contribution). They are also compatible with the requirements of UHV systems, such as storage rings, because they can withstand heat treatment to a few hundred °C during bakeout. The response (output pulse size with particle energy) of silicon diode detectors to heavy ion impingement is governed by:

a) the fraction of the energy that is deposited in electronic processes;

b) the efficiency by which this deposited energy is transferred to electron–hole pair production;

c) the collection efficiency for electron–hole pairs.

Considering first a), the fraction of energy deposited in electronic processes includes both the contribution from the primary particles and the contribution from the cascade of energetic secondary recoils resulting from nuclear scattering. In b) the energy deposited in electronic processes will not all be converted to electron–hole pair production because of the production of X-ray photons, phonons, secondary electrons etc. c) is primarily determined by the electric field distribution over the region where the incoming particle is stopped. This will be strongly affected by the slope, position and width of the potential barrier, low field (contact) regions and passivating oxide layers, and thus by the junction configuration e.g. surface barrier, $p^+$–n, p–i–n etc. In addition the dense electron–hole plasma

along the ion track may strongly modify the electric field and thus the collection efficiency along the track. For high energy ions ($> 1$ $A$ MeV) the response is very close to linear. However for low energy recoils (0.05–0.5 $A$ MeV), which are of interest for our applications, there is no a priori reason why it should be so. The branching changes because the fraction of energy deposited in nuclear collisions becomes larger as the energy decreases [6]. Moreover the density of the electron–hole plasma is sufficiently high along the ion track for recombination to take place [7]. We anticipate that a significant fraction of the projectile energy will be deposited in electronic processes close to the detector surface. Consequently, one expects the response to be dependent on the electron–hole collection efficiency just below the surface. This will be governed by the presence of layers which have low collection efficiency ($SiO_2$ passivating layers, metal contacts etc.) and the field in the surface region. In p–i–n and p–n diodes the charge collection from the undepleted low-field region of the thin p-layer may also contribute through the funneling effect or diffusion in the weak electric field [8,9]. It has been customary to consider these effects in terms of window (or dead layer) thicknesses [10–13] and mass and pulse height defects [12–17]. However in view of the complex branching between the different processes, comparison in terms of such a universal model is clearly inappropriate.

The use of a TOF method [13] to tag the recoil nuclei that impinge on the silicon energy detector with their energy, offers a number of advantages for probing the detector response which can be summarized as follows: It is a simple method to determine the energy per mass unit for each recoil with minimal perturbation of energy and direction. The technique has good energy resolution, especially for low energy recoils (e.g. 25 keV FWHM for 0.1 $A$ MeV $^{40}Ar$ ions with 1 m flight length and time resolution of 500 ps FWHM [18]). It is easy to calibrate and, in combination with a continuous spectrum of particles such as that of the elastic recoils from a thick target as used here, it allows rapid measurement of the response of a detector over a wide range of energies simultaneously (instead of requiring a change of beam energy for each data point).

The objective of the present work is to investigate:

i) The response function of five different silicon diode detectors to heavy ions using the TOF technique discussed above.

ii) Procedures for establishing a relation between pulse height and energy for recoil nuclei with different masses.

iii) The energy resolution, since the previous study [19] showed that the dominant contribution to the mass resolution of a TOF–$E$ detector telescope is associated with the energy resolution of the silicon diode detector.

## 2. Experimental

The measurements were carried out using the ion beam analysis facility of the Royal Institute of Technology, Stockholm. The TOF–$E$ detector telescope system and the experimental setup are described in ref. [19].

Five p–i–n diode detectors were investigated: two identical diffused junction detectors (10 mm diameter), originated from Ame [20]; two ($10 \times 10$ mm) identical detectors from SiTek [21] and one bakeable intertechnique IPB-100-50 detector [22]. In all cases the depleted layer thickness was very much greater than the range of the recoil nuclei. The bias voltages corresponded to the maximum permitted reverse bias voltage. None of the detectors had previously been exposed to heavy ion irradiation with the exception of the intertechnique detector, which was heat-treated at 225°C for 1 h prior to the experiment in an attempt to remove ion-induced damage.

The time detectors, which generate the start/stop signals for the TOF measurements when the recoil nuclei pass through a 5 $\mu g\ cm^{-2}$ thick carbon foil, are of the design due to Busch et al. [23].

The timed flight length between the foils was 738 mm. The projectile ions were 48 MeV $^{81}Br^{8+}$ which were obtained from the Svedberg Laboratory's tandem accelerator. The ion beam was collimated to 2 mm diameter.

Recoiling $^{12}C$ and $^{31}P$ and scattered $^{81}Br$ nuclei with a continuous energy distribution over the range of interest were obtained using the standard glancing incidence/exit configuration for mass and energy dispersive recoil spectrometry [24,25]. The targets were mounted onto a 20 position target wheel fitted to a goniometer in a scattering chamber. The detector telescope [19] was contained in a side arm to the scattering chamber, and the particles scattered/recoiling were detected at 45° to the incident beam direction. Thick carbon and GaP targets were used. The recoiling and scattered nuclei are listed in table 1 together with their maximum energies which correspond to elastically scattered recoiling nuclei from the surface layer of the target. These were obtained from eqs. (5) and (6) of ref [19].

Table 1

| Target | Process | Nuclei | Energy [MeV] |
|---|---|---|---|
| Polished graphite | Recoil | $^{12}C$ | 10.80 |
| GaP | Recoil | $^{31}P$ | 19.22 |
| Au/Si | Scattered | $^{81}Br$ | 37.52 |

## 3. Results and discussion

### 3.1. Data Analysis

The data for each silicon detector was analysed off-line using a sorting code described in ref. [19] which generates two-dimensional energy vs time and mass vs time histograms as well as histograms of the mass, energy and time distributions.

The time scale was established from the edges in the time spectra corresponding to scattered $^{81}$Br and recoiling $^{12}$C and $^{31}$P from the surface layer of the target. A small correction was applied for the energy loss in the foil of the first time detector. The true energy of each recoil entering the silicon detector could then be determined from the TOF after a similar correction had been employed for the energy loss in the foil of the second time detector. The energy losses were calculated using Ziegler's et al. STOP code [26]. The calibration line is shown in fig. 1. No correction was attempted for constant baseline shift in the electronics.

The data was subsequently sorted to yield for each isotope, the pulse height spectra from the silicon detector in energy slices of 5 $A$ keV width, for a series of recoil energies. The windows in the time distribution corresponding to the energy slices are indicated in figs. 2a–2b. For each of the small energy intervals the first and second moment of the pulse height distribution from the silicon detectors were determined by fitting Gaussian distributions to the data.

### 3.2. Pulse height–recoil energy relationship

Fig. 3 shows the pulse height vs recoil energy for a SiTek detector for $^{12}$C, $^{31}$P and $^{81}$Br recoils. Inspection

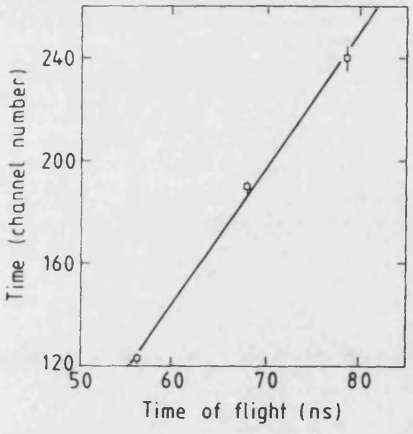


Fig. 1. Time calibration from the positions of surface edges of $^{12}$C and $^{31}$P recoils and $^{81}$Br scattered from $^{197}$Au for a 48 MeV $^{81}$Br incident beam. The error bars represent the spread in the data from several measurements.

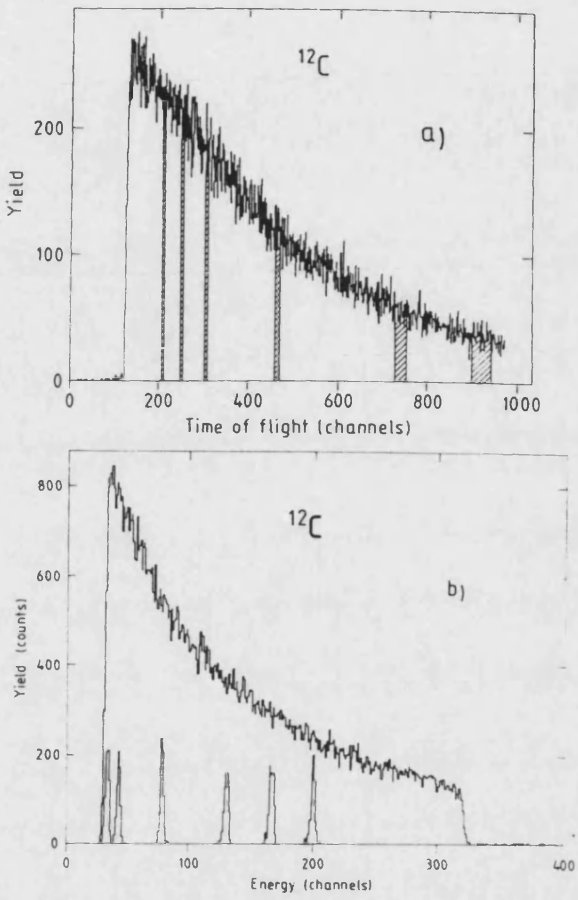


Fig. 2. (a) Time distribution and (b) the energy spectrum for $^{12}$C recoils in the SiTek 2 detector. The time windows are indicated in (a) and the corresponding energy distributions, (normalized to the same area) are shown in (b).

of fig. 3 shows that the pulse height vs energy closely follows a straight line law over the energy region considered here for each individual isotope. The apparent systematic shift in the response with increasing $A$ is associated with both a change in slope and intercept of the pulse height vs energy plot. This straight line behaviour was also observed for all the other detectors investigated, although the slopes and intercepts differed even between detectors from the same manufacturer. This confirms the straight line response (and apparent shift of this line) of silicon diode detectors for low energy $^{12}$C and $^{63}$Cu nuclei reported previously in ref. [22]. Figs. 4 and 5 show the slopes and intercept of straight lines fitted to the energy vs pulse height data as a function of mass number for the different detectors. It can be clearly seen from figs. 4 and 5 that the intercept and slope are in good agreement with a straight line dependence. Check points for $^{69}$Ga lay within reasonable error limits of the fitted lines. These

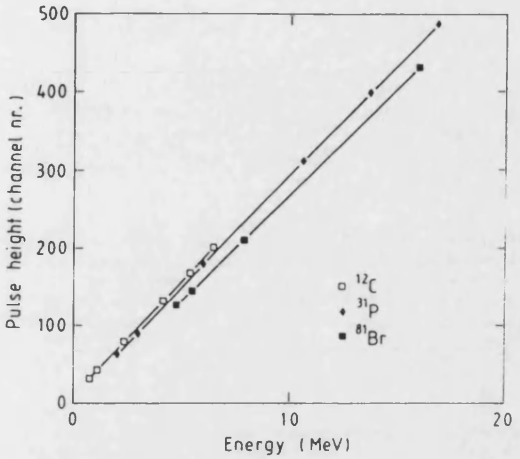


Fig. 3. Pulse height vs energy for the SiTek 2 detector. The lines represent straight line fits to the data. The errors associated with the uncertainty in determining the pulse height are smaller than the data point symbols.

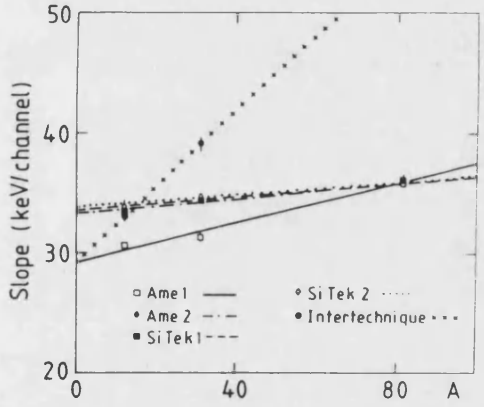


Fig. 4. Variation of the slope of the energy vs pulse height plots with mass number $A$, for different detectors.

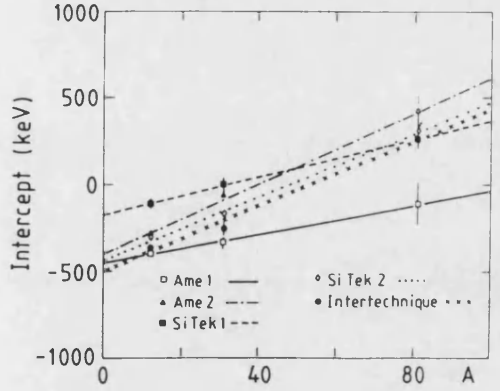


Fig. 5. Corresponding plot of the channel-zero energy of the energy vs pulse height plots with mass number $A$, for different detectors.

data points were excluded from the fitting because of bias associated with cross talk from $^{71}$Ga, which could not be satisfactorily separated in the present setup [19]. This strongly suggests that the simple empirical calibration:

$$E(X, A) = (C_1 A + C_2) X + C_3 A + C_4, \qquad (1)$$

proposed by Schmitt et al. [27–29] can be used over the energy and mass range of interest here. In eq. (1) $X$ denotes pulse height in channels and $C_1$ through $C_4$ are constants that vary from detector to detector, and can be determined by straight line regression as in figs. 4 and 5. The deviation between the true energy determined from the TOF and eq. (1) for the different detectors ranged from 0.5 to 4.5% for $^{12}$C, 1.0 to 2.0% for $^{31}$P and 0.5 to 1.5% for $^{81}$Br. It should be borne in mind that since the straight lines were regressed to recoils of three masses the above uncertainties are a measure of the uncertainty in how well eq. (1) fits our data rather than an absolute uncertainty of the method. The origin of these detector to detector differences is unclear. However one may speculate that, because the detectors are all similar from a stopping viewpoint, the differences are associated with variations in charge carrier collection. Here variations in the average electric field [7] close to the detector surface may lead to differences in charge carrier collection efficiency [34,1]. The effect is unlikely to be associated with radiation damage because the total doses are about 10% those reported by Gujrathi et al. [1] to give a doubling of the virgin leakage current.

Provided the constants $C_1$–$C_4$ are individually determined for each detector, the differing responses present no particular problems for establishment of an energy calibration. In a storage ring equipped with a gas-jet target, the extremely good energy precision of the stored beam and the vanishingly small energy loss in the target may be utilized to generate elastic recoils with extremely precisely defined energy and mass distributions. This may be conveniently carried out by using a gas cocktail with differing atomic masses as the target feed-gas and stepwise ramping of the beam energy.

### 3.3. Energy resolution

The detector energy resolution was determined from the second moment of the pulse height distribution, parameterized by the standard deviation $\sigma_{\mathrm{det}}$. The standard deviation $\sigma_{\mathrm{det}}$ of the detector response was extracted according to:

$$\sigma_{\mathrm{det}}^2 = \sigma_{\mathrm{obs}}^2 - \left(\sigma_{\Delta T}^2 + \sigma_{\mathrm{th}}^2 + \sigma_{\mathrm{str}}^2 + \sigma_{\mathrm{ms}}^2 + \sigma_{\mathrm{geo}}^2\right), \qquad (2)$$

where $\sigma_{\Delta T}^2$ is the second moment broadening contributed by the finite energy gate width $\Delta E$ ($\Delta E = 5\ A$ keV). Here $\sigma_{\Delta T} = \Delta E / 3.46$ was taken, which is appro-

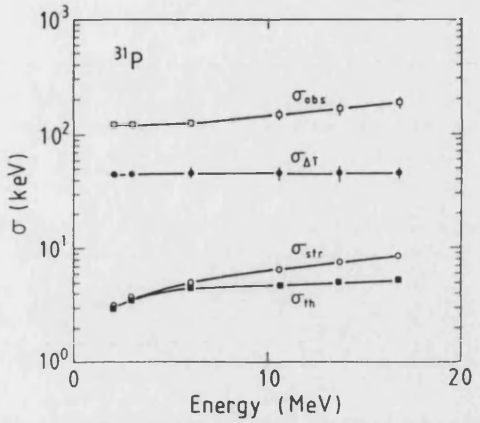


Fig. 6. Relative size of the different instrumental contributions to $\sigma_{obs}$ for the Ame 2 detector for $^{31}$P recoils vs energy.

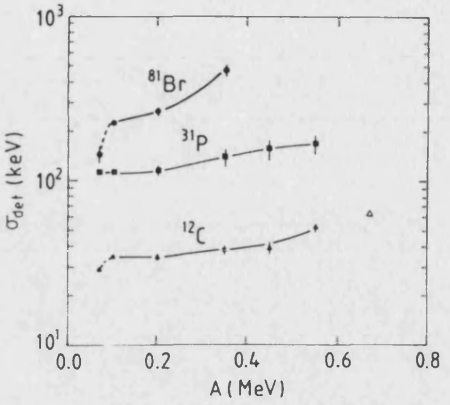


Fig. 7. Second moment of the Ame 2 detector response for $^{12}$C, $^{31}$P and $^{81}$Br recoils. The surface barrier detector $^{12}$C data point △ of Östling et al. [33] is also plotted.

priate for a rectangular time slice. $\sigma_{th}^2$ is the second moment of the energy broadening associated with thickness variations in the carbon foils [19]. Here we assumed the standard deviation of the foil thickness variation to be 5% over the area of the foils. Then the contribution from thickness variations $\sigma_{th} = 0.05\ \epsilon Nx$ where $\epsilon$ is the stopping cross section of the recoil in carbon (taken from Ziegler's et al. STOP code [26]) and $Nx$ the foil thickness in atoms cm$^{-2}$. $\sigma_{str}^2$ corresponds to the energy broadening from energy straggling in the foils. For the low velocity heavy particles considered here, the Bohr formula [30] is not valid and, as in ref. [19], we have applied a correction to this corresponding to the trend line through literature data [31]. $\sigma_{ms}^2$ arises because multiple scattering in the first carbon foil [19] leads to spreading in the ejection angle and thereby spreading in the timed flight length and consequently in the energy. This contribution is generally vanishingly small [32]. $\sigma_{geo}^2$ represents the second moment of the energy broadening from the variations in timed flight length associated with the finite range of acceptance angles for the detector telescope [19].

Fig. 6 illustrates the relative size of the different contributions vs energy for $^{31}$P recoils. Obviously the contributions associated with the carbon foil ($\sigma_{th}$ and $\sigma_{str}$) are negligible. This was also the case for $^{12}$C and $^{81}$Br and all detectors. In fig. 7 we have plotted $\sigma_{det}$ for $^{12}$C, $^{31}$P and $^{81}$Br recoils for one Ame detector which is representative of the others. The surface barrier detector data point of Östling et al. [33] is also included for comparison. We note that the lowest energy data points have larger uncertainties because the broadening associated with the energy gate width $\sigma_{\Delta T}$ becomes comparable with $\sigma_{det}$ (eq. (2)). Clearly the energy resolution is weakly energy dependent over the range 0.1–0.4 $A$ MeV and becomes better as $A$ becomes small, as one might expect. Fig. 8 compares the energy resolution of a number of detectors for $^{81}$Br recoils as well as the literature data of Gujrathi et al. [1]. Evidently the energy resolution varies from detector to detector and the variations show no obvious correlation with the data in figs. 6 and 7. The origin of this scatter is unclear, however it is most probably associated with either the detector resolution $\sigma_{det}$ or the determination of $\sigma_{obs}$ because the contributions (and thereby the effect of the small anticipated uncertainties), in $\sigma_{\Delta T}$, $\sigma_{th}$, $\sigma_{str}$, $\sigma_{ms}$ and $\sigma_{geo}$ are small (fig. 6). The scatter is thus probably associated with either $\sigma_{det}$ or the fitting procedure used to determine $\sigma_{obs}$. It is unlikely to be the latter because the peaks spanned corresponding to each time window spans at least 12 channels in the energy spectra, the pulse shape is well described by a Gaussian distribution and checks indicate the fitting

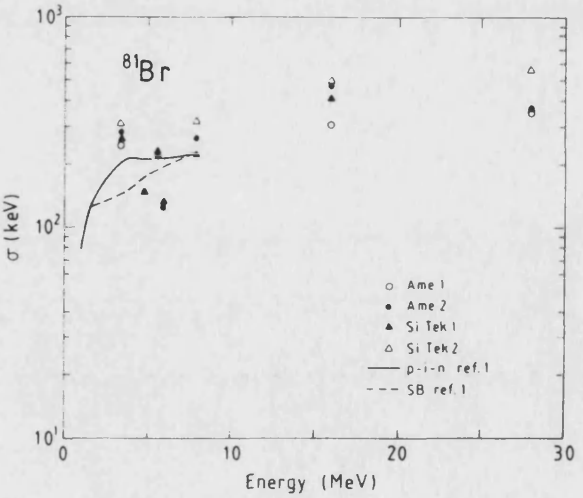


Fig. 8. Comparison of the energy resolution of the five detectors tested for $^{81}$Br recoils and literature Si surface barrier and p-i-n diode data from ref. [1].

routine is well-behaved when the line shape spans even narrower ranges of channels. If the scatter is real it might account for the discrepancy between the energy resolution for p–i–n and surface barrier diodes seen in literature [1]. Again one may speculate that their origin might be associated with the effects of local variations in the electric field [7,34,35] on the second moment of the charge collection efficiency. Plots of $\sigma_{det}$ vs $E^{1/3}$ showed that the data fitted a $\sigma_{det} = A + BE^n$ law reasonably well, where $n = 1/3$ [1,19,36]. (Note here we use $\sigma_{det}$ rather than the FWHM.) The coefficent of correlation for the different detectors varied from 0.81 to 0.99. Although the data lay reasonably close to the fitted lines we cannot rule out the possibility that the data is better described by a law with a different exponent $n$.

## 4. Conclusions

i) The TOF method presented can be used to characterize the response of silicon detectors for low energy (0.05–0.5 $A$ MeV) recoil nuclei.

ii) The pulse height vs energy relationship closely follows a straight line for each recoil isotope. The slope and intercept of these lines exhibit in turn a straight line dependence on mass number $A$, but have values that vary from detector to detector.

iii) The simple relation between energy, pulse height and mass number proposed by Schmitt et al. for fission fragments can be applied to establish an energy scale for 0.05–0.5 $A$ MeV recoil nuclei with $A = 12$ to 81, provided that detector specific constants are used. These constants can be determined from a few fixed points.

iv) The energy resolution of silicon particle detectors is comparable to that of surface barrier detectors but exhibits significant variations from one detector to another.

## Acknowledgements

Financial support from Stiftelsen Blanceflor Boncompagni Ludovisi, född Bildt, and The Swedish National Board of Technical Development (STU-F) is gratefully acknowledged. The Royal Institute of Technology is thanked for loan of their ion beam analysis facility and Lars Westerberg for discussions.

## References

[1] S.C. Gujrathi, D.W. Hetherington, P.F. Hinrichsen and M. Bentourkia, Nucl. Instr. and Meth. B45 (1990) 260.
[2] P.H. Gooda and W.B. Gilboy, Nucl. Instr. and Meth. A255 (1987) 222.
[3] N. Markevich, I. Gertner and J. Felsteiner, Nucl. Instr. and Meth. A269 (1988) 599.
[4] J.B.A. England, Techniques in Nuclear Structure Physics, part 1 (Macmillan, London, 1974).
[5] E.M. Pell, J. Appl. Phys. 31 (1960) 291.
[6] E.L. Hainsen and A.B. Whitehead, Rev. Sci. Instr. 37 (1966) 190.
[7] E.C. Finch, M. Asghar and M. Forte, Nucl. Instr. and Meth. 163 (1979) 467.
[8] C.M. Hsieh, P.C. Murley and R.R. O'Brien, IEEE Electron Devices Lett. EDL-2 (1981) 102.
[9] A.B. Campbell and A.R. Knudson, IEEE Trans. Nucl. Sci. NS-29 (1982) 2067.
[10] L. Cliche, S.C. Gujrathi and L.A. Hamel, Nucl. Instr. and Meth. B45 (1990) 270.
[11] D.W. Potter and R.D. Campbell, Nucl. Instr. and Meth. 153 (1978) 525.
[12] B.D. Wilkins, J.M. Fluss, S.B. Kaufman, C.E. Gross and E.P. Steinberg, Nucl. Instr. and Meth. 92 (1971) 381.
[13] W.N. Lennard, H. Geissel, K.B. Winterbon, D. Phillips, T.K. Alexander and J.S Forster, Nucl. Instr. and Meth. A248 (1986) 454.
[14] H. Funaki, M. Mashimo, M. Shimizu, Y. Oguri and E. Arai, Nucl. Instr. and Meth. B56/57 (1991) 975.
[15] A.H. Krulisch and R.C. Axtman, Nucl. Instr. and Meth. 55 (1967) 238.
[16] N.J. Hansen, Nucl. Instr. and Meth. 96 (1971) 373.
[17] E.C. Finch, Nucl. Instr. and Meth. 113 (1973) 41.
[18] H.J. Whitlow, Proc. High Energy and Heavy Ion Beams in Material Analysis Workshop, Albuquerque, New Mexico, 1989.
[19] H.J. Whitlow, B. Jakobsson and L. Westerberg, Nucl. Instr. and Meth. A310 (1991) 636.
[20] T.E. Hansen, Nucl. Instr. and Meth. A235 (1985) 249.
[21] M. Lindroos and Ö. Skeppstedt, Nucl. Instr. and Meth. A306 (1991) 225.
[22] I. Lavergne-Gosselin et al., Nucl. Instr. and Meth. A276 (1989) 210.
[23] F. Busch, W. Pfeffer, B. Kohlmeyer, D. Schull and F. Puhlhoffer, Nucl. Instr. and Meth. 171 (1980) 71.
[24] B. Terreault, M. Leroux, J.G. Martel, R. St.-Jacques, C. Brassard, C. Cardinal, J. Chabbal, L. Deschênes, J. Labrie and J. L'Ecuyer, Adv. Chem. Ser. 158 (1976) 295.
[25] H.J. Whitlow, A.B.Ch. Andersson and C.S. Petersson, Nucl. Instr. and Meth. B36 (1989) 53.
[26] J.F. Ziegler, J.P. Biersack and U. Littmark, The Stopping and Ranges of Ions in Matter, vol. 1 (Pergamon, New York 1985).
[27] H.W. Schmitt, W.E. Kiker and C.W. Williams, Phys. Rev. 137 (1965) B837.
[28] E. Weissenberger, P. Geltenbort, A. Oed, F. Gönnehwein and H. Faust, Nucl. Instr. and Meth. A248 (1986) 506.
[29] S.B. Kaufman, E.P. Steinberg, B.D. Wilkins, J. Unik, A.J. Gorski and M.J. Fluss, Nucl. Instr. and Meth. 115 (974) 47.
[30] N. Bohr, K. Dan. Vidensk. Selsk. Mat. Fys. Medd. 18 (1948) 8.
[31] F. Besenbacher, H.H. Andersen, P. Hvelplund and H. Kundsen, K. Dan. Vidensk. Selsk. Mat. Fys. Medd. 40 (1981) 9.

[32] P. Sigmund and K.B. Winterbon, Nucl. Instr. and Meth. 119 (1974) 541.
[33] M. Östling, C.S. Petersson, P. Johansson, A. Wikström and P. Possnert, Nucl. Instr. and Meth. B15 (1986) 729.
[34] F.Z. Henari, E.C. Finch and C.F.G. Delaney, Nucl. Instr. and Meth. A228 (1990) 439.
[35] G. Amsel, F. Pászti, E. Szilágyi and J. Gyulei, Nucl. Instr. and Meth. B63 (1992) 421.
[36] G. Amsel, C. Cohen and A. L'Hoir, in: Ion Beam Surface layer Analysis, eds. O. Meyer, G. Linker and F. Kappeler (Plenum, New York, 1976).

# Thin Detectors for the CHICSi ΔE-E Telescope

L. Evensen[1], *Member, IEEE*, T. Westgaard[1], *Member, IEEE*, V. Avdeichikov[2], L. Carlén[2], B. Jakobsson[2], Y. Murin[2], J. Mårtensson[2], A. Oskarsson[2], A. Siwek[2], H.J. Whitlow[3], E.J. van Veldhuizen[4], L. Westerberg[4], and M. Guttormsen[5]

[1]SINTEF Electronics and Cybernetics, P.O.Box 124 Blindern, N-0314 Oslo, Norway

[2]University of Lund, Div. of Cosmic and Subatomic Physics, P.O.Box 118, S-221 00 Lund, Sweden

[3]Lund Institute of Technology, Dept. of Nuclear Physics, P.O.Box 118, S-221 00 Lund, Sweden

[4]Uppsala University, Dept. of Radiation Sciences, P.O.Box 535, S-751 21 Uppsala, Sweden

[5]University of Oslo, Dept. of Physics, P.O.Box 1048 Blindern, N-0316, Oslo, Norway

## *Abstract*

A pilot series of 10 μm to 15 μm thin silicon detectors has been made for the ΔE-E telescopes in the CHICSi detector system. This system will operate at the CELSIUS heavy ion storage ring in Uppsala, Sweden. ΔE-E telescopes provide isotope identification and energy determination of fragments from nuclear collisions. The thin detectors are made as p-i-n diodes in thin etched membranes in 280 μm thick silicon wafers. The membranes are made with anisotropic etching using 25 w% tetramethylammonium hydroxide (TMAH) solution. The etch speed of this solution is very uniform across a wafer. As a result detectors with uniform thickness can be produced. The etch depth varies with less than ± 0.3 μm over a wafer and the surface microroughness is in the range from 2 to 4 nm. Each detector has a 10.0 mm × 10.0 mm active area on a 10.2 mm × 10.2 mm membrane surrounded by a 1.1 mm wide supporting frame. The detectors have leakage currents in the active area of approximately 0.5 nA at 20 V. The breakdown voltage of the detectors is above 100 V. Evaluation experiments with telescopes consisting of a thin detector in combination with a thick detector have shown excellent isotope separation capabilities. Mass separation of $^6$Li and $^7$Li is clearly observable.

## I. Introduction

The CELSIUS Heavy Ion Collaboration (CHIC) has developed a telescope detector array with silicon p-i-n-detectors (CHICSi) that will be used to study intermediate mass fragments (IMF's). These fragments can for example be produced in heavy ion collisions at the CELSIUS ion storage ring at The Svedberg Laboratory (TSL) in Uppsala, Sweden. Each telescope is built from three or four detector elements as shown in Figure 1. The first elements of the telescopes are detectors with silicon thickness $D_{Si}$ of 12 μm with a 280 μm or 500 μm Si detector behind. These are operated in a ΔE-E configuration which allows charge and mass identification. Telescopes in the very forward directions have additional E-detectors made of cerium doped Gadolinium Silicon Oxide (GSO) scintillators read out by photodiodes in order to measure high energy fragments. A 280 μm Si detector (HE flag) at the rear of the telescope is used to identify high energy fragments that pass through all detectors. The detector telescopes are assembled in rings forming a barrel shaped configuration with the detectors directed towards the interaction point. The telescope rings cover scattering angles from 15° to 160°.

A major technological challenge has been the development of technology for production and testing of the thin detectors for the ΔE-E telescopes, since 1200 detectors are required for the experiment. In a thin detector with uniform silicon thickness $D_{Si}$ the energy loss ΔE of a fragment is a function of proton number $Z$ and mass number $A$. (See e.g. [1] for details of the formalism.) This makes it possible to determine energy, proton number, and, for not too high $A$, the mass of an IMF with a ΔE-E detector telescope. Several parameters for the thin detectors need to be optimized to give good mass and energy resolution. In order to extend the capability to measure fragments with higher $Z$ and low energy the absolute thickness of the ΔE-detector should be minimized to the lowest practical one. Unfortunately, thinner detectors imply a smaller signal and a higher capacitance which cause a severe reduction in signal-to-noise ratio. Another important factor is the consequence of detector thickness variations since the energy loss is proportional to the local detector thickness. The

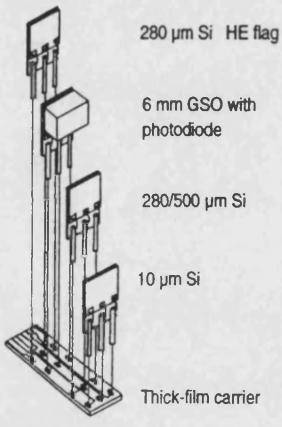


Figure 1: CHICSi detector telescope.

0018-9499/97$10.00 

absolute value of thickness variations is in practice almost independent of detector thickness with the process which has been developed. As a consequence, the ratio of detector thickness variations to average thickness increases with decreasing detector thickness. Identical particles passing the detector in positions with different thickness will produce different charge signals. This effect reduces the resolution of the detector telescope. The minimum detector thickness is therefore set by the value of detector thickness variations and the electronic noise of the detector system. To achieve acceptable resolution with a 10 μm detector the thickness variations should be within 0.5 μm.

An approach to achieve thin detectors which is compatible with standard processing equipment is to process thin p-i-n-diodes on wafers with etched membranes. The design and processing of the thin detectors are then similar to that of conventional silicon detectors. The focus in this study has been on improving the thickness uniformity and reducing the surface microroughness caused by the etch procedure. Tests have been carried out to ensure that the silicon detectors will be compatible with the operation requirements for experiments at the CELSIUS storage ring. The thin detectors have been characterized both mechanically and electrically and their capability for energy and mass separation has been demonstrated.

## II. Etching of Thin Detectors

Several approaches to fabrication of thin detectors have been published [2], [3], [4], [5]. An intuitively straight forward process is to use wafers of adequate thickness. The minimum, commercially available, wafer thickness is in the 10 μm range. Processing of wafers with thickness below 30 μm demands non-standard processing equipment and procedures. Detector handling and mounting are also complicated. For this reason thin detectors have usually been manufactured by etching thin areas for the active part of the detector. With this technique thicker substrates can be used, and thin membranes can be realized with standard processes for detector fabrication. The etching process has to meet three requirements to be useful for detector fabrication:

- It must be possible to etch membranes with a controlled thickness. This can be achieved by using an etch with a stable etch rate or utilizing a stop layer.
- The increase of thickness non-uniformity during the etching process has to be minimized. A common problem is grooves at the border of the etched areas.
- The etch should not increase short-range surface microroughness.

The growth of an epitaxial silicon layer is frequently exploited to achieve stopping of the etching and improve uniformity [4]. This layer can either be highly p-type doped, or n-type doped if it is used with an electro-chemical etching process. The epitaxial silicon is not ideal as detector material because of the density of impurities and defects. Both isotropic and anisotropic etchants can be used for etching. A common isotropic etchant is a mixture of hydrofluoric acid, nitric acid and acetic acid (HNA). The reaction with silicon is extremely exothermic and the etch speed increases considerably with temperature thus making it difficult to achieve a defined and uniform thickness. The mixture is very aggressive and gold or silicon nitride must be used as a mask material. Commonly used anisotropic etchants have been ethylenediamine-pyrocatechol-water (EPW) or potassium hydroxide (KOH) solutions [6]. A problem with both of these etchants has been to achieve uniform membranes with smooth surfaces [4], [5], unless an etch stop layer is used. A process with anodic oxidation of silicon has been reported to circumvent the uniformity problem, but it introduces problems with high doping density and complexity of etching [4]. Thermally grown silicon oxide can easily be used as an etch mask in combination with EPW, while the high etch speed of silicon oxide in KOH requires very thick oxide layers.

Recently a considerable interest has emerged for etching of 3-dimensional silicon micromechanical devices with tetramethylammonium hydroxide (TMAH) because of its compatibility with CMOS processing [7]. Several technological advantages promote the use of TMAH which is known from semiconductor processing as an alternative for metal ion free developer for positive photoresist. TMAH etches silicon dioxide very slowly, almost four orders of magnitude slower than the (100) plane of silicon [7], allowing thermal oxides to be used for masking. This simplifies processing compared to KOH and one avoids the highly toxic and carcinogenic EPW solutions. However, TMAH has been reported to give pyramidal hillocks at concentrations below 15 w% [7]. The quality of the etched surface can be very good at high concentrations (above 25 w%). In section IV a surface microroughness of 3.6 nm is reported for etching with TMAH, which is considerably better than the 33 nm reported for etching with KOH [5]. The etching speed of TMAH is comparable to that of KOH [6], [7], and the etch depth uniformity is excellent without problems with groove formation along the edges of the etched area. At a controlled temperature and with a sufficient volume of etching solution the etch rate is stable. This makes the etch ideal for etching of membranes in float zone silicon with time control for obtaining the target membrane thickness. This method was exploited for producing the ΔE-detectors. The approach requires a precise thickness measurement before the final etching step.

## III. Design and Processing

The 12 μm, 280 μm and 500 μm thick CHICSi silicon detector elements have all been produced with a common front side mask design. The active area of the ΔE-detectors is a 10.0 mm × 10.0 mm p-n junction on a 10.2 mm × 10.2 mm membrane of n-type silicon. A cross section of the detector is shown in Figure 2. The entire active area is covered by Al which is connected to the p-type diffusion by a narrow contact

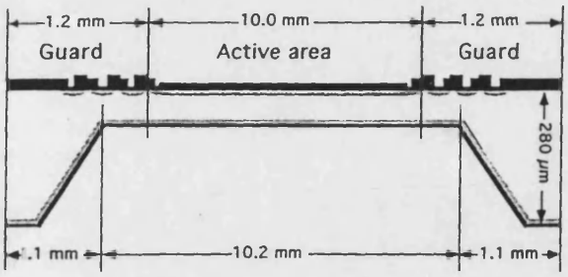


Figure 2. Schematic cross section of a ΔE-detector. Black is aluminum, dark gray is oxide, $n^+$- and $p^+$-diffusions are light gray.

hole along the periphery. A multiguard structure surrounds the active area. The thin region of ΔE-detectors extends out to halfway between the first and second guard rings. Only the first guard ring is of importance for these detectors as they will be operated at low or moderate voltages. This guard ring is grounded and will collect leakage current generated in the frame structure. The distance from the membrane border to the edge of the device is 1.1 mm in order to have a frame which ensures the mechanical integrity of the detectors. A narrower frame would be advantageous because the dead area of the detector system can be reduced, but due to the large number of detectors (~ 2000) for the total detector system it is important to have robust detectors. The frame is wider along the bottom edge where a part of the active area extends out on thick silicon. This design enables external connection with bond wires, but the pads are large enough to allow conventional wires to be glued to the pads.

The full guard structure was optimized for use on E-detectors processed on 500 µm thick silicon. The multiguard structure uses concentric, floating $p^+$-type diffusions with the inner ring contacted (grounded) as for the ΔE-detectors. The other rings are biased by the reach-through (punch-through) mechanism. Metal field plates connected to each $p^+$-type diffusion stabilize the surface potential on the oxide between the diffusions and thereby improve long term stability [8]. To ensure stable operation at full depletion and maximum charge collecton over the life-time of the experiment, the detectors must also withstand considerable overdepletion at the initial testing. The width of 1.2 mm around the active area allows the use of a very stable guard structure. The stabilization of the detectors is important as the primary signal particles are highly damaging nuclear fragments which the detectors must tolerate without serious degradation of performance. It is also required that the detectors survive a low energy background of electrons and X-rays. Since the detectors will be operated in an ultrahigh vacuum environment they must withstand repeated bakeout to 125 - 150 °C. No low vapor pressure materials can be used for mounting the detectors because ultrahigh vacuum conditions are required for the experiment.

High resistivity (5000 Ωcm) phosphorus doped wafers from TOPSIL were used for processing the detectors. The wafers had diameter 100 mm and thickness 280 µm, and the orientation was (100) for compatibility with the anisotropic etching. Both wafer sides were polished to SEMI specifications. Initially an 800 nm thick thermal oxide layer was grown for masking and passivation purposes. A standard photolithography process with etching of the oxide defined the oxide etch mask for etching of thin membranes on the reverse side of the wafers. The membranes were etched at 80 °C in a 25 w% solution of TMAH in water. A two step etching process with time control allowed precise control of the membrane thickness. Openings for the boron implant were defined on the front side of the wafer by lithography after careful cleaning. A thin layer of thermal oxide served as an implant window for boron on the front side and phosphorus on the back side. The implants were activated by an annealing process in $N_2$ at 900 °C. Contact holes were defined by lithography on the front side leaving the back side unprotected. Following etching of the contact holes 0.2 µm thick films of aluminum were sputter deposited on the front and back sides. The front-side metallization was patterned before alloying at 450 °C in forming gas. The wafers were subsequently cut into detector chips with a diamond saw. To produce detectors with a narrower frame, laser cutting of wafers might be a better alternative than diamond saw cutting.

## IV. Evaluation

The wafers and detector chips have been characterized mechanically, electrically, and as detectors.

### *A. Mechanical Evaluation*

One problem with production of thin detectors is to measure the absolute thickness and uniformity. The 10 µm range is outside the range where calibrated thickness standards for mechanical measurements are readily available. Several methods for thickness measurement can be conceived but most of them are not compatible with large volume production of thin detectors. Energy loss measurements of protons or alpha particles are excellent for uniformity measurements but are difficult to calibrate for absolute thickness measurements. Light attenuation has similar problems and must be calibrated, furthermore source and detector variations introduce too large uncertainties to be of practical use. As the index of refraction for silicon is well known, measurement of interference patterns with an FTIR instrument is considered an accurate method, but equipment for these measurements on small areas was not available at SINTEF. During etching mechanical measurements of membrane thickness were performed with a double stylus type instrument (TESA Electronic GND22 with two TESA GT10 measurement probes). Five fixed points were measured on each wafer and the average membrane thickness was used to determine the remaining etch time. The mechanical system was calibrated with shims that could be traced to Norwegian national standards. For 48 wafers a

standard deviation of 0.7 μm for the wafer average of the membrane thickness was achieved. The variation on a single wafer can be larger, because some wafers were wedge-shaped.

The thickness measurement for the final selection of finished ΔE-detectors was done by measuring the detector capacitance at a fixed voltage which was higher than the voltage needed for the depleted region to extend into the $n^+$-type doped region. This method measures the width of the depletion zone of the detector while the total thickness can be computed taking the thickness of dead layers into account. For comparison with mechanical stylus measurements it is better to calculate the total detector thickness $D_{diode}$ including oxide and metal layers in stead of the silicon detector thickness $D_{Si}$. The advantages of the method are that it is compatible with the electrical testing of detectors, it is non-destructive, and it is useful for detector response calibration. In contrast, testing with particle beams is time consuming and expensive. The capacitance method is accurate if an independent absolute measurement of the thickness is available so that a precise value for the dead layer thickness can be extracted. The basis for the calculation of thickness is the formula for the capacitance $C$ of a p-i-n-diode:

$$C = \varepsilon_{Si}\varepsilon_0 \frac{A_{active}}{w_{depl}} \qquad (1)$$

$\varepsilon_{Si}$ is the relative static dielectric constant for silicon, $A_{active}$ is the area of the pn-junction, and $w_{depl}$ is the width of the depletion zone. For an applied voltage above the depletion voltage the total detector thickness $D_{diode}$ is:

$$D_{diode} \approx \varepsilon_{Si}\varepsilon_0 \frac{A_{active}}{C} + x_n + x_p + d_{oxide} + d_{Al} \qquad (2)$$

$x_n$ and $x_p$ are thicknesses of dead layers in silicon on each side of the detector, $d_{oxide}$ is the front oxide thickness and $d_{Al}$ is the total thickness of aluminum layers. The total dead-layer thickness estimated from $x_n$, $x_p$, $d_{oxide}$, and $d_{Al}$ is about 1.4 μm.

If a reliable independent measurement of thickness is available it is better to use:

$$D_{diode} \approx \varepsilon_{Si}\varepsilon_0 \frac{A_{active}}{C} + \Delta_{empirical} \qquad (3)$$

$\Delta_{empirical}$ is an empirically determined thickness correction which includes all dead layers. This dead-layer has been estimated by mechanically measuring the membrane thickness in the center of the membrane and subtracting the depletion thickness calculated from a capacitance measurement. A value of 1.1 μm for $\Delta_{empirical}$ is obtained in this way, based on measurements on 98 detectors. The discrepancy between the dead layer estimate of 1.4 μm from process parameters and 1.1 μm from mechanical measurements is within the combined measurement errors of both methods. For the first estimate it is difficult to determine $x_n$ and $x_p$ with a better precision than ± 0.1 μm, while the offset error in the mechanical measurement is an important error source for the second estimate. As a consequence capacitance measurements can be used to obtain reliable values for the average detector thickness. An average membrane thickness value of 11.4 μm with a standard deviation of 0.8 μm was achieved for 630 ΔE-detectors. Each CHICSi telescope ring will be built from detectors within a small thickness range to have a uniform response in each ring.

Thickness uniformity is important for the detector quality and the yield of the production. Too large variations over a membrane will cause insufficient energy resolution. If the variations over the wafer are too large, few membranes will have the specified thickness. With a time dependent thickness definition, the thickness uniformity of the starting wafer is most critical as it will influence the number of diodes on a wafer that are within the thickness specification. In the extreme case, with an ideal etch, the wafer thickness uniformity will define the thickness uniformity across each detector. Measurements of etch depth with a Tencor Alpha-Step 500 profilometer indicate that the etch depth variation, measured from the starting surface of the wafer down to the etched membrane, varies by as little as ± 0.1 μm. This is about the level of accuracy of the instrument. Formation of grooves along the edges could not be observed for TMAH etching with the instruments available. This implies that the etching process itself does not introduce uniformity problems for the membranes. Most wafers that were measured had an etch depth variation across the wafer which was less than ± 0.3 μm. Temperature variations in the etch bath can cause such variations. This variation alone does not introduce any significant yield reduction. Thus for the TMAH etch the most important parameter determining the uniformity was the thickness uniformity of the starting wafer, because the etch process is nearly ideal with respect to uniformity. In the worst case it was observed as much as 7.4 μm thickness variation of membranes across a wafer which would lead to 1.3 μm variation across a detector. Few detectors of this wafer had the correct thickness, and none had satisfactory uniformity. This implies that the thickness uniformity of the starting wafer will determine how many devices from each wafer that are within specifications.

The short-range surface microroughness is characteristic of the etchant and can indicate the ability to etch uniformly. The surface microroughness $R_a$ was measured with a Tencor Alpha-Step 500 profilometer along a 500 μm long path near the center of the membrane. Leveling was performed between the positions at 50 and 450 μm to reduce the influence of membrane bulging caused by the passivation oxide. $R_a$ is the arithmetic average deviation of the absolute values of the microroughness profile from the mean value along the measurement path. A surface microroughness $R_a$ in the range 2 - 4 nm was measured. A similar measurement was performed with a WYKO optical scanning interferometer which confirmed the mechanical measurements giving $R_a$ = 3.6 nm.

Some detectors have been tested using a collimated beam of α-particles from a $^{241}$Am source. A circular collimator with 1 mm diameter defined the spot on the membrane. The beam was scanned in steps over the detector. The residual energy of the α-particles after they had penetrated the thin detectors was measured with a silicon p-i-n-detector. The thickness of the membrane in the probed spots can be calculated from the energy loss. Results for 5 spots on a detector are shown in Table 1.

Table 1.
α-particle energy-loss thickness measurement on a detector. The thickness measured is the total detector thickness $D_{diode}$. The center of the coordinate system is the center of the active area.

| Position [mm] | Thickness [μm] |
|---|---|
| (0,0) | 12.73 |
| (3.5, -3.5) | 12.51 |
| (3.5, 3.5) | 12.80 |
| (-3.5, -3.5) | 12.55 |
| (-3.5, 3.5) | 12.64 |

## B. Diode evaluation

Every diode has been electrically characterized by measuring the capacitance $C$ and the leakage currents $I_{active}$ and $I_{guard}$ as a function of bias $V$. The depletion voltage is determined to be about 2.5 V from $1/C^2$ versus $V$ curves. This is significantly higher than the value which is expected from the substrate resistivity, but for these thin detectors depletion of the tail regions in the dopant profile for n-type and p-type diffusions contribute significantly to the shape of the curve. The leakage current $I_{active}$ in the active area is typically 0.5 nA at 20 V (approximately 8 times overdepletion) with a guard leakage current $I_{guard}$ of typically 0.2 nA at 20 V. Some detectors have been tested with voltages up to 200 V. The leakage current increases with increasing bias voltage as shown in Figure 3. Due to the large values of the electric field in thin detectors the bulk avalanche effect will cause electrical breakdown when the bias voltage reaches a sufficient value. This breakdown voltage is influenced by the detector thickness, and it will decrease with decreasing thickness.

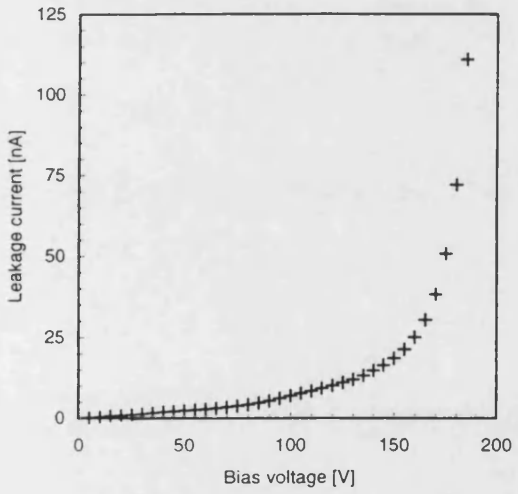


Figure 3. Leakage current as function of bias voltage for a detector with 12 μm silicon thickness.

## C. Detector performance

To provide a source of IMF's for testing of the detectors a detector telescope was set up in the CELSIUS target chamber at a backwards scattering angle of 140°. No tendency of instability in the UHV environment was observed. A beam of protons impinged on a Kr gas target. The energy of the proton beam was slowly ramped from 150 to 500 MeV. The ΔE-E telescope using 12 μm ΔE-detectors and 280 μm E-detectors resolved intermediate mass fragments with atomic numbers up to $Z = 7$. Figure 4 shows a point plot of ΔE vs. E for one of the telescopes that has been tested. The resolution is sufficient to separate $^6$Li from $^7$Li. Inspection of the measurement data reveals that $^7$Be and $^9$Be are resolved as well, but this is not evident from Figure 4 as the production of Be fragments is lower than that of Li fragments for this particular reaction. The low energy threshold which is set by the thickness of the ΔE-detector corresponds to about 1A MeV, while the high

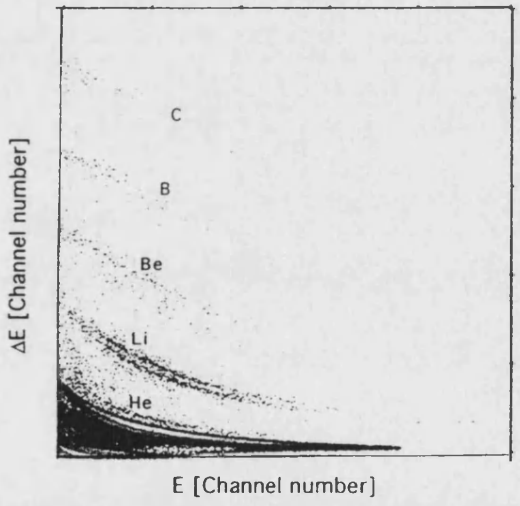


Figure 4: ΔE vs. E plot for intermediate mass fragments emitted at 140° from 150-500 MeV protons incident on a Kr gas target. Light gray indicates the highest density of fragments. The full scale readings are approximately 31 MeV for the E-axis and 23 MeV for the ΔE-axis.

energy threshold is about 6A MeV for the test telescope. This value for the high energy threshold is due to the 280 μm thickness of the E-detector. IMF's with higher values of $Z$ have been found in evaluation experiments with heavier ions performed with CHICSi test telescopes in the CELSIUS target chamber, for instance IMF's up to $Z$=14 have been resolved for the reaction $^{14}N$ on $^{128}Sn$. For the CHICSi experiment the upper limit in energy of IMF's will be 60A MeV in forward telescopes, 14A MeV in mid (~ 90°) telescopes and 6.5A MeV in backward telescopes. These regions of IMF detection are relevant both with respect to empirical knowledge and theoretical estimates [9].

## V. Conclusions

Silicon detectors in the 10 μm thickness range can be produced in commercial quantities for use in telescopes for identification and energy measurement of IMF's. Etched detector membranes of sufficient quality for this purpose have been made by etching in TMAH. The diode processing yielded stable, low leakage current diodes with high voltage capability. Test telescopes have demonstrated that the detectors provide isotope separation capability for light and medium mass fragments.

For future systems it is important to note that the etching of membranes in combination with standard processing with ion implantation gives a moderate cost alternative for large volume applications.

## VI. References


[1] A.G. Seamster, R.E.L. Green, and R.G. Korteling, "Silicon detector ΔE, E particle identification: A theoretically based analysis algorithm and remarks on the fundamental limits to the resolution of particle type by ΔE, E measurements", *Nucl. Instr. and Meth.*, vol. 145, pp. 583-591, 1977.

[2] L. Evensen, "Feasibility of thin detectors", *Proceedings of the ECFA study week on instrumentation for high luminosity colliders, Barcelona September 1989, CERN 89-10, ECFA 89-124*, vol. 1, pp. 351-355, 1989.

[3] L. Lavergne-Gosselin et al., "On the use of thin ion implanted Si detectors in heavy ion experiments", *Nucl. Instr. and Meth.*, vol. A276, pp. 210-215, 1989.

[4] L. Stab, "Thin epitaxial silicon detectors", *Nucl. Instr. and Meth.*, vol. A288, pp. 24-30, 1990.

[5] B. Schmidt, J. von Borany, and D. Schubert "Application of wet chemical selective etching to the fabrication of thin silicon detectors", *Nucl. Instr. and Meth.*, vol. A326, pp. 21-26, 1993.

[6] H. Seidel et al., "Anisotropic etching of crystalline silicon in alkaline solutions", *J. Electrochem. Soc.*, vol. 137, pp. 3612-3632, November 1990.

[7] O. Tabata et al., "Anisotropic etching of silicon in TMAH solutions", *Sensors and Actuators A*, vol. 34, pp. 51-57, 1992.

[8] B.S. Avset and L. Evensen, "The effect of metal field plates on multiguard structures with floating $p^+$ guard rings", *Nucl. Instr. and Meth.*, vol. A377, pp. 397-403, 1996.

[9] "CHICSi - A proposal for a multi-detector ΔE-E particle telescope", edited by M. Guttormsen, *University of Oslo preprint*, UiO/PHYS/93-01, 1993.

ELSEVIER

Nuclear Instruments and Methods in Physics Research B 000 (1997) 000–000

NIM B
Beam Interactions with Materials & Atoms

# Effects of energy deposition by nuclear scattering in silicon p-i-n diode detectors

Harry J. Whitlow [a,*], Sander J. Roosendaal [f], Mohamed El Bouanani [a,b], Roberta Ghetti [c], Peter N. Johnston [a,b], Bo Jakobsson [c], Ragnar Hellborg [a], Håkan Petersson [d], Per Omling [d], Zhanguo Wang [d,f], the CHIC collaboration [g]

[a] *Department of Nuclear Physics, Lund Institute of Technology, Box 118, S-221 00 Lund, Sweden*
[b] *Department of Applied Physics, Royal Melbourne Institute of Technology, GPO Box 2476V, Melbourne 3001, Australia*
[c] *Division of Cosmic and Sub-atomic Physics, Lund University, Box 118, S-221 00 Lund, Sweden*
[d] *Department of Solid State Physics, Lund Institute of Technology, Box 118, S-221 00 Lund, Sweden*
[e] *Debye Institute of Surface and Interface Physics, Utrecht University, Utrecht, The Netherlands*
[f] *Institute of Sciences, Chinese Academy of Sciences, P.O. Box 912, Beijing 100083, People's Republic of China*

**Abstract**

The changes in thick (~300 μm) and thin (15 μm) Si p-i-n diode detectors that take place as a result of alpha particle and $^{63}Cu^{5+}$ ion irradiation have been studied by Deep Level Transient Spectroscopy (DLTS) and by monitoring the reverse-bias leakage currents. A linear increase in reverse-bias current with α-particle dose was observed that could be attributed to the formation of vacancy-associated defects (divacancy, A- and E-centres). Damage within the active layer of the device, characterised by the increase in leakage current per unit active volume, together with literature pion, proton and heavy ion data, exhibited a linear dependence on the energy deposited in nuclear processes over many orders of magnitude. Annealing at temperatures of 150°C for 4 h (vacuum bakeout) resulted in a reduction in leakage current and the size of the DLTS peaks became smaller. This temperature is much lower than expected for removal of divacancies, suggesting that recovery of the reverse bias current is mediated by other defect centres. 

*PACS:* 79.20-m; 61.80.-x; 61.80.Jh
*Keywords:* Si charged particle detectors; p-i-n diodes; Radiation damage; Leakage current; Nuclear stopping

## 1. Introduction

Detectors based on the collection of charge carriers in reversed biased Si diodes [1] have been the workhorse instrument for measuring the energy of light and heavy ions for nuclear physics and MeV-ion beam analysis since the introduction of the Au/

* Corresponding author. Fax: +46-46-222 4709; e-mail: harry.whitlow@nuclear.lu.se.

0168-583X/97/$19.00 
*PII* S0168-583X(97)00632-0

NIMB 5078



n-Si surface barrier detector [2]. Since the mid 1980s Si p-i-n devices produced by planar technology [3] have been steadily replacing the Au/n-Si detectors for many applications. Si p-i-n structures, such as are used for photodiodes, have been found to have comparable [4–6] resolution to conventional Au/n-Si surface barrier detectors for protons, $^4$He and heavy ions [7,8]. A number of characteristics of Si p-i-n devices makes them preferable to Si surface-barrier detectors for many applications in experimental nuclear physics and ion beam analysis. These include lower leakage current ($<1$ nA cm$^{-2}$), UHV compatibility (bakeable to ~200°C) and the possibility of using conventional Si microelectronic processing technology to fabricate detectors of any planar shape and even integrate many detector cells to realise 1- and 2-dimensional position sensitive detectors (e.g. microstrip and pixel detectors). This has led to their large scale adoption in high energy physics which has stimulated a number of theoretical [9–11] and experimental (e.g. [12–23]) studies of the radiation hardness of Si detectors under n- and γ-irradiation. It is an interesting question whether this data can be scaled to the case of ion irradiation where the density of displacement damage is very much greater, especially around the end of range.

A number of studies have been reported on the formation of localised defect centres in Si as a result of ion bombardment. Svensson et al. [23] have observed that proton, or heavier ion, irradiation of Si, lead to the formation of two acceptor levels ~0.25 and ~0.42 eV below the conduction band edge, which were attributed to doubly and singly negative-charged divacancies, respectively. The depth distributions of the two centres were very similar and the amplitude ratio of Deep Level Transient Spectroscopy (DLTS) peaks from the two levels was very similar for different ions ranging from protons to $^{127}I^{10+}$. Other (minor) peaks may be the A-centre (V–O), the E-centre (V–P) and carbon based complexes [9,24,25,21]. Often, these studies have been undertaken from the point of view of minority carrier lifetime control in Si power devices by high energy ion irradiation. Hallen et al. [26] have observed that there is a significant proton dose rate dependence in the formation of electrically active divacancy and A-centres which they could explain in terms of overlap between the vacancy distribution from one ion and the interstitial distribution from another ion stopping in close proximity both in time and space.

The CELSIUS Heavy Ion Collaboration (CHIC) is currently fabricating a 3-π Si-based detector telescope array (CHICSi) for inclusive measurement of (1–60A MeV) intermediate mass fragments from heavy ion collisions at the cluster gas-jet target station of the CELSIUS storage ring accelerator facility [27,28]. This will be based on $\Delta E$–$E$ detector telescopes where the $\Delta E$ detector is formed in a membrane that is etched out of a Si wafer [28–30]. For this, and work on Recoil Spectrometry [31–35] we have an interest in the degradation of Si detectors resulting from ion irradiation. The overall objective of the present work is to relate the energy deposition and defect formation to charged particle irradiation induced changes in Si p-i-n detectors.

## 2. Experimental

$^4$He irradiations were carried out in an off-line ion-pumped UHV chamber at a pressure of $10^{-7}$–$10^{-9}$ mbar using thin bakeable $^{241}$Am and $^{226}$Ra sources. Al apertures were used to define the central area of the diodes that were irradiated. In order to achieve high $^4$He fluences in a reasonable laboratory time scale (days) the distance between source and detector was set at fixed distances in the range 3–5 mm. The detectors under investigation were connected to an Ortec 142B preamplifier. The bias was supplied by a SILENA quad-bias supply 7710. This was also used to measure the leakage current with 1 nA resolution. A conventional spectroscopy amplifier and MCA were used to measure the energy spectra. A counter was connected to register the number of particles impinging on the detector.

In a second series of experiments 18 MeV $^{63}Cu^{5+}$ ions from the Lund NEC tandem Pelletron were scattered from a thick Au target at 90° to simulate low energy target residues from heavy ion collisions and heavy recoiling target atoms in Recoil Spectrometry. The maximum energy of the scattered ions corresponded to 0.15 A MeV.

Hamamatsu p-i-n diodes were collimated with a 3 mm diameter aperture and the particle dose to the detector was measured directly by operating the diode as a counter. Irradiation was carried out in a series of doses up to $3 \times 10^8$ $^{63}Cu^{5+}$ ions $cm^{-2}$. The chamber pressure for the measurements at the Pelletron was about $10^{-5}$ mbar.

Three types of Si p-i-n detectors were used for the tests. For most of the tests Hamamatsu S-1223-01 p-i-n photodiodes were used. These have an active area of $3.05 \times 3.05$ $mm^2$, ~300 μm thickness and are mounted in TO-5 package. The metal cap together with the glass window were carefully removed by parting-off in a lathe to leave a naked p-i-n photodiode on its header. These p-i-n diodes have an active region defined by a diffused $p^+$ layer on a weakly doped n-type substrate. The active area is covered with a thin passivating $SiO_2$ layer [38]. Contact to the $p^+$ layer is made by an Al contact around the edge of the active area. C–V measurements revealed that the background n-type doping in the i-region was $4.6 \times 10^{12}$ $cm^{-3}$ uniform with depth and with an absence of electrically active centres indicated by a flat featureless DLTS spectrum. The bias voltage at which the reverse-bias current was measured was 25 V. According to the manufacturers data [38] this corresponds to depletion into the $n^+$ layer (e.g. over biased).

The other two types of detectors investigated were fabricated by SINTEF [28] as prototype detectors for the CHICSi detector telescope array. These were of two thicknesses a nominal 15 μm thick and active area 10 × 10 $mm^2$ fabricated by a special etching technique [28] and a thicker 280 μm detector. These detectors were supplied as naked Si chips and were mounted on a copper plate. Thermosetting Ag-loaded epoxy resin [37] was used to bond the detector to the copper plate and also attach the 1 μm Al–Si wire used for electrical connections to the front contact and guard electrode pads. The bias voltages at which the reverse bias current was measured were 6 and 30 V for the ~15 and 280 μm detectors, respectively. This was selected on the basis of C–V measurements to correspond to a depleted layer that extends into the $n^+$ region (e.g. over biased).

A Semilab DLS-83D Boxcar integrator DLTS spectrometer controlled by a personal computer was used for the DLTS measurements of the α-particle irradiated Hamamatsu diodes from liquid nitrogen to room temperature. A similar spectrometer was used to measure DLTS spectra from the $^{63}Cu^{5+}$ irradiated diodes from liquid-helium to room temperature.

Annealing of the Hamamatsu diodes was carried in a laboratory oven in air (4 h at 150°C) whilst the SINTEF diodes were heat-treated during a bakeout cycle of the UHV chamber.

## 3. Results and discussion

The increase in reverse-bias current density $\Delta J$ vs. $^4$He-particle fluence for a thin SINTEF detector and a thick Hamamatsu detector is shown in Fig. 1. $\Delta J$ is the increase in leakage current, $\Delta I$, per unit active volume which is taken to be the product of the irradiated area defined by the collimator, and the range of ions in the detector. The range of $^4$He was estimated using the TRIM-96b code [39]. In the case of the thin detectors where the $^4$He are not stopped in the detector, the irradiated volume was taken to be the product of the collimator area and Si membrane thickness. $\Delta J$ and fluence both depend inversely on the irradiated area, thus the results in Fig. 1 are independent of uncertainties in this parameter. The leakage current prior to irradiation was less than 1 nA for all diodes (corresponding to 0.37 pA $cm^{-3}$). Evidently

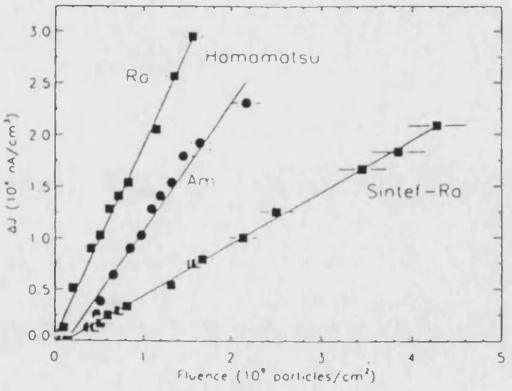


Fig. 1. Reverse bias leakage current density vs. $^4$He dose for Hamarmatsu phototodiodes and 15 μm SINTEF photodiode for $^4$He from $^{226}$Ra and $^{241}$Am.

NIMB 5078



Table 1
Values of the damage constant $\alpha$ and the ratio of damage constant to average energy deposited in nuclear scattering $S_n$ in the active layer

| Detector | Ion | Range (μm) | $S_n$ (keV μm$^{-1}$) | $\alpha$ (fA cm$^{-3}$ ion$^{-1}$) | $C$ ($10^{-7}$ nA MeV$^{-1}$) |
|---|---|---|---|---|---|
| | $^{241}$Am-α | 27.3 | 0.873 | 14.5 | 1.65 |
| Hamamatsu | $^{241}$Am-α | 27.3 | 0.873 | 11.8 | 1.34 |
| S1223-01 | $^{226}$Ra-α | 30.4 | 0.801 | 18.3 | 2.32 |
| | $^{226}$Ra-α | 30.4 | 0.801 | 18.6 | 2.37 |
| SINTEF | $^{226}$Ra-α | 12 | 0.138 | 4.7 | 3.38 |
| 15 μm | $^{226}$Ra-α | 12 | 0.145 | 1.9 | 1.33 |

$\Delta J$ is linearly dependent on fluence and does not show any saturation effects. The slope of the lines, termed the damage factor, $\alpha = \Delta J/\Phi$, where $\Phi$ is the ion fluence is presented in Table 1 together with the average $^4$He energies for our measurements.

Fig. 2 shows $\Delta J$ for a SINTEF detector that was subject to a 13 h vacuum bakeout during the irradiation. The detector was surrounded by, and only in thermal contact with, the vacuum chamber. Estimates using the Stefan–Boltzman law showed the detector would be within 1°C of the final chamber temperature within a minute. The chamber temperature reached 110°C after some hours. The slopes ($\Delta J/\Phi$) before and after the heating–cooling cycle are identical. However, the bakeout has led to smaller value of $\Delta J$ than predicted by the straight line dependence on $\Phi$ seen in Fig. 1. Thus the bakeout has led to a reduction in reverse-bias current. This is noteworthy because divacancy centres ($V_2^-$, $V_2^{2-}$) which have previously been reported as being the dominating centres in ion-irradiated Si [23] are, on the basis of electron irradiation experiments [40], not expected to become mobile and annealed out at temperature below about 340°C over periods of 30 min. The same behaviour in the leakage current was also observed for the diodes irradiated with $^{63}Cu^{5+}$ ions after heat treatment at 200°C.

In order to identify the defect centres formed, DLTS measurements were undertaken. Fig. 3 shows the DLTS temperature spectrum of a Hamamatsu diode irradiated with alpha particles

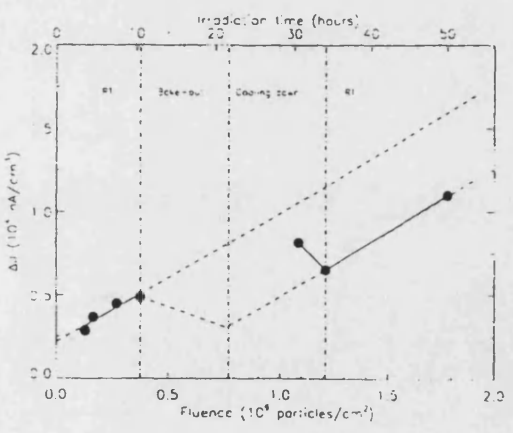


Fig. 2. Leakage current per unit active volume vs. time for a 15 μm SINTEF photodiode subjected to a ~110°C vacuum bakeout during irradiation with $^4$He from $^{226}$Ra.

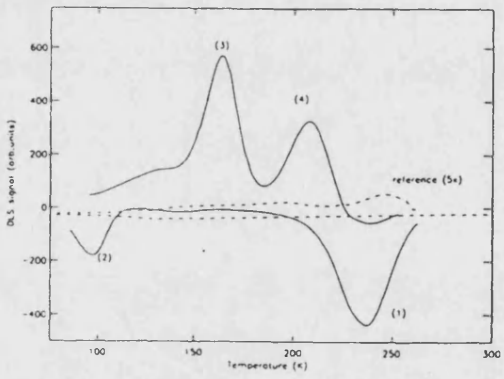


Fig. 3. DLTS spectrum for a Hamamatsu photodiode irradiated with $^4$He from $^{241}$Am. Negative going signals correspond to electron traps seen during minority carrier injection only mode. Positive going signals correspond to hole traps seen during minority and majority carrier injection mode. The dashed lines correspond to the DLTS signals before irradiation. Peaks (1)–(4) are assigned to $E_c - 0.424$, $E_c - 0.116$, $E_v + 0.374$ and $E_v + 0.296$ eV energy levels, respectively.

NIMB 5078



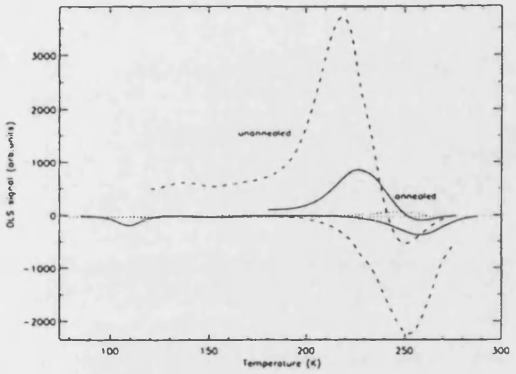


Fig. 4. DLTS spectrum for a Hamarmatsu photodiode irradiated with $^4$He from $^{241}$Am. Before (dashed lines) and after (solid lines) annealing at 150°C in air. Negative going signals correspond to electron traps seen during minority carrier injection only mode. Positive going signals correspond to hole traps seen during minority and majority carrier injection mode.

changes in the defect population ~~that lead to~~ which in turn cause an apparent shift in the composite DLTS peak position.

The fact that the leakage current density recovers as a result of annealing at temperatures below 250°C also suggests that the peak (1) in Fig. 3 cannot be uniquely associated with divacancies, but most likely also E-centres. This is because annealing of divacancies in e-beam irradiated material requires heat treatment at ~350°C [40]. E-centres are reported to anneal out at about 150°C [43]. One might also speculate that B, C, O and P impurity atoms could provide a low-temperature annealing out mechanism for divacancies by acting as efficient trapping sites for vacancies [25]. The peak at about 110 K, (Fig. 4) formed after annealing and tentatively assigned to A-centres might be indicative of such a process. This hypothesis is supported by Brotherton and Bradley's [25] observation that divacancy annealing rates are considerably greater and E-centre formation smaller in MeV e-beam irradiated Schottky diodes as compared to p-i-n diodes where a high oxygen content was believed to be incorporated during fabrication. It is also supported by Li's [10] simulation study of the space charge density in n-irradiated Si. It is difficult to draw conclusions without detailed knowledge of the impurity contents and single- and divacancy-concentrations in our samples, however such mechanisms can explain reports [7,10,12,15,18,20,44] of reverse current recovery in irradiated diodes stored for months at room temperature or subjected to low temperature (~100°C) heat treatment.

Fig. 5 shows the damage factor $\alpha$ vs. $S_n$, the average energy deposited per unit length by primary and secondary particles in nuclear processes averaged over the trajectory of the particle in the detector. The damage factors are from our data (thick and thin detectors) and also literature values [7,15,17,20,45–47] for a wide range of charged particles from relativistic minimum ionising pions and protons to 50 MeV $^{110}$Xe and energies and several types of Si detectors. $S_n$ and particle ranges were estimated for alpha particles and heavy ions using TRIM-95 [39] with a simple Kinchin and Pease estimate of damage. To minimise uncertainties in TRIM calculations [48] of thin films when the mean free path between collisions is not much less than film thickness, $S_n$ was calculated without taking account of the rear 10% of layer thickness for the case where particles completely traverse the detector. $S_n$ for high energy protons and heavy ions which were estimated by scaling the TRIM estimate of damage for 15 MeV protons, (where inelastic contributions are anticipated to be

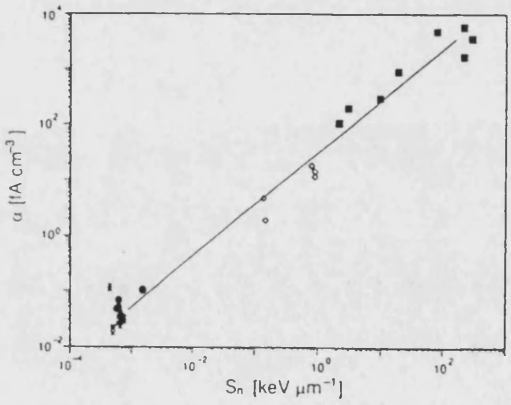


Fig. 5. Damage factor $\alpha$ vs. energy deposited in nuclear processes within the active layer of the detector for literature and the present data. The data points denoted by crosses, circles, diamonds and squares correspond to pions, protons, alpha particles and heavy ions, respectively.

NIMB 5078



Table 2
Tentative assignment of the defect centres observed in irradiated diodes

| Irradiation (ions $cm^{-2}$) | Energy level (eV) | $\sigma_t$ (b) | Type | Possible defect centres |
|---|---|---|---|---|
| | $E_c - 0.42$ | 1.4 | Electron | $V_2^-$, E |
| $^{226}Ra$ | $E_c - 0.12$ | 0.02 | Electron | A, $O^+$ |
| $1.6 \times 10^9$ | $E_v + 0.40$ | 2.0 | Hole | V–O–C, $VO_3$ |
| | $E_v + 0.30$ | 3.4 | Hole | $C_i$–$O_i$? |
| | $E_c - 0.43$ | 1.7 | Electron | $V_2^-$, E |
| $^{226}Ra$ | $E_c - 0.13$ | 0.05 | Electron | A, $O^+$ |
| $1.6 \times 10^9$ | $E_v + 0.41$ | 2.8 | Hole | V–O–C, $VO_3$ |
| | $E_v + 0.30$ | 3.4 | Hole | $C_iC_s$ |
| | $E_c - 0.43$ | 1.9 | Electron | $V_2^-$, E |
| $^{241}Am$ | | | | A, $O^+$ |
| $2.2 \times 10^9$ | $E_v + 0.40$ | 2.0 | Hole | V–O–C, $VO_3$ |
| 18 MeV | $E_c - 0.2$ | | Electron | $V_2^{2-}$ |
| $^{63}Cu^{5+}$ | $E_c - 0.18$ | | Electron | A, $O^+$ |
| $3 \times 10^8$ | $E_c - 0.41$ | | Electron | $V_2^-$, E |
| | $E_v + 0.25$ | | Hole | Cu |
| $^{241}Am$ | $E_c - 0.41$ | 0.77 | Electron | $V_2^-$, E |
| $2.2 \times 10^9$ | $E_c - 0.15$ | 0.36 | | A, $O^+$ |
| Annealed 4 h 150°C | $E_v + 0.52$ | 28.8 | Hole | V–O–C |

from $^{241}Am$. Evidently the irradiation has led to the formation of defect centres in the depleted region of the diode. Ahrenius plots of the emission rate vs. reciprocal temperature were used to characterise the energy levels and make tentative assignment of the defect centres responsible, based on literature trap level data (Table 2). The peaks cannot be assigned to a single defect because of strain broadening and because the DLTS peaks associated with some centres overlap. (e.g. $V_2^-$ centre at $E_c - 0.41$ eV and E-centre at $E_c - 0.45$ eV.)

The peaks observed in the $^{241}Am$ alpha particle irradiations were also observed for a sample of the same type irradiated with α-particles from $^{226}Ra$. An additional peak was also observed in the latter sample at $E_t - E_v = 0.404$ eV.

In the case of the diodes irradiated with $^{63}Cu^{5+}$ ions broad peaks became discernible in the DLTS data at a dose of $\sim 1 \times 10^8$ Cu $cm^{-2}$. Broadening of the peaks, which is probably associated with strain, made it difficult to assign reliable energy levels to these centres. These levels might be associated with the $V_2^{2-}(E_c - 0.218$ eV), $V_2^-(E_c - 0.416$ eV) and A-centres ($E_c - 0.18$ eV). In addition an unidentified peak corresponding to $E_v + 0.25$ eV was observed under majority and minority carrier injection conditions. This might be associated with $C_iC_s$ [41] or Cu/Cu–Cu centres [42] that are ion implanted during irradiation.

Fig. 4 shows the DLTS temperature scan for a diode irradiated with $^4He$ from $^{241}Am$ before and after annealing at 150°C for 4 h in air. Clearly the peaks have been significantly reduced in amplitude and shifted as a result of heat treatment for both minority, and minority + majority carrier injection. Strain leads to broadening of the DLTS peaks [22] and we cannot rule-out that relaxing of the strain during heat treatment has led to net shift of the composite DLTS peak. However, this would not alter the total number of defect centres. Another, more likely, possibility is that the peaks in Fig. 4 are associated with more than one type of defect centre or different configurations of a single defect centre [9,10]. In this case the heat treatment may have brought about interactions between different types of defects that lead to

NIMB 5078



minimal) using proton and pion displacement damage curves [11]. As Kurokawa et al. and Summers et al. have reported [45,49] the data are distributed about a straight line with unity slope on a double logarithmic plot with a span of over six decades. The deviation of the data points from the straight line in Fig. 5 can be attributed to the differences between starting material and fabrication technique [11] as well as different degrees of annealing of the damage at room temperature [9,10,46]. The $\pi^{\pm}$ and proton data will be more uncertain than data for alpha and heavy particles because of the uncertainties in the calculated inelastic cross sections [11,46]. A correlation between $\alpha$ and ion energy was also looked for, but none was found. The absence of such a correlation indicates that the increase in $\Delta J$ cannot be associated with energy deposited in electronic processes because the majority of energy of the ions is deposited by electronic excitation. To further confirm that the damage is not associated with energy deposited in electronic processes, purely electronic cascades were simulated by an intense unfiltered primary beam from a crystallographic X-ray tube with Cu anode run at 30 kV and 20 mA. Exposure for periods up to 30 min leads to no observable increase in leakage current of an unbiased Hamamatsu diode. The energy of these X-rays is too low to cause displacement damage. This is in broad agreement with Fretwurst et al. [17] who observed a small $\Delta J$ of $\sim$1 nA cm$^{-3}$ after $10^4$ Gy in Si surface-barrier diodes. It is conceivable that Fretwurst et al. [17] observation can be attributed to oxide charge effects [50,51]. The proportionality between $\alpha$, the damage factor and the energy deposition in nuclear processes is consistent with the observation of DLTS signals that probably originate from vacancy-associated defects such as $V_2^-$ and E-centres. However, we cannot rule out the possibility that interstitial-based complexes (e.g. C based [9,10]) also contribute to $\Delta J$.

The straight line dependence of $\alpha$ on $S_n$ (Fig. 5) implies that $\Delta J$ is associated with displacement damage. The DLTS data suggest that $\Delta J$ is predominantly associated with the generation current through the Frenkel-pair based centres. Then it follows that if the population of vacancies and vacancy-based centres is at or near-equilibrium, $\alpha = (eN_i/2)N_v\zeta$. Here $N_i$ is the intrinsic carrier concentration for Si ($\sim 1.2 \times 10^{10}$ cm$^{-3}$) $N_v$ the average number of vacancies produced along the ion track that have not been annihilated at sinks or by interstitials and $\zeta$ a factor that describes the contribution from the different type and configuration of centres (e.g. A-, E- etc.) to the generation current. From the Kinchin and Pease theory of displacement damage [39] $N_v \approx \nu S_n/E_d$, where $\nu$ is a factor to allow for annihilation by an interstitial or sink and $E_d$ is the mean displacement energy. Then we may write, $\alpha = CS_n$ where $C$ (Table 1) is given by $C = eN_i\zeta\nu/(2E_d)$. Cast in this way, it is easy to see that the variations in $C$ seen in Table 1 and scatter of data points about the trend line in Fig. 5 can be associated with $\nu$, the probability of vacancy survival and $\zeta$ which describes how the generation current is distributed amongst the different possible centres [9,10]. It follows that the deviations from the straight line in Fig. 5 are associated with $\nu$ and $\zeta$ only, because $N_i$ and $E_d$ are fundamental material parameters for Si. In the limit that recombination of Frenkel defects is small or constant (dilute damage) $\nu$ will be constant. Under these conditions we anticipate $\zeta$ will be a constant that depends on the concentrations of impurities in the active volume [10] for a particular detector and temperature. This picture is not significantly altered if interstitial-based centres also contribute to $\Delta J$ because according to the Kinchin and Pease theory their contribution will also be proportional to $N_v$. This simple phenomenological model suggests that in the limit of spatially separated displacement damage $\alpha$ scales with $S_n$. This is consistent with the fact that our alpha particle measurements lie close to the scaling line for both the thick and thin detectors even though the maximum in the nuclear energy deposition is $\sim$3000 times smaller in the latter. This scaling, coupled with the observation of similar room- or at low-temperature ($T \leqslant 200$°C) leakage current recovery to that observed in our diodes, strongly suggests that the data that is being gathered for LHC and other high energy physics projects can be scaled in a straightforward way to the case of heavy ion irradiation. We anticipate deviations from this scaling in the limit where the displacement cascade is no longer dilute so that

NIMB 5078



significant self-annealing of defects takes place (e.g. for low energy heavy ions).

## 4. Conclusions

(a) The increase in leakage current resulting from ion irradiation of the detectors investigated here probably originates from vacancy associated defect centres (e.g. $V_2^-$, and E).

(b) The damage factor $\alpha$ is proportional to the average energy deposited in nuclear processes within the active volume of Si detectors. The proportionality extends over 6 decades (from minimum ionising pions to 0.5 A MeV Xe).

(c) Recovery of the leakage current is observed after annealing at 150°C and cannot be explained by annealing out of isolated divacancies.

## Acknowledgements

We are grateful to Trond Westgaard and Lars Evensson SINTEF Instrumentation and Lars Westerberg, Uppsala University for helpful discussions and assistance. Knut and Alice Wallenbergs Foundation are acknowledged for support of the CHICSi program, SR participated under the auspices of the ERASMUS student exchange programme. M.E-B. is grateful to the Werner Gren Foundation for a Fellowship. P.J. was partly funded by the Strängs Donationsfond. Support for R.G. from Stiftelsen Blanceflor Boncompagni Ludovisi född Bildt is also gratefully acknowledged.

## References

[1] K.G. McKay, Phys. Rev. 84 (1951) 829.
[2] J.M. McKenzie, D.A. Bromley, Bull. Am. Phys. Soc. 4 (1959) 422.
[3] J. Kemmer, Nucl. Instr. and Meth. 169 (1980) 499.
[4] P.H. Gooda, W.B. Gilboy, Nucl. Instr. and Meth. A 255 (1987) 222.
[5] N. Mardkevich, I. Gertner, J. Felseiner, Nucl. Instr. and Meth. A 269 (1988) 599.
[6] T. Maisch, R. Günzler, M. Weiser, S. Kalbitzer, W. Weslser, J. Kemmer, Nucl. Instr. and Meth. A 288 (1990) 19.
[7] S.C. Gujrathi, D.W. Hetherigton, P.F. Hinrichsen, M Bentourkia, Nucl. Instr. and Meth. B 45 (1990) 260.
[8] M. Oetiker, Nucl. Instr. and Meth. A 337 (1993) 145.
[9] G. Lutz, Nucl. Instr. and Meth. A 377 (1996) 134.
[10] Z. Li, Nucl. Instr. and Meth. A 342 (1994) 105.
[11] M. Huhtinen, P. Aarnio, Nucl. Instr. and Meth. A 335 (1993) 580.
[12] K. Riechmann, K.T. Knöpfle, V.M. Pugatch, Nucl. Instr. and Meth. A 377 (1996) 276.
[13] E. Fretwurst, C. Dehn, H. Feick, P. Heydarpoor, G. Lindström, M. Moll, C. Schütze, T. Schultz, Nucl. Instr. and Meth. A 377 (1996) 258.
[14] H. Feick, E. Fretwurst, G. Lindström, M. Moll, Nucl. Instr. and Meth. A 377 (1996) 217.
[15] P. Arino, M. Huttinen, M. Pimiä, K. Kaita, M. Laasko, A. Numminen, P. Ryytty, Nucl. Instr. and Meth. A 326 (1993) 344.
[16] E. Fretwurst, W. Hildesheim, G. Lindström, M. Seidel, Nucl. Instr. and Meth. A 372 (1996) 368.
[17] E. Fretwurst, H. Herdan, G. Lindström, U. Pein, M. Rollwagen, H. Schatz, P. Thomsen, R. Wunstorf, Nucl. Instr. and Meth. A 288 (1990) 1.
[18] T. Angelescu, A.E. Cheremukhin, V.M. Ghete, N. Ghiordâescu, I.A. Goltuvin, S. Lazanu, I. Lazanu, A. Mihul, A. Radu, N. Yu Susova, A. Vailescu, N.I. Zamyatin, Nucl. Instr. and Meth. A 357 (1995) 55.
[19] R. Bruzzi, A. Baldini, E. Borchi, I. Lukianov, Nucl. Instr. and Meth. A 326 (1993) 344.
[20] E. Barbaris, J.G. Boissevaun, N. Cartglia, J.A. Ellion, P. Feruson, J.K. Fleming, K. Holzscheiter, S. Jerger, D. Joyce, J.S. Kaputinski, J. Leslie, C. Lietzke, J.A.J. Matthews, A.P.T. Palounek, D. Pitzl, W.A. Rowe, H.F.-W. Sadronzinski, D. Skinner, W.F. Sommer, W.E. Sondheim, S.J. Winpenny, H.J. Ziock, Nucl. Instr. and Meth. A 326 (1993) 373.
[21] Z. Li, C.J. Li, E. Verbitskaya, V. Eremin, Nucl. Instr. and Meth. A 385 (1997) 321.
[22] S.J. Bates, C. Furetta, M. Glaser, F. Lemeilleur, E. León-Florián, C. Gößling, B. Kaiser, A. Rolf, R. Wunstof, H. Freick, E. Fretwurst, G. Lindström, M. Moll, G. Taylor, A. Chilingarov, Nucl. Instr. and Meth. A 379 (1996) 116.
[23] B.G. Svensson, B. Mohadjeri, A. Hallén, J.H. Svensson, J.W. Corbett, Phys. Rev. B 43 (1991) 2292.
[24] J.W. Walker, C.T. Sah, Phys. Rev. B 7 (1973) 4587.
[25] S.D. Brotherton, P. Bradley, J. Appl. Phys. 53 (1982) 5720.
[26] A. Hällén, D. Fenyö, B.U.R. Sundqvist, R.E. Johnston, B.G. Svensson, J. Appl. Phys. 70 (1991) 3025.
[27] V. Avdechikov, L. Carlén, M. Guttormsen, A. Fokin, B. Jakobsson, Yu. Murin, J. Mårtensson, A. Oskarsson, E.J. van Veldhuizen, L. Westerberg, H.J. Whitlow, Nuclear Physics (accepted).
[28] L. Evensen, T. Westgaard, H.J. Whitlow, B. Jakobsson, IEEE Trans. Nucl. Sci. 44 (1997) 629.

NIMB 5078



[29] L. Lavergne-Gosselin, L. Stab, M.O. Lampert, H.Å. Gustafsson, B. Jakobsson, A. Kritiansson, A. Oskarsson, M. Westenius, A.J. Kordyasz, K. Aleklett, L. Westerberg, M. Rydehell, O. Tengblad, Nucl. Instr. and Meth. A 276 (1989) 210.
[30] B. Schidt, J. von Borany, D. Schubert, Nucl. Instr. and Meth. A 326 (1993) 21.
[31] M. Hult, M. El Bouanani, L. Persson, H.J. Whjitlow, M. Andersson, C. Zaring, M. Östling, D.D. Cohen, N. Dytewski, I.F. Bubb, S.R. Walker, Nucl. Instr. and Meth. B 101 (1995) 263.
[32] M. El Bouanai, M. Hult, L. Persson, E. Swietlicki, M. Andersson, M. Östling, N. Lundberg, C. Zaring, D.D. Cohen, N. Dytlewski, P.N. Johnston, S.R. Walker, I.F. Bubb, H.J. Whitlow, Nucl. Instr. and Meth. B 94 (1994) 530.
[33] J.W. Martin, D.D. Cohen, N. Dytlewski, D.B. Garton, H.J. Whitlow, G.J. Russel, Nucl. Instr. and Meth. B 94 (1994) 277.
[34] H.J. Whitlow, G. Possnert, C.S. Petersson, Nucl. Instr. and Meth. B 27 (1987) 448.
[35] H.J. Whitlow, B. Jakobsson, L. Westerberg, Nucl. Instr. and Meth. A 310 (1991) 636.
[36] R. Ghetti, B. Jakobsson, H.J. Whitlow, Nucl. Instr. and Meth. A 317 (1992) 235.
[37] Epo Tek™ H20E. Supplied by MPE mickrosystems Skärholmen, Sweden.
[38] Hamarmatsu Photodiode Catalog.
[39] J.F. Ziegler, J.P. Biersack, U. Littmark, The stopping and ranges of ions in solids, in: J.F. Ziegler (Ed.), The Stopping and Ranges of Ions in Matter, vol. 1, Pergamon Press, New York, 1995.
[40] A.O. Evwaraye, E. Sun J. Appl. Phys. 47 (1976) 3776.
[41] J. Matheson, M. Robbins, S. Watts, Nucl. Instr. and Meth. A 377 (1996) 224.
[42] M. Shultz, in: M. Shultz, O. Madelung (Eds.), Impurities and Defects in Group IV Elements and III-V compounds, vol. 22 Semiconductors: (Supplements and extensions to vol. III/17), Landolt-Börnstein, Numerical Data and Functional Relationships in Science and Technology, O. Madelung (Ed.), Springer, Berlin, 1989, p. 270.
[43] L.C. Kimerling, H.M. DeAnglis, C.P. Carnes, Phys. Rev. B 3 (1971) 427.
[44] Trond Westgaard, Private Communication, 1995.
[45] M. Kurokawa, T. Motobayashi, K. Leki, S. Shimoura, Y. Ikeda, S. Morya, Y. Yanagisawa, T. Nomura, IEEE Trans. Nucl. Sci. 42 (1995) 163.
[46] G.N. Taylor, F. Fares, S.J. Bates, C. Furetta, M. Glaser, F. Lemeilleur, E. Leon-Florian, C. Gößling, B. Kaiser, A. Rolf, R. Wustorf, H. Feick, E. Fretwurst, G. Lindström, M. Moll, A. Chiligarov, Nucl. Instr. and Meth. A 383 (1996) 144.
[47] D. Kollewe, Nucl. Instr. and Meth. A 254 (1987) 637.
[48] J. F. Ziegler, TRIM 89.9 notes.
[49] G.P. Summers, E.A. Burke, C.F. Dale, E.A. Wolicki, P.W. Marshall, M.A. Gehlhausen, IEEE Trans. Nucl. Sci. NS 34 (1987) 1134.
[50] R. Wunstorf, H. Freick, E. Fretwurst, G. Lindström, G. Lutz, C. Osius, R.H. Richter, T. Rohe, A. Rolf, P. Schlichthärle, Nucl. Instr. and Meth. A 377 (1996) 290.
[51] W. Füssel, M. Schmidt, H. Angermann, G. Mende, H. Flietner, Nucl. Instr. and Meth. A 377 (1996) 177.
[52] J. Latita, N. Keskitalo, A. Hallén, C. Jagadish, B.G. Svensson, Nucl. Instr. and Meth. B 120 (1996) 27.

ELSEVIER

Nuclear Instruments and Methods in Physics Research B 000 (1998) 000–000

NIM B
Beam Interactions with Materials & Atoms

# Extremely thin silicon $\Delta E$ detectors for ion beam analysis

Harry J. Whitlow [a,*], Thomas Winzell [a], Göran Thungström [b]

[a] *Department of Nuclear Physics, Lund Institute of Technology, Box 118, S-22100 Lund, Sweden*
[b] *Royal Institute of Technology, Solid State Electronics, P.O. Box E229, S-16440 Kista, Sweden*

**Abstract**

Recent developments in silicon nanotechnology have made feasible the fabrication of $\Delta E$ detectors with thickness of 1 μm or less. The CHICSi collaboration has been developing thin $\Delta E$ detectors for study of reaction products from intermediate energy heavy ion collisions in an ultra high vacuum storage-ring environment. In this paper, we highlight these developments from an ion beam analysis (IBA) viewpoint. The initial part of the paper outlines the characteristics for these detectors for, nuclear reaction analysis (NRA), elastic recoil detection (ERD) using $\Delta E$–$E$ detector telescopes and accelerator mass spectrometry (AMS). Quasi-empirical estimates of the maximum $\Delta E$ detector thickness and separating power for the limit of low energy particles (down to 0.1 Å MeV) reveal that energy straggling is an important limiting factor. Subsequently different methods are presented for fabricating both self-supported and vertically integrated $\Delta E$ detectors including recently developed wafer bonding techniques which open up the possibility of producing $\Delta E$–$E$ detector telescopes where the $\Delta E$ element is in the hundreds of nm range. Ultimately consideration is given to special requirements for the readout electronics because of the high capacitance presented by the thin $\Delta E$ detectors. © 1998 Elsevier Science B.V.

*PACS:* 29.40.Wk; 85.30.k; 61.80.JH; 61.85.-p; 73.40.Vz
*Keywords:* $\Delta E$ detectors; Si p–i–n diodes; Nuclear reaction analysis; Elastic recoil detection; Accelerator mass spectrometry; Self-supporting membranes; Energy loss; Straggling; Particle identification; Integrated detectors

## 1. Introduction

In many situations in ion beam analysis (IBA) it is of interest to measure the identity of a charged particle as well as its energy. A number of different schemes have been developed for particle identification such as, magnetic-sector momentum analysis, velocity measurement with an electrostatic sector or Time of Flight (ToF) system and determination of the effective charge on the nucleus from the ionisation rate using a $\Delta E$–$E$ detector. These methods are generally combined with measurement of energy using a conventional ionisation detector. Mainly, gas ionisation $\Delta E$ detectors in combination with Si $E$ (stop) detectors have been used for IBA applications [1–13]. Although some use of thin Si detectors has been made in IBA, [14–18] they have not found wide application. This is most probably because thin Si detectors have

* Corresponding author. Fax: +46-46-222 4709; e-mail: harry_j.whitlow@nuclear.lu.se.


*PII* S0168-583X(97)00875-6

until now not been readily available at low cost with thickness under ~30 μm. Compared to gas ionisation $\Delta E$ detectors thin Si $\Delta E$ detector have a number of advantages such as, Si $\Delta E$ detectors are smaller and more compact. Also Si p–i–n detectors can easily be made UHV compatible [19,20] with entrance windows (tens of nm) which are much thinner than for gas ionisation $\Delta E$ detectors. They also have a lower susceptibility to secondary nuclear reactions [8] than for hydrocarbon gas ionisation medium. Furthermore gas ionisation $\Delta E$ detectors require an expensive and complex gas handling system and vacuum degradation associated with gas diffusion through the entrance window may be a problem unless precautions are taken [2,3]. On the other hand, Si $\Delta E$ detectors are susceptible to radiation damage (which may be removed by a low temperature (~150°C) anneal [21]) and precautions should be taken to avoid channelling. Furthermore, the detector thickness is fixed and cannot be adjusted as in the case of gas ionisation detectors.

For a number of years the CHIC collaboration has been developing thin Si $\Delta E$ detectors using nanometer scale fabrication technology for measuring intermediate mass fragments ~~with~~ 0.7–60 A MeV from heavy ion collisions in a UHV intermediate energy heavy ion storage-ring environment [19]. The objective of this paper is to highlight these developments from an IBA viewpoint and present considerations that are important for their application in IBA.

### 1.1. IBA applications of thin Si detectors

Thin Si detectors have many potential applications in IBA. For brevity, no detailed review is attempted here, but the requirements set by different applications are outlined. One of the most obvious applications is for improving the energy (depth) resolution in nuclear reaction analysis (NRA) [22] by replacing the absorber foil with a $\Delta E$ detector for separation of scattered beam and charged reaction products (e.g. from (d,p) reactions). Other potential applications in NRA are separation of reaction products from interfering reactions (e.g. $^{10}$Be($^3$He,p)$^{12}$C and $^9$Be($^3$He, α) $^8$Be) and detection of the full energy of low energy products in a thin $\Delta E$ detector whilst suppressing a significant part of the energy of scattered high energy projectiles [23,24]. Generally the particles of interest in NRA are light reaction products with energies of 1–2 A MeV (see e.g. Figs. 6.6 and 6.7 of Ref. [22]).

For elastic recoil detection (ERD) applications detector telescopes based on thin Si detectors have already been reported [14–18]. $\Delta E$–$E$ detector telescopes are better suited than ToF-E systems for light element detection because even for very light elements they have a detection efficiency close to one. The separating power is similar to that of ToF-E ERD systems [25] for light- and medium heavy- mass recoil analysed with ion beams with less than 1 A MeV energy. The planar geometry of thin Si $\Delta E$ detectors implies that very compact $\Delta E$–$E$ detector telescopes can be constructed that subtend much larger solid angles (close to 1.5π sr) than is possible with gas $\Delta E$–$E$ (~100 msr) or ToF-E (1 msr) detector telescopes. This feature is of particular interest for nuclear microprobes as well as for biological and polymer analysis where large solid angle detector systems are important for minimising radiation damage. In contrast to AMS and NRA, the energies of interest are lower for ERD at tandem energies because of energy loss on the inward and outward trajectories in the material. For typical analytical situations (e.g. analysis at $\phi = 30°$ of, $^1$H with 2 MeV $^4$He, $^{16}$O with 30 MeV $^{35}$Cl, $^{28}$Si with 48 MeV $^{81}$Br and $^{75}$As with 90 MeV $^{127}$I) the minimum recoil energies (taken as ~~1/3~~ of the energy for recoiling from the surface) lie in the range 0.55–0.85 A MeV.

Gas $\Delta E$ detectors are widely used for accelerator mass spectrometry (AMS) for separation and identification of interfering signals from ions of 1–2 A MeV energy. Although gas $\Delta E$ detectors are well suited for AMS application, the compactness and no requirement for a gas handling system will make Si $\Delta E$ detectors well suited for small mini-C-14 analysers that are under development for medical applications.

## 2. Fundamental considerations

The lowest energy that can be detected by a $\Delta E$–$E$ detector telescope is governed by the re-

quirement that the particle must have sufficient energy to traverse the $\Delta E$ detector and deposit sufficient energy, to generate a signal to be registered in the $E$ detector. It follows that to achieve a low threshold energy the $\Delta E$ detector and all associated dead layers must be as thin as possible. Fig. 1 presents an estimate of the maximum thickness of Si $t_{max} = R_p - 2\sigma_p$ vs. energy per nucleon for representative light (protons), intermediate ($^{16}$O) and heavy ($^{75}$As) charged particles. The projected range $R_p$ and straggling $\sigma_p$ were estimated using the TRIM code [26]. This estimate of $t_{max}$ corresponds to a detection efficiency for a $\Delta E$–$E$ detector telescope close to one for gaussian range distributions because less than 2.3% of the particles will come to rest in the $\Delta E$ detector and thus (probably) not give rise to a signal in the $E$ detector. It follows from the above that for many NRA and AMS applications $\Delta E$ detector thickness of 12-μm can be used, however to achieve wide dynamic range in $\Delta E$–$E$ ERD a thickness of 3–5 μm or less is appropriate.

In order to use the $\Delta E$–$E$ telescope for identification, the signals for different nuclides of interest must be separated on a plot of the $\Delta E$ detector signal vs. $E$ detector signal for each incident particle. (This is preferable for plotting the $\Delta E$ vs. $\Delta E + E$ signal, which is sometimes done, because the particles can be identified before establishing the energy calibration for each nuclide of interest and the electronic noise contributions to the $\Delta E$ and $E$ signals are uncorrelated.) It is an interesting question whether $\Delta E$–$E$ detector telescopes can be used for particle identification in the limit of low particle energy and thereby small detector thickness $t$. In the absence of an established energy loss distribution theory for heavy ions close to the stopping maximum we have used TRIM [26] to estimate the energy deposited in electronic excitation and the quasi empirical formula of Yang et al. [27] to estimate heavy ion straggling. A number of other instrumental factors also influence the separating power such as, incident particle collimation, thickness variations and electronic noise contributions but these are rather trivial to estimate and will not be considered further.

In Fig. 2 the electronic energy deposition $\Delta E$ vs. the energy deposited in the $E$ detector is shown for a $\Delta E$–$E$ detector telescope with a 1 μm Si $\Delta E$ detector for the nuclides ($Z$, $A$) for Be (4,7), O (8, 16), Si (14, 28) and As (33, 75) in the energy range 0.1–10 A MeV. No attempt has been made to correct for the response functions of the detectors. The hatched regions correspond to the ±2 fwhm width assuming the distribution of energy straggling is gaussian. The lines correspond to the mean electronic energy deposition for the nuclei ($Z$ + 1, $A$) i.e. a nuclide with the same mass but with a one unit greater nuclear charge. Inspection of Fig. 2 reveals that the hatched regions are separated both over the entire energy range that

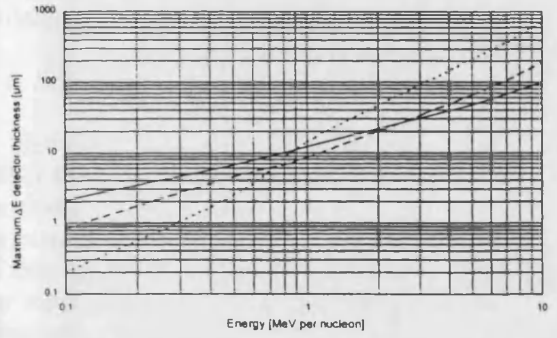


Fig. 1. TRIM estimate of the maximum $\Delta E$ detector thickness $t_{max}$ vs. particle energy for the short dashed, long dashed and solid lines correspond to protons, $^{16}$O and $^{75}$As, respectively.

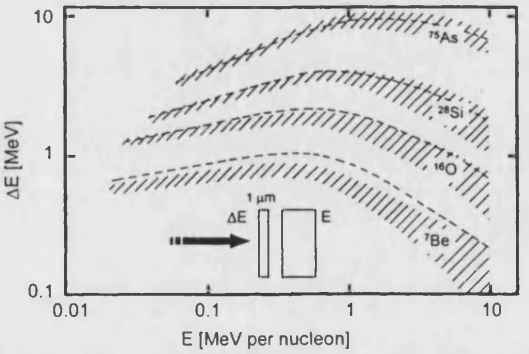


Fig. 2. Estimate of $\Delta E$ vs. $E$ for 0.1–10 A MeV ions of $^{7}$Be, $^{16}$O, $^{28}$Si and $^{75}$As calculated using TRIM [26]. The hatched regions denote the ±2 fwhm width associated with electronic straggling estimated from Yang et al. [27]. The dashed lines denote the position of the centroid corresponding to an isotope with the same mass number but with one unit larger atomic number.

spans the maximum in energy deposition. This implies that a 1 μm thick Si $\Delta E$ detector can be used to identify particles with different atomic number both above and below the stopping power maximum. Inspection of the dotted lines in Fig. 2 which correspond to the centroid for the $(Z_1^0 + 1, A_1^Y)$ isotopes reveals that, except for the lightest isotopes, the anticipated spreading from electronic energy straggling will not allow complete separation of elements with adjacent atomic number e.g. Si and P. This is in contrast to what is experimentally observed in the case of thicker detectors where even isotopic separation is possible e.g. Fig. 3 Refs. [19,20]. This may be attributed to the relatively larger contribution from straggling for thin detectors or details in the electron–hole pair production by electronic excitation.

## 3. Fabrication of thin Si $\Delta E$ detectors

Two main approaches have been used to construct thin Si $\Delta E$ detectors. Either the detector is realised in the form of a self-supported membrane or the detector is vertically integrated with an underlying substrate. (For example, a thick $E$ detector.) Although self-supported Si membranes are remarkably strong, the need for mechanical stability during processing and operation limits practical detectors to greater than ~5 μm thickness and a few tens of $mm^2$ area. In the case of detectors fabricated on an underlying substrate, the mechanical stability is better and below 1 μm thickness and hundreds of $mm^2$ active areas are possible.

### *3.1. Self-supporting detectors*

Self-supported detectors can be fabricated either by directly forming the detector from a wafer that is thinned down to the desired thickness or by etching thin membranes for the active regions of thin detectors from thicker substrates. The need for mechanical stability during processing restrict detectors made using thinned wafers to greater than ~30 μm thickness. For 5–30 μm thick detectors the membrane etch technique is best suited because standard wafer processing and handling technology can be used and the active membrane region has identical thermal expansion characteristics to the surrounding support. The etching process must have a uniform, controlled etch-rate and not increase short-range roughness. Etch-stops in the form of a highly doped layer may be used [28–30], possibly in combination with electrochemical etching. Another approach has been successfully used by SINTEF to produce several thousand 10 and 12 μm thick detectors for the CHICSi programme [19,20]. This is based on a technique for anisotropic etching of micromechanical components and nanostructures defined by $SiO_2$ masks produced using a conventional lithography. 10 × 10 mm, 10 and 12 μm thick membranes were produced in a two-step tetra-methyl ammonium hydroxide (TMAH) solution etch [20]. Subsequently two step p–i–n detector structure with multi-guard [31] was formed using standard processing [20,32]. P–i–n detector structures which can be constructed with thin windows [33] may be heat treated for UHV bake-out and annealing away of radiation damage [21]. Heat treatment cannot be applied to conventional Au/Si Schottky barrier detectors because Au in-diffusion causes an unacceptable increase in leakage current.

### *3.2. Integrated Si $\Delta E$-$E$ detector telescopes*

A number of schemes have been proposed for realising integrated $\Delta E$–$E$ detector telescopes [34–37]. Unlike the case where the $\Delta E$ detector is self-supported, vertical integration of the $\Delta E$ detector implies that the $\Delta E$ and $E$ elements are in physical contact, which can lead to cross-talk because of, charge carriers funnelling [34] between the two detector elements. Kemmer and Lutz [34] proposed a $n^+$–n–$p^+$–n–$n^+$$\Delta E$–$E$ structure where the buried p-layer serves as a common contact. Detectors of this type with a 1 μm $\Delta E$ layer have been realised by the Catania group [39] using a 900 keV $B^+$ implantation and Husimi et al. [35,36] who used gas-phase epitaxy to produce integrated $\Delta E$–$E$ and $\Delta E_1$–$\Delta E_2$ detector structures with an active thickness of 5 μm. Both these types of detectors have thick buried dead layers (1.3 and 1.15 μm, respectively) which can be associated with the width of the buried contact layer which

is governed by implant straggling and/or gas dynamics in the epi-reactor. The thickness and doping level represents a compromise between the requirement of a minimum dead layer thickness and the need to provide a sufficiently high doping level to control cross-talk associated with "funnelling" of charge carriers [39].

Thin buried silicide layers with good electrical properties produced by wafer bonding under uniaxial pressure during heat treatment of Co coated wafers [40] have been exploited by Thungström et al. [37] to make rugged integrated $\Delta E$–$E$ detector telescope structures with a 6.5 μm thick $\Delta E$ element (Fig. 3). In contrast to the ion-implanted and epitaxial detector telescopes discussed above, these detectors have a buried dead contact-layer of a few hundred nm or so. Although the dead layer is extremely thin, the metallic electronic structure of $CoSi_2$ inhibits charge carrier funnelling. Fig. 3 shows the data for intermediate mass fragments from a Cu foil bombarded with 32 MeV $^{14}N$ ions. Clearly isotopic resolution of $^{6}Li$ and $^{7}Li$ and possibly $^{7}Be$ and $^{9}Be$ is achieved. The technique is well suited to low-cost volume production because it uses standard microelectronic processing techniques and by using a thin starting wafer for the $\Delta E$ detector combined with a built-in etch-stop, extremely thin (1 μm or less) $\Delta E$ layers can be realised.

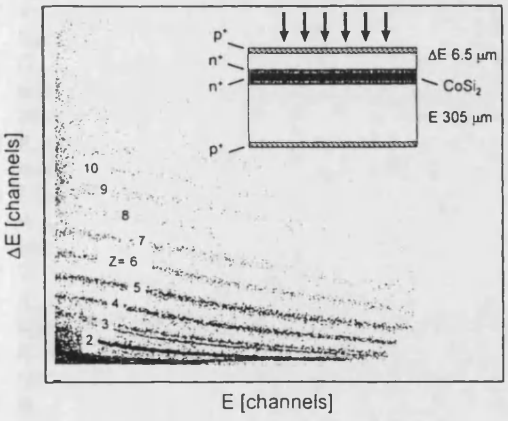


Fig. 3. $\Delta E$ vs. $E$ data from an integrated $\Delta E$–$E$ detector telescope with 6.5. μm $\Delta E$ element for intermediate mass fragments from a 32 A MeV $^{14}N^{7+}$ incident on a copper foil (after [37]).

## 4. Electronic noise considerations

Control of electronic noise will be important for the practical use of thin $\Delta E$ detectors especially when they are used to measure light particles. This is because the collected $\Delta E$ charge pulse becomes proportionately smaller as $t$ decreases whilst the detector capacitance $C_{det}$ becomes very large. $C_{det}$, which is 5.3 nF for a 1 μm thick 50 mm$^2$ detector, will be poorly matched by most conventional preamplifiers which are optimised for $C_{det} \leq 500$ pF. The equivalent noise charge (ENC) referred to the input, is generally dominated by the channel white noise [41] of the input Metal Oxide Semiconductor Field Effect Transistor (MOSFET). Optimal noise matching of $C_{det} = 5.3$ nF to achieve an ENC corresponding to 14 KeV fwhm with a spectroscopy amplifier peaking time of 3μs, requires a special MOSFET with $C_{oxide} = 1.8$ nF and $g_m = 3.6$ AV$^{-1}$. Such a device represents the limit of feasibility with conventional (1.2 μm gate length) microelectronic technology because the MOSFET will consume a large area of Si (~8 mm$^2$) and have a high power dissipation (~0.6 W). However, the power consumption can be dramatically reduced using more advanced process technologies that are being developed with a smaller gate length (e.g. ~26 mW for a 0.25 μm process).

## 5. Conclusions

1. $\Delta E$ detectors with ~10 μm thickness are suited for NRA and AMS applications. The wider dynamic range required for $\Delta E$–$E$ ERD requires thinner detectors with thickness of 3–5 μm or less.
2. Separation of signals from different elements is possible for energies down to 0.1 MeV energy is possible with a 1 μm thick $\Delta E$ detector, however, energy straggling in thin detectors presents a fundamental limitation to the separating power.
3. Thin $\Delta E$ detectors with thickness below 10 μm have been produced both as self-supported and integrated $\Delta E$ detectors. Integrated $\Delta E$–$E$ detector telescopes with $\Delta E$ elements thinner

than 1 μm are feasible, however in this range the resolution will be limited by energy straggling.

4. Optimal noise performance requires development of special preamplifiers with a large input capacitance and transconductance for matching thin detectors.

## Acknowledgements

Valuable discussions and help from Lars Evensen, Trond Westgaard, Gier Førre and Joar Martin Østby (SINTEF) and Sture Petersson (KTH-Stockholm) as well as collaborators in the CHICSi programme are gratefully acknowledged.

## References

[1] M. Petrascea, I. Berceanu, I. Branucus, A. Buta, C. Grame, I. Lazar, I. Mahai, M. Petrovic, V. Simon, M. Mahaila, I. Gita, Nucl. Instr. and Meth. B 4 (1984) 396.
[2] L. Siberling, Nucl. Instr. and Meth. B 24/25 (1987) 526.
[3] A.M. Behrooz, R.L. Hedrick, L.E. Seiberling, R.W. Zurmühle, Nucl. Instr. and Meth. B 28 (1987) 108.
[4] J. P. Stocuert, G. Guillaume, M. Hage-Ali, J.J. Grob, C. Ganter, P. Siffert, Nucl. Instr. and Meth. B 44 (1989) 184.
[5] R. Beirisch, R. Grötzschel, E. Hentschel, W. Assman, Nucl. Instr. and Meth. B 68 (1992) 245.
[6] D.K. Avasthi, D. Kabiraj, A. Bhagwat, G.K. Mehta, V.D. Vankar, S.B. Ogale, Nucl. Instr. and Meth. B 93 (1994) 480.
[7] V.M. Prozesky, H. Huber, W. Asman, R. Behrisch, Nucl. Instr. and Meth. B 118 (1996) 327.
[8] G. Dollinger, M. Boulouednine, A. Bergaier, T. Faestermann, C.M. Frey, Nucl. Instr. and Meth. B 118 (1996) 291.
[9] R. Siegels, W. Assmann, J.A. Davies, J.S. Forster, Nucl. Instr. and Meth. B 118 (1996) 283.
[10] J.S. Forster, P.J. Currie, J.A. Davies, R. Siegle, S.G. Wallace, D. Zelensky, Nucl. Instr. and Meth. B 113 (1996) 308.
[11] W. Assmann, Th. Reichelt, T. Eisenhammar, H. Huber, A. Mahr, H. Schellinger, R. Wohlemuth, Nucl. Instr. and Meth. B 113 (1996) 303.
[12] R. Behrisch, V.M. Prozesky, H. Huber, W. Assmann, Nucl. Instr. and Meth. B 118 (1996) 262.
[13] W. Assmann, J.A. Davies, G. Dollinger, J.S. Forster, H. Huber, Th. Reichelt, R. Siegele, Nucl. Instr. and Meth. B 118 (1996) 242.
[14] F.H.P.M. Habraken, Nucl. Instr. and Meth. B 68 (1992) 181.
[15] C.H.M. Mareé, A. Kleinpenning, A.M. Vredenburg, F.H.P.M. Habraken, Nucl. Instr. and Meth. B 118 (1996) 301.
[16] M. Wiellunski, M. Mayer, R. Behrisch, J. Roth, B.M.U. Scherzer, Nucl. Instr. and Meth. B 122 (1997) 113.
[17] W.M. Arnold Bik, C.T.A.M. de Laat, F.H.P.M. Habraken, Nucl. Instr. and Meth. B 64 (1992) 832.
[18] M. El Bounani, P.N. Johnston, I.F. Bubb, H.J. Whitlow, in: J.L. Duggan, I.L. Morgan (Eds.), CP392, Application of Accelerators in Research and Industry, AIP, New York, 1997, p. 647.
[19] V. Avdeichikov, L. Carlén, M. Guttormsen, A. Fokin, B. Jakobsson, Yu. Murin, J. Mårtensen, A. Oskarsson, E.J. van Veldhuizen, L. Westerberg, H.J. Whitlow, Nucl. Phys., in press.
[20] L. Evensen, T. Westgard, V. Avidechikov, L. Carlén, B. Joakobsson, Yu. Murin, J. Mårtensson, A. Oskarsson, A. Siwek, H.J. Whitlow, E.J. Van Veldhuizen, L. Westerberg, M. Guttormsen, IEEE Trans. Nucl. Sci., in press.
[21] H.J. Whitlow, S.J. Roosendaal, M. El Bouanai, R. Ghetti, P.N. Johnston, B. Jakobsson, R. Hellborg, H. Petersson, P. Omling, Z. Wang and the CHIC Collaboration, Nucl. Instr. and Meth. B, submitted.
[22] G. Vizkeleth in: J. Tesmer, M. Nastasi, J.C. Babour, C.J. Maggiore, J.W. Mayer (Eds.), Handbook of Modern Ion Beam Materials Analysis, Materials Research Society, Pittsburg, 1995, p. 139.
[23] F. Abel, G. Amsel, D. Artemare, C. Ortega, J. Siejka, G. Vizkelethy, Nucl. Instr. and Meth. B 45 (1990) 101.
[24] G. Amsel, F. Pászti, E. Szilágyi, J. Gyulai, Nucl. Instr. and Meth. B 63 (1992) 421.
[25] H.J. Whitlow, B. Jakbsson, L. Westerberg, Nucl. Instr. and Meth. A 310 (1991) 636.
[26] J.F. Ziegler, J.P. Biersack, U. Littmark, The Stopping and Ranges of Ions in Matter, vol 1, Plenum Press, New York, 1985.
[27] Q. Yang, D.J. O'Connor, Z. Wang, Nucl. Instr. and Meth. B 61 (1991) 149.
[28] B. Schmidt, J. von Borany, D. Schubert, Nucl. Instr. and Meth. A 326 (1993) 21.
[29] L. Stab, Nucl. Instr. and Meth. A 288 (1990) 24.
[30] L. Lavergne-Gosselin, L. Stab, M.O. Lampert, H.-Å. Gustafsson, B. Jakobsson, A. Kristansson, A. Oskarsson, M. Westenius, A.J. Kordyasz, K. Aleklett, L. Westerberg, M. Rydehell, O. Tengblad, Nucl. Instr. and Meth. A 276 (1989) 210.
[31] L. Evensen, A. Hanneborg, B. Sundby Avset, M. Nese, Nucl. Instr. and Meth. A 337 (1993) 44.
[32] J. Kemmer, Nucl. Instr. and Meth. 169 (1980) 499.
[33] T. Maisch, R. Günzler, M. Weiser, S. Kalbitzer, W. Welser, J. Kemmer, Nucl. Instr. and Meth. A 288 (1990) 19.
[34] J. Kemmer, G. Lutz, Nucl. Instr. and Meth. A 253 (1987) 365.
[35] K. Husimi, S. Ohkawa, C. Kim, S. Osada, F. Shiraishi, Nucl. Instr. and Meth. 196 (1982) 131.

NIMB 3498



[36] Y. Kim, C. Kim, K. Husimi, S. Ohkawawa, Y. Fuchi, S. Osada, Nucl. Instr. and Meth. 226 (1984) 125.
[37] G. Thungström, E.J. van Veldhuizen, L. Westerberg, L.O. Norlin, C.S. Petersson, Nucl. Instr. and Meth. A, in press.
[38] A.B. Cambell A.R. Knudsen, IEEE Trans. Nucl. Sci. NS-29 (1982) 2067.
[39] C. Hu, IEEE Electron. Dev. Lett. EDL-3 (1982) 31; G. Cardella, F. Amorini, M. Cabibbo, A. Di Pietro, G. Fallicia, G. Franzó, P. Figera, S. Li, A. Musumarra, M. Pappa, G. Pappalardo, G. Percolla, F. Priolo, V. Privitera, F. Rizzo, S. Trudisco, Nucl. Instr. and Meth. A 378 (1996) 262.
[40] K. Lundberg, A. Södergärg, A.L. Tinsuu, S. Johansson, G. Thungström, C.S. Petersson, J. Electrochem. Soc. 141 (1994) 2829.
[41] E. Nygård, P. Aspell, P. Jarron, P. Weilhammer, K. Yoshioka, Nucl. Instr. Meth. A 301 (1991) 506.

T 16

LF

This should be:

[38] A.B. Cambell, A.R. Knudsen, IEEE Trans. Nucl. Sci. NS-29 (1982) 2067
C. Hu, IEEE Electron. Dev. Lett. EDL-3 (1982) 31.

[39] G. Cardella, F. Amorini, M. Cabibbo, A. Di Pietro, G. Fallicia, G. Franzó, P. Figera, S. Li, A. Musumerra ~ - - o -~

145.

Nuclear Instruments and Methods in Physics Research B40/41 (1989) 595–598
North-Holland, Amsterdam



# ION-IMPLANTATION-INDUCED FLUORINE AGGLOMERATION IN TUNGSTEN DISILICIDE PREPARED BY LOW-PRESSURE CHEMICAL VAPOUR DEPOSITION

C. Sture PETERSSON and Harry J. WHITLOW

*The Royal Institute of Technology, Department of Solid State Electronics, Box 1298, S-164 28 Kista, Sweden*

Juhani KEINONEN

*University of Helsinki, Accelerator Laboratory, Hämeentie 100, SF-00550 Helsinki 55, Finland*

François M. d'HEURLE, Françoise K. Le GOUES, Rajiv V. JOSHI, Gerald SCILLA and Olivier THOMAS

*IBM Thomas J. Watson Research Centre, Yorktown Heights, New York 10598, USA.*

Boron and antimony were implanted in tungsten disilicide/silicon structures. The silicide films with a Si/W ratio of 2.3 were prepared by low pressure chemical vapour deposition (LPCVD) from a mixture of $WF_6$ and $SiH_4$. The films were subsequently annealed at 1000 ° C prior to implantation. The effect of implantation and subsequent heat treatments on the distribution of fluorine have been investigated by means of transmission electron microscopy (TEM), secondary ion mass spectroscopy (SIMS) as well as the nuclear resonance broadening technique using the reaction $^{19}F(p, \alpha\gamma)^{16}O$. After implantation with $5\times10^{14}$ 150 keV $^{121}Sb^+$ ions $cm^{-2}$ the fluorine depth distribution was bimodal with one peak located about the silicide/silicon interface and a second peak at a depth corresponding approximately to the limit of the implant range distribution. This is also the position in the film where TEM revealed the presence of a large number of voids. The same observations were made in samples implanted with $^{11}B$. Some of the fluorine is lost from the implantation-induced peak after heat treatment at 300 ° C for 30 min, yet most of the fluorine remains even after annealing at 900 ° C. The overall picture is not substantially modified by raising the substrate temperature during implantation to 400 ° C.

## 1. Introduction

Solid diffusion sources, prepared by implantation of the atomic species to be diffused into refractory metal silicides, are finding increasing application not only for the fabrication of shallow emitter and junction structures but also for doping of polycrystalline silicon gate structures in metal oxide semiconductor (MOS) technology. The latter application is particularly interesting since the diffusion source can be formed, in-situ, by implantation of the silicide contact to the polycrystalline silicon gate electrode. Tungsten silicide diffusion sources can be formed by thermal reaction with a deposited tungsten layer. Application of this technique may be limited because of the consumption of silicon and thermal budget restrictions. In an attempt to overcome these restrictions, ion-implanted diffusion sources with nominal composition $WSi_2$ that were prepared by low-pressure chemical vapour deposition (LPCVD) from a mixture of $SiH_4$ and $WF_6$ have been investigated. After ion implantation, the films were observed to have a greater sheet resistance. Transmission electron microscopy (TEM) showed that voids had formed as a consequence of ion implantation whilst depth profiling using secondary ion mass spectrometry (SIMS) showed an enhancement in the fluorine signal at depths around the maximum in the projected range distribution of the implanted ions. These voids were not observed in ion-implanted $TiSi_2/Si$ structures prepared by metal–silicon reaction [1].

We have measured the fluorine depth profiles in films subjected to different annealing and heat treatment conditions. A quantitative determination of the fluorine depth profile was obtained by the nuclear resonance broadening (NRB) method which (unlike techniques based on sputtering) is insensitive to the state (i.e. chemical bonding of fluorine, fluorine bubble formation etc.) of the fluorine in the sample.

## 2. Experimental

Two batches of LPCVD-tungsten silicide/silicon structures with different silicide thicknesses were prepared by LPCVD [2,3]. The deposition of silicon-rich silicide films with a Si/W ratio of 2.3 was carried out at a temperature of 380 ° C at a pressure of 150 mbar. The feed gas flow rates for $WF_6$ and $SiH_4$ were 10 and 1000

0168-583X/89/$03.50 

SCCM [3]. The Si/W ratio and thickness of the thin films prior to annealing was determined by Rutherford backscattering spectrometry (RBS) using 2.4 MeV α-particles scattered through 168° to be $2.3 \pm 0.1$ and $3.2 \times 10^{17}$ $WSi_{2.3}$ formula units $cm^{-2}$, corresponding to about 130 nm, assuming the density of the films to be 9.4 g $cm^{-3}$, which corresponds to bulk $WSi_2$. In the case of the thick samples (which were used to study the detailed form of the fluorine depth profile) these were annealed for 6 h at 1000 °C in purified He to homogenize the films [4]. The Si/W ratio determined by RBS after annealing was close to 2 implying that the excess silicon moves towards the W/Si interface. Subsequently the thick films were implanted at room temperature with $5 \times 10^{14}$ 150 keV $^{121}Sb^+$ ions $cm^{-2}$. The thin samples (which were used to determine the fluorine behaviour under different implantation and heat treatment conditions) were implanted with $5 \times 10^{13}$ 150 keV $^{121}Sb^+$ ions $cm^{-2}$ or $1 \times 10^{15}$ 30 keV $^{11}B$ ions $cm^{-2}$. Implantation of the thin samples was carried out at room temperature or 400 °C (maintained by heater). The wafers were subsequently divided and part of each wafer was annealed at 900 °C for 30 min under a vacuum of better than $10^{-5}$ mbar.

Quantitative depth profiles of the fluorine were determined by means of the NRB technique using the 340 keV proton energy resonance in the $^{19}F(p, \alpha\gamma)^{16}O$ reaction which because of its large cross section and small width ($\Gamma = 2.8$ keV [5,6]) is most suitable for depth profiling fluorine in microelectronic structures [7–10]. A proton beam from the University of Helsinki 2.5 MV Van de Graaff accelerator was used and the gamma rays in an energy window 2.6–6.2 MeV were detected in a 12.7 cm diameter × 10.4 cm NaI(Tl) scintillation detector. SIMS profiling was carried out using a Cameca 4f instrument with a 10 keV $^{133}Cs^+$ primary beam. The SIMS depth scale was obtained by monitoring the tungsten signal.

### 3. Results and discussion

TEM studies of sections transverse to the thick LPCVD-$WSi_{2.3}$/Si sample surface showed that the implanted film became amorphous to a depth of about 80 nm. The void concentration after Sb implantation was also greatest at this depth. These voids are clearly seen in fig. 1 which shows an approximately 100 nm thick TEM section parallel to the surface. The voids appear

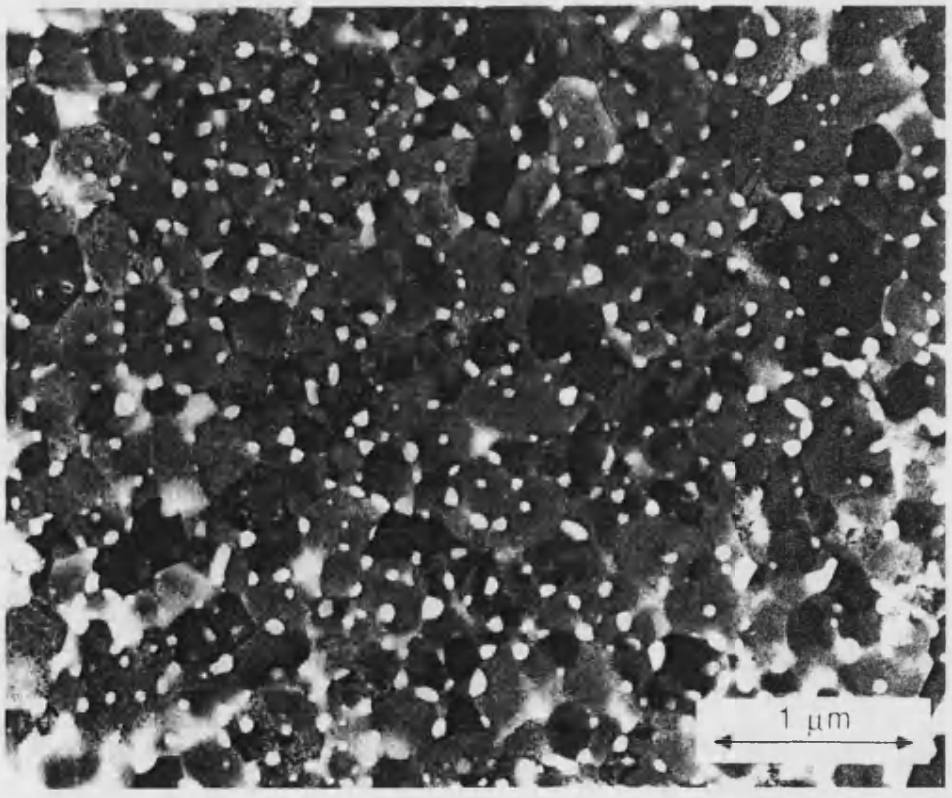


Fig. 1. TEM micrograph of a section parallel to the surface of the thick LPCVD-tungsten disilicide film after implantation with $5 \times 10^{15}$ 150 keV $^{121}Sb^+$ ions $cm^{-2}$

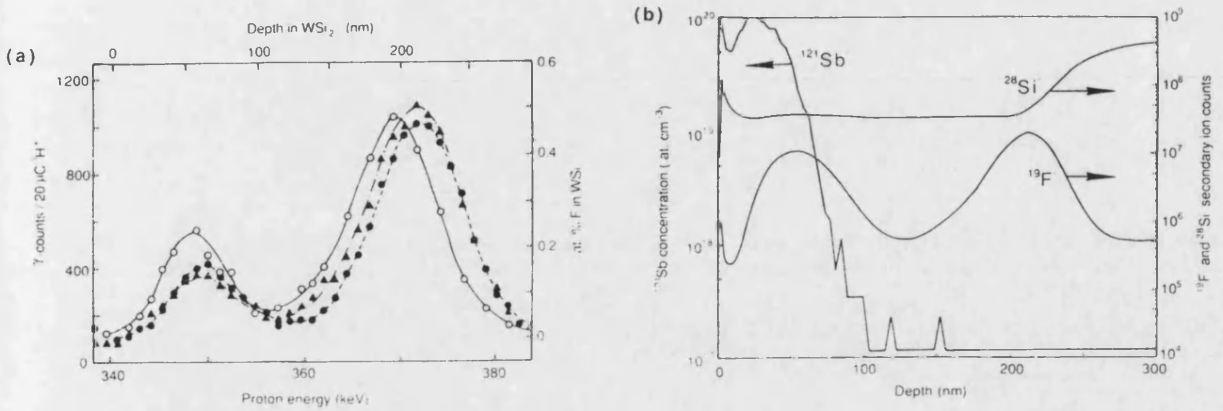


Fig. 2. Depth distributions for the thick LPCVD-tungsten disilicide film after implantation with $5 \times 10^{15}$ 150 keV $^{121}Sb^+$ ions $cm^{-2}$. (a) Depth distributions of fluorine obtained by NRB, the open circles, closed circles and closed triangles denote the as-implanted film, 300 °C and 900 °C 30 min annealed samples respectively. (b) SIMS depth profile for $^{121}Sb$, and the secondary ion yields vs depth for $^{19}F^-$ and $^{28}Si^-$. The depth scales in (a) and (b) have been approximately normalized.

as light regions. The facet structure seen in fig. 1 can be associated with the grains in the polycrystalline tungsten disilicide film, which are of similar dimensions to the tungsten disilicide layer thickness.

The fluorine depth profiles measured by NRB (fig. 2a) and SIMS (fig. 2b) are in good agreement. The total fluorine content of the sample that was not heat treated after annealing was $5.9 \times 10^{15}$ F at. $cm^{-2}$. The deeper peak in the fluorine depth profile(s) corresponds to fluorine at, or close to, the silicide/silicon interface [9,11,12] which, according to RBS measurements, is at a depth of 240 nm (assuming the density in the film is that of bulk $WSi_2$). Similar interface peaks have also been observed in LPCVD-W films on Si substrates [7,9]. The concentration scale in fig. 2a should be regarded as a lower limit for the interfacial fluorine peak since this peak may not be fully resolved because of the natural resonance width and the straggling of the proton beam. The shallow fluorine peak was only observed in implanted specimens. The fluorine distribution within as-deposited films was observed to be constant in agreement with SIMS data in the literature [12,13]. Inspection of fig. 2b shows that the mode of the unannealed fluorine depth profile corresponds to a depth in the deep tail of the $^{121}Sb$ SIMS profile where the $^{121}Sb$ ion current (concentration) is about 15% of the maximum value. The concentration of voids was also greatest at depths corresponding to the maximum of the fluorine distribution. The fluorine content of the near-surface implantation-induced fluorine peak is $1.6 \times 10^{15}$ at. $cm^{-2}$, combining this information with a void volume per unit surface area of $6.1 \times 10^{14}$ $nm^3$ $cm^{-2}$ estimated from fig. 1, and assuming all the fluorine is trapped in the voids, yields a gas pressure in the voids of about 1 bar. The fluorine might be incorporated in the voids as a silicon and/or tungsten fluoride, such as $SiF_4$ which is formed when fluorine reacts with excess silicon. In connection with this, it is noteworthy that voids have been observed in $BF_2$-ion-implanted and annealed silicon wafers at depths in the deep tail of the implant range distributions [14,15].

Comparison of the data for different annealing temperatures (fig. 2a) shows that the deep peak is essentially unchanged on annealing at temperatures up to 900 °C for 30 min. (The shift in position of the interfacial fluorine peak is associated with variations in the thickness of the tungsten disilicide film and is of no consequence for this analysis.) The content of the near-surface fluorine peak is reduced after 300 °C annealing for 30 min. However, the content of the implantation-induced peak was independent of temperature for annealing between 500 and 900 °C. This implies that the fluorine that is lost after 300 °C annealing is weakly bound whilst the fluorine that remains in the implantation-induced peak after annealing at 500 °C and above is effectively trapped. The effective trapping of fluorine at high temperatures and the moderate void gas pressure that would result if all the fluorine were trapped in the voids constitutes strong, but not conclusive, evidence that the voids contain fluorine. If this is so the fluorine loss after annealing at 300 °C may be associated with fluorine that is incorporated in the tungsten disilicide.

Ion-implantation-induced trapping of fluorine was also observed in thin LPCVD-$WSi_2$ film samples that were implanted with $5 \times 10^{15}$ 30 keV $^{11}B$ ions $cm^{-2}$, although after annealing at 900 °C for 30 min the total fluorine retention in the samples ($80 \pm 2\%$) did not differ significantly from that of an unimplanted control sample ($78 \pm 2\%$). Similar samples that were implanted with even a low dose of $5 \times 10^{13}$ 150 keV $^{121}Sb$ ions $cm^{-2}$ on the other hand retained 89% of the fluorine

after annealing at 900 °C for 30 min. This is indicative that the damage produced by the displacement cascade is responsible for the void formation. In an effort to inhibit the buildup of the near-surface fluorine peak by annealing out of the defects $^{11}B$ and $^{121}Sb$ implantations into samples maintained at 400 °C by means of a heater were investigated. The fluorine depth profiles were, however, identical to those obtained after room temperature irradiations.

## 4. Conclusions

(a) Implantation with 30 keV $^{11}B$ or 150 keV $^{122}Sb^+$ ions of tungsten disilicide films formed by LPCVD from a gas mixture of $WF_6 + SiH_4$ leads to enhancement in the fluorine concentration at the deep extent of the implanted region and the formation of voids which are most probably fluorine-filled.

(b) Although some loss of fluorine from the $5 \times 10^{15}$ $^{121}Sb^+$ ions $cm^{-2}$ implantation-induced peak takes place as a result of post-implantation annealing at 300 °C for 30 min, most of the fluorine is trapped at temperatures up to 900 °C.

(c) The implantation-induced buildup of fluorine was not inhibited by implantation at 400 °C.

## References

[1] P. Gas, G. Scilla, A. Michel, F.K. Le Goues, O. Thomas and F.M. d'Heurle, J. Appl. Phys. 63 (1988) 5335.

[2] M.J. Cooke, Vacuum 35 (1985) 67.

[3] R.V. Joshi, Thin Solid Films, accepted for publication.

[4] M.Y. Tsai, F.M. d'Heurle, C.S. Petersson and R.W. Johnson, J. Appl. Phys. 52 (1981) 5350.

[5] D. Dieumegard, B. Maurel and G. Amsel, Nucl. Instr. and Meth. 168 (1980) 93.

[6] A. Anttilla, S. Brandenburg, J. Keinonen and M. Bister, Nucl. Phys. A334 (1980) 205.

[7] H.J. Whitlow, Th. Eriksson, M. Östling, C.S. Petersson, J. Keinonen and A. Anttilla, Appl. Phys. Lett. 50 (1987) 1497.

[8] H.J. Whitlow, J. Keinonen, C. Zaring and C.S. Petersson, Semicond. Sci. Technol. 2 (1987) 625.

[9] Th. Eriksson, J.-O. Carlsson, J. Keinonen and C.S. Petersson, J. Appl. Phys., 64 (1988) 3229.

[10] A. Anttilla and J. Keinonen, Int. J. Appl. Radiat. Isot. 24 (1973) 293.

[11] Y. Shioya, T. Itoh, I. Kobayashi and M. Maeda, J. Electrochem. Soc. 133 (1986) 1445.

[12] M. Fukumoto and T. Ohzone, Appl. Phys. Lett. 50 (1987) 894.

[13] D.L. Brors, J.A. Fair, K.A. Monnig and K.C. Saraswat, Proc. 9th Int. Conf. on Chemical Vapour Deposition, eds. McD. Robinson, C.H.J. van den Brekel, G.W. Cullen, J.M. Blocher Jr. and P. Rai-Choudhury (Electrochem. Soc., Pennington NJ, 1984) p. 275.

[14] C.W. Nieh and L.J. Chen, Appl. Phys. Lett. 48 (1986) 1528.

[15] C.W. Nieh and L.J. Chen, J. Appl. Phys. 60 (1986) 3114.

Nuclear Instruments and Methods in Physics Research B 89 (1994) 346–349
North-Holland

NIM B
Beam Interactions with Materials & Atoms

# $^{1}H(^{15}N, \alpha\gamma)^{12}C$ nuclear resonance broadening measurements of hydrogen incorporation during plasma etching of GaAs and $Ga_xIn_{(1-x)}As$ quantum wells

Leif Persson [a,*], Harry J. Whitlow [a], Juhani Keinonen [b], Pauli Torri [b], Ivan Maximov [c], Lars Samuelsson [c], John Knox [d] and Klas G. Malmqvist [a]

[a] *Department of Nuclear Physics, Lund Institute of Technology, Sölvegatan 14, S-223 62 Lund, Sweden*
[b] *Accelerator Laboratory, University of Helsinki, P.O. Box 43, FIN-00014, Helsinki, Finland*
[c] *Department of Solid State Physics, Lund Institute of Technology, Sölvegatan 14, S-223 62 Lund, Sweden*
[d] *Idaho State University, Department of Physics, Box 8106, Pocatello, ID 83209, USA*

Hydrogen incorporated during plasma etching in a $CH_4/H_2/Ar$ electron cyclotron resonance (ECR) plasma might be associated with reported modification of the cathodoluminescence (CL) spectra from quantum well (QW) structures. To investigate this, GaAs substrates and metal organic vapour phase epitaxy (MOVPE)-grown GaAs/$Ga_xIn_{(1-x)}As$/GaAs QW structures were subjected to etching in a $CH_4/H_2/Ar$ plasma with different substrate bias voltages relative to the ECR source.

Hydrogen profiling was carried out using the 6.385 MeV $^{15}N$ energy resonance in the $^{1}H(^{15}N, \alpha\gamma)^{12}C$ nuclear reaction using the low background profiling facility at the University of Helsinki tandem accelerator. The results show that the amount of hydrogen incorporated within 100 nm of the surface is dependent on the plasma bias voltage. Comparison of the QW and GaAs profiles showed that the amount of hydrogen diffusing and trapping at the first buried QW interface must correspond to less than the detection limit of $1.4 \times 10^{18}$ at. $cm^{-3}$ (30 at.ppm). The maximum migration depth was about 100 nm which extends down to the first QW after etching. The photoluminescence (PL) spectra from the QW structures showed no shift or broadening from the unetched samples.

## 1. Introduction

The incorporation of hydrogen into different materials can drastically alter their properties, for example H embrittlement of metals and passivation of electrically active centers in semiconductors [1]. This has led to hydrogenation being an important area of research and considerable research effort has been directed towards semiconductors in order to obtain a better understanding of the effect of hydrogenation in semiconductors. The initial work concentrated on the group IV elements but extensive effort during the last decade has led to an increasing understanding of the effect on III–V materials, even though some properties are still poorly understood such as the diffusion of hydrogen [1]. It is now well known that atomic hydrogen has the ability to passivate and reactivate shallow donors, shallow acceptors and some deep impurity levels in III–V semiconductors [2,3]. During etching in a methane/hydrogen mixture there is a competition between introduction of radiation damage and hydrogen passivation of radiation-induced effects in III–V semiconductors. Photoluminescence (PL) yield enhancements by a factor up to 100 due to hydrogen passivation have been reported [4].

Two sets of experiments were conducted in this study in which both PL and hydrogen profiling measurements were utilised. The first experiment sought to establish if migration and trapping of hydrogen at buried quantum well (QW) structures could be associated with etch induced changes in the luminescence spectra [5]. The QWs were located at different depths to act as probes for detecting process-induced damage. The method of using multiple QWs buried at varying depths as probes for detecting process-induced damage was first introduced by Wong et al. in 1988 [6]. The second experiment sought to determine if the PL signal from the near surface of GaAs is modified by Electron Cyclotron Resonance (ECR) plasma etch associated hydrogen.

## 2. Experimental

Hydrogen profiling was carried out using the $^{1}H(^{15}N, \alpha\gamma)^{12}C$ resonant nuclear reaction method at

* Corresponding author.


*SSDI* 0168-583X(93)E0828-5

the University of Helsinki accelerator laboratory low background facility. $^{15}N^{2+}$ ions from the accelerator laboratory EGP-10-II tandem accelerator were used to excite the 6.385 MeV $^{15}N$ energy resonance [7] and the resulting 4.43 MeV $\gamma$ rays were detected using a coaxial bismuth germanate (BGO) detector. This detector was enclosed in a plastic scintillator for active suppression of cosmic particles and the whole surrounded with 10 cm Pb. The ceiling of the low background facility consisted of $\sim 17$ m of granite rock.

The absolute hydrogen concentration was established using reference samples of Si into which $1 \times 10^{16}$ 20-keV $H^+$ ions $cm^{-2}$ had been implanted in experiment one and $1 \times 10^{16}$ 40-keV $H^+$ ions $cm^{-2}$ in experiment two. In determining the depth scale in GaAs a $^{15}N$ stopping power of 426 eV/$10^{15}$ at. $cm^{-2}$ was used [8] and it was assumed that the GaAs density was that of crystalline bulk GaAs. For Au a stopping power of 655 eV/$10^{15}$ at. $cm^{-2}$ was used. The depth resolution was about 15 nm FWHM at the surface and worsened with increasing depth due to energy straggling. The detection limit, when defined as three times the standard deviation for the background, was $1.4 \times 10^{18}$ at. $cm^{-3}$ (30 at.ppm).

Two types of samples were used for these experiments. One was a semi-insulating GaAs (100), Cr-doped substrate used for the hydrogen profiling characterisations in the second experiment. The second was a QW sample of lattice-mismatched GaAs/$Ga_{0.85}In_{0.15}As$ material containing 3 QWs with the same thickness of 10 monolayers. The barrier layers had a thickness of 200 nm and the top GaAs layer was also 200 nm thick. The whole structure was grown on a thick GaAs buffer layer. The QWs were produced by metal organic vapour phase epitaxy (MOVPE) under reduced pressure.

The reactor used for metal organic reactive ion etching (MORIE) consists of an ECR plasma source with permanent magnets and a downstream chamber. Microwave energy (2.45 GHz) is introduced into the reactor via a coaxial transmission line and a quarter wave antenna which is isolated from the discharge by a ceramic cup. $SmCo_5$ magnets are placed near the cup to provide the 875 G of magnetic field strength required for resonance. A quartz liner is inserted into the source to reduce the loss of active species to the walls. Reactive gases ($CH_4$, $H_2$, Ar) are supplied directly to the ECR discharge zone. In order to control the ion energy, the substrate holder can be negatively biased by a capacitively coupled, 13.56 MHz, variable radio frequency (RF) input power. This made it possible to control the ion energy from about 10 to 300 V which is not easily available for conventional reactive ion etching (RIE) systems. Details of the ECR-MORIE etching reactor have been described elsewhere [9].

The MORIE process was carried out with flow rates of $H_2$, $CH_4$ and Ar of 10.0, 1.5 and 3.6 SCCM, respectively. The pressure in the chamber was about 2 mTorr and the substrate holder was negatively biased to $-50$, $-100$ or $-200$ V during the etching process. The etching rate of GaAs was approximately 5 nm $min^{-1}$ at a bias of 100 V. The estimated temperature of the sample was below 80°C.

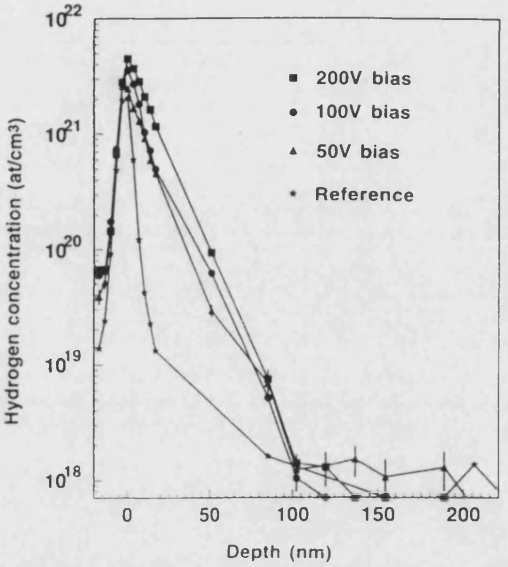


Fig. 1. Hydrogen depth profiles for $Ga_xIn_{(1-x)}As/GaAs$ quantum well structures exposed to ECR plasma etching with various voltages applied. Typical error bars are included for the 50 V biased sample. No noticeable buildup of hydrogen can be seen at around 100 nm where the first well is located.

For optical characterisation a low temperature (5 K) PL setup was used. As an excitation source a continuous wave $Ar^+$ laser with a maximum output of 15 mW at 488 nm was used. An optical fibre was utilised both for excitation of the sample and for collecting emitted light which was dispersed through a double monochromator and detected by an $LN_2$ Ge photo-detector.

Etching of bulk GaAs samples was carried out for 50 min while etching of GaAs/GaInAs QW structures was shorter to remove only about half of the top GaAs layer. Immediately after ECR etching the bulk samples were placed into the evaporation chamber to minimise the exposure to air. A gold film of about 80 nm thickness was evaporated by thermal evaporation ex situ onto the four samples.

## 3. Results and discussion

Fig. 1 shows the hydrogen profiles vs depth for different bias voltages between the ECR plasma and sample in experiment one. Evidently the hydrogen content within 100 nm of the surface increases with

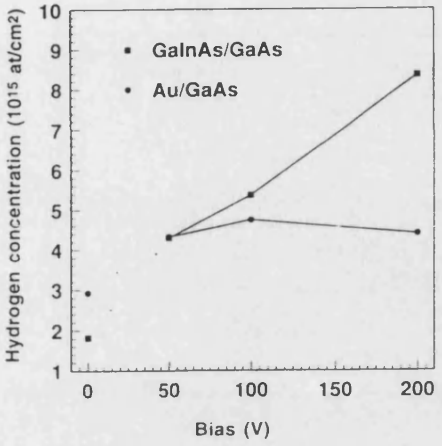


Fig. 2. Correlation between hydrogen concentration and applied bias for the $Ga_xIn_{(1-x)}As/GaAs$ sample and the Au/GaAs sample. Note that 0 V bias means that the samples have not been exposed to any plasma.

bias, see Fig. 2. It may be also clearly seen that no detectable build-up of hydrogen is observed at 100–120 nm where the buried first QW is located. This is consistent with Fig. 3 which presents the recorded PL spectra from the QW samples. Ion irradiation with hydrogen [10] into $In_{0.09}Ga_{0.91}As/GaAs$ QW structures is observed to form satellite PL peaks in thick 4, 8 and 16 nm wells some 15–22 meV below the transitions in the QWs, but no satellite peak was seen in the thinnest 2 nm well. No such peaks are seen in the data of Fig. 3. The reported increase in luminescence intensity from 50 V H plasma and 100 V H or Ar plasma by Swaminathan et al. [5] is not seen in the PL spectra. The damage introduced by the $CH_4/H_2/Ar$ plasma used in this study most likely dominates over the hydrogen passivation mechanism, thereby leading to a decrease in intensity.

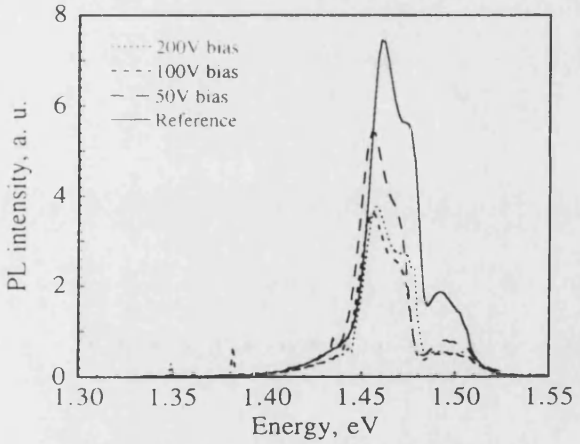


Fig. 3. Normalised PL spectra recorded from the $Ga_xIn_{(1-x)}As/GaAs$ quantum well structures exposed to ECR plasma etching at various biases. No hydrogen related peaks are seen in the spectra.

Surprisingly in the second experiment, in which the samples were covered with a Au layer immediately after etching, the strong correlation between the amount of hydrogen in the (buried) surface layer of GaAs and bias voltage was not observed, see Fig. 2. Again no changes were seen in the PL spectra. Comparison of this finding with that of experiment one suggests that either; (i) the uptake of hydrogen from the atmosphere is correlated with the plasma induced damage in the surface layer; or (ii) deposition of the Au layer leads to loss of ECR-etch induced near surface hydrogen from GaAs.

Regarding (i) we note that the samples for the first experiment were exposed to air for several days prior to analysis, whereas for the second experiment transfer to vacuum took place within minutes of etching and thereafter the deposition of Au. It is also possible that the deposition of Au has led to release of hydrogen from the sample. The energy of Au atoms, $\sim kT$, at the boiling point of Au is small ($\sim 265$ meV) as compared to the energy of the bombarding ions (50, 100 or 200 eV). We do not therefore anticipate physical loss of H due to Au atom bombardment. However, we note that the Au–Ga–As ternary phase diagram [11,12] indicates that at elevated temperatures ($\sim 300$°C) a limited amount of Ga and somewhat less As may be dissolved to form a ternary solid solution [11,12]. We cannot rule out the possibility that such phase formation has led to loss of hydrogen.

It is interesting to speculate why the ECR plasma etch did not lead to hydrogen associated peaks in the PL spectra or hydrogen profiles. 100 eV hydrogen ion exposure [10] is reported to lead to satellite peaks in the PL spectra from $In_{0.09}Ga_{0.91}As/GaAs$ QWs. However, no satellite peak was seen to occur for the 2 nm thick well. It could be that the QWs used in this study, 10 monolayers thick ($\sim 3$ nm), were too thin for any noticeable build-up of hydrogen to occur. We also note that the ECR etch will introduce displacement damage in the surface layers. The maximum kinetic energy transfer to Ga or As atoms by 100 eV $H^+$ is 5.2 eV which is less than the anticipated bulk displacement energies of $\sim 15$–30 eV. Even at the lowest ECR etch bias, 50 V, the carbon and argon ions can transfer sufficient energy, 23 resp. 45 eV, to create sub-surface displacement damage. It may be that this damage acts as an effective getter for hydrogen preventing its migration deeper into the QWs.

## . Conclusion

– Hydrogen migration during ECR etching in a $H_4/H_2/Ar$ plasma does not lead to any noticeable uild-up of hydrogen at buried 10 ML lattice mis-ıatched GaAs/GaInAs QWs, nor any observed ıanges in the PL emission from the QWs.

– Hydrogen incorporation in the surface layers (< )0 nm) of GaAs during ECR etching depends on the as. Plasma etching may lead to enhanced hydrogen ɔtake from the atmosphere (water vapour).

## cknowledgements

This work was funded in part through the FR/NUTEK nanometer structure consortium, and part through the Academy of Finland.

## eferences

[1] S.M. Myers, M.I. Baskes, H.K. Birnbaum, J.W. Corbett, G.G. DeLeo, S.K. Estreicher, E.E. Haller, P. Jena, N.M. Johnson, R. Kirchheim, S.J. Pearton and M.J. Stavola, Rev. Mod. Phys. 64 (1992) 559.

[2] S.J. Pearton, J.W. Corbett and T.S. Shi, Appl. Phys. A43 (1987) 153.

[3] W.C. Dautremont-Smith, Mater. Res. Soc. Symp. Proc. 104 (1988).

[4] W.C. Dautremont-Smith, J.C. Nabity, V. Swaminathan, M. Stavola, J. Chevallier, C.W. Tu and S.J. Pearton, Appl. Phys. Lett. 49 (1986) 1098.

[5] V. Swaminathan, M.T. Asom, U.K. Chakrabarti and S.J. Pearton, Appl. Phys. Lett. 58 (1991) 1256.

[6] H.L. Wong, D.L. Green, T.Y. Liu, D.G. Lishan, M. Bellis, E.L. Hu, P.M. Petroff, P.O. Holtz and J.L. Merz, J. Vac. Sci. Technol. B7 (1989) 1462.

[7] H.J. Whitlow, J. Keinonen, M. Hautala and A. Hautojärvi, Nucl. Instr. and Meth. B 5 (1984) 505.

[8] J.F. Ziegler, J.P. Biersack and U. Littmark, The Stopping and Ranges of Ions in Matter, vol. 1 (Pergamon, New York, 1985).

[9] I. Maximov, A. Gustafsson, H.-C. Hansson, L. Samuelsson, W. Seifert and A. Wiedensohler, J. Vac. Sci. Technol. A 11 (1993) 748.

[10] Z. Sobiesierski, D.A. Woolf, A. Frova and R.T. Phillips, J. Vac. Sci. Technol. B 10 (1992) 1975.

[11] C.J. Cooke and W. Hume-Rothery, J. Less-Common Met. 10 (1966) 42.

[12] R. Beyers, K.B. Kim and R. Sinclair, J. Appl. Phys. 61 (1987) 2195.

# APPENDIX 1

# EXTENT OF CONTRIBUTION TO THE PAPERS INCLUDED IN THIS THESIS

Accelerator-based research by its nature leads to multi-author papers. Moreover, some of my latter work has been done together with Ph.D. students whom I have supervised and the work been included in their theses. To approximately specify my contribution to each stage of a paper the following code, is used. * 0-33 %, ** 33-67 %, *** 67-100 %. The following types of contribution are defined as follows:

- *Instigation* – the extent to which I have been responsible for initiation and development of the idea.
- *Leadership* – the extent to which I have lead the work leading to the paper including obtaining financial support
- *Experimental* – the degree to which I have participated in the experimental measurements
- *Analysis* – the extent to which I have carried out the analysis
- *Manuscript* – the extent of my contribution to the work of manuscript preparation.
- *Docent* – Denotes if the paper has been submitted as part of the evaluation for the Swedish "oavlönad docent" title.
- *Others Ph.D./licentiate* – Denotes if the paper has constituted part of one of my students Ph.D. /licentiate thesis.

**Table A-I Extent of Contribution to the Papers**

| *Paper* | *Instigation* | *Leadership* | *Experi-mental* | *Analysis* | *Manuscript* | *Docent* | *Other Ph.D./licentiat* |
|---|---|---|---|---|---|---|---|
| I | *** | ** | *** | *** | *** | Yes | |
| II | ** | ** | ** | ** | *** | Yes | |
| III | *** | *** | * | * | ** | - | M. Hult |
| IV | *** | *** | * | * | *** | - | |
| V | *** | *** | *** | *** | *** | - | |
| VI | *** | *** | ** | * | * | - | L. Persson |
| VII | *** | *** | ** | ** | * | - | M. Hult |
| VIII | *** | *** | ** | * | * | - | M. Hult |
| IX | ** | ** | ** | * | * | - | M. Hult |
| X | *** | *** | ** | ** | * | - | R. Ghetti |
| XI | ** | ** | * | * | * | - | |
| XII | ** | *** | * | * | *** | - | |
| XIII | *** | *** | ** | *** | *** | - | |
| XIV | ** | * | *** | *** | *** | - | |
| XV | *** | *** | ** | * | ** | - | L. Persson |

# APPENDIX 2

# CURRICULUM VITAE AND SUMMARY OF RESEARCH AND TEACHING WORK

# Curriculum Vitae


| | |
|---|---|
| **Name:** | Harry James WHITLOW |
| **Title:** | Docent |
| **Address:** | Gullregnsvägen 12, S-224 56 LUND, Sweden |
| **Telephone:** | 046-211 1074 (home) 046-222 7630 (work) |
| **Civil status:** | Married, 3 children |
| **Date and place of birth:** | 31 March 1954, Eltham, London, England. |
| **Nationality:** | U.K. Citizen. |
| **Languages:** | English, Swedish. |
| **Present Position:** | Senior lecturer (universitetslektor)<br>Department of Nuclear Physics, Lund Institute of Technology,<br>Box 118, S-221 00 Lund, Sweden. |


---

**Academic Education**

| **Date** | **Institute** | **Academic degree.** |
|---|---|---|
| Oct. 72 - June 76 | School of Physics, University of Bath<br>Claverton Down, BATH, England | Bachelor of Science (B.Sc.) honours<br>Physics with physical electronics. |
| Oct. 76 - Oct. 77 | Department of Applied Physics,<br>Brighton Polytechnic<br>Moulsecoombe<br>BRIGHTON, England | Master of Science (M.Sc.)<br>Applied solid state physics. |
| Oct. 77 - Oct. 80 | School of Mathematical and<br>Physical Sciences<br>University of Sussex<br>Falmer, BRIGHTON, England | Doctor of Philosophy (D.Phil.)<br>Thesis: Low energy ion<br>implantation of silicon. |
| Oct. 87 | The Royal Institute of Technology<br>E-section<br>S-100 44 STOCKHOLM, Sweden | Oavlönad docent (Engl. reader) in<br>Solid State Electronics |

---

**Appointments**

| **Date** | **Position** | **Place of work** |
|---|---|---|
| July 73 - Dec. 73 | Electron microscopist | The Paint Research Assoc.<br>Waldegrave Road<br>TEDDINGTON, England |
| Apr. 77 - Oct. 77 | M.Sc. dissertation<br>(financed by SERC) | Philips Research Laboratories<br>REDHILL, England |
| Nov. 80 - Apr. 81 | Research assistant | University of Sussex<br>Falmer, BRIGHTON, England. |
| May 81 - May 83 | Guest researcher | Det fysiske institut, Aarhus Universitet |
| | (NATO Postdoctoral Fellow) | DK-8000 ÅRHUS Danmark |
| May 83 - Jan. 85 | Researcher<br>(tutkja) | University of Helsinki,<br>Accelerator Laboratory,<br>Hämeentie 100<br>SF-00550 HELSINKI 55, Finland |
| Jan. 85 - Jan. 86 | Research assistant | Tandemacceleratorlaboratoriet<br>Uppsala Universitet, Box 533<br>751 21 UPPSALA, Sweden |

| | | |
|---|---|---|
| Jan. 86 - Nov. 88 | 1st. Research engineer | Institutionen för Mikrovågsteknik |
| Dec. 88 - Nov. 89 | Locum senior lecturer | The Royal Institute of Technology |
| Dec. 89 - Feb. 90 | 1st. Research engineer | S–100 44 STOCKHOLM Sweden |
| Feb. 90 - May 90 | 1st. Research engineer (50%) | |
| May 90 – July 90 | 1st. Research engineer | |
| Feb. 90 - May 90 | 50% "arvodesanställning" as senior lecturer | Division of Cosmic and Subatomic Physics, University of Lund, |
| Aug. 90- Dec. 90 | Locum research engineer | Box 118, |
| Jan. 91 - June 91 | Locum research engineer 25% | S-221 00 LUND, Sweden |
| Jan. 91 - June 91 | Locum senior lecturer 75% | Department of Nuclear Physics |
| July 91 - Aug 94 | Locum senior lecturer | Lund Institute of Technology |
| Sept 94 - | Senior lecturer (Ion Physics) | Box 118, |
| | | S-221 00 LUND, Sweden |

---

**Participation in International Conferences**

4th. International Conference on Ion-Beam Analysis. Århus, Denmark. June 1979.
9th. International Conference on Atomic Collisions in Solids. Lyon, France. July 1981.
3rd. All Union Conference on Interaction of Atomic Particles with Solids. Minsk, USSR. Sept. 1981
3rd. International Conference on Ion-Beam Modification of Materials. Grenoble, France. Sept. 1982.
10th. International Conference on Atomic Collisions in Solids. Bad Iburg, W. Germany. June 1983.
1st. Nordic Conference on Physics in Industry. Tampere, Finland. May 1984.
3rd. Nordic Conference on Application of Scientific Methods in Archaeology. Mariehamn, Åland. Oct. 1984.
7th. International Conference on Ion-Beam Analysis. Berlin, W. Germany. July 1985.
3rd. International Conference on Radiation Effects in Insulators. University of Surrey, U.K. July 1985.
Symposium on Sputtering. Spitz-an-der-Donau, Austria. June 1986.
16th. European Solid State Device Conference. Cambridge, U.K.. Sept. 1986.
4th. International Conference on Radiation Effects in Insulators. Lyon, France. July 1987.
17th. European Solid State Device Research Conference. Bologna, Italy. Sept. 1987.
13th. Nordic Semiconductor Meeting. Saltsjöbaden, Sweden. June 1988.
*Invited* 10th. Conf. on Application of Accelerators in Research and Industry. Denton, USA. Oct. 1988.
1988 Materials Research Society Fall Meeting. Boston, USA. Nov. 1988.
*Invited Speaker at* Workshop on High Energy and Heavy Ion Beams in Material Analysis. Albuquerque, New Mexico, USA. June 1989.
13th. International Conference on Atomic Collisions in Solids. Århus, Denmark. August 1989.
Nuclear Physics at Storage Rings, Lund, Sweden, Sept. 1991.
7th. Nordic meeting on Nuclear Physics, Vigsø Denmark. August 1992.
4th. European Vacuum Conference, June 1994, Uppsala, Sweden,
8th Australian Conference on Nuclear Techniques of Analysis, Lucas Heights NSW, November 1993.
*Invited speaker, Session chairman, session organiser* 13th Int. Symp. on Microanlytical Techniques, Montreux, May 1994
*Invited speaker:* 9th Australian Conference on Nuclear Techniques of Analysis, Newcastle NSW, November 1995.
13th International Conference on Atomic Collisions in Solids, Beijing China July 1997
*Invited speaker, session chairman, session organiser* 13th International Conference on Ion Beam Analysis, Lisbon, Portugal, July 1997

---

**Other Merits**

International Collaborations: working and

CERN WA 93 (August 1990 - June 1991).
CHIC (CELSIUS Heavy Ion Collaboration) from February 1990 (member of CHICSI group from Sept. 1991, CHICSI project manager from 1 Jan. 1993).
Swedish - Australian recoil spectrometry collaboration (LTH-KTH-RMIT (Melbourne)-ANSTO-AINSE) (Swedish delegation leader for experiment in Australia October 1992 November 1993.)

Member of: Swedish Physical Society, European Physical Society,
Svenska vakuumsällskapet (SVS),
Editor of SVS journal "Vakuum Nytt" (Jan. 89 -July 90)
Referee panels: Thin Solid Films (since 1983), Nuclear Instruments and Methods in Physics Research - Section B (since 1984), Nuclear Instruments and Methods in Physics Research -Section A (since 1990).

**M.Sc. Project Students**

| | |
|---|---|
| Ulf Stein | *Computational studies of the stopping ratio for channeled and non-channeled ion trajectories* (Carried out at Univ. of Newcastle NSW) (G) |
| Åsa Karlsson | *Utveckling av ett kompakt rekyldetektorteleskop för experiment vid CELSIUS* (VG) |
| Anneke Kleinpenning | *Characterisation of thin porphyrin layers using ion beam techniques: a study of the effects of ion irradiation* (ERASMUS student Utrecht Univ.) (VG) |
| Anette Gimsenius | *Regional and seasonal variation of seasalt aerosols in New South Wales Australia.* (VG) |
| Thomas Winzell | *Elastic Recoil Detection analysis of hydrogen in polymers and ferroelectrics (VG)* |
| Sander Roosendaal | *Radiation damage in silicon nuclear particle detectors* (VG) (ERASMUS student U. of Utrecht) (VG-cum laude) |
| Mats Leandersson | *Evaluation of Pulse Shape Discrimination techniques for use in the CHICSi detector array* (VG) |
| Jacek Jaworowski | *Characterisation of ΔE-E detector telescopes for CHICSi* (VG) |
| Partik Jönsson | *Development of data evaluation procedures for ToF-E dispersive Recoil Spectrometry* (VG) |
| Per Hansson (Carried | *Development of capilary X-ray optics for PIXE and X-ray diffraction* out at Beijing Normal University) |
| David Lidblom Bath | *Photoluminescence in rare earth metaphosphate glasses* (Carried out at University UK) (G) |

**Supervision of Licentiate degrees**

| | |
|---|---|
| 1990 - 1992 Mikael Hult, | *Rutherford Backscattering and Recoil Spectrometry: Related techniques investigate matter using MeV ions and a nuclear microprobe.* |
| 1995 -1997 Yanwen Zhang, | *Ion Beam Studies of GaAs and Some Metalic Silicides.* |

**Supervision of Doctoral degrees**

| | |
|---|---|
| 1990 - 1994 Mikael Hult, | *Mass and Energy Dispersive Recoil Spectrometry of GaAs Structures* |
| 1992 - 1995 Leif Persson | *Ion Beam Characterisation of Nanometre Structures* |
| 1995 - Yanwen Zhang | Ongoing |
| 1996 - Thomas Winzell | Ongoing |

**Examiner for postgraduate degrees**

Licentiate: *examiner/ opponent*
1995 Elf Erlesand, (KTH, Sweden), *Semiconducting iron disilicide (β-$FeSi_2$) on Silicon: Formation, properties and electrical evaluation*

*detector*
*1997* Göran Thungström (KTH and Sundsvall, Sweden), *An integrated ΔE-E silicon by wafer bonding using cobalt disilicide as a buried ohmic contact*

Ph.D.: *in examiner/ opponent*
1995 Ziwei Fang (U. of Newcastle, Australia) *Time-of-flight detector and its application high energy heavy ion scattering.*

*of*
1994 Qing Yang (U. of Newcastle, Australia) *Stopping Power, Straggling and Scattering Ions in Condensed Matter.*

1996 T. Mareé (Utrecht, Holland) *Ion Beam Studies of Organic Solar Cell Structures*

Member of Ph.D. Examination
Lars Jönsson (Lund, Sweden) 1995,
Fredrik Stillesjö (Uppsala, Sweden) 1995

Board:

**Expert referee for Appointment Boards (sakkunnig)**

1996 Full professorship in Radiation Physics, Royal Melbourne Institute of Technology, Australia.

1997 Associate professorship in Radiation Physics, Royal Melbourne Institute of Technology, Australia.

**Patents**

Swedish patent (ansökan 9601235-6) *An integrated silicon detector* (G. Thungström, C.S. Petersson and H.J. Whitlow)

---

H.J. Whitlow

I certify that the above curriculum vitae is a true record of the facts as known to me.

PETER EKSTRÖM

KLAS MALMQVIST

# Summary of Research Work

Harry J. Whitlow (540331-2233)

## 1. Introduction

The central aspect of my research has been *the interaction of energetic ions with materials and how these interactions can be applied to analyse and modify materials as well as for detecting and characterisation of the bombarding radiation.* This work was been conducted at a number of institutes in England and the Nordic countries. This has not only given a unique insight into the different research cultures in these countries, but most important, the close contacts made through the years have led to establishment of very fruitful long-term collaborations between the various institutes.

My M.Sc. research project was carried out at Philips Research Laboratories, Redhill, U.K. It concerned a study of deep trapping levels in silicon [a] introduced during heat treatment. The objective of this work was identification of the factors responsible for formation of these traps.

## 2. D. Phil. research at the University of Sussex (1977-81)

The initial work concerned development of a U.H.V. scattering chamber, connected to the University of Sussex 3 MeV accelerator, in order to facilitate surface and near-surface ion solid interactions. This chamber was instrumented with a LEED/RHEED/Auger system, UHV compatible surface barrier detectors for Rutherford Backscattering Spectrometry (RBS), high precision 6-axis goniometer with hot stage and a residual gas analyser [b]. The system was used in the latter part of my D.Phil. studies for *measurements of the range distribution and annealing behaviour of low-energy (5-25 keV) arsenic and indium implants in silicon* [2]. This work was undertaken to obtain technologically important data on both the range distributions, in an energy region where the LSS theory was inadequate, and the annealing characteristics of implanted layers with a high implant concentration.

A short period was spent after my D.Phil. work commissioning a microcomputer system for data collection and analysis in luminescence [7] and acoustic experiments [8].

## 3. Postdoctoral work at Aarhus universitet (1981-1983)

After I completed my doctorate at the university of Sussex I was awarded a NATO postdoctoral fellowship to work at the University of Aarhus. Two closely related aspects of atomic transport associated with ion bombardment were investigated. Namely, atomic transport during sputtering of metal alloys and the (then) recently "discovered" phenomena of ion beam mixing.

In the experiments on atomic transport in metal alloys during sputtering, RBS was used to characterise sputtered material collected as a function of ion fluence [12] and ejection angle [4]. The latter type of measurement was developed as *a technique for the in-situ determination of the presence of a composition gradient within the sputter escape-depth.* (i.e. ion-induced surface segregation.) Subsequently the method was used to determine how these concentration gradients were influenced by alloy composition, ion energy, chemical driving force [5] and temperature [4,5,13].

The ion beam mixing studies concentrated on identification of the underlying mechanisms responsible for this phenomena. Mixing experiments at low temperatures (below stage I) with Cu/Al thin film structures with 500 keV Xe [3] and also thin Pt marker layers in Fe [11] gave the important results that *ion-beam mixing has components from long-range anisotropic knock-on as well as isotropic cascade effects and that the latter is coupled to trapping and diffusion of interstitials.*

During the period in Århus I also undertook some *archaeometric studies of patination and wear traces on flint artifacts* [10,20] using RBS, Particle Induced X-ray Emission (PIXE) and Nuclear Reaction Analysis (NRA).

## 4. Research at the University of Helsinki (1983-1985)

My activities at the University of Helsinki accelerator laboratory focused on continuation of the work on ion beam mixing and initiation of work on analysis of hydrogen in materials using the (then) newly commissioned 5 MV tandem van de Graaff accelerator.

Chemical binding effects during ion beam mixing in Al/$SiO_2$ [14] and Al/Si [15] structures have also been studied using the Nuclear Resonance Broadening (NRB) technique and infrared reflection spectrometry.

Hydrogen depth profiling using the NRB technique ($^1H(^{15}N,\alpha\gamma)\,^{12}C$ resonance method) was used to study irradiation-induced defect trapping of hydrogen in silicon [16], for the development of stable hydrogen standards for ion beam analysis and also for precise measurement of the range distributions of ion implanted hydrogen in silicon [19]. I had applied this technique earlier, in the field of archaeometry, to demonstrate that the formation of *worked-material characteristic microwear on the edge of a flint tool* is associated with changes in the chemical composition of the worked edges [10].

A highly significant aspect of my work in Helsinki was the realisation of a long and very fruitful collaboration with docent Mikko Hautala on the application of Monte-Carlo methods in the study of ion solid interactions. Anisotropic effects in the atomic transport that were observed in both the ion beam mixing [3,11,21] and sputtering experiments [4,17] were studied using Monte Carlo simulation. The results showed *that low energy recoils close to the surface have a significant backwards-directed momentum but are forwards directed at greater depth* [18,21,23]. After leaving Helsinki, this work was extended to study the *effect of crystalline structure on recoil flux anisotropies* [23] as well as the *spatial dependence of energy deposition in biological materials* [29]. More recently, we have turned our attention to the problem of how low energy ions with velocity comparable to or below the electron orbital velocities excite charge carriers in band-gap materials [52].

**5. The Uppsala tandem years (1985-1990)**

After moving from Finland in early 1985, I was first attached to the Ion Physics group in Uppsala. After initial work on the development of a large-area ion irradiation system for modification of semiconductors and polymers, I subsequently joined the Department of Solid State Electronics at The Royal Institute of Technology, Stockholm (KTH).

My research activities at KTH were concentrated on the development of MeV ion beam analytical methods for application in semiconductor process technology. In connection with this I have designed and built an *analysis chamber fitted with a computer controlled 20-sample goniometer for RBS and channeling measurements.* The goniometer and associated dedicated data collection system permit automatic analysis of up to 20 samples with a high degree of reproducibility. *This instrument has been the principle instrument for Ion Beam Analysis in Uppsala for the past 11 years.* Following this, I lead the design and construction work on two computer controlled goniometer systems that were constructed for other laboratories.

During this time my close contacts with the University of Helsinki accelerator laboratory led to establishment of a collaboration Helsinki on the study of fluorine redistribution by Nuclear Resonance Broadening (NRB). (Fluorine is involved in many microelectronic processing steps and it degrades the breakdown characteristics of $SiO_2$ films.) Within this collaboration I have led work on: fluorine diffusion in W/Si structures formed by Low Pressure Chemical Vapour Deposition (LPCVD) from $WF_6$ [21,25], fluorine segregation in $BF_2^+$ ion implanted $SiO_2$/Si structures [27,28] and, together with I.B.M. T.J. Watson Research Laboratories Yorktown Heights, bubble formation in LPCVD-$WSi_2$ [36].

The development since 1986 of a new quantitative ion beam analysis method for depth profiling — *mass and energy dispersive recoil spectrometry* [26,32,37] been a major achievement. In this new technique, target atoms which recoil out of a sample that is irradiated with high energy (30-400 MeV) heavy ions, are detected in a detector telescope which measures the velocity and energy for every recoil atom. Subsequent processing of the data yields separate depth profiles for the elements with different masses in the sample. This technique is complimentary to RBS since it is most applicable to measurement of light and medium heavy elements, which are often difficult to analyse by RBS. The investigations that have so far been carried out using the new technique include: mass- and energy resolution [26], suitability of thermally grown $SiO_2$/Si structures as oxygen standards [35], oxygen influence on silicide formation [26,34], depth profiling of Al in $Ga_xAl_{(1-x)}As$ quantum-well structures [26], formation of buried layers by Ion Beam Synthesis (IBS) [30,31,33] and the influence of oil additives on the formation and breakdown of boundary lubricating films [43,66].

During 1989/90 I was also responsible for the development of numerical methods based on Kirchhoff's formalism for the analysis of shallow implant thermal diffusion from secondary ion mass spectrometry data [40,42].

**6. Research in Lund (1990-1996)**

Following the move to Lund my research my research has continued to centre around on heavy ion-matter interactions. This has lead to the instigation of a research group focusing on how ion-matter interactions can be used not only for characterising

and modifying material but also as the basis for detection of radiation.

The accelerator-based materials research is mainly carried out within the NFR-NUTEK Nanometre Structure Consortium. My work in the collaboration has mainly concentrated on solid-phase interactions between thin metal films and III-V semiconductors, which are important for microcircuit contact metallurgy and metallisation. Similarly, the work on detector science and development has been carried on in the CELSIUS Heavy Ion Collaboration (CHIC) which is a Lund based international collaboration that uses heavy ion collisions to study the nuclear phase diagram in states of high compression which are believed to be representative of conditions in super-novae and neutron-stars. Although at first sight the two topics appear rather unrelated, they are unified through the two aspects of ion-matter interactions making possible a number of collaborative investigations [41,45] as well as cross-fertilisation [e.g. 74] where the developments in one field have found application in the other.

***6.1 Materials Research with MeV Ion Beams***

This research has mainly concentrated on the development and application of the Recoil Spectrometry (RS) technique that was developed at KTH for separately profiling Ga and As in GaAs based structures [44] for the study of solid-phase reactions in thin-film metal/III-V and metalloid/III-V semiconductor systems. These systems are important for contact metallurgy. At the present time contact technology is a major limiting factor to why III-V technology is not as developed as Si technology. The aims of the programme are to gather fundamental data on the solid phase interactions of thin-film metal/semiconductor systems and how these are related to predictions based on the equilibrium phase diagrams. *The success of this programme has stimulated the establishment of other research collaborations.* Especially noteworthy has been initiation of a collaboration with Utrecht University on ion-organic semiconductor interactions and a collaboration with Beijing Normal University (BNU) which involves a joint Ph.D. programme for a doctoral student from BNU and initiation of a project on compact X-ray lenses. This work has also been a key ingredient in setting up collaborations with Peking University and Tsinghua University in Beijing as well as a collaboration with the University of Newcastle in Australia.

The first RS study was the Co/GaAs system during rapid thermal annealing [47]. *This represented a significant milestone and it has attracted considerable international interest.* Most significant has been that it lead to the initiation of the informal Australian-Swedish Recoil Spectrometry Collaboration, with researchers from the Royal Melbourne Institute of Technology (RMIT) and the Australian Nuclear Science and Technology Organisation (ANSTO), as well the Department of Solid State Electronics, KTH, Stockholm and Department of Inorganic Chemistry, Uppsala University. *In October 1992 and November 1993 I led the Swedish groups which travelled to Australia to perform measurements using the recently commissioned ANSTO tandem accelerator at Lucas Heights.*

The most extensive investigation undertaken by the collaboration has been a systematic study of strong phosphide forming (Cr,Ti,Ni) [64] and near noble (Pd,Pt) [63,64] transition metals on InP [55,57,59]. This study, which utilised RS and X-ray diffraction measurements, showed that at intermediate temperatures, the near-noble metals formed ternary compounds (including one previously unknown phase, $Pd_5In_2P_2$). At higher temperatures ~500 °C binary metal indides were observed and phosphorus was lost (Pd) or bound in metal phosphide (Pt). The metals that have a strong phosphide-forming tendency (Ti and Cr) formed metallic phosphides and metallic In.

The collaboration has also undertaken studies on a wide range of other systems including:

- Study of the formation of $CoSi_2$ on GaAs [48].
- Study of Na diffusion in $CuInSe_2$ compound solar cells
- Oxygen in $Si_xGe_{(1-x)}$ materials [49].
- Elemental stoichiometry in MOCVD $Al_xGa_{(1-x)}As$ [56].
- High Tc superconductor substrate interactions in the YCBO/MgO system [58].
- Formation of Ni silicide by ion implantation [58].
- Relaxation phenomena in ferroelectric films for DRAM applications.
- Ion beam induced changes in porphyrin organic semiconductors (with Utrecht Univ.)
- Hydrogen loss from polymers under ion bombardment [62,81].
- Synthesis of silicide surface layers using a MEVVA ion source [81,82].

One of my main interests within the collaboration has been the development of the RS technique for *quantitative analysis* of thin films. In this respect I have led development of a multivariate technique [52] for calibration of ToF-E recoil detector telescopes

that not only establishes the absolute energy in terms of recoil mass and channel number, but also simplifies the assignment of recoil masses over wide energy ranges by removing distortions associated with detector non-linearity. This work was extended to develop a semi-empirical equation that describes the width of the mass distribution [54]. This is important in the analysis of III-V semiconductor structures where the mass signals may be partially overlapping. A number of different strategies for signal decomposition have been investigated including, selection of mass gates to minimise cross talk [44], fitting mass distributions [56], pseudo-2D fitting of the mass-energy distributions [63] and application of Ryan and Jamieson's Direct Analysis method [70] (which was developed for PIXE mapping). The most promising and universal method (which is being developed with Dr. Peter Johnston at RMIT) is a refinement technique based on comparison of a theoretical recoil ToF-E spectrum with the experimental data [71]. However, more work needs to be done on accounting for multiple scattering and energy straggling effects [68]. More recently, the focus has shifted towards the use of recoil detector telescopes based on thin Si ΔE detectors [69,83] such as those described below.

We have also applied ion beam methods to other areas of nanometre science such as a study of plasma-etch induced hydrogen defect centres in quantum well structures [51]. This work was a collaboration with the Accelerator laboratory in Helsinki where we used the low background profiling facility to measure ppm levels of hydrogen. Other completed and on-going studies include:

- The development of an atomic nitrogen ion source for group-III nitride epitaxy.
- A photoluminescence study of single dopant atoms introduced into quantum wells by ultra-low dose ion implantation. (With N. Bohr Institute, University of Copenhagen).
- The production of doped regions with nanometre depth and lateral dimensions by e-beam lithography combined with low energy ion implantation.
- Sea-salt aerosol transport in NSW, Australia [65]

***6.2 Research on Detector Science and Technology***

During the first year in Lund I participated in the development of so-called charge-sensitive pad-readout for Multi-Step Avalanche Chambers (MSAC). These will be used for charge particle tracking in ultrarelativistic collision experiments with high charged particle multiplicity (1000 — 3000 for 200 A GeV Pb -> Pb) by the WA 93 collaboration at CERN. In particular I was responsible for design, construction and testing of a flexible test chamber and preamplifier electronics that has been used for study of the charge signals and the obtainable lateral resolution [70].

The main part of my work on detectors has, as noted above, been carried out in the CHIC collaboration. This was initiated from work on developing a ToF-E recoil spectrometer array for the CHIC collaboration. This will be used to measure recoiling target residue fragments from intermediate energy heavy ion reactions at CELSIUS. These particles, have up till now been inaccessible for electronic detectors because their low energy (□ 0.05-0.3 A MeV) which implies that most of them will be completely stopped in conventional target foils. I was responsible for the design study. This included investigation of the factors that govern the mass resolution of ToF-E detector telescopes [41], determination of the response [45] and radiation damage [75] of silicon diode detectors. These findings were exploited in the design of a new type of ToF-E telescope that is more compact than other designs and can be stacked in arrays to span large solid-angle intervals. The prototype has been constructed at The Niels Bohr Institute in Copenhagen and has been successfully tested at The Svedberg-Laboratory in Uppsala.

In 1991 CHIC began planning and developing a Si detector telescope array that will allow characterisation of intermediate mass fragments over about ~3π of solid angle. Since its initiation in September 1991 I have played a central part in the CHICSi working group. (Jan. 1993-July 1997 as technical manager and coordinator of CHICSi). The work which has taken ~50% of my time, has required extensive interaction with European industrial companies as well as coordination of development activities in Sweden, Norway, Denmark and Russia.

CHICSi consists of an array of ~550 detector telescopes in a barrel-shaped configuration [46,80] each with a 12μm Si ΔE, 280/500 μm Si E and a 280 μm flag detector (for flagging events where particles that have passed right through the telescope). These detector telescopes will allow detection of ~0.8-7A MeV intermediate mass fragments. In the most forward directions the telescopes will be augmented with 6 mm thick GSO(Ce) scintillators [50,80] that are read-out by Si photodiodes to facilitate detection of particles up to 60A MeV. Each detector telescope is read out by means of a Si ASIC chip that was developed as part of CHICSi and fabricated using a 1.2 μm Bi-CMOS technique. The chip performs all the analogue signal handling as well as fast digital processing for pile-up flagging and low-level trigger handling.

In particular, I have been responsible for supervision of the work contracted to a Norwegian Industrial Agency (SINTEF) on development of the technology for large-scale production of extremely thin (12 μm) Si □E detectors using an anisotropic etching technique [67,80,83]. Considerable effort had to be put into orchestrating the purchase, according to EC procedures, of the development of production methods and fabrication, because of the performance of the goods could not be specified explicitly. Recent tests of these detectors [78,80] show that these detectors satisfy, or exceed, the specifications defined by the requirements of the CHICSi measurement programme. I was also been responsible for leading the development of the ASIC read-out chip. This is a complex chip that combines the analogue signal chains for all the detectors in a telescope as well as fast and slow shapers, analogue and digital multiplexing,. In addition the chip has fast logic processing that enables on-chip handling of IMF identification as well as identification of global and local pile up. A novel feature of this chip is that it will be mounted inside the UHV scattering chamber. This approach is economically advantageous because by serial read-out of chains of chips the number of expensive vacuum feedthroughs and fast high resolution ADCs needed can be substantially reduced. Leading the development of this chip has involved drawing up the specifications, purchase and consultation on the prototype and simulation work. I also supervise the testing of the prototype chips, which have been shown to function according to specifications.

The requirements of CHICSi lead to the instigation of a detail study on radiation damage in Si detectors [78]. This confirmed that the damage factor is proportional to energy deposition in nuclear scattering over almost 7 decades corresponding to relativistic $\pi_{\pm}$ to low energy heavy Xe. Furthermore the effects of this damage could, to a large degree, be recovered by ~150 °C heat treatment.

Another major on-going project is the development and purchase of the detector and readout chip mounting.

The CHICSi programme has also stimulated work on other schemes for detecting intermediate mass fragments. In particular I have been responsible for leading the testing of a new method based on charge carrier dynamics [61] as well as the development of a calibration technique for IMFs in thin (12-15 μm Si ΔE detectors.) [61]. With colleagues from KTH Stockholm, I have also developed a novel type of integrated Si detector telescope [83]. A patent application for this was filed in March 1996.

**Summary of Teaching and Administration Experience**

**1977-80**

- Demonstrator at Sussex University with responsibility for development and teaching (total about 50 hours ) a laboratory course in crystallography and X-ray diffraction. This was a modular course, which could be altered to suit differing types of students, such as research students, B.Sc. final year students and Swedish students participating in the Uppsala-Sussex exchange programme.

**1980**

- Demonstrator at Sussex University in a laboratory course in electronics (about 20 hours).

**1981-82**

- In Århus, responsible for day to day supervision of two Danish kand. scient. Students' research project.

**1985/86**

- Planned, lectured and examined a 5 point postgraduate course on "Rutherford backscattering spectrometry and other quantitative ion beam analytical methods" (EH 938) at The Royal Institute of Technology (20 hours inc. laboratory exercise)

- Lectured on "Rutherford Backscattering Spectrometry" in a special course for researchers in industry "Avancerade strålnings- och partikelmetoder för materialanalys" organised by "kurssekretariatet vid Uppsala universitet" (5th May 1985) (4 hours).
- Developed and lead laboratory work in RBS for the course "Tillämpad kärnfysik" given at Uppsala University (1986-88)(16 hours).

- Lectured on "The physics and properties of semiconductors" on the course EH 901 "Halvledarekomponenter" at the Royal Institute of Technology (about 3 hours).

**1986/87**

- Planned, lectured and examined on a 4 point course EH 201 "materialfysik" at the undergraduate level on the physics of materials, at the Royal Institute of Technology (36 hours).

**1987/88**

- Planned, lectured and examined a 5 point postgraduate course on "Rutherford backscattering spectrometry and other quantitative ion beam analytical methods" (EH 938) at The Royal Institute of Technology. (20 hours inc. laboratory exercise).

- Planned, lectured and examined a 4 point course EH 201 "materialfysik" at the undergraduate level on the physics of materials, at the Royal Institute of Technology (36 hours).

- Responsible for supervision of two project students. Furthermore, I have been *del facto* responsible for supervision of research students in ion beam analysis and mechanical construction.

**1988/89**

- Planned, lectured and examined a new 2 point postgraduate course: Methodology of Scientific research and Presentation. (8 hours).

- October 1988 to March 1989. Responsible for supervising a postgraduate student .I have been *del facto* responsible for supervision of other research students in ion beam analysis and mechanical construction.

**1990/91**

- Planned, undertook most of the lecturing and examined a 4-point postgraduate course in The Department of Nuclear Physics, LTH on "Quantitative depth profiling methods with MeV ions) (12 hours).

- Planned, lectured and examined a 4-point postgraduate course in The Department of Nuclear Physics, LTH on "Material analysis with MeV ions) (12 hours).

- Supervised a doctoral student (Mikael Hult) in recoil spectrometry from July 1990. Assistant supervisor for a doctoral student in Cosmic and Subatomic Physics. (Roberta Ghetti) from Nov. 1990.

**1991/92**

- Planned, lectured and examined a 5-point continuing education course on "Accelerator Techniques in Materials Science"(TNF-020).

- Responsible for supervision of a doctoral student in recoil spectrometry. From July 1990 assistant supervisor for a doctoral student in Cosmic and Subatomic Physics. (Roberta Ghetti)

**1992/93**

- Technical Chairperson and Co-ordinator of CHICSi collaboration

- Planned, lectured and examined a 5-point continuing education course on "Modern physical measurement methods in Materials Science" (TNF-021).

- Responsible for supervision of two doctoral students in applied nuclear physics (Mikael Hult, Leif Persson)

- Supervised a post-doctoral research worker. (Dr. Mohamed El Bounanai)

- Supervised two project students. (One of which was out stationed at the University of Newcastle, New South Wales, Australia.)

- Taught on a number of laboratory exercises and other short courses:

**1993/94**

- Technical Chairperson and Co-ordinator of CHICSi collaboration

- Supervised two doctoral students. (Mikael Hult and Leif Persson).

- Planned, lectured and examined a 5-point continuing education course on "Modern physical measurement methods in Materials Science" (TNF-021) (12 hours).

- Supervised an ERASMUS student project from Utrecht (Anneke Kleinpenning).

- Supervised a student project on ToF detectors for CHICSi (Åse Karlsson).

**1994/95**

- Technical chairperson and co-ordinator of CHICSi collaboration.

- Lead the preparation of the Invitation to Tender, Detailed Specifications and Assessment of Tenders and agreement of contract for development and fabrication of Si detectors for CHICSi. (This was a complex "public sector purchase" because (i) it involved purchase of the development of an advanced state of the art product and possible purchase of that product if

it achieved our specifications and (ii) the purchase was carried out following EU rules.)

- Responsible for preparation of the Invitation to Tender, Detailed Specifications and Assessment of Tenders and agreement of contract for development and prototype of Si ASIC readout chip for CHICSi.

- External Ph.D. examiner University of Newcastle, Australia (Qing Yang).

- External Licentiate examiner, Royal Institute of Technology, Stockholm (Ulf Erlesand).

  Member of Ph. D. examination board in Uppsala (Fredrik Stillesjö) and Lund (Lars Jönsson).

- Supervised two doctoral students. Leif Persson and Yanwen Zhang. Responsible for negotiation of joint Ph.D. programme for Zhang with Beijing Normal University.

- Responsible for a post-doctoral research worker. (Mohamed El Bouanani)

- Supervised a senior guest researcher (P.N. Johnston, RMIT, Melbourne)

- Supervised two project students (Mats Leandersson and Jacek Jaworowski) in Si detector science.

**1995/1996**

- Technical Chairperson and Coordinator of CHICSi collaboration

- Planned, lectured and examined a 5-point continuing education course on "Modern physical measurement methods in Materials Science" (TNF-021)(12 hours).

- External Ph. D. examiner University of Newcastle, Australia (Ziwei Fang)

- Responsible for a post-doctoral research worker. (Mohamed El Bouanani)

- Supervised a student project on aerosol transport in NSW Australia. (Annette Gimsenius)

- Responsible for supervision of a student project on recoil spectrometry (Patrick Jönsson).

- External expert referee for appointment of Full Professor in Radiation Physics, Royal Melbourne Institute of Technology, Australia.

- Responsible for recruiting a new doctoral student. Supervised two doctoral students (Leif Persson and Yanwen Zhang).

- External Ph. D. opponent at University of Utrecht (Tom Mareé).

- Responsible for planning a new course (5-credits) on accelerators in applied science for teachers.

- Lead negotiations on setting up exchange agreements with Beijing Normal University, Peking University and Tsinghua University in China.

**1996/97**

- Technical Chairperson and Coordinator of CHICSi collaboration. (till 970830)

- Responsible for supervision of two doctoral students (Thomas Winzell, Yanwen Zhang)

- Conducted discussions for instigation of inter-university agreement with Royal Melbourne Institute of Technology, Victoria, Australia.

- Responsible for purchasing according to EU procedures, development and fabrication of CHICSi detector module circuit boards.

- Responsible for supervision of a Swedish students project on X-ray lenses in Beijing (Per Hansson).

- Established and co-supervised a student project at The University of Bath, UK (David Lindblom)

- Expert referee for appointment of associate professorship at Royal Melbourne Institute of Technology, Australia.

- Examiner for Licentiate thesis at KTH/Mitthögskolan (Göran Thungström).

**1997/98**

- Conducted successful negotiations on inter-university exchange between Lund University and Peking University, China.

- Conducted successful negotiations on inter-university exchange between Lund University and Tsinghua University, China.

- Responsible for invitation to tender, evaluation of bids and official purchase of CHICSi detector mounting.

- Responsible for guest professor working on quantification problems in ToF-E recoil spectrometry. (Prof. Ian Bubb)

- Instigated an on-going industrial research project with ABB-Atom with participation and recruitment of foreign guest professor.

- Partly responsible for lecturing and leading exercises in introductory physics course D1 (Kinematics and experimental methods) for first year computer Science students at LTH.

- Lead exercises in F1 (fluid mechanics and thermodynamics) for first-year technical physics students at LTH.

utskrift: 1998-01-11 Revised: 970111

# Appendix 3
# LIST OF SCIENTIFIC PUBLICATIONS

**Publikationslista** H.J. Whitlow (540331-2233) *(List of publications)*

**Publicerade artiklar** *(Published papers)*

1. Inst.Phys. Conf. Ser. No. 35(1977)35. *Solubility of the group IV chalcogenides in I-III-$VI_2$ compounds.* B.R. Pamplin, T. Ohachi, S. Maeda, P. Negrete, T.P. Elworthy, R. Sanderson and H.J. Whitlow.

2. Nucl. Instrum. and Method. 200(1982)491. *Range distributions and thermal-annealing properties of low-energy arsenic and indium implants in silicon.* H.J. Whitlow, P. Blood, B.W. Farmery, D.J. O'Connor, J.M. Shannon and M.W. Thompson.

3. Appl. Phys. A29(1982)141. *Short- and long-range ion-beam mixing in Cu:Al, Influence of interfacial oxide.* F. Besenbacher, J. Bøttiger, S.K. Nielsen and H.J. Whitlow.

4. Surface Sci. 123(1982)39. *Measurements of angular distributions of sputtered material as a new tool for surface-segregation studies: segregation in CuPt alloys.* H.H. Andersen, V. Chernysh, B. Stenum, T. Sørensen and H.J. Whitlow.

5. Nucl. Instrum. and Method. 209/210(1983)487. *Surface segregation during alloy sputtering and implantation.* H.H. Andersen, B. Stenum, T. Sørensen and H.J. Whitlow.

6. J. Nucl. Material. 115(1983)347. *Lateral stress-induced blistering of aluminium films under helium irradiation.* S.E. Donnelly, M. Renier, A.A. Lucas and H.J. Whitlow.

7. Radiation Effects 72(1983)245. *Measurements of the emission spectra of LiF during thermoluminescence.* P.D. Townsend, K. Ahmed, P.J. Chandler, S.W.S. McKeever and H.J. Whitlow.

8. Catgut Acoust. Soc. Newslett. 40(1983)21. *Analysis of sound spectra from bowed violins and violas.* P. Barnes, P.J. Chandler, L. Cooke, S. Fredin, G. Hammel, P.D. Townsend, H.J. Whitlow and L. Wilzen.

9. Vacuum 33(1983)411. *Apparatus for measurement of the angular distribution of particles sputtered from targets at high temperatures.* H.H. Andersen, B.J. Jeppesen, S. Olesen, B. Stenum, T. Sørensen and H.J. Whitlow.

10. Nucl. Instrum. and Method.218(1983)468.*Wear traces and patination on Danish flint artefacts.* H.H. Andersen and H.J. Whitlow.

11. Nucl. Instrum. and Method. 218(1983)684. *Low-temperature ion-beam mixing of platinum markers in iron.* J. Bøttiger, S.K. Nielsen, H.J. Whitlow and P. Wriedt.

12. Nucl. Instrum. and Method. B2(1984)601. *Transients in the composition of material sputtered from alloy targets.* H.H. Andersen, B. Stenum, T Sørensen and H.J. Whitlow.

13. Nucl. Instrum. and Method. B2(1984)623. *Temperature dependence of the angular distribution of material sputtered from a CuPt alloy.* H.H. Andersen, B. Stenum, T. Sørensen and H.J. Whitlow.

14. Thin Solid Films 115(1984)125. *Ion beam mixing of aluminium films on fused $SiO_2$.* M. Erola, J. Keinonen, H.J. Whitlow, A. Anttila and M. Hautala.

15. Proc. 1st. Nordic Conf. on Physics in Industry. M. Vulli and G. Graeffe (ed.): *Ion beam mixing of Al on Si and $SiO_2$.* J. Keinonen, H.J. Whitlow and M. Erola.

16. Nucl. Instrum. and Method. B5(1984)505. *Thermal- and radiation-stability of hydrogen implanted silicon standards for ion-beam analysis.* H.J. Whitlow, J. Keinonen, M. Hautala, and A. Hautojärvi.

17. Nucl. Instrum. and Method. B6(1985)459. *Angular distribution of particles sputtered from Cu, Pt, and Ge targets by keV ion bombardment.* H.H. Andersen, B.Stenum, T. Sørensen and H.J. Whitlow.

18. Nucl. Instrum. and Method. B6(1985)466. *Momentum and recoil-flux anisotropies in collision-cascades: Influence on sputtered particle angular distributions.* M. Hautala and H.J. Whitlow.

19. Physics Lett. 109A(1985)344. *Range profiles of 25-250 keV hydrogen in silicon.* M. Hautala, J. Keinonen, H.J. Whitlow, P. Tikkanen, M. Uhrmacher and K.P. Lieb.

20. Proc. 3rd. Nordic Conf. on the Application of Scientific Methods in Archaeology, ISKOS 5, T. Edgren and H. Jungner (eds.): *Ion beam analysis methods for determining major and minor element concentrations in artefacts.* H.H. Andersen and H.J. Whitlow.

21. J. Appl. Phys. 58(1985)3248. *Mixing of Al in Si by $Ne^+$ ions.* H.J. Whitlow, J. Keinonen and M. Hautala.

22. Late-News Paper presented at 16th. European Solid State Device Conference, Univ. of Cambridge, U.K. 8-11 Sept. 1986. *Thermal redistribution of process induced fluorine in LPCVD-W/Si contact structures.* H.J. Whitlow, J. Keinonen, T. Erikson, A. Anttila, M. Östling and S. Petersson.

23. Nucl. Instrum. and Method. B18(1987)370. *Ballistic collision cascade anisotropies in amorphous, polycrystalline and single-crystal solids.* H.J. Whitlow and M. Hautala.

24. Le Vide Les Couches Minces N° 236(1987)55. *Formation of imbedded $CoSi_2$ layers by high energy implantation and annealing.* C. Zaring, H. Jiang, M. Östling, H.J. Whitlow and C.S. Petersson.

25. Appl. Phys. Lett. 50(1987)1497. *Fluorine in LPCVD-W/Si contact structures: Inclusion and thermal stability.* H.J. Whitlow, Th. Erikson, M. Östling, C. S. Petersson, J. Keinonen and A. Anttila.

26. Nucl. Instrum. and Meth. B27(1987)448. *Quantitative mass and energy dispersive elastic recoil spectrometry: resolution and efficiency considerations.* H.J. Whitlow, G. Possnert and C. S. Petersson.

27. Semiconductor Science and Technology. 2(1987)625. *Thermal redistribution of fluorine in $BF_2^+$ implanted $SiO_2$/Si Structures*. H.J. Whitlow, J. Keinonen, C. Zaring, and C.S. Petersson.

28. *Redistribution of fluorine from $BF_2^+$ implants in MOS structures.* H.J. Whitlow, J. Keinonen, C. Zaring and C.S. Petersson. in:*Solid State Devices*, (eds.) G. Soncini and P.U. Calzolari, (Elsevier, North Holland, 1988)p.417.

29. International Journal of Mass Spectroscopy and Ion Processes 78(1987)329. *Collision cascade parameters for slow particles impinging on biomolecule targets.* H.J. Whitlow, M. Hautala and B.U.R. Sundqvist.

30. Appl. Phys. Lett. 52(1988)1871. *Mass-dispersive recoil spectrometry studied of oxygen and nitrogen redistribution in ion-beam synthesised buried oxy-nitride layers in silicon.* H.J. Whitlow, C.S. Petersson, K.J. Reeson and P.L.F. Hemment.

31. Proc. European SOI workshop: from material to devices , Meylan, France, 15-17th. March 1988,(ed.) D. Bensahel and G. Bomchil. *Evaluation of light element contamination in SIMOX substrates by Recoil and SIMS analysis.* K.J. Reeson, H.J. Whitlow, R. J. Chater, J. Kilner, C.S. Petersson and P.L.F. Hemment.

32. *Mass-Dispersive Recoil Spectrometry — a new method for quantitative depth profiling in microelectronic technology.* H.J. Whitlow and C. S. Petersson. Proc. Nordic Semiconductor Meeting, Stockholm June 5—8, 1988.(ed.) M. Östling, p 360.

33. *Mass- and energy dispersive recoil spectrometry studies of light element contamination in ion beam synthesised buried oxide layers in silicon.* H.J. Whitlow, K.J. Reeson, P.L.F. Hemment and C.S. Petersson. in:

*Selected Topics in Electronic Materials*,(eds.) B.R. Appleton, D.K. Bielsen, W.L. Brown and J.A. Knapp, Materials Research Society Extended Abstracts EA18(1988)149.

34. J. Appl. Phys.65(1989)567. *A quantitative study of oxygen behaviour during $CrSi_2$ and $TiSi_2$ formation.* H. Jiang, H.J. Whitlow, M. Östling, E. Niemi, F.M. d'Heurle and C.S. Petersson.

35. Nucl. Instrum. and Methods B36(1989)53.*Thermally grown $SiO_2$ films as standards for elastic recoil detection analysis.* H.J. Whitlow, A.B.Ch. Andersson and C.S. Petersson.

36. Nucl. Instrum. and Methods B40/41(1989)595.*Ion implantation induced fluorine agglomeration in tungsten disilicide prepared by low-pressure chemical vapour deposition.* C.S. Petersson, H.J. Whitlow, J. Keinonen, F. M. d'Heurle, F.K. Le Goues, Rajiv V. Joshi, Gerald Scilla and O. Thomas.

37. *Mass and energy dispersive recoil spectrometry, a new quantitative depth profiling technique for microelectronic technology.* H.J. Whitlow, Proc. High energy and heavy ion beams in materials analysis workshop, Albuquerque, New Mexico, June 14-17, 1989, Edited by J.R. Tesmer, C.J. Maggiore and M. Natasi, J.C. Barbour and J.W. Mayer, (Materials Research Society, Pittsburgh, 1990), p.73.

38. *Time of flight spectrometry methods for analysis of materials with heavy ions.* H.J. Whitlow, Proc. High energy and heavy ion beams in materials analysis workshop, Albuquerque, New Mexico, June 14-17, 1989, Edited by J.R. Tesmer, C.J. Maggiore and M. Natasi, J.C. Barbour and J.W. Mayer, (Materials Research Society, Pittsburgh, 1990), p.243.

39. Vakuum Nytt no 49(1989)23. *Introduction to Rutherford Backscattering Spectrometry and Recoil Spectrometry*, H.J. Whitlow.

40. Thin Solid Films 193/194(1990)244, *Lattice diffusion of boron in bulk cobalt disilicide,* C. Zaring, P. Gas, B.G. Svensson, M. Östling, and H.J. Whitlow.

41. Nucl. Instrum. and Methods A310(1991)636, *Mass resolution of recoil fragment detector telescopes for 0.05—0.5 A MeV heavy recoiling fragments.* H.J. Whitlow, B. Jakobsson and L. Westerberg.

42. Mat. res. Soc. Proc. 187(1990)131. *Boron diffusion in bulk cobalt disilicide.* ,P. Gas, C. Zaring, B.G.Svensson, M. Östling, H.J.Whitlow and T. Barge.

43. Nucl. Instrum. and Methods Section–B63(1992)445,*Recoil Spectrometry studies of oil additive associated compositional changes in sliding metal surfaces.* H. J. Whitlow, E. Johansson, P.A. Ingemarsson and S. Hokmark.

44. Appl. Phys. Lett. 60(1992)219. *High resolution recoil spectrometry for seperate characterization of Ga and As in $Ga_xAl_{(1-x)}As$ structures.* M. Hult, H.J. Whitlow and M. Östling.

45. Nucl. Instrum. and Meth. A317(1992)235. *Measurements of the response function of silicon diode detectors for heavy ions using a time of flight technique.* R. Ghetti, B.Jakobsson and H.J. Whitlow.

46. Proc. 7th. Nordic meeting on Nuclear Physics, Vigsø, Denmark 17-21 Aug. 1992. *Development of CHICSI: a multi-detector particle telescope for intermediate energy heavy ion physics at CELSIUS.* H.J. Whitlow, V. Avdeichikov, M. Guttormsen, B. Jakobsson, J. Nyberg, K. Nybø, A. Oskarsson, L. Westerberg and the CHIC collaboration.

47. J. Appl. Phys. 75(1994)835. *Rapid thermal Annealing Induced Reactions of Co/GaAs Thin Film Structures: studies using mass and energy dispersive recoil spectrometry* . M. Hult, H.J. Whitlow, M. Östling, M. Andersson, Y. Andersson, I. Linderberg and K. Ståhl.

48. Nuclear Instrum. and Methods B85(1994)916. *RBS and recoil spectrometry of $CoSi_2$ formation on GaAs.* M. Hult, H.J. Whitlow, M. Östling, N. Lundberg, C. Zaring, D.D. Cohen, N. Dytlewski, P.N. Johnston and S. R.Walker.

49. Nuclear Instruments and Methods-B85(1994)907. *Mass and energy dispersive recoil spectrometry of $Si_xGe_{1-x}$ grown by electron beam evaporation,* P.N. Johnston, S. R. Walker, I.F. Bubb, D.D. Cohen, N. Dytlewski, M. Hult, H.J. Whitlow, C. Zaring and M. Östling.

50. Nuclear Instrum. and Methods A336(1993)381, *Light output and energy resolution of BGO and GSO scintillators for light ions,* V.V. Aveideichikov, L. Bergholt, M. Guttormsen, J.E. Taylor, L. Westerberg, H.J. Whitlow, Yu. A. Bordenko and S.F. Burachas .

51. Nuclear Instum. and Methods Section-B B89(1994)346 *$^{15}N(^1H,\alpha\gamma)^{12}C$ Nuclear resonance broadening measurements of hydrogen incorporation during plasma etching of GaAs and $Ga_xIn_{(1-x)}As$ quantum wells.* L.Persson, H.J. Whitlow, J. Keinoinen, P. Torri, I. Maximov, L. Samulesson, J. Knox and K.G. Malmqvist.

52. Nucl. Instrum and Methods B94(1994)530. *Multivariate analysis method for energy calibration and mass assignment in recoil spectrometry,* M. El Bouanani, H.J. Whitlow, M. Hult, L. Persson, M. Andersson, P.N. Johnston, S. R. Walker, I.F. Bubb, D.D. Cohen, N. Dytlewski, C. Zaring and M. Östling.

53. J. Appl. Phys. 77(1995)2435. *Formation of thin films of $CoSi_2$ on GaAs.* M. Hult, L. Persson, M. El Bouanani, H.J. Whitlow, M. Andersson, M. Östling, N. Lundberg, C. Zaring, K. Georgsson, D.D. Cohen, N. Dytlewski, P.N. Johnston, S. R. Walker.

54. Nucl. Instrum. and Methods B101(1995)263. *Empirical characterisation of mass distribution broadening in ToF-E recoil spectrometry,* M. Hult, M. El Bouanani, L. Persson, H.J. Whitlow, M. Andersson, C. Zaring, M. Östling, D.D. Cohen, N. Dytewski, I.F. Bubb, P.N. Johnston and S.R. Walker.

55. Vacuum,46(1995)737. *Metal/InP thin film reactions: studies using mass and energy dispersive recoil spectrometry,* H.J. Whitlow, M. Andersson, M. Hult, L. Persson, M. El Bouannani, M. Östling, C. Zaring, N. Lundberg, D.D. Cohen, N. Dytlewski, P.N. Johnston, I.F. Bubb and S. R. Walker.

56. Nucl. Instrum. and Methods, A353(1994)563. *Mass and energy dispersive recoil spectrometry of MOCVD grown $Al_xGa_{(1-x)}As$.* S.R. Walker, P.N. Johnston, I.F. Bubb, W.B. Stannard, D.D. Cohen, N. Dytlewski, M. Hult,H.J. Whitlow, C. Zaring, M. Östling and M. Andersson.

57. *Recoil Spectrometry: a suitable method for studing interfacial reactions in metal-InP systems.* L. Persson, M. Hult, H.J. Whitlow, M. El Bouanani, M. Andersson, I.F. Bubb, P.N. Johnston, S.R. Walker, D. D. Cohen, N. Dytlewski, N. Lundberg, C. Zaring and M. Östling. in: Application of Particle and Laser Beams in Materials Technology, (ed.) P. Misaelides, (Kluwer Academic Publishers, Netherlands) p. 471.

58. Nucl. Instrum. and Methods B94(1994)277. *Materials characterisation using heavy ion time of flight spectrometry.* J.W. Martin, D.D. Cohen, N. Dytlewski, D.B. Garton, H.J. Whitlow and G.J. Russel.

59. Mikrochimica Acta 120(1995)171, *Recoil Spectrometry: Ion accelerator based elemental characterisation of surface layers.* H.J. Whitlow, M. Andersson, M. Hult, L. Persson, M. El Bouanai, M. Östling, C. Zaring, N. Lundberg, D.D. Cohen, N. Dytlewski, P.N. Johnston, I. F. Bubb, S.R. Walker, E. Johannson, S. Hogmark and P. A. Ingemarsson.

60. H.J. Whitlow, M. El Bouanani, L. Persson, M. Hult , P. Jönsson, M. Andersson, M. Östling, C. Zaring, P.N. Johnston, I.F. Bubb, S.R. Walker, W.B. Stannard, D.D. Cohen and N. Dytlewski. *Multivatiate techniques of analysis for ToF—E Recoil Spectrometry Data.* Proc, 9th Australlian Conference on Nuclear Techniques of Analysis.Newcastle NSW, 1995 (ed.) D.J. O' Connor, p.158

61. H.J. Whitlow, J. Jaworowski, M. Leandersson, M. El Bouananai, B. Jakobsson, J. Romanski, L. Westerberg, E.J. Van Veldhuizen and the CHICSi collaboration. *Development of Si-based detectors for intermediat e*

*energy heavy-ion physics at a storage ring accelerator.* Proc, 9th Australlian Conference on Nuclear Techniques of Analysis.Newcastle NSW, 1995 (ed.) D.J. O' Connor, p.2

62. T.R.H. Winzell, I.F. Bubb, R. Short, H.J. Whitlow and P.N. Johnston, *Elastic Recoil Detection Analysis of Hydrogen in Polymers*, Proc, 9th Australlian Conference on Nuclear Techniques of Analysis.Newcastle NSW, 1995 (ed.) D.J. O' Connor, p.164

63. J. Vac. Sci. Tech. A14(1996)2405. *Recoil spectrometry of thin film reactions in the Pd/InP system.* L. Persson, M. El Bouanani, M. Hult, P. Jönsson, H.J. Whitlow, M. Andersson, K. Georgsson, I.F. Bubb, P.N. Johnston, S. R. Walker, D.D. Cohen, N. Dytlewski C. Zaring and M. Östling.

64. J. Appl. Phys. 80(1996)3346. *Interfacial Reaction Studies of Cr, Ni, Ti and Pt Metallisation on InP*, L.Persson, M. El Bouananai, M. Hult, H.J. Whitlow, M.Andersson, I.F. Bubb, P.N. Johnston, S.R.Walker, D.D. Cohen, N.Dytlewski, C. Zaring and M. Östling.

65. *Regional and seasonal variations of fine particle seasalt near the New South Wales Coast during 1992 and 1993.* A. Gimsenius, D.D. Cohen and H.J. Whitlow. Proc. 13th Int. Clean Air Conf. Adelaide, Australia, 22-25 Sept 1996 p. 227-231.

66. Tribologica 16, No. 1(1997)3. *Surface analysis of lubricated sliding metal contacts,* Part 1, *Comparison between conventional and unconventional surface analytical techniques.* E. Johansson, P. A. Ingemarsson, S. Hogmark, P. Redelius, H.J. Whitlow, T. Ericsson and U. Gelius.

67. I.E.E.E. Trans. Nucl. Sci. 44(1997)629. *Thin Detectors for the CHICSi ΔE-E telescope* L. Evensen, T. Westgaard, V. Avdeichikov, L. Carlén, B. Jakobsson, Y. Murin, A. Oskarsson, A. Siwek, H.J. Whitlow, E.J. van Veldhuizen, L. Westerbergy and M. Guttormsen. H.J. Whitlow and B. Jakobsson

68. *Simulation of Time of Flight and Energy Recoil Data in Two Dimensions*, P.N. Johnston, M. El Bouanani, W.B. Stannard, I.F. Bubb, P. Jönsson, Y. Zhang and H. J. Whitlow, in: CP 392, Application of accelerators in Research and Industry, (eds.) J.L. Duggan and I.L. Morgan, (AIP Press, NewYork, 1997). p. 715

69. *Internal Calibration of Hydrogen ERD Spectra Using the Forward Scattered He Signal from a Silicon ΔE-E Telescope.* M. El Bouanani, P.N. Johnston, I.F. Bubb and H.J. Whitlow, in: CP 392, Application of accelerators in Research and Industry, (eds.) J.L. Duggan and I.L. Morgan, (AIP Press, NewYork, 1997). p. 647

70. Nucl. Instrum. and Methods A 391(1997)492, *Two-dimensional electronic readout system for multi-step-avalanche chambers*, L. Carlén, S. Garpman, H.-Å. Gustafsson, H. Löhner, J. Nystrand, A. Oskarsson, I. Otterlund, T. Svensson, E. Stenlund, K. Söderström and H.J. Whitlow.

71. Microelectronic Engineering 37/38(1977)499, *Formation of thin surface films of Ni-, V- and Co-silicide by low energy implantation with a metal vapour vacuum arc ion source*, Y. Zhang, H.J. Whitlow and T. Zhang.

72. *Rutherford Backscattering Spectrometry and Recoil Spectrometry*, H.J. Whitlow and M. Östling, in: Surface *Characterization: A users sourcebook*, (Eds.) D. Brune, R. Hellborg, H.J. Whitlow and O. Hunderi (Scandinavian Scientific Press –Wiley-VCH,Weinheim, 1997) p. 1.

73. *A guide to Surface Analysis*, H.J. Whitlow, K. Kristiannson and O. Hyndari, , in: *Surface Analysis: A users sourcebook*, (Eds in: Surface *Characterization: A users sourcebook*, (Eds.) D. Brune, R. Hellborg, H.J. Whitlow and O. Hunderi (Scandinavian Scientific Press –Wiley-VCH,Weinheim, 1997) p. 244.

74. *Nuclear reaction Analysis*, H.J. Whitlow and R. Hellborg, in: *Surface Analysis: A users sourcebook*, (Eds in: Surface *Characterization: A users sourcebook*, (Eds.) D. Brune, R. Hellborg, H.J. Whitlow and O. Hunderi (Scandinavian Scientific Press –Wiley-VCH,Weinheim, 1997) p. 244.

75. *Reference data tables*, H. J. Whitlow, in: *Surface Analysis: A users sourcebook*, (Eds in: Surface *Characterization: A users sourcebook*, (Eds.) D. Brune, R. Hellborg, H.J. Whitlow and O. Hunderi (Scandinavian Scientific Press –Wiley-VCH,Weinheim, 1997) p. 32.

**Artiklar under utarbetande** *(Papers in preparation)*

76. J. Applied Physics *Monte Carlo studies of energy deposition in silicon diode detectors by energetic heavy ions.* M. Hautala and H.J. Whitlow (In manuscript.)

77. Nucl. Instrum. and Methods B, *Seperation of Mass-Overlapped Recoil Spectrometry Data using Ryan and Jamieson's Dynamic Analysis Method.* L. Persson, H.J.Whitlow, M. El Bouanani, M. Andersson, I.F. Bubb, D.D. Cohen, N. Dytlewski, M.Hult, P.N. Johnston, S.R. Walker, C. Zaring and M.Östling. (Submitted).

78. Nucl. Instrum and Methods. Section B *Effects of energy deposition by nuclear scattering in silicon p-i-n dioded detectors.* H.J. Whitlow, S. Roosendaal, M. El Bounanai, R. Ghetti, P.N. Johnston, B. Jakobsson, R. Hellborg, H. Petersson, P. Omling, Z. Wang and the CHIC collaboration. (Accepted)

79. Nucl. Instrum. and Methods B, *Recoil Spectrometry Studies of thin film reactions in the Si/Pd/GaAs and* $Si/Pd/Al_xGa_{(1-x)}As$ *systems* Y. Zhang, M.Hult, M., L. Persson, H.J.Whitlow, M. El Bouanani, M. Andersson, I.F. Bubb, P.N. Johnston, S.R. Walker, D.D. Cohen, N. Dytlewski, C.Zaring and M.Östling. (In press).

80. Nuclear Physics *CHICSi a* $3\pi$ *detector system for studying heavy ion interactions inside a storage ring.* V. Avdeichikov, L. Carlén, M. Guttormsen, A. Fokin, B. Jakobsson, J. Mårtensson, A.Oskarsson, E.J. van Veldhuizen, L. Westerberg and H.J. Whitlow (Accepted).

81. Nucl. Instrum. and Methods B, *Ion Irradiation degradation of polymers*, Thomas Winzell, I.F. Bubb, R. Short, H.J. Whitlow and P.N. Johnston (Submitted).

82. Nucl. Instrum. and Methods Section B, *Foreign atom incorporation during metal silicide formation by ion beam synthesis*, Y.Zhang, H.J. Whitlow and T. Zhang (Accepted)

83. Nucl. Instrum. and Methods-Section B, *Extremely thin Si* $\Delta E$ *detectors for ion beam analysis*, H.J. Whitlow, T. Winzell and G. Thungström (Accepted)

84. Nucl. Instrum and Methods-Section B, *Detection efficiency of ToF-E recoil telescopes.*, H.J: Whitlow, Y. Zhang, I. F. Bubb, W. Lovland, L. Westerberg and E.J. van Veldhuizen (In manuscript).

**Andra publikationer** *(Other publications)*

A1. Nucl. Instrum and Methods A272(1988)925. **Book Review**, *Symposium of NorthEastern Accelerator Personnel, Nuclear Structure Laboratory, University of Notre Dame, Nov. 3-6, 1986, eds. E.D. Berners, U. Garg and C.P. Browne (World Scientific Publishing Co., Singapore, 1987),* H.J. Whitlow and G. Possnert.

A2. Vakuum Nytt nr. 48 maj 1989, Svenska Vakuumsällskapet, Edited by: H.J. Whitlow.

A3 Vakuum Nytt nr. 49 dec 1989, Svenska Vakuumsällskapet, Edited by: H.J. Whitlow.

A4 Vakuum Nytt nr. 50, jun 1990, Svenska Vakuumsällskapet, Edited by: H.J. Whitlow.

A5. Nucl. Instrum. and Methods B47(1990)477. **Book Review**,*High Energy Ion Beam Analysis of Solids.*, G. Götz and K. Gärtner (eds.), (Akademie-Verlag, Berlin, 1988) H.J. Whitlow

A6. Book Editor: , in: *Surface Analysis: A users sourcebook*, (Eds in: Surface *Characterization: A users sourcebook*, (Eds.) D. Brune, R. Hellborg, H.J. Whitlow and O. Hunderi (Scandinavian Scientific Press – Wiley-VCH,Weinheim, 1997)

A7. *Detector telescopes for low energy recoil nuclei.* H.J. Whitlow, R. Ghetti, R. Hellborg, M. Hult, G. Hyltén, J. Pallon, B. Jakobsson, L. Westerberg, Z. Wang and P. Omling. Nuclear Physics Report LUTFD" / (TFKF-3073) 1-7 / (1993) (Department of Nuclear Physics, Lund Institute of Technology, Sweden, May 1993)

**Avhandlingar** *(Theses)*

B1. *The characterization of recombination levels in silicon introduced by heat treatment.* H.J. Whitlow M.Sc. Dissertation. Brighton Polytechnic 1977.

B2. *Low energy implantation of silicon.* H.J. Whitlow. D. Phil. Thesis. Univ. of Sussex 1980.

**Rapporter m. fl.** *(Reports etc.)*

C1. ПОВЕРХНОСТЬ. *The elemental angular distribution of material sputtered from copper-platinum alloys.* H.H. Andersen, V. Chernysh, B. Stenum, T. Sørensen and H.J. Whitlow. (Refereed and accepted for publication in Russian, status unknown)

C2. *Terminal report on work carried out during tenure of NATO postdoctoral fellowship B/RF/6150.* H.J. Whitlow.

C3. *Notes on the use of thoriated-tungsten filaments in the duoplasmatron ion-source of the Helsinki Tandem Accelerator.* H.J. Whitlow, Dept. of Physics, Univ. of Helsinki, SF-00170 Helsinki, Finland. April 1984.

C4. *KTH goniometer control system* . H.J. Whitlow, KTH Mikrovågsteknik, Stockholm, Sweden. (opublicerad rapport).

C5. *KTH goniometer.* H.J. Whitlow, KTH Mikrovågsteknik, Stockholm, Sweden.

C6. J. Archaeol. Sci. *Characteristic changes in the water concentration profiles in microwear on flint tools.* H.H. Andersen, H.J. Whitlow and H. Juel. Jensen. (In manuscript)

C7. H.J. Whitlow, L. Hansson, C.S. Petersson, R. Bornhed, and G. Wahlsten, *Automatic RBS measurements for semiconductor research: goniometer and data acquisition system design considerations.* Report. TRITA-FTE-8901, KTH Avdelningen för Fasta Tillståndets Elektronik, Stockholm 1988.

C8. M. Guttormsen, V. Avdeichikov, L. Carlén, A. Oskarsson, L. Westerberg, H.J. Whitlow, B. Jakobsson and C. Ekström. *CHICSI (vesion II) A proposal for a multi-detector ΔE-E particle telescope.* M. Guttormsen (ed.) (University of Oslo report UiO/PHYS/93-01 , 1992)

C9. H.J. Whitlow, *TASS Turbo Analysis Support for recoil spectrometry using the CERN Physics Analysis Workstation (PAW) software.* (Dept. of Nuclear Physics, Lund Institute of Technology, Sweden, 1993).

C10. H.J. Whitlow, *A readout scheme for CHICSI in a one VLSI chip per detector telescope senario.* CHICSI technical note. (October 1993).

C11. *Travel Report on visit to Australia and China 20 November 7 December 1995.*

**Undervisningsmaterial** *(Teaching material)*

D1. *Mass dispersive recoil spectrometry — an introduction,* H.J. Whitlow, KTH Avdelningen för Fasta Tillståndets Elektronik, Stockholm 1988.

D2. Laboratory excercise in Rutherford Backscattering Spectrometry, KTH - Avdelningen för Fasta Tillståndets Elektronik, Stockholm, 1988.

D3. Rutherford backscattering spectrometry - laboratoy notes. Avdelningen för kärnfysik, Lunds Tekniska Högskola, Lund 1992.

D4. Computer simulation of ion-solid interactions. Avdelningen för kärnfysik, Lunds Tekniska Högskola, Lund 1992.

# REFERENCES


1. N. Bohr, K. Dan. Vidensk. Mat. Fys. Medd.,18 (1948)No. 18.
2. B.A. Young, B. Cabrera, A.T. Lee and B.L. Dogherty, Nucl. Instrum. Methods A311(1992)195.
3. H. Kraus, J. Jochum, B. Kennather, M. Gutsche, F. V. Fietitzsch and R.L. Mössbauer, Nucl. Instrum. and Methods A326(1993)172.
4. E. Fiorini and T.O. Niinikoski, Nucl. Instrum. and Methods, 224(1984)83.
5. S.A.E. Johansson and J.L. Cambell, PIXE: A novel Method for Elemental Analysis, (Wiley, New-York 1988).
6. S.A.E. Johansson, J.L. Cambell and K.G. Malmqvist Particle-Induced X.ray Emission Spectrometry, (Wiley, New-York 1995).
7. S.A.E. Johansson, Nature. Nature 165,(1950),396.
8. P.D. Townsend and J.C. Kelly, Colour Centres and Imperfections in Insulators and Semiconductors, (Sussex Univ. Press, 1973)p58.
9. H.J. Whitlow and M. Östling, in: Surface Characterization: A Users Source Book. (eds.) D. Brune, R. Hellborg, H.J. Whitlow and O. Hunderi, (VCH-Wiley, 1997)p.254.
10. W.-K- Chu, J.W. Mayer and M.-A. Nicolet, Backscattering Spectrometry. (Academic Press, 1978)
11. J.A. Leavitt, L.C. McIntyre, Jr. and M.R. Weller, in: Handbook of Modern Ion Beam Analysis. (eds.) J.R. Tesmer, M. Nastasi, J.C. Barbour, C.J. Maggiore and J.W. Mayer. (Materials Research Society, Pittsburgh, 1995).
12. H.J. Whitlow and R. Hellborg, in: Surface Characterization: A Users Source Book. (eds.) D. Brune, R. Hellborg, H.J. Whitlow and O. Hunderi, (VCH-Wiley, 1997) p.244.
13. H.H. Andersen, V. Chernysh, B. Stenum, T. Sørensen and H.J. Whitlow., Surface Sci. 123(1982)39.
14. H.H. Andersen, B. Stenum, T. Sørensen and H.J. Whitlow. Nucl. Instrum. and Method. 209/210(1983)487.
15. H. H. Andersen, in: Ion Implantation and Beam Processing of .Materials. (eds.) J.s. Williams and J.M. Poate, (Academic Press,1984)p127.
16. F. Besenbacher, J. Bøttiger, S.K. Nielsen and H.J. Whitlow.,Appl. Phys. A29(1982)141.
17. H.H. Andersen, B. Stenum, T Sørensen and H.J. Whitlow, Nucl. Instrum. and Method. B2(1984)601.
18. G. Amsel, Nucl. Instrum. Methods B118(1996)52.
19. Forward Recoil Spectrometry: Applications to hydrogen determination in solids, (eds.) J. Tirira, Y. Serruys and P. Trocellier, (Academic Press, 1995) p.209..
20. Paper II
21. B.L. Cohen, C.L. Fink and J.H. Degnan, J. Appl. Phys. 43(1972)19.
22. H.J. Whitlow in:, Proc. High energy and heavy ion beams in materials analysis workshop, Albuquerque, New Mexico, June 14-17, 1989, Edited by J.R. Tesmer, C.J. Maggiore and M. Natasi, J.C. Barbour and J.W. Mayer, (Materials Research Society, Pittsburgh, 1990), p.73.

23. J.C. Barbour and B.L. Doyle, in: Handbook of Modern Ion Beam Materials Analsysis, (Eds.) J.R. Tesmenr, M. Nastasi, J.C. Barbour, C.J. Maggiore and J.W. Mayer, (Materials Research Society, Pittsburg, 1995) p. 83.
24. J. L'Ecuyer, C. Brassard, C. Cardinal, J. Chabbal, L. Deschenes, J.P. Labrie, B. Terrault, J.G. Martel and R. St.-Jacques, 47(1976)881.
25. M.W. Thompson, Defects and radiation Damage in Metals, (Cambridge University Press, 1969) p. 90.
26. Ibid ref.10, p. 77.
27. H. Hoffsäs in; Forward Recoil Spectrometry: Applications to hydrogen determination in solids, (eds.) J. Tirira, Y. Serruys and P. Trocellier, (Academic Press, 1995) p.209.
28. J.A. Moore, I.V. Mitchell, M.J. Hollis, J.A. Davis, and L.M. Howe, J. Appl. Phys. 46(1975)52.
29. K.A. Sjölund, P. Kristiansson, M. Elfman, K.G. Malmqvist, J. Pallon, R.J. Utui and C. Yang, Nucl. Instrum. and Methods B124(1997)639.
30. H.J. Whitlow in Proc. High energy and heavy ion beams in materials analysis workshop, Albuquerque, New Mexico, June 14-17, 1989, Edited by J.R. Tesmer, C.J. Maggiore and M. Natasi, J.C. Barbour and J.W. Mayer, (Materials Research Society, Pittsburgh, 1990), p.243.
31. K.J. Reeson, H.J. Whitlow, R. J. Chater, J. Kilner, C.S. Petersson and P.L.F. Hemment in: Proc. European SOI workshop: from material to devices , Meylan, France, 15-17th. March 1988,(ed.) D. Bensahel and G. Bomchil.
32. H.J. Whitlow, K.J. Reeson, P.L.F. Hemment and C.S. Petersson. in: Selected Topics in Electronic Materials,(eds.) B.R. Appleton, D.K. Bielsen, W.L. Brown and J.A. Knapp, Materials Research Society Extended Abstracts EA18(1988)149.
33. H. Jiang, H.J. Whitlow, M. Östling, E. Niemi, F.M. d'Heurle and C.S. Petersson. J. Appl. Phys.65(1989)567.
34. H.W. Schmitt, W.E. Kiker and C.W. Williams, Phys. Rev. 137(1965)B837.
35. H. J. Whitlow, E. Johansson, P.A. Ingemarsson and S. Hokmark. Nucl. Instrum. and Methods Section–B63(1992)445.
36. S.R. Walker, P.N. Johnston, I.F. Bubb, W.B. Stannard, D.D. Cohen, N. Dytlewski, M. Hult,H.J. Whitlow, C. Zaring, M. Östling and M. Andersson.Nucl. Instrum. and Methods, A353(1994)563.
37. Y. Zhang, H.J. Whitlow and T. Zhang. Microelectronic Engineering 37/38(1977)499.
38. E. Johansson, P. A. Ingemarsson, S. Hogmark, P. Redelius, H.J. Whitlow, T. Ericsson and U. Gelius.Tribologica 16, No. 1(1997)3.
39. J.W. Martin, D.D. Cohen, N. Dytlewski, D.B. Garton, H.J. Whitlow and G.J. Russel. Nucl. Instrum. and Methods B94(1994)277.
40. L. Persson, M. Hult, H.J. Whitlow, M. El Bouanani, M. Andersson, I.F. Bubb, P.N. Johnston, S.R. Walker, D. D. Cohen, N. Dytlewski, N. Lundberg, C. Zaring and M. Östling. in: Application of Particle and Laser Beams in Materials Technology, (ed.) P. Misaelides, (Kluwer Academic Publishers, Netherlands) p. 471.
41. L. Persson, H.J.Whitlow, M. El Bouanani, M. Andersson, I.F. Bubb, D.D. Cohen, N. Dytlewski, M.Hult, P.N. Johnston, S.R. Walker, C. Zaring and M.Östling. (Submitted). Nucl. Instrum. and Methods B.

42. P.N. Johnston, M. El Bouanani, W.B. Stannard, I.F. Bubb, P. Jönsson, Y. Zhang and H. J. Whitlow, in: CP 392, Application of accelerators in Research and Industry, (eds.) J.L. Duggan and I.L. Morgan, (AIP Press, NewYork, 1997). p. 715.
43. H.J. Whitlow, M. Andersson, M. Hult, L. Persson, M. El Bouannani, M. Östling, C. Zaring, N. Lundberg, D.D. Cohen, N. Dytlewski, P.N. Johnston, I.F. Bubb and S. R. Walker. Vacuum, 46(1995)737.
44. M. Hult, H.J. Whitlow, M. Östling, N. Lundberg, C. Zaring, D.D. Cohen, N. Dytlewski, P.N. Johnston and S. R.Walker. Nuclear Instrum. and Methods B85(1994)916.
45. L. Persson, M. El Bouanani, M. Hult, P. Jönsson, H.J. Whitlow, M. Andersson, K. Georgsson, I.F. Bubb, P.N. Johnston, S. R. Walker, D.D. Cohen, N. Dytlewski C. Zaring and M. Östling. J. Vac. Sci. Tech. A14(1996)2405..
46. L.Persson, M. El Bouananai, M. Hult, H.J. Whitlow, M.Andersson, I.F. Bubb, P.N. Johnston, S.R.Walker, D.D. Cohen, N.Dytlewski, C. Zaring and M. Östling. J. Appl. Phys. 80(1996)3346.
47. Y. Zhang, M.Hult, M., L. Persson, H.J.Whitlow, M. El Bouanani, M. Andersson, I.F. Bubb, P.N. Johnston, S.R. Walker, D.D. Cohen, N. Dytlewski, C.Zaring and M.Östling. Nucl. Instrum. and Methods B. (In press).
48. L. Van der Hove, R. Wolters, K. Maex, R. De Keersmaecker and G. Declerk, J. Vac. Sci. Technol. B4(1986)1358.
49. C. Zaring Ph.D. thesis, Department of Solid State Electronics, Royal Institute of Technology, Stockholm.
50. K.G. McKay, Phys. Rev. 84(1951)829.
51. J.M. McKenzie, Nucl. Instrum. Methods 162(1979)49.
52. P.H. Gooda, W.B. Gilboy, Nucl. Instrum. Methods A255(1987)222.
53. N. Mardkevich, I. Gertner, J. Felseiner, Nucl. Instrum. Methods A269(1988)599.
54. T. Maisch, Günzler, M. Weslser, S. Kalbitzer, W. Weslser and J. Kemmer, Nucl. Instrum. and Methods A288(1990)19.
55. H. Bethe, Ann. Phys. 5(1930)325.
56. F. Bloch, Ann. Phys. 16(1933)285.
57. E. Bonderup, Penetration of charged particles through matter, 2nd. Edition. Lecture notes, (Institute of Physics, University of Aarhus,1981) p. 40-65.
58. V. Avdeichikov, L. Carlén, M. Guttormsen, A. Fokin, B. Jakobsson, J. Mårtensson, A.Oskarsson, E.J. van Veldhuizen, L. Westerberg and H.J. Whitlow Nuclear. (In press).
59. G. Amsel, C. Cohen and A. L'Hoir in: Ion Beam Surface Layer Analysis, eds. O. Meyer, G. Linker and F. Kappeler, (Plenum, New York, 1976).
60. Swedish patent application. 9601235-6.
61. G. Vizkelethy in: Handbook of Modern Ion Beam Analysis. (eds.) J.R. Tesmer, M. Nastasi, J.C. Barbour, C.J. Maggiore and J.W. Mayer. (Materials Research Society, Pittsburgh, 1995) p. 139
62. J.P. Hirvonen, in: Handbook of Modern Ion Beam Analysis. (eds.) J.R. Tesmer, M. Nastasi, J.C. Barbour, C.J. Maggiore and J.W. Mayer. (Materials Research Society, Pittsburgh, 1995)p.167.
63. K. Horn, W.A. Lanford, K. Rodell and P. Fcalora, Nucl. Instrum. and Methods. B26(1987)559.

64. S.J. Pearton, J.W. Corbett and T.S. Shi, Appl. Phys. A43(1987)153.

65. W.C. Dautremont-Smith, , J.C. Nabity, V. Swaminathan, M. Stavola, J. Chevallier, C.W. Tu and S.J. Pearton, Appl. Phys. Lett. 49(1986)1908.

66. E.J. Sternglass Phys. Rev. 108(1957)1.

67. H.J. Whitlow, D.Phil thesis, University of Sussex 1980.